

# Young stars in the Carina Nebula Complex: Clusters, jets and indications for triggered star formation observed in the mid-infrared with the Spitzer Space Telescope

Henrike Ohlendorf  
B. Sc., M. Sc. hon.

Universitätssternwarte München



Dissertation  
der Fakultät für Physik  
der Ludwig-Maximilians-Universität München

*21. Oktober 2013*

**1. Gutachter:** Prof. Dr. Thomas Preibisch

**2. Gutachter:** Prof. Dr. Roland Diehl

**Datum der mündlichen Prüfung:** 12. Dezember 2013



# Danke

denen, die mit mir diskutiert und Rätsel gelöst haben,  
denen, die sich Löcher in den Bauch haben fragen lassen,  
denen, die Geduld mit mir hatten,  
denen, die mich beruhigt, motiviert und wieder aufgebaut haben,  
denen, die mit mir Ihr Wissen und Ihre Erfahrung geteilt haben,  
denen, die mich immer wieder angetrieben haben,  
denen, die geduldig meine Texte wieder und wieder gelesen haben,  
denen, die gefunden haben, was falsch, unvollständig und falsch geschrieben war,  
denen, die nunki gebändigt haben,  
denen, die mich zusammengestaucht haben, wenn es nötig war,  
denen, die mir Fragen gestellt haben, aus denen ich gelernt habe,  
denen, die mir geholfen haben, egal wie spät es war und wo sie waren,  
denen, die mit mir zusammen an den Papern gearbeitet haben,  
denen, die zugehört haben, wenn mal wieder ein Problem unlösbar erschien,  
denen, die mich mit Lösungen meiner Probleme überraschten,  
denen, die aus den rauchenden Trümmern meiner Festplatte alle meine Daten zogen,  
denen, die mit mir Tee und Schokolade und schräge Gespräche geteilt haben,  
denen, die mir immer wieder Mut gemacht haben,  
denen, ohne die diese Seiten nicht geschrieben worden wären.

The Carina Nebula Complex is known to be an active star-formation region. This work presents a large catalogue of point-like sources assembled from archive data of the Infrared Array Camera (IRAC) onboard the *Spitzer* Space Telescope. This catalogue covers a region of  $2.3^\circ \times 3.0^\circ$ , which makes it the most extended mid-infrared survey undertaken of the Carina Nebula Complex to date. From the catalogue a subsample of candidate young stellar objects is extracted utilising the fact that young stellar objects exhibit typical mid-infrared excesses.

These catalogues are employed to characterise the young stellar population of the Carina Nebula Complex. Using them, it was possible to identify three new extended green objects and five compact green objects and find the probable sources for 28 further objects connected with jets emitted from young stars, such as molecular hydrogen emission-line objects and Herbig-Haro jets. For 17 of them, observational data from the near-infrared (from HAWK-I and 2MASS) to the far-infrared (from the *Herschel* Space Observatory) could be collected and their spectral energy distributions fitted. From the fit parameters, stellar characteristics such as stellar and disk masses could be estimated. No young stellar objects with masses above  $10 M_\odot$  could be evidenced, pointing towards an intermediate-mass population currently forming.

It could be shown that the Gum 31 region on the outer periphery of the Carina Nebula Complex is not only part of the complex but also an important centre of star formation. A large sample of candidate young stellar object was obtained from the WISE All-Sky Data Release, which allowed a detailed comparison with both the candidate young stellar objects from the IRAC catalogue and those identified from *Herschel* observations. Evidence could be found that two modes of triggered star formation are going on in the H II region: Young stellar objects are found in and in front of dust pillars, which is an indicator of radiative triggering, and a ‘collect and collapse’ model of the region was shown to produce results in agreement with the observations.

An objective and large-scale search for clusters of young stellar objects in the complex was performed using a nearest-neighbour algorithm. This search derived 22 clusters not described before. Nine of those are new detections in the fields of previous studies of clusters while the majority are found in fields surveyed for clusters for the first time here. Clusters are also found in agreement with previous studies where study fields overlap, thus corroborating the validity of the study. It is found that  $\sim 40\%$  of the young stellar objects in the Carina Nebula Complex occur in clusters while up to 60% are part of a distributed population. A total population for the  $2.3^\circ \times 3.0^\circ$  study field of  $\sim 200\,000$  young stars is estimated.



Der Carina-Nebel ist als Sternentstehungsregion bekannt. In dieser Arbeit wird ein umfassender Katalog von Punktquellen vorgestellt, der aus Archivdaten der Infrared Array Camera (IRAC) des *Spitzer*-Weltraumteleskops erstellt wurde. Der Katalog deckt eine Region von  $2.3^\circ \times 3.0^\circ$  ab, was diese Studie zur größten Studie des Carina-Nebels im mittleren Infrarotbereich macht, die bisher durchgeführt wurde. Unter Ausnutzung des Umstandes, dass junge Sterne einen typischen Exzess im mittleren Infrarotbereich besitzen, werden aus diesem Katalog Kandidaten für junge Sterne selektiert.

Mithilfe dieser Kataloge wird die junge Sternpopulation des Carina-Nebelkomplexes untersucht. Drei neue ausgedehnte grüne Objekte (*extended green objects*, EGOS) und vier kompakte grüne Objekte konnten entdeckt werden. Für 28 weitere Objekte, die mit Jets aus jungen Sternen verknüpft sind, wie sogenannte *molecular hydrogen emission-line objects* (MHOS) und Herbig-Haro-Jets, konnten die wahrscheinlichen Quellen ermittelt werden. Für 17 von diesen konnten Beobachtungsdaten vom Nahinfraroten (HAWK-I, 2MASS) bis ins Ferninfrarote (*Herschel*-Weltraumteleskop) zusammengetragen und ihre spektralen Energieverteilungen gefittet werden. Aus den Parametern dieser Fits konnten die Eigenschaften der jungen Sterne, wie ihre Masse und die Masse ihrer Scheiben, abgeschätzt werden. Es konnten keine Sterne mit Massen höher als  $10 M_\odot$  nachgewiesen werden, was darauf hinweist, dass die derzeitige Generation junger Sterne sich im mittleren Massenbereich befindet.

Es konnte gezeigt werden, dass die Region Gum 31 im Randgebiet des Carina-Nebelkomplexes nicht nur Teil des Komplexes ist, sondern auch ein wichtiges Zentrum der Sternentstehung. Aus dem WISE-Punktquellenkatalog des gesamten Himmels (WISE All-Sky Data Release) wurde eine umfassende Liste junger Sterne erstellt, die es erlaubte, diese Population junger Sterne mit denen zu vergleichen, die aus *Herschel*-Beobachtungen bekannt sind, sowie mit dem hier erstellten IRAC-Punktquellenkatalog. Es wurden Belege dafür entdeckt, dass in der H II-Region zwei verschiedene Prozesse der getriggerten Sternentstehung aktiv sind: Junge Sterne wurden in und direkt vor Staubsäulen („pillars“) entdeckt, was auf radiatives Triggern hinweist, und es konnte gezeigt werden, dass ein Modell der Region, das auf dem sogenannten „Collect and collapse“-Modell beruht, mit den Beobachtungen gut übereinstimmt.

Eine auf objektiven Kriterien beruhende Suche nach Haufen von jungen Sternen wurde für den gesamten Komplex mithilfe eines „Nearest neighbour“-Algorithmus durchgeführt und 22 neue Haufen konnten gefunden werden. Bei neun von diesen Haufen handelt es sich um Neuentdeckungen im Feld vorhergehender Studien. Die Mehrheit der Neuentdeckungen befindet sich in einem Gebiet, das hier zum ersten Mal nach Haufen durchsucht wird. In den Bereichen, wo Überlappungen mit vorhergehenden Studien auftreten, werden bekannte Haufen auch in dieser Studie identifiziert, was die Gültigkeit der verwendeten Methoden bestätigt. Etwa 40% der jungen Sterne im Carina-Nebelkomplex befinden sich in Haufen, während bis zu 60% sich in einer verteilten Population befinden. Die gesamte Population junger Sterne des Komplexes wird auf  $\sim 200\,000$  abgeschätzt.



# Contents

<b>1</b>	<b>Introduction</b>	<b>13</b>
<b>2</b>	<b>Star formation and young stars</b>	<b>14</b>
2.1	Young stellar objects . . . . .	14
2.1.1	Disks . . . . .	17
2.1.2	Protostellar and early stellar phases . . . . .	18
2.2	Jets and their sources . . . . .	20
2.2.1	Herbig-Haro jets . . . . .	20
2.2.2	Extended and compact green objects . . . . .	21
2.3	Triggered star-formation . . . . .	22
<b>3</b>	<b>The Carina Nebula Complex</b>	<b>24</b>
3.1	Clouds . . . . .	25
3.2	Clusters . . . . .	25
3.3	Gum 31 and NGC 3324 . . . . .	27
3.4	Massive stars . . . . .	28
3.4.1	$\eta$ Carinae and the Homunculus . . . . .	28
3.4.2	Supernovae . . . . .	29
3.5	Young stellar objects . . . . .	30
3.5.1	Pillars . . . . .	32
3.5.2	Star formation rate . . . . .	34
3.5.3	The Pan-Carina YSO Catalogue . . . . .	34
<b>4</b>	<b>Instruments and surveys</b>	<b>37</b>
4.1	Spitzer . . . . .	37
4.1.1	IRAC . . . . .	38
4.1.2	MIPS . . . . .	42
4.2	Herschel . . . . .	43
4.2.1	Pre-stellar and protostellar cores . . . . .	44
4.3	WISE . . . . .	45
4.4	VISTA . . . . .	46
4.5	HAWK-I . . . . .	48
4.6	2MASS . . . . .	49
4.7	LABOCA . . . . .	50
<b>5</b>	<b>Source detection and photometry</b>	<b>51</b>
5.1	MOPEX . . . . .	51
5.1.1	Basic image corrections . . . . .	51
5.1.2	Why not perform simple aperture photometry? . . . . .	52

5.2	Mosaicking . . . . .	52
5.2.1	Initial Setup . . . . .	53
5.2.2	Overlap Settings . . . . .	54
5.2.3	Fiducial Image Frame . . . . .	54
5.2.4	MedFilter . . . . .	54
5.2.5	Detect . . . . .	55
5.2.6	Mosaic Interpolate . . . . .	57
5.2.7	Overlap Correction . . . . .	58
5.2.8	Mosaic Settings . . . . .	58
5.2.9	MedFilter . . . . .	58
5.2.10	Mosaic Interpolate and Detect . . . . .	58
5.2.11	Mosaic Projection . . . . .	59
5.2.12	Mosaic Coverage . . . . .	59
5.2.13	Mosaic Dual Outlier . . . . .	59
5.2.14	Level . . . . .	60
5.2.15	Mosaic Outlier . . . . .	60
5.2.16	Mosaic Box Outlier . . . . .	60
5.2.17	Mosaic RMask . . . . .	60
5.2.18	Mosaic Reinterpolate . . . . .	61
5.2.19	Mosaic CoAdder and Mosaic Combiner . . . . .	61
5.3	Photometry . . . . .	61
5.3.1	APEX Multiframe Settings . . . . .	61
5.3.2	Detect MedFilter . . . . .	62
5.3.3	Point Source Probability . . . . .	62
5.3.4	Detect . . . . .	62
5.3.5	Extract MedFilter . . . . .	62
5.3.6	Fit Radius . . . . .	62
5.3.7	Select Detect . . . . .	63
5.3.8	Source Estimate . . . . .	63
5.3.9	Aperture Photometry . . . . .	63
5.3.10	Select . . . . .	63
5.4	Bandmerging . . . . .	64
5.4.1	Bandmerge and creation of the Bandmerge Spitzer Catalogue (BSC) . . . . .	64
5.4.2	Creation of the Spitzer Point-Source Catalogue (SPSC) . . . . .	64
5.4.3	Sensitivity and completeness . . . . .	66
5.4.4	BSC and SPSC . . . . .	68
5.4.5	Comparison to the catalogue by Smith et al. [2010b] . . . . .	70
<b>6</b>	<b>Identifying young stellar objects</b>	<b>72</b>
6.1	A sample of infrared point sources: Which are young? . . . . .	73
6.2	Selection by IRAC colours . . . . .	73
6.2.1	The SYCC . . . . .	75
6.2.2	Using the full SPSC? . . . . .	77
6.3	Selection by WISE colours . . . . .	77
6.3.1	Contaminant removal . . . . .	77
6.3.2	YSO selection . . . . .	78

6.4	Possible contaminants . . . . .	80
6.5	Comparison with other IRAC cYSO catalogues . . . . .	81
6.5.1	Smith et al. [2010b] . . . . .	81
6.5.2	Povich et al. [2011a]: The PCYC . . . . .	82
<b>7</b>	<b>Jet-driving protostars in the Carina Nebula Complex</b>	<b>87</b>
7.1	Motivation . . . . .	87
7.2	Observational data . . . . .	89
7.2.1	Spitzer images and photometry . . . . .	89
7.2.2	Herschel far-infrared fluxes . . . . .	89
7.2.3	LABOCA sub-mm fluxes . . . . .	89
7.2.4	HAWK-I and 2MASS . . . . .	90
7.3	Revealing jet sources in the Carina Nebula . . . . .	90
7.3.1	The search for sources of the Herbig-Haro jets . . . . .	90
7.3.2	The search for sources of the molecular hydrogen emission-line objects . . . . .	94
7.3.3	The search for extended green objects and compact green objects . . . . .	94
7.4	Characteristics of jet sources . . . . .	95
7.4.1	Radiative transfer modelling of the SEDs . . . . .	95
7.5	Discussion . . . . .	106
7.6	Conclusions . . . . .	107
<b>8</b>	<b>Discovering young stars in the Gum 31 region</b>	<b>108</b>
8.1	Motivation . . . . .	108
8.2	Observational data . . . . .	109
8.2.1	Spitzer images and photometry . . . . .	110
8.2.2	Herschel far-infrared maps . . . . .	112
8.2.3	VISTA near-infrared images . . . . .	113
8.2.4	WISE . . . . .	113
8.3	Morphology . . . . .	113
8.4	Young stellar objects in the Gum 31 region . . . . .	115
8.4.1	Identification of YSO candidates . . . . .	115
8.4.2	Identification of protostars from Herschel data . . . . .	118
8.4.3	Spatial distribution of the candidate young stellar objects . . . . .	119
8.5	SED modelling for sources with both Herschel and Spitzer counterparts . . . . .	130
8.5.1	Modelling of the SEDs . . . . .	131
8.5.2	Results of SED modelling . . . . .	132
8.6	Sources of HH jets . . . . .	134
8.7	Discussion . . . . .	135
<b>9</b>	<b>Clustering properties of the young stellar population of the Carina Nebula Complex</b>	<b>137</b>
9.1	How many cYSOs are indeed YSOs? . . . . .	137
9.2	Combining the MIR-selected samples with a Herschel sample of prestellar objects and protostars . . . . .	139
9.3	Finding clusters . . . . .	141
9.3.1	How to identify YSO clusters? . . . . .	141
9.3.2	YSO density maps . . . . .	143

9.3.3	Defining clusters . . . . .	145
9.4	Investigation of the clusters . . . . .	147
9.4.1	The Gum 31 region . . . . .	147
9.4.2	The central Carina Nebula . . . . .	156
9.5	Comparison to other studies of YSO clusters . . . . .	167
9.5.1	The CCCP X-ray clusters of Feigelson et al. [2011] . . . . .	167
9.5.2	Spitzer cYSO clusters of Smith et al. [2010b] . . . . .	168
9.5.3	The ‘butterfly collection’ of Povich et al. [2011a] . . . . .	168
9.6	Discussion and conclusions . . . . .	169
<b>10</b>	<b>Summary</b>	<b>173</b>
<b>A</b>	<b>Instrument zeropoints</b>	<b>176</b>
<b>B</b>	<b>Removing contaminants from the WISE YSO catalogue</b>	<b>177</b>
<b>C</b>	<b>Reducing the PCYC in ten easy steps</b>	<b>181</b>
<b>D</b>	<b>Test: Why do we not classify sources as cYSOs from the PCYC when they are in the SYCC?</b>	<b>185</b>
<b>E</b>	<b>Minor clusters of young stellar objects</b>	<b>187</b>
<b>F</b>	<b>The X-ray clusters of Feigelson et al. [2011]</b>	<b>194</b>
	<b>Acknowledgements</b>	<b>i</b>
	<b>Abbreviations</b>	<b>ii</b>
	<b>Bibliography</b>	<b>v</b>
	<b>List of Figures</b>	<b>xxiii</b>
	<b>List of Tables</b>	<b>xxvi</b>

# 1 Introduction

The Carina Nebula Complex (CNC) is a large star-forming complex (Chapter 3). It has been the subject of a number of studies, large and small, in wavelengths from the sub-millimeter, with LABOCA, to the X-ray, with *Chandra*. At the same time, it is quite poorly studied in parts, because past studies generally focussed on the central Carina Nebula (CN), disregarding the outer reaches of the complex. The study presented in this work for the first time has uniform coverage of the CNC. It does not focus on the historically well-studied immediate surroundings of  $\eta$  Car nor the prominently star-forming South Pillars. Instead, it applies the same methods for all the field, yielding new results especially in the regions so far unstudied.

The study collects near-infrared observations with the *Spitzer* Infrared Array Camera (IRAC) and combines them with observations in other wavelengths, such as the far-infrared with the *Herschel* Space Observatory and the near-infrared with 2MASS (Chapter 4), to gather information of the very young stars in the complex. Beginning with the raw IRAC observational data, photometry is performed and an unprecedentedly large catalogue of point-like mid-infrared sources in the CNC compiled (Chapter 5).

From this catalogue of infrared-bright point-like sources, candidate young stellar objects (cYSOs) are selected utilising the fact that they display infrared excesses (Chapter 6). With this catalogue of cYSOs that has the largest spatial extent of a CNC young-star catalogue to this point, the large-scale characteristics of the young stellar objects (YSOs) can be studied. Studying them reveals details about the processes governing star-formation (Chapter 2).

One of the phenomena connected with young stars are jets. Known jet objects in the CNC are traced back to their probable sources. The new catalogue provides probable sources and their individual characteristics can be studied (Chapter 7).

Furthermore, a region hitherto poorly studied is brought into focus: The Gum 31 region towards the north-west of the central CN is demonstrated to be a part of the CNC complex. Its young stellar population is described (Chapter 8). Compiling information available not only in the mid-infrared with IRAC, but covering the entire infrared range with 2MASS, WISE and *Herschel*, individual objects can be studied as well as the large-scale distribution characterised.

Finally, the complete IRAC catalogue of cYSOs is subjected to a search for clusters (Chapter 9). There have been studies of YSO clusters in the CN before, but never has such a large region been covered with uniform methods. A list of clusters is derived and while some corroborate clusters discovered by previous studies, a group of twenty-two clusters is entirely new. In some cases this is due to the region being studied for the first time (e. g. in the Gum 31 region), in some cases clusters are discovered in previously studied areas.

Chapters 7, 8 and 9 are based on publications with *Astronomy & Astrophysics* and *The Astronomical Journal* [Ohlendorf et al. 2012, 2013a,b]. These were written in collaboration with Thomas Preibisch, Benjamin Gaczkowski, Thorsten Ratzka, Veronica Roccatagliata, Rebekka Grellmann, Judith Ngoumou and Anna Faye McLeod. Some relevant parts of these publications were also adapted into the introductory chapters of this thesis.

## 2 Star formation and young stars

The work presented here is dedicated to a better understanding of the way stars form in a large stellar association as the Carina Nebula Complex (Chapter 3). The way young stars interact with each other and with their environment, especially more massive stars, can be assessed through this small outtake of the complex environment that is our sky.

The attempt to understand the way a star forms is an essential part of astronomy. However, as the time scales on which a star develops are far outside the reach of any human or even generations of humans (the collapse of a molecular cloud into stars happens on a free-fall timescale on the order of several  $10^5$  yr), the process is, as a *process*, completely inaccessible to observations. It can only ever be accessed through *snapshots* of different stars in different stages of evolution which, collected, emerge into a consistent picture. This is why large surveys play an important role in the study of forming and young stars.

An additional challenge is the fact that the processes in the interior of a star are simply inaccessible to any observer. Fortunately, indirect methods via measurements of temperature, size or emission allow a great deal of understanding even without probing a star. The data gleaned through these methods can be combined with physical knowledge to infer many of the processes taking place inside a star. In this way, the understanding of star formation has developed greatly over the past years and decades. It is, however, very much a study in process. The notions astrophysics has formed about star formation change according to latest research.

The analysis presented in this work will draw on vocabulary like “young stellar object” and “disk”. This chapter aims to lay the foundation for the coming chapters by summarising the basics of star formation and young stars, as understood currently.<sup>1</sup> It does not, and cannot, give a comprehensive overview of the mechanisms of star formation as it is understood today. Stellar evolution from the main sequence and further on is not described, while an emphasis is put on the phenomena connected with young stars that will play a role in coming chapters, such as circumstellar disks (Chapters 6, 7 and 8) and jets (Chapters 7 and 8).

### 2.1 Young stellar objects

From their nascency to their demise, stars undergo many different stages of evolution. In the context of this work, the proto- and early stellar phases are most important. Lada [1987] defines a protostar as “*that part of a molecular core within whose boundary the star formation efficiency approaches 100%.*”

Roughly, the process of low-mass star formation begins with a dense, rotating core forming from a collapsing molecular cloud. The point of instability is reached when the

---

<sup>1</sup>Where no source is given, the fact is “textbook knowledge”. Especially the works of Carroll and Ostlie [1996], Huang and Yu [1998], Hanslmeier [2007], Zinnecker and Yorke [2007] and Bradt [2008] were used in compiling this information.

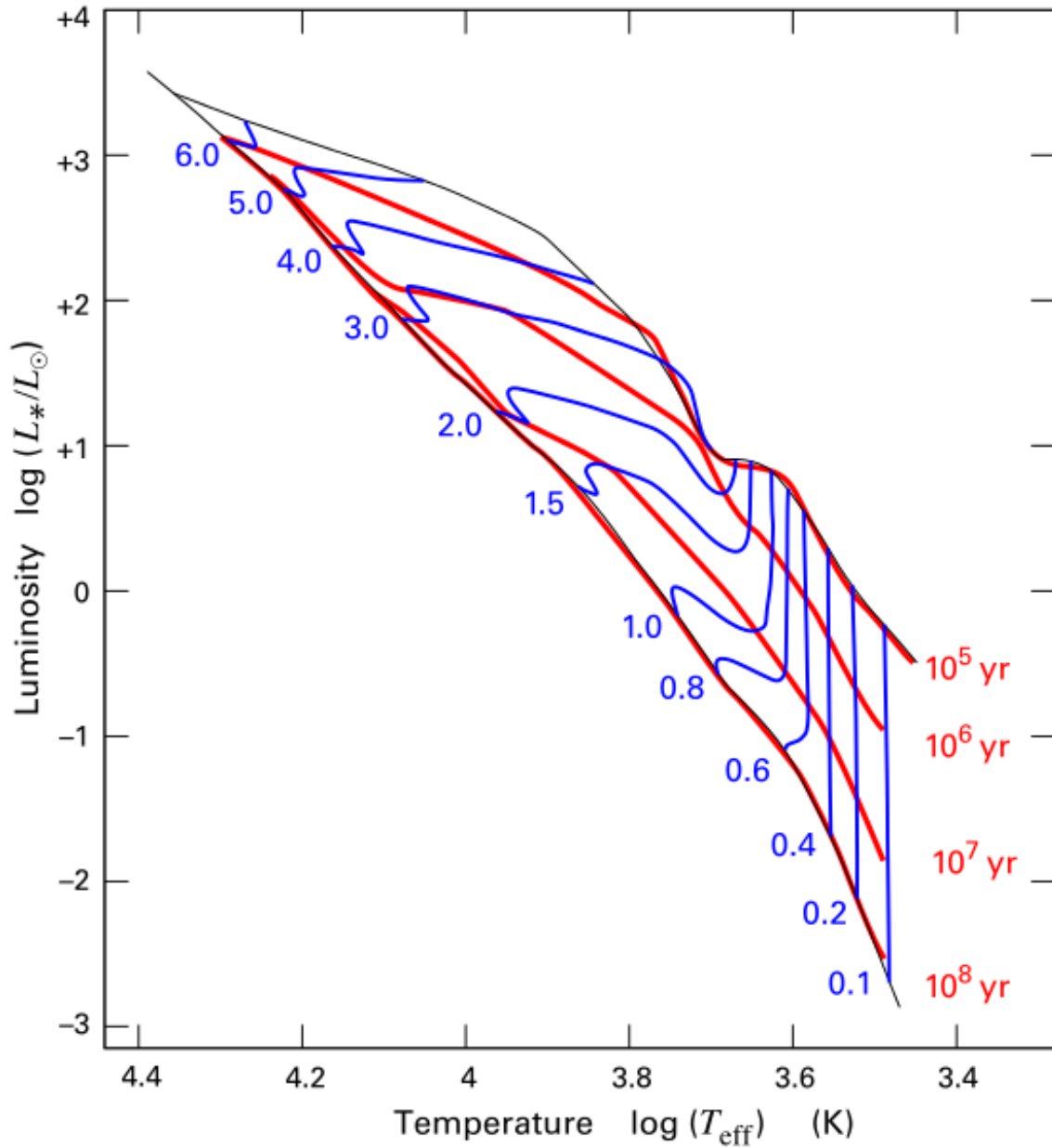


Figure 2.1: The HR diagram [image taken from Stahler and Palla 2004] illustrates the stellar pre-main-sequence evolution. Stars of the masses given in blue in units of the solar mass move towards the main sequence along the different Hayashi tracks given in blue. The red lines are isochrones for the given ages.

molecular cloud surpasses the Jeans mass [Jeans 1902]

$$M_J = \left( \frac{5kT}{G\mu m_H} \right)^{\frac{3}{2}} \left( \frac{3}{4\pi\rho_0} \right)^{\frac{1}{2}}. \quad (2.1)$$

In this equation,  $G$  is the gravitational constant,  $k$  is the Boltzmann constant,  $T$  the cloud temperature,  $m_H$  and  $\mu$  are the hydrogen atomic mass and the mean molecular weight,

## 2 Star formation and young stars

i. e. the mean mass of a gas particle in units of  $m_{\text{H}}$ ;  $\rho_0$  denotes the cloud's initial mass density.

Radiative cooling during the cloud collapse means that the collapse is isothermal. This means that the cloud density rises rapidly. According to Eq. (2.1) the Jeans mass drops and small inhomogeneities in the mass distribution may exceed the Jeans mass. Fragmentation, local collapse, begins. In this way, a single very massive molecular cloud can form many low-mass stars.

Cloud temperatures are typically 10–20 K whereas stars are notably hot. This means that the assumption of isothermality that goes into the derivation of the Jeans mass must at some point be broken. When during the collapse the gas becomes optically thick, thermal energy arising in the collapse cannot be radiated away efficiently any more. The process now becomes slowly adiabatic and the temperatures rise rapidly. Consequently, the initial assumption of isothermality becomes invalid and, since in an adiabatic environment the Jeans mass grows with growing density, fragmentation eventually ends.

The cores created in this process then become unstable and undergo a nonhomologous inside-out collapse. The resulting collapsed core is called a protostellar object when hydrostatic equilibrium is reached, i. e. self-gravity and gas pressure balance out. The centre of this clump then turns into the dense core of the newly forming star. Because necessarily angular momentum must be conserved during the collapse, a disk forms from infalling material. This will remain well into the main-sequence phase of the star.

A protostar is defined as being before hydrogen burning, but there *is* a short phase of deuterium burning in protostars. It has a lower reaction threshold than hydrogen burning and therefore will ignite earlier. When it has ended, the former protostar has reached the Hayashi line of the HR diagram [over the entire luminosity range and at nearly constant effective temperature, it designates the boundary of hydrostatic stability; Hayashi 1966] and is now called a pre-main-sequence (PMS) star.

In this phase, the inflow has ended, while the remaining envelope and disk have dissipated. From the time hydrogen burning ignites and for the main part of its evolution, the star will now stay on the main sequence (cf. Fig. 2.1).

High-mass stars probably follow different mechanisms in their formation than their low-mass companions [e. g. Zinnecker and Yorke 2007]. Due to observational difficulties caused by their nature (low number count, formation on shorter time scales and consequently heavier embedding in undispersed natal clouds) these stars are less well understood.

There are different ways in which the presence of forming or very young stars makes itself known to the observer: Active star formation is, e. g., indicated by  $\text{H}_2\text{O}$  maser emission and bipolar outflows [Billot et al. 2010]. Only in their late phases do protostars begin to emit X-rays [Povich et al. 2011a], which are then a good diagnostic criterion for identifying young stars. The X-ray emission in these stages is due to shocks in their winds for massive stars and to magnetic reconnection flares. It is 2–3 orders of magnitude larger than the X-ray emission observed from the field-star population [Fang et al. 2012]. The perhaps most common tool for the identification, however, and that used in this work, is infrared (IR) excess.

### 2.1.1 Disks<sup>2</sup>

Stars and protostars are often identified from a large sample of point-like sources by their characteristic IR excess. This is defined as the amount of radiation that is detected in excess of that which would be expected from a stellar photosphere. IR excess emanates from dusty circumstellar disks and envelopes [Povich et al. 2011a].

This infrared-excess emission distinctive of very young stars is relatively short-lived. As described above, disks (illustrated in Fig. 2.2) are formed out of dust and gas during the initial collapse of the cloud fragment that is to be a star, conserving angular momentum. The precise formation mechanism is still under debate, especially as the influence of magnetic fields is concerned [Williams and Cieza 2011]. During the further evolution of the young star, the disk is slowly destroyed so that finally the star loses its disk. Within a few Ma, the disk excess fraction in stellar associations—and with it the IR excess fraction—falls rapidly [Haisch et al. 2001a, Briceño et al. 2007] down to a few percent [e.g. Hernández et al. 2007, Preibisch et al. 2011a].

While the star goes through its PMS evolution, the disk is slowly destroyed: Some material is simply accreted onto the star itself. This is true especially in the early stages of the star forming and ceases slowly as the star grows older [Williams and Cieza 2011]. The ultraviolet (UV) radiation of the central star or of nearby stars drives the photoevaporative dissipation of the disk [e.g. Clarke 2007, Williams and Cieza 2011]. Encounters with passing stars also destroy the fabric of the disk.

In intermediate-mass young stellar objects (YSOs) the disk destruction is dominated by photoevaporative dissipation driven by the central star [Hollenbach et al. 1994]. Consequently, the disk lifetime decreases as a function of stellar mass [e.g. Roccatagliata et al. 2011]. A typical disk-evaporation timescale for intermediate-mass stars (including Herbig Ae/Be stars) is  $\lesssim 0.5$  Ma [Hernández et al. 2007, Povich et al. 2009, Povich and Whitney 2010].

For the disk lifetime of a solar-mass classical T Tauri star a typical timescale of disk destruction is  $\sim 2\text{--}3$  Ma [Haisch et al. 2001b, Fedele et al. 2010]. Haisch et al. [2001a] find a maximum lifetime of  $\sim 6$  Ma in their study of young clusters. For high-mass stars the typical disk lifetime is not well restricted [Zinnecker and Yorke 2007]. Disk frequency consequently is dependent on mass, with stars upwards of  $1.2\text{--}1.8 M_{\odot}$  having a far lower disk frequency and therefore lower likelihood of displaying near-IR (NIR) or mid-infrared (MIR) excess [Carpenter et al. 2006, Dahm and Hillenbrand 2007].

The disks themselves are very non-uniform between different candidate young stellar objects (cYSOs). The dust properties within the disk, e.g., depend heavily on the distance towards the central star [van Boekel et al. 2006]. Disk sizes and masses are strongly varied: Williams and Cieza [2011, see references therein] have collected estimates for disk sizes that range from  $\sim 30$  AU to  $\sim 1100$  AU. Observed masses for disks in, e.g., the Orion Nebula Cluster vary between  $0.01\text{--}0.5 M_{\odot}$  [Eisner et al. 2008] and  $0.003\text{--}0.07 M_{\odot}$  [Mann and Williams 2010].

---

<sup>2</sup>The study of disks is very dynamic and currently a topic under much investigation. Therefore, I will give a short overview over the aspects relevant to this work where the indirect detection of disks will later be used as a proxy for the detection of young stars. Disks are also thought to provide the material from which ultimately planetesimals and planets form [e.g. Williams and Cieza 2011]. Because this is an entire and busy field of research in itself and does not touch the subject of this work, it will not be discussed in detail here.

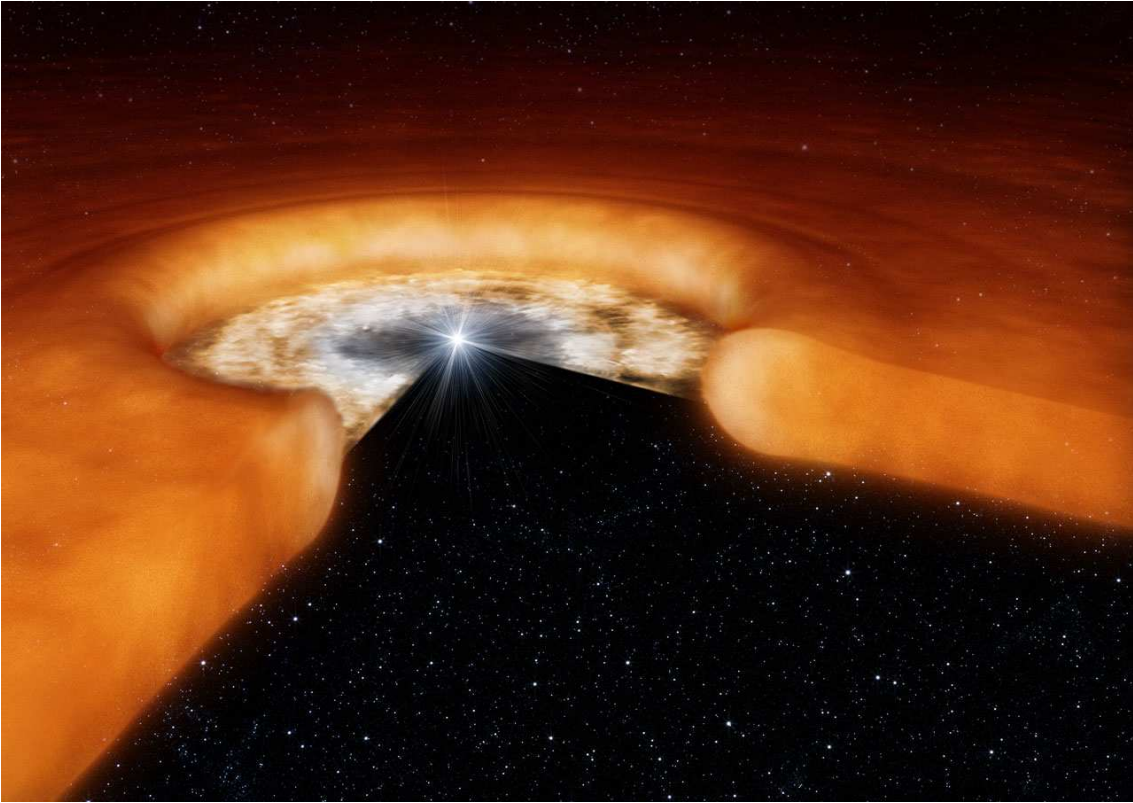


Figure 2.2: Artist’s impression of a YSO with disk. The image is not to scale. (ESO image release eso0835a, image credit: ESO/L. Calçada).

### 2.1.2 Protostellar and early stellar phases

For low-mass stars below about  $2 M_{\odot}$ , nascent stars are commonly grouped into four classes, numbered from 0 to III. This distinction was introduced by Lada [1987] and much refined in later years [e. g. André et al. 1993, Greene et al. 1994, van Boekel et al. 2006]. These classes are, however, only a basic outline and intermediate stages [e. g. Greene et al. 1994] do exist that share characteristics of some states.

Roughly, the protostellar classes trace an evolutionary sequence driven by stellar winds and outflows and are distinguishable by the shape of their spectral energy distributions (SEDs), especially in the NIR and MIR. To achieve a simple means of classification, Lada [1987] defined a spectral index between  $\sim 2$  and  $\sim 10 \mu\text{m}$ :

$$a = \frac{d \log (\lambda F_{\lambda})}{d \log (\lambda)}. \quad (2.2)$$

The shape of an SED, however, also depends on other parameter than the stellar evolutionary stage, for instance the angle under which the disk is observed. Robitaille et al. [2006] therefore caution the reader about the universal application of this terminology and especially the side-by-side use to indicate evolutionary stage on the one hand and SED shape on the other hand. These authors introduce a different classification and refer directly to evolutionary stages instead of classes (see below).

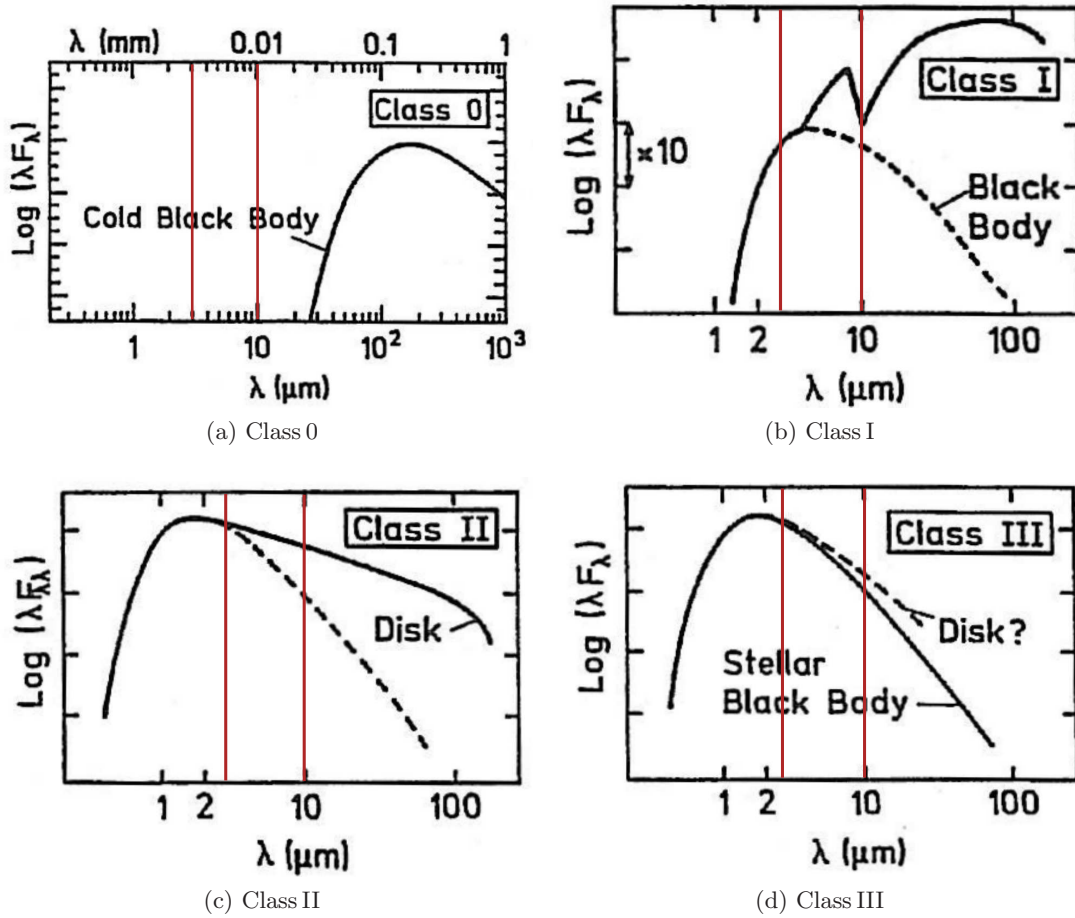


Figure 2.3: Protostellar and early stellar phases [image adapted from André 1994]. The IRAC (Sect. 4.1.1) bands lie approximately between the red lines.

**Class 0** Not stars or even protostars yet, Class 0 objects are molecular cloud fragments that have begun to collapse, forming a core with rapidly increasing density. Through the conservation of the angular momentum that this infalling material carries, these structures acquire disks although the infall is mostly spherically symmetrical. Being in a state before nuclear fusion becomes possible, these objects are cold and only visible in mm and far-IR (FIR) wavelengths, as shown in Fig. 2.3a. Therefore, with IRAC (Sect. 4.1.1), they are undetectable. They are, however, visible in the FIR with, e.g., *Herschel* (Sect. 4.2.1), as Fig. 2.3a illustrates.

**Class I** Class I YSOs still build up mass by accreting circumstellar matter and consequently still are surrounded by disks. However, their centres have become more compact. At this point in their evolution, before their burning processes have become ignited, the objects draw their energy mainly from gravitational energy.

Their spectral index (Eq. 2.2) is  $0 < a \lesssim 3$ , their energy distributions are broader than usual blackbody spectra with the typical excess in the MIR above  $\sim 2 \mu\text{m}$  (Fig. 2.3b) due to their being enshrouded by the gas and dust in their disks. Consequently, they usually are heavily obscured and invisible in the optical [Lada 1987],

but very bright in the IR [van Boekel et al. 2006]. Together with Class II objects and due to their IR excess, they are the YSOs that with IRAC we are able to identify and study.

**Class II** Low-mass Class II objects are known as T Tauri stars after the first discovered specimen of this kind in the constellation of Taurus, the Taurus T association being possibly the best known example of an unbound association. At this point the YSO keeps contracting and so becomes continually smaller and hotter. Those objects have spectral indices (Eq. 2.2) of  $-2 \lesssim a \lesssim 3$ .

Since the obscuring dust that is possibly a remnant of the infalling envelope has been dispensed in this stage, Class II objects are optically visible. In addition, their bright disks can be seen in IR and mm wavelengths (Fig. 2.3c). These disks will disperse within a time span of some millions of years. They are now often referred to as ‘protoplanetary disks’ (‘proplyds’) instead of ‘protostellar disks’. This indicates the changeover in their importance in forming the central star and now in forming planetesimals and planets to orbit the newly-formed star.

**Class III** Some Class III objects retain a gas-poor debris disk. Because most of them are diskless, their spectra show little or no excess IR emission (Fig. 2.3d) and spectral indices (Eq. 2.2) of  $-3 < a \lesssim -2$ . With IRAC, those retaining disks and consequently IR excess may be identifiable. For the others, the MIR portion of a regular stellar photosphere is observed.

### Evolutionary stages of YSO models

A different classification system is introduced by Robitaille et al. [2006]. These authors use evolutionary stages instead of the class system that refers to SED shape. Objects embedded in infalling envelopes are classified as Stage 0/Stage I. These objects may or may not possess disks. When they have acquired an optically thick circumstellar disk they fall into Stage II, whether they have lost their envelopes or not. YSOs have advanced to Stage III when their disks have become optically thin.

## 2.2 Jets and their sources

### 2.2.1 Herbig-Haro jets

Herbig-Haro jets (HH jets)<sup>3</sup> are a prominent phenomenon directly related to star-formation. The release of gravitational potential energy caused by matter accreting onto a nascent star powers bipolar outflows from the very young star. This outflow may occur in the form of a highly collimated, high velocity jet [e. g. Dopita et al. 1982]. More than 450 HH jets are known to date [Reipurth 2000].

HH jets are found to have many different morphologies [for an overview see e. g. Reipurth and Bally 2001], but mostly can be distinguished by their clear jet-like form, possibly enhanced by bow shocks at either ends. Giant HH jets can reach up to about 10 pc.

---

<sup>3</sup>After GEORGE H. HERBIG and GUILLERMO HARO, who described them first [Herbig 1950, 1951, Haro 1952, 1953].

In the strong shocks within the jet flows, or at locations where the jet impacts surrounding clouds, the gas is strongly heated and collisionally excited. This can result in strong, shock-excited line emission, depending on the state of the flowing material and the surrounding clouds. Jets propagating in the diffuse, atomic gas outside the dense molecular clouds often produce prominent atomic emission lines, such as  $H\alpha$  or  $[SII]$  [e.g. Raga and Reipurth 2004]. These lines can be observed in optical images such as those taken by the *Hubble* Space Telescope (HST). If, on the other hand, the jet propagates within a dense molecular cloud, emission from collisionally excited molecular hydrogen is often seen. The radiative decay of the excited molecules via ro-vibrational transitions produces strong emission lines in the NIR and MIR.

### 2.2.2 Extended and compact green objects

In Spitzer IRAC red/green/blue (RGB) images<sup>4</sup> some objects strike the observer by a very peculiar appearance. They are, though extended, very bright in a narrow wavelength range in comparison to the remainder of the IR spectrum. These objects are commonly referred to as extended green objects (EGOs) or “Green Fuzzies”, because in the IRAC RGB images they appear strikingly green. In the commonly chosen RGB colours, any object with a strong  $4.5\ \mu\text{m}$  excess over the other three IRAC bands will appear to be green.

From numerical simulations Smith and Rosen [2005] have shown that  $H_2$  (2-1 O(7), 0-0 S(11), 0-0 S(10), 2-1 O(8), 1-0 O(9), 0-0 S(9), 0-0 S(8)) emission would appear to be most luminous in the  $4.5\ \mu\text{m}$  filter. The  $2.12\ \mu\text{m}$   $\nu = 1-0$  S(1) ro-vibrational emission line of molecular hydrogen is another widely used tracer of these shocks [e.g. McCaughrean et al. 1994, Smith et al. 2007, Davis et al. 2008]. Spectroscopic observations of two of the EGOs in the Cyganowski et al. [2008] catalogue by De Buizer and Vacca [2010] indeed showed  $H_2$  to be responsible for the major part of enhanced  $4.5\ \mu\text{m}$  emission in these sources [cf. also Noriega-Crespo et al. 2004]. This band also encompasses the Bracket- $\alpha$  line and CO emission, cited by Marston et al. [2004] as the most prominent source of enhanced  $4.5\ \mu\text{m}$  emission in the complex they analysed, while De Buizer and Vacca [2010] do not detect CO from the EGOs in their study at all.

Since EGOs are usually more extended than typical stars, Chambers et al. [2009] argue that it is unlikely for them to be simply extinguished background stars, especially since infrared dark clouds (IRDCs), with which EGOs are frequently associated [Cyganowski et al. 2009], are so dense that they would make background stars difficult to detect. Although there have been many studies into the subject during the past few years, the exact nature of EGOs is still unclear. They are thought to be caused by jets impacting on a molecular cloud [Araya et al. 2007], for example HH jets (Sect. 2.2.1). However, Smith et al. [2010b] in their catalogue of EGOs in the Carina Nebula (CN) found no association with known HH jets.

A majority of EGOs is also associated with  $CH_3OH$  Class I maser emission [Chen et al. 2009, around two thirds of the EGOs in their study] and especially Class II  $CH_3OH$  masers [Cyganowski et al. 2009, again around two thirds]. Such maser emission is typically found associated with nascent massive stars only [e.g. Minier et al. 2003]. Chen et al. [2010] analysed the CO emission of EGOs and found evidence that the mass infall rates and

---

<sup>4</sup>Commonly, blue is chosen for the  $3.6\ \mu\text{m}$  band, green for  $4.5\ \mu\text{m}$  and red for  $8.0\ \mu\text{m}$ , leaving out the  $5.8\ \mu\text{m}$  band.

infall velocities as derived from measured rates of CO emission in a number of objects associated with EGOs are consistent with values typically found in massive young stellar objects (MYSOs). Consequently, EGOs might be MYSOs in a rapidly accreting stage of protostellar evolution, with strong outflows [see also Chen et al. 2013].

Compact *Spitzer* sources with  $4.5\ \mu\text{m}$  excess emission are observed and referred to as compact green objects (CGOs) here. They could be unresolved analogues of EGOs. Povich and Whitney [2010] found the CGOs they observed in the M17 proto-OB association predominantly to be associated with Stage 0/Stage I YSOs.

### 2.3 Triggered star-formation

Stars in their evolved stages can exhibit strong winds and radiation. These can influence the surrounding interstellar medium (ISM) in a way to cause the formation of a new generation of stars. This process is generally referred to as ‘triggered star-formation’.

Triggering lets a ‘wave’ of star formation spread through a population [e.g. Elmegreen and Lada 1977, Preibisch et al. 2002]. An older generation of stars develops into their late phases and then triggers a second generation in their vicinity. This second generation is then spatially separate from the original stars and of course it is also younger. There is not one ‘definite’ mode of triggering. Different channels can be discriminated and each has to be tested separately for its validity as a means of advancing star formation.

So-called pillars of dust (sometimes somewhat jokingly referred to as ‘elephant trunks’) are often seen in combination with sites of recent star formation [Hester et al. 1996] and are commonly linked to triggering [see e.g. Smith et al. 2010b, Billot et al. 2010, and references therein]. They are sculpted by winds and radiation from young massive stars and are regarded as signposts of recent star formation. Pillars are often delineated by photo-dissociation region (PDR) regions, which are bright in  $3.6\ \mu\text{m}$ ,  $5.8\ \mu\text{m}$  and  $8.0\ \mu\text{m}$  emission in IRAC images [Smith et al. 2010b].

There are different processes possible to explain YSOs appearing in conjunction with pillars, either in their very tips or shortly before them. The young stars could be formed within the dust and then uncovered by the radiation impacting on it from older generations of stars. Alternatively, a ‘collect and collapse’ scenario could be responsible for their formation or radiative triggering could have caused their development [Smith et al. 2010b]. Smith et al. [2010b] observed that while in several of the South Pillars single or clustered YSOs are found, many are in fact found *in front* of the pillar head seen from the direction of the supposed exhiting star.

One suggested formation mechanism for such pillars is the ‘Capstone effect’, whereby a clump of dense material remains behind when its surroundings are photoevaporated away. This capstone, for example an evaporating gaseous globule (EGG), that is evaporated more slowly than its surroundings, keeps the material behind it from being irradiated [Hester et al. 1996, Thompson et al. 2002]. Such an EGG may contain a YSO that, as the surrounding EGG slowly evaporates away, is now seen to sit on top of a pillar.

Gritschneder et al. [2010] simulated the development of turbulent molecular clouds subjected to ionising radiation emitted by a nearby star numerically. They find that this initial situation (in their necessarily simplified approach) leads to pillars that appear very similar to those observed, including the capstones shielding the rest of the pillar from the radiation. It is interesting to note that this simulation neglects stellar winds so that it

appears winds could not be necessary in the formation of pillars.

The ‘collect and collapse’ model [Whitworth et al. 1994] implies that a shock, e. g. from a supernova (SN), impacts on gas and sweeps it up into a shell or that two clouds collide with each other. In this way, the material is *collected* and compressed in a way to allow it to *collapse* to form stars. This leads, for example, to young stars being observed following the shape of the shell of an H II bubble.

It is also important to keep in mind that external influence can just as easily disperse the natal environments of stars. The impact of stellar winds, for example, can have both a positive effect on a molecular cloud by inducing collapse or a negative effect by dispersing the cloud and thus ending star formation. Which effect comes into play is a complex system, depending for example on the wind momentum and temperature [Foster and Boss 1996] and ionising radiation [Freyer et al. 2003, Klassen et al. 2012]. Not only the clouds themselves are subject to such erosion, but there can also be a competition between a nascent star accreting its envelope matter and dispersal of said envelope by an ionisation front [Whitworth and Zinnecker 2004, Clarke 2007]. Because this work deals with young stars that *have already formed* this negative feedback will not play a role and the coming chapters will concentrate on possible evidence for positive feedback.

Mechanisms of triggering star formation are manifold and because it necessarily cannot ever be observed in process, whether or not triggering occurs is always a matter of interpretation of the data. As in many fields of astrophysics it is a matter of clever conjecture and piecing evidence together. The evidence in favour of the different triggering phenomena is overwhelming. It cannot be completely excluded, however, that other explanations might fit the observations.

### 3 The Carina Nebula Complex

The Carina Nebula Complex (CNC), NGC 3372 in the New General Catalogue [Dreyer 1888], is a star-forming region in the southern sky, located at a distance of 2.3 kpc from the sun [Smith 2006c]. Of course, there are other, much closer, star-forming regions such as the Orion Nebula Cluster at a distance of 410–420 pc [Menten et al. 2007, Kim et al. 2008, see also Muench et al. 2008]. These, compared to the CNC, however have the downside of also containing far fewer massive stars. Compared to the Orion Nebula’s lone O star, the more than 70 stars of spectral types O and B found in the CNC (see Sect. 3.4) represent a very large sample. Massive stars are main drivers in forming star-formation regions and massively influence their environments. Consequently, this makes the CNC a very worthwhile object for the study of star formation and feedback processes. On the other hand, large and rich star-formation regions are mostly much farther away from the sun, such as 30 Dor at  $\sim 49$  kpc [Selman et al. 1999]. Lower distance, though, allows higher spatial resolution in observations. Coupled with the highest surface brightness in the southern sky [Smith and Brooks 2008], this combination of closeness and richness makes the CNC an important target of research.

This chapter is intended as a short introduction to the CNC as the region the detailed study in this work focuses on. Therefore, details concerning star formation will be described more thoroughly, while the bigger picture is mainly summarised. The review by Smith and Brooks [2008], for instance, provides a good starting point for further reading.

The CNC is supposed to be in the early stages of forming an unbound OB association [Smith and Brooks 2008, Smith et al. 2010b]. Although the stars presently forming appear to be of low to intermediate masses [Ohlendorf et al. 2012, Gaczkowski et al. 2013], the Carina Nebula (CN) contains a large number of massive stars.

The CNC contains a number of prominent objects. Apart from the several star clusters within its boundaries (see Sect. 3.2), these are predominantly the star  $\eta$  Car with its surrounding Homunculus nebula and the peculiarly shaped Keyhole nebula. The latter took its name from a drawing by WILLIAM HERSCHEL which resembles a keyhole. Today’s observations show a different shape and brightness distribution which is attributed to changes in the form of the nebula and its illumination due to the Great Eruption (Sect. 3.4) of  $\eta$  Car [Smith and Brooks 2008].

An important caveat is that the CNC is placed so that observing towards it we are looking down the Sagittarius-Carina arm [Smith and Brooks 2008] and that therefore a large contamination by e. g. background and foreground stars is present in the observations. A major number of sources seen *in projection* with the CNC are not actually *part* of the complex. Smith and Brooks [2008] also caution that while the distance to  $\eta$  Car, its Homunculus nebula, the Keyhole nebula and Tr 16 is fairly well established, the other clusters described below are generally *assumed* to be part of the same complex as they are kinematically similar and appear to be associated with the complex nebulosity.

### 3.1 Clouds

The raw material for star formation is of course the matter that is dispersed throughout the region. The cold dusty clouds in the region were mapped with the Large APEX Bolometer Camera (LABOCA) in the 870  $\mu\text{m}$  band by Preibisch et al. [2011d]. This large ( $\sim 1.5 \text{ deg}^2$ ) sub-millimeter (sub-mm) survey of the CNC provided in-depth information about the structure and properties of the cold clouds. It showed the majority (94%) of the flux in the region to originate from thermal dust emission, while the remaining 6% are contributed by free-free emission from the H II region. The study also found the morphology at 870  $\mu\text{m}$  to agree well with the morphology at 8  $\mu\text{m}$ , the longest-wavelength IRAC band. The FIR clouds, however, show a less spatially concentrated structure [Roccatagliata et al. 2013].

Preibisch et al. [2011d] estimate  $\sim 10\%$  of the clouds to be in a sufficiently dense state to be available for star formation. This fraction may increase through further compression and especially the influence of the SNe expected to occur in the region in future [Preibisch et al. 2011d]. This kind of feedback effect would explain the high star-formation rate (SFR) the CNC exhibits [cf. Sect. 3.5.2; Roccatagliata et al. 2013]. The effects of stars present in the CNC are demonstrated by Preibisch et al. [2012], who find that only  $\approx 25\%$  of the original molecular gas remain in molecular form while  $\approx 75\%$  have been transformed into atomic gas. Roccatagliata et al. [2013] find that radiative feedback from the stars also shapes the temperature distributions within the clouds, which is found to vary between 35–40 K in the central parts of the CNC and 26 K in the outlying regions. Nearly all cloud surfaces are strongly irradiated and the map of far-UV (F-UV) radiation correlates well with the temperature map.

Cloud masses in the region were found to vary strongly, between a few  $M_{\odot}$  to several  $10^3 M_{\odot}$  [Preibisch et al. 2011d]. LABOCA sub-mm observations yielded a total cloud mass of  $\sim 60\,000 M_{\odot}$ , with an uncertainty of a factor 2–3 [Preibisch et al. 2011d]. The total cloud mass was derived to be  $\sim 655\,700 M_{\odot}$  from FIR observations of a larger field [Preibisch et al. 2012]. For an area corresponding to the LABOCA survey, the same study finds  $\sim 427\,000 M_{\odot}$ . The authors attribute this to LABOCA’s tracing only the masses of the densest clouds, whereas *Herschel* also allows the observations of less dense clouds. The total cloud mass estimate from the *Herschel* study is  $\lesssim 890\,000 M_{\odot}$  [Preibisch et al. 2012].

### 3.2 Clusters

The CNC has been described as a ‘cluster of clusters’ [e.g. Feigelson et al. 2011, Povich et al. 2011a].<sup>1</sup> The major clusters in the region are Tr 14, Tr 15 and Tr 16<sup>2</sup>, Cr 228<sup>3</sup> and Bochum 10 and Bochum 11<sup>4</sup>. Tr 14 and particularly Tr 16 are by far the most dominating ones in the large context of the CNC while the others influence predominantly their local environment [Smith and Brooks 2008]. Tr 16 is  $\sim 3 \text{ Ma}$  old, Tr 14 at  $\sim 1 - 2 \text{ Ma}$  slightly younger. Tr 15, with stars several  $10^6$  years old [Tapia et al. 2003], and Bochum 10 are older. Bochum 11 is younger than 1 Ma [Smith and Brooks 2008]. In radio observations,

<sup>1</sup>Townsley et al. [2011b] use the term in a specific way to identify a part of the central CN (see their Fig. 1b).

<sup>2</sup>After the catalogue by ROBERT J. TRUMPLER [Trumpler 1930]

<sup>3</sup>After the catalogue by PER COLLINDER [Collinder 1931]

<sup>4</sup>After the catalogue produced at Ruhr-Universität Bochum [Moffat and Vogt 1975a,b,c, Fitzgerald et al. 1976]

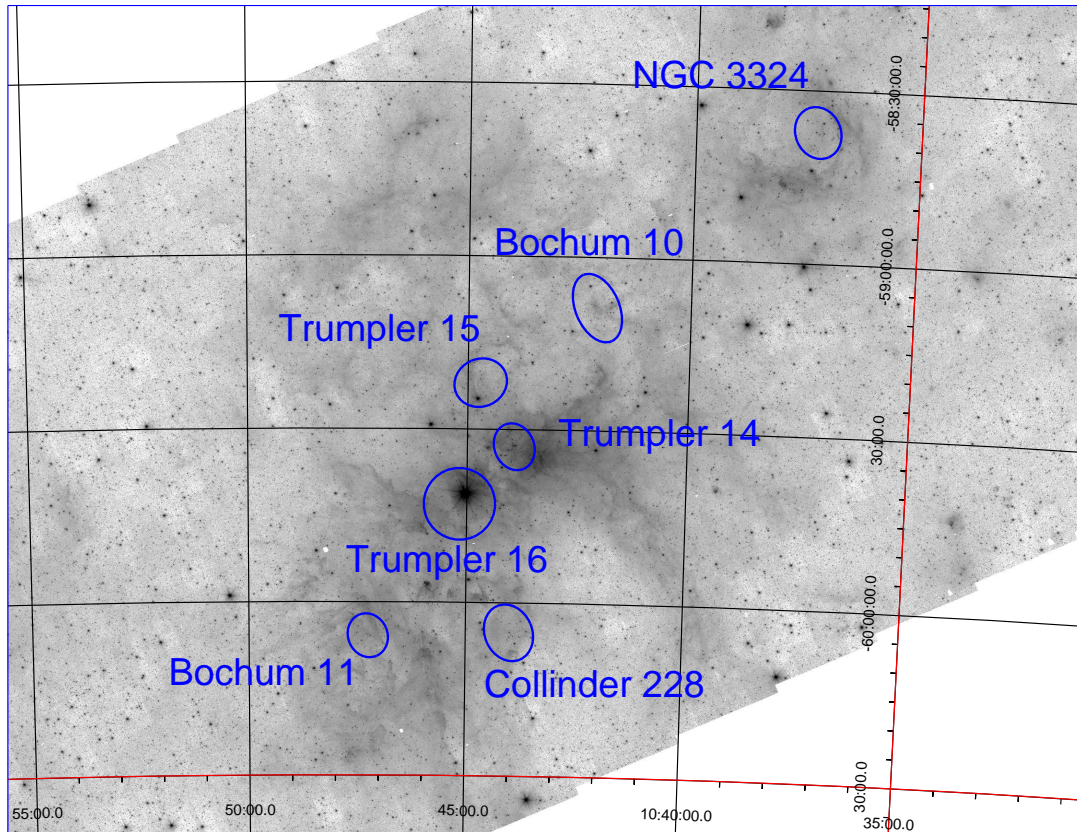


Figure 3.1: Clusters in the CNC shown on the background of a *Spitzer* IRAC 4.5  $\mu\text{m}$  image. Positions are given as listed by SIMBAD.

the inner CN is seen to be parted into two distinct regions, known as Car I and Car II; Car I being influenced by Tr 14 and Car II by Tr 16.

There are differing theories supported by observations as to how these clusters are connected or separated. Smith and Brooks [2008] state Cr228 was “*generally considered to be part of Tr 16*” [e.g. Walborn 1995]. On the other hand, Cr 228 has also been stated to be a defined separate cluster [Carraro and Patat 2001]. Patat and Carraro [2001] also find Bochum 9, Bochum 10, and Bochum 11 to be small, poor and young open clusters.

No significant star formation appears to be going on within Tr 14 and Tr 16 [Smith and Brooks 2008], but studies like those of DeGioia-Eastwood et al. [2001] and Tapia et al. [2003] find IR-excess YSOs in the clusters (cf. our detection of cYSOs in Sect. 9.4.2). These detections are consistent with the age spread of the stellar population of low and intermediate masses [Smith and Brooks 2008].

As this work concentrates on the IR-excess emitters in the CNC and predominantly the cYSOs among them, these large stellar clusters are only a side issue. I concentrate on the numerous small clusters that can be found among the YSO population [eg Smith et al. 2010b, Feigelson et al. 2011] and especially the newly detected ones. A detailed description of the clusters found and a comparison to other studies can be found in Chapter 9.

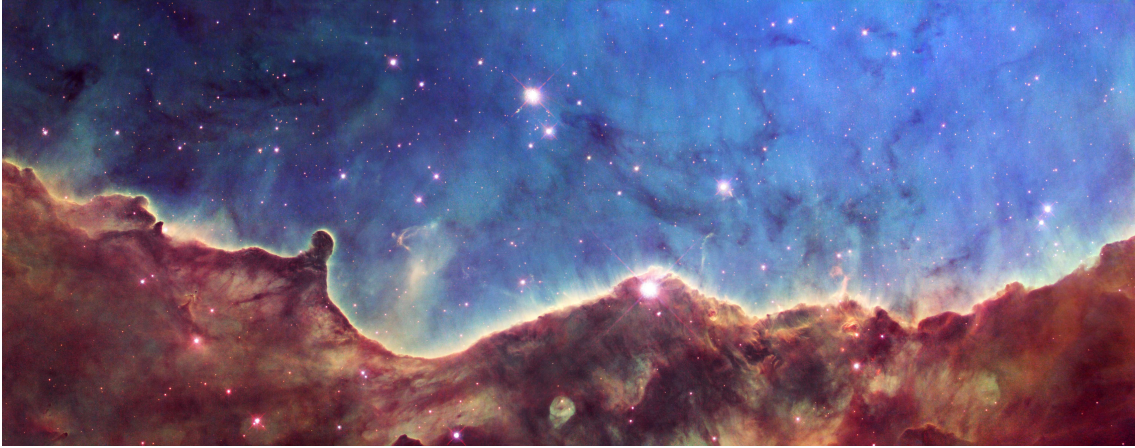


Figure 3.2: HST image of the ionisation front bordering NGC 3324 (Hubble News Release STScI-2008-34, image credit: NASA, ESA, and The Hubble Heritage Team (STScI/AURA)). The RGB colours are red: WFC2 S II filter (673 nm), green: ACS H $\alpha$  + N II filter (658 nm), blue: WFC2 O III filter (502 nm). North is to the right, east is up.

### 3.3 Gum 31 and NGC 3324

A distinct bubble-shaped region  $\approx 1^\circ$  north-west of the CN is very prominent from IR images. This is the ionized hydrogen (HII) region Gum 31 encircling the stellar cluster NGC 3324. The diameter of the HII region itself is  $\sim 15'$  (10 pc at a distance of 2.3 kpc). This HII region in turn is surrounded by an expanding non-ionized hydrogen (HI) shell which encloses it almost completely [Cappa et al. 2008]. Though the region has such an entrancing shape (dubbed the ‘perfect bubble’ by Preibisch et al. [2012]), it is very poorly studied. Doubtlessly this is because of its proximity to the all-overshadowing Carina Nebula in its immediate vicinity. HST images of its western rim (Hubble News Release STScI-2008-34) are often shown as prime examples of an ionising front at the edge of a star-formation region (Fig. 3.2), but have not sparked much research interest in the region.

The physical relation between NGC 3324 and the CNC is still unclear (but see Sect. 8.3). Recent distance determinations of Gum 31 and NGC 3324 yielded values of 2.3 kpc for the cluster NGC 3324 [Catalogue of Open Cluster Data; Kharchenko et al. 2005] and  $2.5 \pm 0.3$  kpc for the clouds in and around Gum 31 [Barnes et al. 2010]. This implies that NGC 3324/Gum 31 are located at the same distance as the CN [2.3 kpc; see Smith 2006c].

The available information about the stellar population of NGC 3324 is restricted to the brightest stars. The brightest system is the multiple star HD 92206, which is constituted by two O6.5V stars HD 92206 A and B and the O8.5V star HD 92206 C [Maíz-Apellániz et al. 2004]. A further bright star in the region is the A0 supergiant HD 92207 (= v370 Car,  $V = 5.49$ ). This object is a very luminous ( $\log(L/L_\odot) = 5.56$ ), massive ( $M_{\text{initial}} \approx 30 M_\odot$ ), evolved star [age  $\approx 7 \pm 1$  Ma; Przybilla et al. 2006] that drives a very strong stellar wind [ $\dot{M} = 1.3 \times 10^{-6} M_\odot \text{ a}^{-1}$ ; Kudritzki et al. 1999]. The membership of HD 92207 is not entirely clear: Clariá [1977] and Carraro et al. [2001] assume it not to be part of the cluster. However, Forte [1976, from its being wrapped in a nebular shell associated with Gum 31] and Baumgardt et al. [2000, from proper motions] determine it to be a member.

### 3 The Carina Nebula Complex

Carraro et al. [2001] identify 25 candidate members of NGC 3324 with optical photometry and suggest that the cluster is very young ( $\lesssim 2\text{--}3\text{ Ma}$ ). With three O-type stars ( $M \geq 18 M_{\odot}$ ), the field star initial mass function (IMF) representation by Kroupa [2002] suggests that there should be  $\approx 1500$  low-mass ( $0.1 M_{\odot} \leq M \leq 2 M_{\odot}$ ) stars present. This implies that the vast majority of the stellar population of NGC 3324 is still unknown.

In addition to the optically visible stellar cluster NGC 3324 in the H II region, there is a population of young stars embedded in the molecular cloud surrounding the H II region. This population is only seen in infrared images [Cappa et al. 2008] or traced by their protostellar jets [Smith et al. 2010a]. Cappa et al. [2008] sampled point sources in a region of  $20'$  radius centred on NGC 3324 from the Infrared Astronomical Satellite (IRAS), Midcourse Space Experiment (MSX) and Two Micron All-Sky Survey (2MASS) point-source catalogues and identify 12 (IRAS), 9 (MSX) and 26 (2MASS) cYSOs using colour-colour criteria. Due to the limited sensitivity and angular resolution of these data, the currently known few dozen of embedded infrared sources represent only the tip of the iceberg; many more embedded YSOs must be present in this area and waiting to be discovered.

The study of the distribution of cYSOs in the CNC presented in Chapter 9 clearly shows that the Gum 31 region is an important star-formation region in its own right. In Chapter 8 an in-depth study of the YSOs in the region is detailed.

## 3.4 Massive stars

The CNC was the first region where the earliest O stars were recognized [Walborn 1973] and holds a considerable number of O-type and Wolf-Rayet stars (WR stars). Apart from the most prominent member  $\eta$  Car (see Sect. 3.4.1), the CNC contains the O2 star HD 93129A in Tr 14 [Walborn et al. 2002], three nitrogen- and helium-rich WR stars (WNH stars) [Smith and Brooks 2008] in Tr 16 and a number more of O stars to make up a total of more than 70 known high-mass stars [Smith 2006a] – among them several of the most massive ( $M > 100 M_{\odot}$ ) and luminous stars known in our Galaxy. There might even be more: Povich et al. [2011b] caution that the completeness of the sample of known O stars may be only 50%.

There are two WNH stars found within the South Pillars region (cf. Sect. 3.5.1), but Smith et al. [2010b] suggest that they might be projected into the region instead of being members. They do not appear to influence the pillars in their immediate (projected) neighbourhood, something which a WR star would clearly be expected to do [Smith et al. 2010b].

### 3.4.1 $\eta$ Carinae and the Homunculus

The luminous blue variable (LBV)  $\eta$  Car<sup>5</sup> is arguably the most prominent star in the CNC. Its brightness and striking variability has made it a popular target of study for centuries [for an overview see Smith and Brooks 2008]. Its brightness reached a peak visual magnitude of  $\sim -1$  mag during its *Great Eruption* in the 1850s [historical light curves of Frew 2004, Fernández-Lajús et al. 2009] and has steadily faded since then, with a minor eruption to  $\sim 6$  mag around 1890, to  $\sim 8$  mag around the turn of the century, slowly rising again since

---

<sup>5</sup>Spectroscopic evidence for  $\eta$  Car being a binary with a hotter, less bright companion on an eccentric orbit is reported by Damiani et al. [2000].



Figure 3.3: ESO WFI optical image of the central region of the CN, with  $\eta$  Car and the Homunculus in the bright v-shaped region to the left (ESO Image Release eso1031b, image credit: ESO). The RGB colours are red:  $R$  band, green:  $V$  band, blue:  $B$  band. North is up, east is to the left.

then to its current value of  $\sim 5\text{--}6$  mag [Reed 2003, Fernández-Lajús et al. 2009] with a minor peak in 2006 [Fernández-Lajús et al. 2009]. The cause for the Great Eruption is still unknown [Smith and Brooks 2008].

The matter ejected during the Great Eruption formed the Homunculus nebula [Smith 2006c, Fig. 3.3], so called because its shape resembles that of a small fat man with short arms. Detailed description and a good pointer to the relevant literature on the Homunculus can be found in the dedicated study by Smith [2006c]. The nebula effectively shields  $\eta$  Car so that its radiation currently does not contribute to influencing its surroundings [Smith and Brooks 2008], but is absorbed in the Homunculus. However, before the Great Eruption it did shape the CNC strongly (see especially Sect. 3.5.1).

### 3.4.2 Supernovae

Whether or not SNe have already occurred in the CN is a topic currently under debate. While it used to be canonical knowledge that no SNe had yet occurred in the CNC, in past years this has been challenged. Hamaguchi et al. [2007] in *Suzaku* X-ray observations centred on  $\eta$  Car found that an inhomogeneous distribution in silicon and iron abundances throughout their study field could be explained by local enrichment through a supernova remnant. The bright X-ray source 2XMM J104608.7–594306, described by Pires et al. [2009] and Hamaguchi et al. [2009], is dubbed a “*smoking gun*” by the latter, being a probable 1 Ma-old neutron star. Voss et al. [2012] modelled the  $^{26}\text{Al}$  emission they observe towards the CNC with INTEGRAL. The radioactive isotope  $^{26}\text{Al}$  is produced in stellar winds and SNe and is thus a tracer of massive stars. While they find that wind emission dominates their  $^{26}\text{Al}$  models, only  $\sim 80\%$  can be accounted for in this way. A SN contribution to the total emission of  $\sim 20\%$  is estimated, which is another pointer towards past SN explosions.



Figure 3.4: HAWK-I NIR image of the CN (ESO Image Release eso1208a, image credit: ESO/T. Preibisch). The very bright star at the lower left edge is  $\eta$  Car. The RGB colours are red:  $K_s$  band, green:  $H$  band, blue:  $J$  band. North is up, east is to the left.

There is no doubt, though, that the most massive stars in the CN,  $\eta$  Car being the most prominent among them, are quickly approaching the ends of their evolutionary spans. SNe and the resultant re-shaping of the matter in the region are therefore to be expected soon.

### 3.5 Young stellar objects

The view of CN as star-forming originated only in the past decade [Povich et al. 2011a]. In 1979, Harvey et al. saw the Carina Nebula in the FIR as a “well-evolved, older H II region“. This view was still prevailing in 1988, when Ghosh et al. explained the compact FIR sources they observe as dust-gas clumps heated by the OB stars in the region.<sup>6</sup>

However, de Graauw et al. [1981] from their CO observations in the inner CN around Tr 14, Tr 15 and Tr 16 speak of young star clusters in an H II region. They propose that sequential triggering (cf. Sect. 2.3) is in process here, with the young stars interacting with the remnants of the original molecular cloud. Smith et al. [2000] observed a number of MIR sources within the South Pillars (Sect. 3.5.1) and sparked off a number of IR studies of

---

<sup>6</sup>Smith et al. [2000] note that those studies do not include the South Pillars (Sect. 3.5.1), which constitute the most prominent star-forming region within the CN. This might be a reason the region was seen as being evolved and past star formation.

the region in which subsequently evidence was found for plenty of star-formation going on within the CN. The possibility of different triggering processes (Sect. 2.3, cf. Sect. 3.5.1) being ongoing in the region became a topic much under discussion (see also e. g. Sect. 8.7, Sect. 9.6).

Smith et al. [2000] analysed MSX data of the Carina Nebula when it was still believed to be mainly an old, quiescent H II region that had no ongoing star formation, following up on the detection of IRAS 10430–5931 as star-forming by Megeath et al. [1996] (Sect. 3.5.1). From their observation, they found a number of embedded MIR sources which constituted good candidates for ongoing star formation in the CN. Several of them are placed in the heads of dust pillars (Sect. 3.5.1) or behind ionisation fronts, leading the authors to propose these sources to have been triggered.

The HH jet (see Sect. 2.2.1) HH 666 discovered by Smith et al. [2004] was the first protostellar outflow detected in the CN. A later study by Smith et al. [2010a] used the Advanced Camera for Surveys (ACS) camera on the HST to look for more jets in the CNC in a deep H $\alpha$  narrow-band imaging survey. They detected 40 HH jets and HH jet candidates within the  $\sim 0.8^\circ \times 1.1^\circ$  area that was partly covered by their observations. These form the basis of the work done in Chapter 7, where a search for the sources of these jets is carried out.

YSOs in the CN exhibit a high degree of clustering [e. g. Smith et al. 2010b, Feigelson et al. 2011]. Rathborne et al. [2004] observed candidate embedded clusters among the South Pillars (Sect. 3.5.1). Later studies of YSOs in the CN in the infrared [Smith et al. 2010b] or in X-rays [Feigelson et al. 2011, within the *Chandra* Carina Complex Project (CCCP)] have corroborated the presence of a high number of YSO clusters. Those studies confirm the presence of YSO clusters in the South Pillars. In Chapter 9 we will search for cYSO clusters in a much larger part of the CNC. We will also compare the number of stars in clusters to the number of those in a uniformly distributed population. Previous studies find the distributed population to account for  $\approx 50\%$  of the YSOs in the CNC [Feigelson et al. 2011, Preibisch et al. 2011c].

From *Spitzer* images Smith et al. [2010b] obtained a photometry catalogue of 48 642 point sources, and a catalogue of 909 YSOs identified through SED fits in a study region focused on the South Pillars. They find a YSO mass function (YMF) in accordance with the canonical IMF and argue from this that star-formation in the South Pillars must have been roughly continuous over the past  $\sim 3$  Ma. This is in accordance with the findings of Rathborne et al. [2004], who studied the South Pillars in a multi-wavelength study and found ongoing massive-star formation over the entire South Pillars region. They, too, argue that it must have been constant over the past  $\sim 3$  Ma.

Smith et al. [2010b] argue the case for a locally varying IMF that gets washed out over the entirety of the complex. They find that while in some clusters YSOs are found together with evolved O stars, the ratio of these varies strongly and a number of cluster hold no evolved massive stars. They interpret this as a possible sign of a locally varying IMF.

The *Chandra* X-ray observatory obtained a deep wide-field ( $\sim 1.4$  deg<sup>2</sup>) X-ray survey of the Carina complex [see Townsley et al. 2011a] that led to the detection of 14 368 X-ray point sources [Broos et al. 2011b] as well as copious amounts of diffuse X-ray emission [Townsley et al. 2011a]. The sample was enhanced by observations in the IR, e. g. with HAWK-I [Preibisch et al. 2011a] and *Spitzer* [Povich et al. 2011a].

The CCCP sample was sub-classified according to each source’s individual detections in different wavelength bands [Broos et al. 2011a], which yielded 1609 probable contaminants

### 3 The Carina Nebula Complex

(i. e. foreground stars, Galactic background stars and active galactic nuclei (AGN)). This analysis of the X-ray and infrared properties of the point sources suggested that 10 714 objects are young stars in the CNC [Broos et al. 2011a].

A very deep near-infrared survey of the central 1280 arcmin<sup>2</sup> area performed with the High-Acuity Wide-field *K*-band Imager (HAWK-I) at the ESO 8 m Very Large Telescope [Preibisch et al. 2011c] has revealed more than 600 000 IR sources (see Sect. 4.5). This IR catalogue was combined with the list of X-ray sources from the CCCP to study the properties of the stellar populations in the CNC [Preibisch et al. 2011a]. Preibisch et al. find HAWK-I matches for 88% of the CCCP sources within the HAWK-I study field (6583 out of 7472), improving strongly over the detection rate in the *J*, *H* and *K<sub>s</sub>* bands with 2MASS. The infrared excess fraction is found to vary considerable between the clusters, between 2% for Tr 15 and 10% for Tr 14. Overall, the authors find the IR excess fraction to be consistently lower than for comparable clusters of similar age [Preibisch et al. 2011a]. From this they conclude that disk dispersal happens more rapidly in the CNC than elsewhere, as a consequence of massive-star feedback.

Only a fraction of the total young stellar population of the CNC has been studied so far. Because the IMF dictates that low-mass (and therefore faint) stars far outnumber the high-mass ones, every study will miss a major part of the population. Better and better instruments make higher percentages of the total population available for observation. Preibisch et al. [2011c] and Feigelson et al. [2011] estimate a total young-star population of  $\sim 104\,000$  in the CNC from the CCCP study. Povich et al. [2011a] estimate a total YSO population of  $\gtrsim 5.8 \cdot 10^4$  with a total stellar mass of  $(4.9\text{--}8.6) \cdot 10^4 M_{\odot}$ .

#### 3.5.1 Pillars

A well-studied and very peculiar region within the CNC are the “South Pillars” to the south of  $\eta$  Car. These are a number of dust structures that appear in (projected) shape in IR images remarkably like the architectural feature, with their tips pointing towards  $\eta$  Car. The pillars are also traced by PDRs, which are a common feature throughout the CNC [Rathborne et al. 2004].

Here a giant molecular cloud (GMC) is being destroyed by stellar winds and UV radiation from Tr 14 and particularly Tr 16 [Smith et al. 2000, Rathborne et al. 2004, Smith and Brooks 2008]. A denser core within the GMC material shields the material behind it, so that a pillar remains behind when the remainder of the cloud is irradiated away [Rathborne et al. 2004]. While the region is home to a large number of young stars, it also contains several evolved massive stars (10–20 O stars and WNH star HD 93131 [Smith et al. 2010b]).

Star-formation activity in the South Pillars was the first evidence that star formation in the CN is still going on. It was first found from wide-field IR observations with IRAS and the detection of IRAS 10430–5931 in a molecular clump along with a number of highly reddened embedded stars in the South Pillars [Megeath et al. 1996]. The authors reported the IR colours of IRAS 10430–5931 to be in agreement with its being a YSO. Rathborne et al. [2004] from MSX MIR observations identified 11 compact H II regions and one candidate MYSO. They reported that of their candidate young clusters several appeared to be associated with pillars or embedded within them.

Among the MIR-bright compact objects there is a compact H II region, G287.84–0.82 [Rathborne et al. 2004, Smith et al. 2005], in the head of a pillar pointing towards  $\eta$  Car and Tr 16 [Smith et al. 2005]. Both the pillar and the cluster embedded in it are frequently

referred to as the ‘Treasure Chest’. The cluster itself is very young [ $\leq 0.1$  Ma, Smith et al. 2005]. It is currently forming a cavity inside the top of its host pillar [Smith and Brooks 2008].

Smith et al. [2010b] in a *Spitzer* study of the South Pillars find some YSOs within pillars and a larger number just outside pillar heads. They conclude that the pillars are being eroded with the YSOs having developed within them being left behind. Smith et al. [2010b] also show that those YSO outside pillar heads are found predominantly between the pillars and massive stars and argue that the massive stars must have triggered their formation. However, the authors also found that these pillars are not necessarily dominated by the emission from the massive stars in Tr 14 and Tr 16. In their Fig. 12 they illustrate the pillar axes, which exhibit a range of orientations. The authors concluded from this that the local O stars within the South Pillars influence the region more strongly than the stars of Tr 14 and Tr 16 do.

Smith et al. [2010b] also described that within large pillars with a clear axis there are smaller mini-pillars and protrusions that point in entirely different directions. This kind of substructure is evident in *Spitzer* IRAC MIR images (see Sect. 4.1.1) upon zooming in. Smaller and smaller mini-pillars can be seen, often superset on the edges of larger pillars. Smith et al. [2010b] suggested that these phenomena arise from changes in the currently dominating source within the region, for example by a newly formed massive star beginning to dominate over stars farther away. They also suggested that  $\eta$  Car’s strong variability may be a reason: In its current state it has little influence over the region, but this maybe a very recent state (see Sect. 3.4.1), and this change may be reflected in the general pillar directions being now deflected away from  $\eta$  Car by locally dominating stars.

Smith et al. [2010b] describe in detail how a group of older stars is thought to be able to erode a pillar, leaving behind a group of stars of mixed ages, triggered during different stages of pillar erosion (their Fig. 15). They explicitly describe how such a process, going on in not only a single pillar at any one time, but in a complex and interacting environment, together with the inherent motions of the newly formed stars leads to a region with clusters that may or may not be associated with the pillars in which they formed. It should be stressed again here that a large and dynamic region as the South Pillars and even the entire CNC is much more complicated than simplifying sketches can convey and that the interactions are what makes the CNC such a rewarding field of study.

It should also be noted that in the Smith et al. [2010b] study (as well as our own; cf. Chapters 8 and 9) several pillars show no signs of association with YSO clusters or single YSOs. Of course, this is not contradictory to the idea of their being associated with star formation. If star formation is supposed not to occur in one single burst but in a sequence of small events spread out in time, then naturally one would expect it to have taken place already in some place and to be about to take place in others. In other words, these observation support a hypothesis that the star formation in the CN is far from over.

Rathborne et al. [2004] generated a visual extinction map of the South Pillars region and found it to have  $A_V = 7\text{--}15$  mag, corresponding to a  $\text{H}_2$  column density of  $9\text{--}19 \cdot 10^{21} \text{ cm}^{-2}$ . From  $^{12}\text{CO}$  (2–1) to  $^{13}\text{CO}$  (2–1) ratios they derived an  $\text{H}_2$  column density of  $7\text{--}22 \cdot 10^{21} \text{ cm}^{-2}$ , which agrees well. They also find a dust temperature of 42–44 K in the region. Preibisch et al. [2011d] found a maximum extinction of  $A_V = 50$  mag ( $N_{\text{H}_2} \sim 4 \cdot 10^{22} \text{ cm}^{-2}$ ) in the cloud associated with the Treasure Chest cluster from sub-mm observations (assuming cloud temperatures of 30 K).

### 3.5.2 Star formation rate

Today, the South Pillars appear to be the most recent and currently most active star-formation region within the CNC [Smith et al. 2010b, see also Sect. 9.3]. There is, however, star formation activity of varying strength to be found in all parts of the complex.

Povich et al. [2011a], as described below, estimate the present-day SFR of the CNC to be  $> 0.008 M_{\odot} \text{ a}^{-1}$  and  $0.010\text{--}0.017 M_{\odot} \text{ a}^{-1}$  averaged over the past  $\sim 5$  Ma, with interspersed bursts of star formation. Smith et al. [2010b] conclude from the extrapolated numbers in their cYSO sample (see also Sect. 6.5.1) that the SFR would have been approximately constant over the entire lifetime of the region. Gaczkowski et al. [2013] derived a higher SFR of  $0.017 M_{\odot} \text{ a}^{-1}$  as an average over the past few  $10^5$  a and found this to be in agreement with the values found by Povich et al. [2011a] taking into account the differing study areas.

Roccatagliata et al. [2013] find that the star formation rate per unit mass in the dense clouds of the CNC is higher than in comparable regions, i.e. that the star formation efficiency is unusually high. They find a characteristic star-formation time scale of 1.3 Ma. From this they conclude that in the CNC it is not simply a matter of turning clouds into stars which should then not be going on still after  $\sim 5$  Ma, but that feedback from massive stars forms dense clouds throughout the evolution of the CN, thus replenishing the supply of matter. This is evidenced by YSO being found predominantly at pillar tips and irradiated cloud surfaces [Smith et al. 2010b, Gaczkowski et al. 2013, Chapters 8 and 9].

### 3.5.3 The Pan-Carina YSO Catalogue

A number of IR studies have been undertaken on the CNC over the years. I will describe one in more detail here as it will be relevant in later chapters. Povich et al. [2011a] searched the  $1.42 \text{ deg}^2$  field of the CCCP for YSOs, which resulted in the Pan-Carina YSO Catalogue (PCYC) containing 1439 YSOs. In Sect. 6.5.2 I will compare this catalogue of cYSOs to the one derived in this work.

Combining *Spitzer* IRAC<sup>7</sup> and MIPS<sup>8</sup> observations with 2MASS Point Source Catalogue data, they identify cYSOs by their IR excess. The *Spitzer* survey contains 60 515 sources within the CCCP field. Photometry reaches down to  $[3.6] \lesssim 15.5$  mag (apart from regions of bright nebular emission). The MIPS detection fraction in the PCYC is only  $\sim 10\%$  (plus some upper limits), which is similar to what we find for our study.

Photometry for the PCYC was derived with the GLIMPSE point-source extractor based on DAOPHOT. Note that this is a method differing completely from the one we used for our cYSO catalogue (Chapter 5). This difference in a central analysis step makes the comparison between both catalogues meaningful although they are drawn from the same basic data set.

To obtain the PCYC, the  $1\text{--}24 \mu\text{m}$  IR SEDs<sup>9</sup> were fitted using the Robitaille et al. [2007] SED models (cf. Sect. 7.4.1, Sect. 8.5.1) for all objects in the survey that were detected in at least four out of seven bands (210 742 sources, 54 155 of them in the CCCP region) and fitted with reddened stellar photospheres [Castelli and Kurucz 2004]. In doing this,

---

<sup>7</sup>“Galactic Structure and Star Formation in Vela-Carina” programme; PI: Steven R. Majewski, PID: 40791 [the same data as used in this work, cf. 4.1.1]

<sup>8</sup>“MIPSCAR: A Far-Infrared Survey of the Carina Nebula” programme, PI: Nathan Smith, PID: 30848

<sup>9</sup>2MASS *J*, 2MASS *H*, 2MASS *K<sub>s</sub>*, IRAC 3.6  $\mu\text{m}$ , IRAC 4.5  $\mu\text{m}$ , IRAC 5.8  $\mu\text{m}$ , IRAC 8.0  $\mu\text{m}$ , MIPS 24  $\mu\text{m}$ .

Povich et al. [2011a] allowed  $A_V = 0 \dots 40$  mag [Indebetouw et al. 2005] and a distance of  $2.3 \pm 0.05$  kpc [Smith 2006c] (the same as the parameters assumed in Sects. 7.4.1 and 8.5.1). This assumes that the CN is roughly spherical with a diameter of  $\sim 50$  pc (observed). The uncertainties were manually set to  $\leq 10\%$ , similar to what is done in the relevant analysis in this work (cf. Sects. 7.4.1 and 8.5.1).<sup>10</sup> From the obtained SED fits they considered only sources with  $\chi_{\text{best}}^2/\nu \leq 2$  (with  $\nu$  representing the number of data points) for the later analysis and, of those, only models within the range of  $\chi^2/\nu - \chi_{\text{best}}^2/\nu \leq 2$ .<sup>11</sup> To each model, the authors assigned a  $\chi^2$ -weighted normalised probability. With these they weighted the means of the distributions of the stellar and circumstellar parameters derived from the Robitaille et al. [2007] models.<sup>12</sup>

From this sample, all objects that were well fit with reddened stellar photospheres were removed (50 586; 93.4%). Furthermore, sources with IR excess emission only in [5.8] or [8.0] were filtered out (cf. the method of Smith et al. [2010b] described in Sect. 6.5.1). The remainder were then de-reddened using

$$E([3.6] - [4.5]) = A_V \frac{(\kappa_{3.6} - \kappa_{4.5})}{\kappa_V} \quad (3.1)$$

with  $\kappa_\lambda$  being the opacities following the extinction law of Indebetouw et al. [2005]. The selection criteria for cYSOs were then

$$\begin{aligned} & [3.6] - [4.5] > \delta([3.6] - [4.5]) + E([3.6] - [4.5]) \\ \text{or } & |[4.5] - [5.8]| > \delta([4.5] - [5.8]) \\ \text{and } & [5.8] - [8.0] > \delta([5.8] - [8.0]). \end{aligned} \quad (3.2)$$

This procedure left 1646 IR excess sources.<sup>13</sup>

Such a sample of IR excess sources in a region like the CNC necessarily contains a number of contaminants (cf. e.g. Sect. 6.4), which need to be removed as carefully as possible. To this end, Povich et al. applied a colour cut to remove possible asymptotic giant branch (AGB) stars:

$$[8.0] - [24] > 2.2 \text{ mag}, \quad (3.3)$$

which removed 1% of sources. Redder AGB stars would be extremely luminous and therefore distinguishably bright [Whitney et al. 2008, Povich et al. 2009, as cited by Povich et al. 2011a].

For further contaminant removal, they inspected the clustering properties of the excess sources. YSOs in the CN are expected to cluster (see Sect. 3.5) while contaminants are distributed uniformly. The authors used a nearest-neighbour group-finding algorithm [Povich et al. 2009] to identify groups of  $\geq 10$  sources and to find sources that show clustering with respect to control fields outside CCCP area. As control fields, they chose two boxes of  $0.5^\circ \times 0.5^\circ$  centred on  $(l = 286.4^\circ, b = -0.9^\circ)$  and  $(l = 286.6^\circ, b = 0.2^\circ)$ . This yielded a mean cYSO surface density of  $200 \text{ deg}^{-2}$  outside the CCCP field and  $1150 \text{ deg}^{-2}$  inside it—resulting in an expected contamination fraction of 17%. After sources not showing clustering had been removed, the mean surface density inside the CCCP area was  $1000 \text{ deg}^{-2}$ ,

<sup>10</sup>The same minimum uncertainties are chosen by Smith et al. [2010b] in their search for YSOs.

<sup>11</sup>This method is adapted from the methods used by Povich et al. [2009], Povich and Whitney [2010] and Smith et al. [2010b].

<sup>12</sup>Method of Povich et al. [2009].

<sup>13</sup>The rejected sources were examined again by Povich et al. [2011b].

### 3 The Carina Nebula Complex

which means that the remaining contaminants were  $50 \text{ deg}^{-2}$ , equalling 5%.<sup>14</sup> (Compare these values to those found in our catalogue of cYSOs described in Sect. 9.1).

Of this overall sample of 1439 cYSOs in the PCYC, 1029 are not in the CCCP X-ray catalogue while 410 have X-ray counterparts. 62 of the latter are candidate protostars and tend to be more evolved than candidate protostars without X-ray detection. Povich et al. find the dominant mass range of the candidate protostars to be  $2 M_{\odot}$ – $10 M_{\odot}$  (cf. Sect. 7.4.1). The authors extrapolate their sample to a total population of  $> 2 \cdot 10^4$  YSOs and a SFR of  $> 0.008 M_{\odot} \text{ a}^{-1}$  (cf. Sect. 3.5.2). They determine the global SFR of the CN to have been approximately constant over the last  $\sim 5$  Ma. The YMF is found to have a power-law form  $\Psi(\log m) = m^{-\Gamma_{\text{YMF}}}$  with  $\Gamma_{\text{YMF}} = 3.2 \pm 0.3$  in the range  $3.1 M_{\odot} < m < 10 M_{\odot}$ , below which the sample is incomplete.

The general distribution of the PCYC cYSOs within the CNC, though distributed, shows an emphasis on the central regions and along a broadened line connecting the Tr 14 and Tr 16 clusters with the South Pillars region. cYSOs are found close to the ends of pillars and the edges of molecular clouds, within H II regions. They also occur embedded in the ends of dust pillars, partly as driving sources of the HH jets identified by Smith et al. [2010a]. (For a study of the driving sources of HH jets in the CNC see also Chapter 7.) Povich et al. [2011a] find YSO clusters associated with Tr 14 and Tr 16, but not with Tr 15 and Bochum 11 although they are associated with X-ray star clusters. In Sect. 6.5.2 these results will be compared to the results from the catalogue of cYSOs derived in this work.

---

<sup>14</sup>Inside the CCCP before removal ( $1150 \text{ deg}^{-2}$ ) minus control field ( $200 \text{ deg}^{-2}$ ): density of 'real' YSOs ( $950 \text{ deg}^{-2}$ ); inside CCCP field after removal ( $1000 \text{ deg}^{-2}$ ) minus 'real' YSOs ( $950 \text{ deg}^{-2}$ ): density of remaining contaminants ( $50 \text{ deg}^{-2}$ ).

## 4 Instruments and surveys

### 4.1 Spitzer

The *Spitzer* Space Telescope, originally referred to as the Space Infra-Red Telescope Facility (SIRTF), is part of NASA's Great Observatories programme [NASA 2007]. These four observatories were built to cover a large wavelength range: The Compton Gamma-Ray Observatory (CGRO) and *Chandra* cover the high energies, the HST is well-known for observing in the optical and NIR range and *Spitzer* completes the set towards the MIR.

The telescope has three focal-plane instruments attached to its 85 cm telescope. Only two of them, IRAC and MIPS, provided the data used in this work and will therefore be described below. The third instrument, the Infrared Spectrograph (IRS), was not used here and is not further described for this reason.<sup>1</sup>

Launched in August 2003 with the aim of a 30-month mission [NASA 2007], *Spitzer* is still under operation ten years later, albeit under changed conditions. In *Spitzer*'s current status, IRS, MIPS and two out of four IRAC bands are no longer available. *Spitzer* will continue operating until 2014, with an option to prolong this until 2016 [*Spitzer* Space Telescope Handbook v2.1, 2013].

---

<sup>1</sup>Further information can be found in the publication by Houck et al. [2004] and starting from the *Spitzer* Science Center (SSC) IRS documentation homepage <http://irsa.ipac.caltech.edu/data/SPITZER/docs/irs/>.

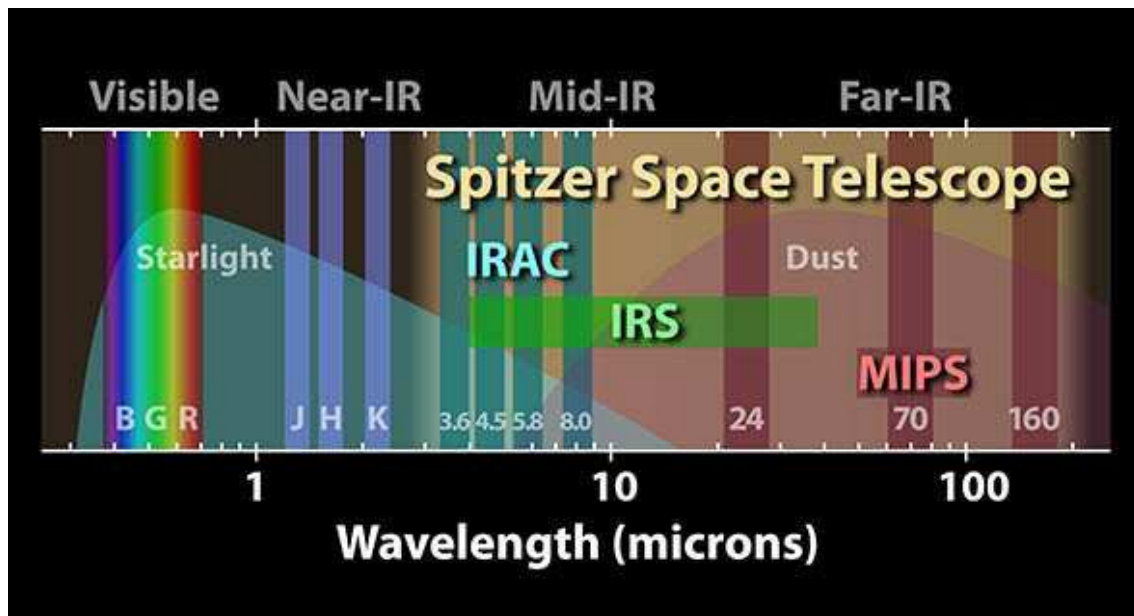


Figure 4.1: Wavelength ranges of the *Spitzer* instruments [Courtesy NASA/JPL-Caltech].

### 4.1.1 IRAC

The Infrared Array Camera (IRAC) is a multi-purpose instrument. Though its main design aim was the study of galaxy evolution [Fazio et al. 2004], we are using it here for an entirely different purpose: The wavelength filters originally selected to be ideal for the observation of stellar photospheres [which dominate the 3.6  $\mu\text{m}$  band; Smith et al. 2010b] are also well suited to characterising the MIR part of a YSO’s SED and allow for the selection of cYSOs from a large sample of sources due to their IR excess. The ability to conduct deep, large-area surveys that is also a requirement of IRAC’s intended use is put to excellent use with our kind of study as well. Although IRAC had the four design aims of studies on the early universe, brown dwarfs and superplanets, AGN and protoplanetary and planetary debris disks [Fazio et al. 2004], its uses are expressly not limited to these fields. The instrument was intended and has been used for a broad range of study types. IRAC has often been used for the search for and study of young stars and their surroundings [e.g. Allen et al. 2004, Harvey et al. 2006, 2007, Winston et al. 2007, Whitney et al. 2008, Smith et al. 2010b, Povich et al. 2011a, Roccatagliata et al. 2011, Fang et al. 2012].

IRAC could observe simultaneously in four different wavelength bands. The filter centre values are 3.6  $\mu\text{m}$ , 4.5  $\mu\text{m}$ , 5.8  $\mu\text{m}$ , and 8.0  $\mu\text{m}$ ; with bandwidths of 0.8  $\mu\text{m}$ , 1.0  $\mu\text{m}$ , 1.4  $\mu\text{m}$ , and 2.9  $\mu\text{m}$  [IRAC Instrument Handbook v2.0.3, 2013, cf. Figs. 4.2 and 4.3a]. These four values were required to optimise for sensitivity in order to enable galaxy detection to the pursued standard [Fazio et al. 2004]. The fact that there are no filter wheels but four fixed filters is due to the requirement of minimising the amount of movable parts within the telescope so as to avoid potentially failure-prone equipment [Fazio et al. 2004].

The 3.6  $\mu\text{m}$  and 4.5  $\mu\text{m}$  detector arrays are InSb and were held at an operating temperature of 15 K. The 5.8  $\mu\text{m}$  and 8.0  $\mu\text{m}$  detector arrays are made of Si:As and were operated at a lower temperature of 6 K. The peak-to-peak variations in these temperatures were kept below 10 mK [Fazio et al. 2004]. The difference in detector material between high and low wavelength is the reason for their differing operability at the present, high temperatures (see below). Pixels sizes, however, are the same: All four detectors have arrays of 256 pixels  $\times$  256 pixels each, with pixels sizes of 30  $\mu\text{m}$  [Fazio et al. 2004].

With IRAC, data are taken by integrating over a defined “stare” time [Fazio et al. 2004], the “IRAC map” method. For all observations we use, effective integration times per pixel of 1.2 s and a frame integration time of 2 s were employed. The nominal point-source sensitivities for this integration time can be taken from the IRAC Instrument Handbook v2.0.2 [2012]: For a high-background situation the  $1\sigma$  point-source sensitivities are given as 34  $\mu\text{Jy}$ , 41  $\mu\text{Jy}$ , 180  $\mu\text{Jy}$  and 156  $\mu\text{Jy}$  for 3.6  $\mu\text{m}$ , 4.5  $\mu\text{m}$ , 5.8  $\mu\text{m}$  and 8.0  $\mu\text{m}$  (cf. Table 4.1). However, we chose to derive individual sensitivities directly from the data (see Sect. 5.4.3, Table 5.3 and Fig. 4.3b). The CNC is close to the Galactic plane and viewed along an arm of the Galaxy, which makes it a very-high background case. We will therefore not discuss the image quality here, but in the relevant chapters where further processing is described and the eventual processed data evaluated.

The four detector arrays are arranged in groups of two, with 3.6  $\mu\text{m}$  and 5.8  $\mu\text{m}$  sharing one field of view and 4.5  $\mu\text{m}$  and 8.0  $\mu\text{m}$  sharing the other [Fazio et al. 2004, see Fig. 4.4]. This particular arrangement results in very slightly shifted images between the groups and not entirely consistent coverage in the very edges of the final field. This necessarily leads to a small number of point-like sources detected in only one or two bands. These skew the total numbers slightly because the reason of their non-detection is not their faintness in

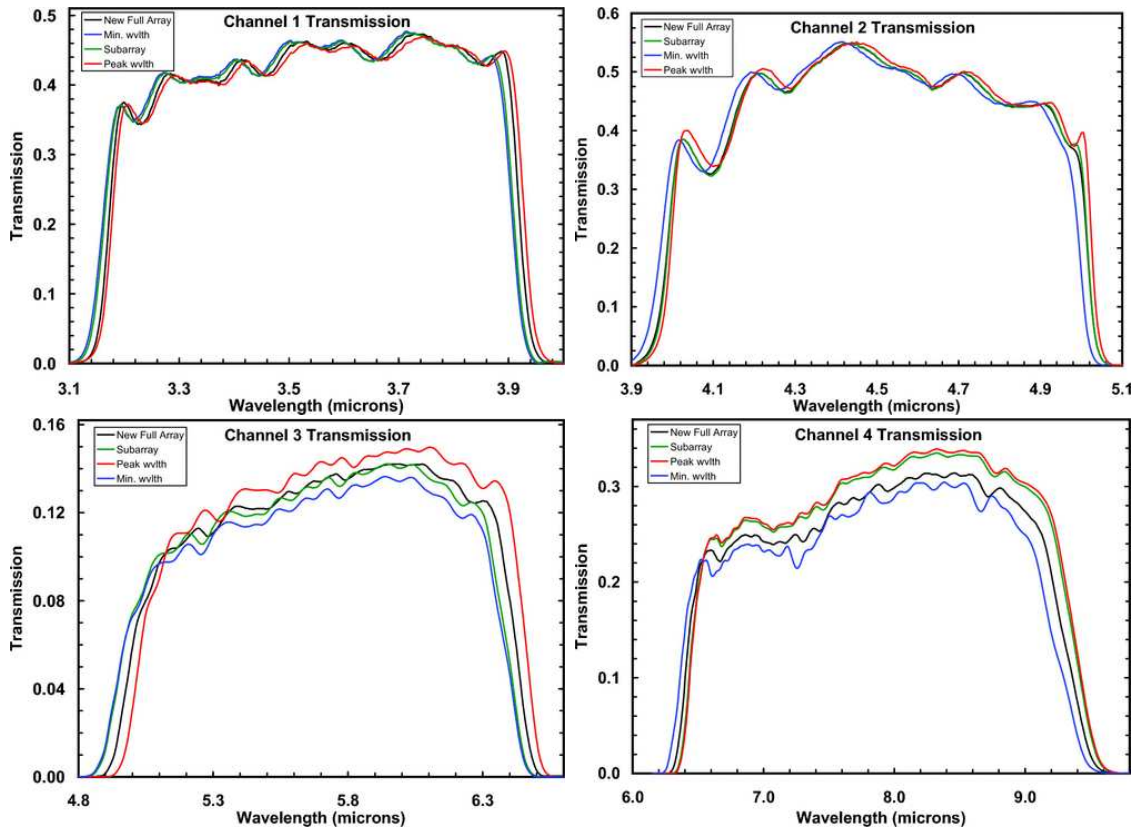


Figure 4.2: The four IRAC bandpasses [images taken from Hora et al. 2008]. Blue and red lines show the pixels with the lowest and highest nominal wavelengths, black shows the full array average (effective wavelengths vary slightly; cf. Hora et al. [2008]). (A  $32 \text{ pixels} \times 32 \text{ pixels}$  subarray [green curve], is not employed here.)

the relevant wavelength range but the fact that they are simply not fully covered. This, however, merely lets sources at the very edges drop out of our *CYSO* catalogue because for their selection we require detection in all four IRAC bands (cf. Chapter 6). Effectively this limits the study area, but otherwise has no scientific impact on our study.

The incident light is reflected into the optics system by two pickoff mirrors (Fig. 4.4). These are slightly tilted with respect to each other so that the beam is sent towards the two sets of detector arrays. In this way, a separation between the two image centres of  $6.8'$  is achieved. In each setup, the focal plane of *Spitzer* is re-focussed on the detector arrays with the means of lenses. In each case imaging on two detector arrays is achieved by a beamsplitter in the converging beam [Fazio et al. 2004].

IRAC uses a transmissive rather than a reflective optics system out of space considerations [Fazio et al. 2004]. The optical assembly used to be cooled to  $\sim 1.2 \text{ K}$  [Fazio et al. 2004], which it still was at the time the data we are using were taken (July 2008, see below). This “cold mission phase” ended when the coolant helium ran out in May 2009 [*Spitzer* Space Telescope Handbook v2.1, 2013] and the “warm mission phase” began, extending *Spitzer*’s intended lifetime. Although only the  $3.6 \mu\text{m}$  and  $4.5 \mu\text{m}$  detector arrays are operable any more, observations with IRAC are still well underway.

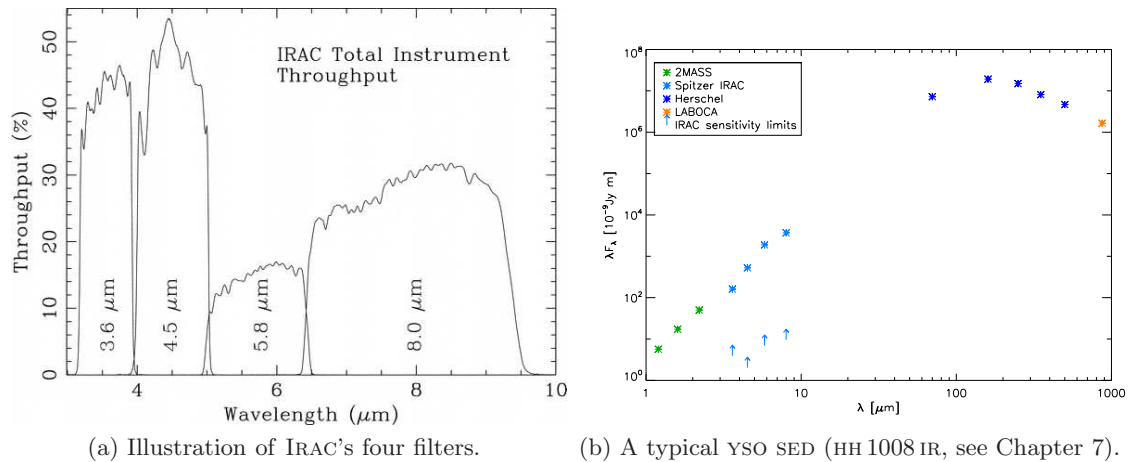


Figure 4.3: Fig. 4.3a [taken from Fazio et al. 2004] illustrates that the wavelength range between  $\sim 3\mu\text{m}$  and  $\sim 10\mu\text{m}$  is nearly completely covered by IRAC. It also shows the differing widths and sensitivities of the four filters. Their completeness limits in our study (cf. Sect. 5.4.3) are illustrated by comparison to a typical YSO SED in Fig. 4.3b.

Table 4.1: Overview of IRAC detector and image characteristics.

	IRAC 1 3.6 $\mu\text{m}$	IRAC 2 4.5 $\mu\text{m}$	IRAC 3 5.8 $\mu\text{m}$	IRAC 4 8.0 $\mu\text{m}$
Field of view <sup>a</sup>	256 pixels $\times$ 256 pixels			
Physical pixel size <sup>a</sup>	30 $\mu\text{m}$			
Integration time/pixel	1.2 s			
Integration time/frame	2 s			
Image pixel size <sup>b</sup>	1.221''	1.213''	1.222''	1.220''
FWHM of centred PRF <sup>b</sup>	1.44''	1.43''	1.49''	1.71''
Sensitivity <sup>b</sup>	34 $\mu\text{Jy}$	41 $\mu\text{Jy}$	180 $\mu\text{Jy}$	156 $\mu\text{Jy}$

**Notes.** The sensitivities given are the nominal  $1\sigma$  point-source sensitivities for a high-background case. (For the values obtained from observations, see Table 5.3.)

(<sup>a</sup>) Fazio et al. [2004] (<sup>b</sup>) IRAC Instrument Handbook v2.0.2 [2012]

The warm ( $\sim 10^\circ\text{C}$ ) part of IRAC (the Warm Electronics Assembly) houses all electrical interfaces. From here, the science data are downlinked to the ground station at regular intervals every 12 hours [Fazio et al. 2004].

The raw (Level 0) data transferred from the spacecraft are processed into the Level 1 data products known as basic calibrated data (BCD). Data processed further are available from the SSC, but our analysis as presented beginning in Chapter 5 works directly with the BCD as retrieved from the *Spitzer* Heritage Archive (SHA)<sup>2</sup>. The BCD are flux-calibrated as well as purged of the basic instrumental signatures affecting the data quality [IRAC Instrument Handbook v2.0.2, 2012].

<sup>2</sup><http://sha.ipac.caltech.edu/applications/Spitzer/SHA/>

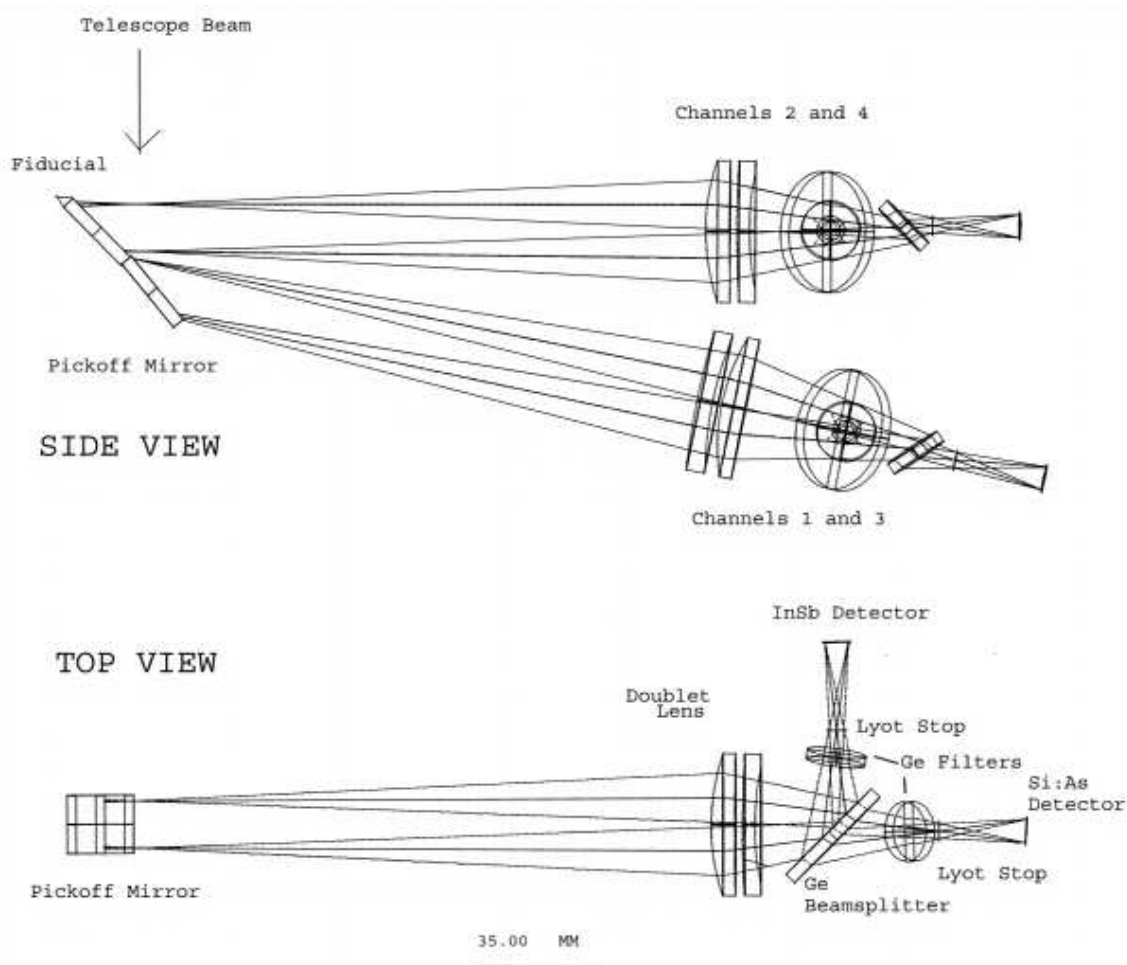


Figure 4.4: Illustration of IRAC's optical design [image taken from Fazio et al. 2004, Hora et al. 2008]. The side view shows how two bands each share a field of view due to the design of the two-part pickoff mirror.

IRAC data come in units of astronomical observation requests (AORs). Each AOR collects the data collection events (DCEs) or single-frame exposures covering a defined area. The DCEs are square, due to the square detector arrays. Slightly overlapping, they are joined into strips of observations to cover the width required for the observation field. In our case, each AOR typically consists of 212 DCEs per channel, making 848 DCEs overall. The AORs overlap slightly (just as the DCEs overlap within the AOR strips), which is an effect that will have to be accounted for in the data processing (see Chapter 5). The BCD for all four channels are bundled into AORs and are downloadable from the SHA in this form.

### Retrieval of data

The data used here were taken during the *Spitzer* cold mission phase, in July 2008. They were part of the "Galactic Structure and Star Formation in Vela-Carina" programme

observations<sup>3</sup>, following the model of the Galactic Legacy Infrared Mid-Plane Survey Extraordinaire (GLIMPSE) [Benjamin et al. 2003]. They were retrieved through the SHA. A detailed overview of the AORs used is given in Table 5.1.

Using the Mosaicker and Point source Extractor (MOPEX) software package, we assembled the BCD into mosaics covering the area around  $\eta$  Car, incorporating the whole extent of the CNC. In Sect. 5.1 I describe in detail how point sources were detected and photometric data obtained.

### 4.1.2 MIPS

The second, longer wavelength instrument onboard *Spitzer* is the Multiband Imaging Photometer for *Spitzer* (MIPS) [Rieke et al. 2004]. The instrument has three bands at 24  $\mu\text{m}$ , 70  $\mu\text{m}$  and 160  $\mu\text{m}$ , of which we will only be using the first. The bandwidths of the filters are  $\sim 5 \mu\text{m}$ ,  $\sim 19 \mu\text{m}$  and  $\sim 35 \mu\text{m}$ . The anchor point for the wavelengths chosen was the 70  $\mu\text{m}$  band which is “*in the heart of the far-infrared but not at so long a wavelength as to be overwhelmed by confusion noise*” [Rieke et al. 2004]. From there, the 24  $\mu\text{m}$  band is placed (logarithmically) halfway to the 8  $\mu\text{m}$  IRAC band and the 160  $\mu\text{m}$  band halfway to the ground-accessible sub-mm wavelength 350  $\mu\text{m}$  (e. g. SABOCA [Siringo et al. 2010]) [Rieke et al. 2004].

The detector array of Si:As has  $128 \times 128$  pixels, resulting in a  $5' \times 5'$  field of view (FOV) [Rieke et al. 2004]. Like the channels of IRAC, the MIPS channels also share mirrors. Two pickoff mirrors took the light to the 70  $\mu\text{m}$  detector separately and to the 24  $\mu\text{m}$  and 160  $\mu\text{m}$  detectors together, where the light paths were only separated on a second image plane [Rieke et al. 2004]. MIPS was operated at temperatures of  $\sim 5.15 \text{ K}$  [Rieke et al. 2004] and is inoperable in the present warm mission phase.

The data used here were obtained using the “photometry” mode, one of four modes of which MIPS was capable [MIPS Instrument and MIPS Instrument Support Teams 2011]. In this mode, the spacecraft remains basically stable, pointed in one direction with minimal movements. The combination of these and small scan mirror movements is used to provide dithering [Rieke et al. 2004].

### Photometry using StarFinder

A 24  $\mu\text{m}$  map observed in June 2006 as part of the “*Spitzer* Follow-up of HST Observations of Star Formation in H II Regions” programme<sup>4</sup> was retrieved through the SHA. Photometry on the MIPS images was not performed in one sweep on the complete image, but on a case-by-case basis on individual sources, where MIPS fluxes were needed to supplement a source’s SED for the analysis in Chapters 7 and 8. The MIPS images were searched by eye for point-like sources coinciding with the previously identified IRAC and *Herschel* (Sect. 4.2) sources. Because this field is only sparsely populated with point-like sources in the 24  $\mu\text{m}$  band, they were easily found by eye. MIPS has a point-spread function (PSF) of  $6''$  full width at half maximum (FWHM) in the 24  $\mu\text{m}$  band, slightly degrading towards the edges of the FOV, sampled on pixels with a size of  $2.55''$ . According to the MIPS Instrument Handbook v3.0 [2011] the 24  $\mu\text{m}$  sensitivity is highly dependent on the observed sky region; in an ideal case it is expected to be  $\approx 35 \mu\text{Jy}$ .

---

<sup>3</sup>PI: Steven R. Majewski, PID: 40791

<sup>4</sup>PI: Jeff Hester, PID: 20726

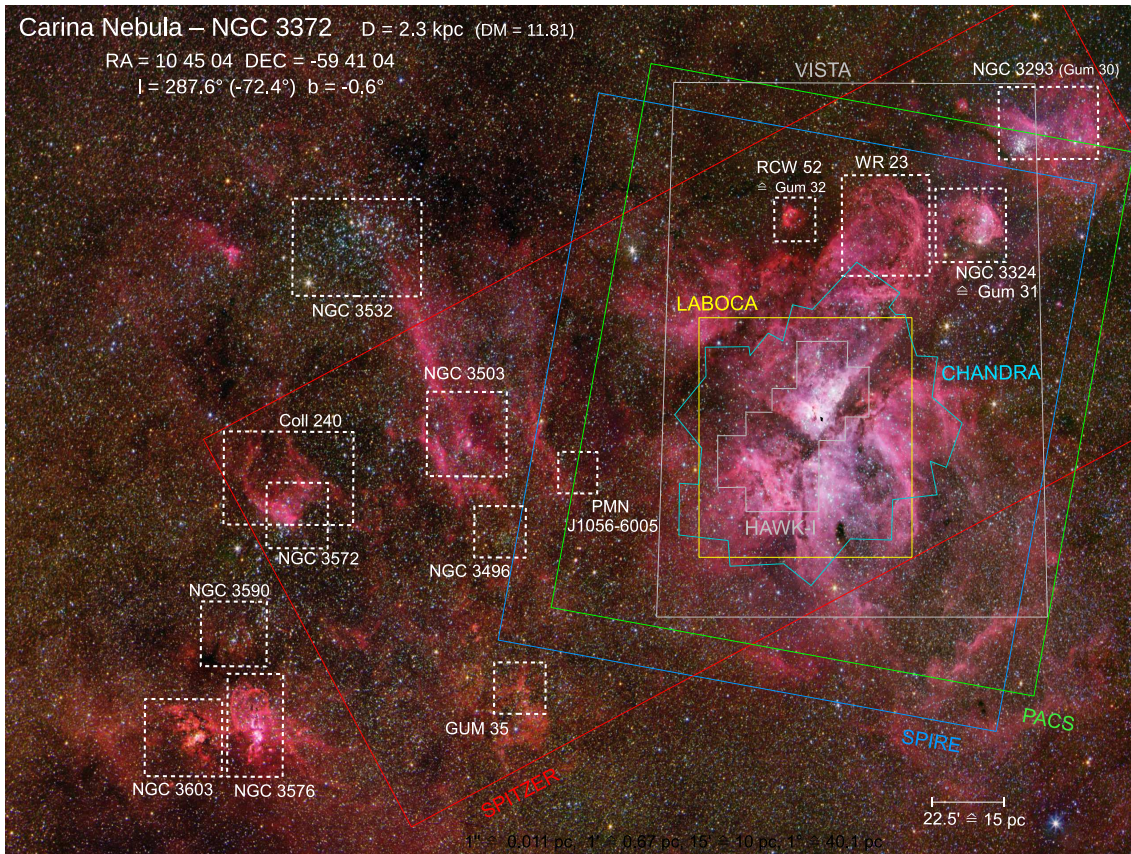


Figure 4.5: The CNC has been observed many times in different wavelengths. This image illustrates the very differing fields of view of the multi-wavelength studies. Data taken by *Spitzer* IRAC are the main focus of this work. We also use observations with *Spitzer* MIPS, *Herschel*'s PACS and SPIRE, and VISTA. The studies with HAWK-I, LABOCA and *Chandra* are repeatedly referred to.

For each individual source we performed PSF-fitting photometry with StarFinder<sup>5</sup> [Diolaiti et al. 2000]. The PSF was derived as a median value from four point sources. It was then fitted to each identified point source together with a slanting plane for the background and taking into account the contribution of bright stars adjacent to the fitting region. In this way the sub-sample of MIPS point-like sources defined by IRAC and *Herschel* detection was analysed from the brightest to the faintest objects.

## 4.2 *Herschel*

The *Herschel* Space Observatory, formerly known as the Far Infrared and Sub-millimetre Telescope (FIRST), was a space facility designed to cover FIR wavelengths up to the sub-mm, unique in this respect [ESA 2010]. It was launched together with *Planck*<sup>6</sup> [Planck Collaboration et al. 2011] in May 2009 and ended its lifetime in April 2013 when its

<sup>5</sup><http://www.bo.astro.it/StarFinder/index.htm>

<sup>6</sup><http://www.rssd.esa.int/index.php?project=Planck>

coolant helium was depleted. Through this time, *Herschel* observations were possible with its three instruments: The Heterodyne Instrument for the Far Infrared (HIFI), the Photodetecting Array Camera and Spectrometer (PACS) and the Spectral and Photometric Imaging Receiver (SPIRE).

The observations that provided the data used in in this work were performed in December 2010<sup>7</sup>, using the parallel fast scan mode at  $60''\text{s}^{-1}$ . With simultaneous five-band imaging with PACS [Poglitsch et al. 2010] at  $70\ \mu\text{m}$  and  $160\ \mu\text{m}$  and SPIRE [Griffin et al. 2010] at  $250\ \mu\text{m}$ ,  $350\ \mu\text{m}$  and  $500\ \mu\text{m}$  two orthogonal scan maps were obtained to cover an area of  $2.3^\circ \times 2.3^\circ$ . The total observation time was 6.9 hours. HIFI, the spectrometer onboard, has completely different scientific use and is not employed in the context of this work.

In Chapters 7, 8 and 9 I will be using the *Herschel* point-source catalogue assembled from these observations by Gaczkowski et al. [2012]. A full description of the observations and the subsequent data processing is given by Preibisch et al. [2012] and Gaczkowski et al. [2013]. A more detailed account of the catalogue characteristics can also be found there.

The angular resolutions of the maps are  $5''$ ,  $12''$ ,  $18''$ ,  $25''$ , and  $36''$  for the  $70\ \mu\text{m}$ ,  $160\ \mu\text{m}$ ,  $250\ \mu\text{m}$ ,  $350\ \mu\text{m}$ , and  $500\ \mu\text{m}$  band, mapped onto pixels of  $3.2''$ ,  $4.5''$ ,  $6''$ ,  $8''$ , and  $11.5''$ . At a distance of  $2.3\ \text{kpc}$  this corresponds to physical scales from  $0.06$  to  $0.4\ \text{pc}$ . The faintest sources still detectable are around  $1\text{--}2\ \text{Jy}$ , which characterises the detection limit without the presence of strong background. A very rough estimate of completeness limits was achieved by the modal values of the flux distributions which are  $10\ \text{Jy}$ ,  $15\ \text{Jy}$ ,  $10\ \text{Jy}$ ,  $10\ \text{Jy}$  and  $6\ \text{Jy}$  for the five bands.

One needs to keep in mind that the angular resolution of *Herschel* is comparatively low and that this means that even rather large sources can still appear point-like in *Herschel* observations. An  $18''$  source would still appear as a point-like source in the  $500\ \mu\text{m}$  band. This size corresponds to  $0.2\ \text{pc}$  at a distance of  $2.3\ \text{kpc}$ . Gaczkowski et al. [2013] argue that a pre-stellar cloud core ( $\lesssim 0.1\ \text{pc}$ ) would thus appear point-like for *Herschel* and be listed in the catalogue.

The catalogue suffers the same problem as all other IR catalogues of the CNC: A high probability of contamination. In this case, it was minimised as far as possible for example by only retaining those sources that were detected independently in at least two *Herschel* bands. This resulted in 642 sources for the entire CNC. Gaczkowski et al. [2013] explain why those objects are most likely real YSOs and not contaminants, as the sensitivity of *Herschel* severely restricts the possibility of picking up extragalactic contaminants or evolved stars.

### 4.2.1 Pre-stellar and protostellar cores

In Chapter 9 I will rely heavily on the *Herschel* catalogue to compare the distribution of sources within it to the IRAC and Wide-field Infrared Survey Explorer (WISE) catalogues of cYSOs (Chapter 6). There, *Herschel* point-like sources are split into two categories: Prestellar objects and protostars.

This distinction relies on the shape of the SEDs of protostars and starless (i. e. pre-stellar) cores: For the latter, the IR flux falls steeply towards wavelengths shorter than

---

<sup>7</sup>Open time project, PI: Thomas Preibisch, PID: OT1-tpreibis-1

Table 4.2: Overview of completeness and sensitivity limits for WISE data.

		WISE 1	WISE 2	WISE 3	WISE 4
		3.4 $\mu\text{m}$	4.6 $\mu\text{m}$	12 $\mu\text{m}$	22 $\mu\text{m}$
Sensitivity limit	[mJy]	0.036	0.047	0.430	2.800
	[mag]	17.3	16.4	12.1	8.7
Completeness limit	[mJy]	3.0	1.8	11	30
	[mag]	12.5	12.4	8.6	6.1

around 100  $\mu\text{m}$  [Ragan et al. 2012]. Therefore, for such a pre-stellar core, no 70  $\mu\text{m}$  flux should be detectable. Consequently, Gaczkowski et al. [2013] assigned all point-like sources *with* 70  $\mu\text{m}$  detection protostars and all *without* pre-stellar objects and found that roughly 50% of their sample fall in either category.

### 4.3 WISE

Especially in Chapters 8 and 9 I will use the point-source catalogue of the WISE [Wright et al. 2010] All-Sky Data Release [Cutri and al. 2012]. These data (referred to as the WISE catalogue here) were taken during the WISE cold mission phase from January to August 2010 [Cutri et al. 2012]. Like the earlier and ground-based 2MASS, WISE surveyed the full sky. This means that data for the CNC can be taken from the full survey, providing a large catalogue at four MIR wavelengths. The four bands are centred at 3.4  $\mu\text{m}$ , 4.6  $\mu\text{m}$ , 12  $\mu\text{m}$  and 22  $\mu\text{m}$ . In Chapter 8 we will not be using the 22  $\mu\text{m}$  band.

I used the standard aperture-corrected magnitudes obtained with apertures of 8.25'' and corrections of 0.222 mag, 0.280 mag, and 0.665 mag for 3.4  $\mu\text{m}$ , 4.6  $\mu\text{m}$ , and 12  $\mu\text{m}$  [Cutri et al. 2012]. The WISE observations have an angular resolution of 6.1'', 6.4'', 6.5'', and 12.0'' for 3.4  $\mu\text{m}$ , 4.6  $\mu\text{m}$ , 12  $\mu\text{m}$ , and 22  $\mu\text{m}$  [Wright et al. 2010]. In our survey area (a 2° circle centred on  $\eta$  Car) the catalogue contains 20 739 point sources with a detection in at least one band.

In a way parallel to that described in Sect. 5.4.3 for investigating the IRAC data, I estimated the sensitivity and completeness limits of the catalogue from histograms (Fig. 4.6). Because the WISE All-Sky Data Release covers an area much larger than the CNC and these limits are dependent on, e. g., the nebulosity in the study field, for the determination of the limits I chose an area comparable to the IRAC study area: A 3° × 3° square region centred 5' east and 20' north of  $\eta$  Car, that is at  $\alpha_{2000} = 10:42:03.5$ ,  $\delta_{2000} = -59:21:04$ . This yields completeness limits of  $\approx 3.0$  mJy,  $\approx 1.8$  mJy,  $\approx 11$  mJy and  $\approx 30$  mJy in the four bands. The sensitivity limits are 36  $\mu\text{Jy}$ , 47  $\mu\text{Jy}$ , 430  $\mu\text{Jy}$ , and 2800  $\mu\text{Jy}$  for 3.4  $\mu\text{m}$ , 4.6  $\mu\text{m}$ , 12  $\mu\text{m}$ , and 22  $\mu\text{m}$  (Table 4.2).

Comparing these values to those obtained from the Spitzer Point-Source Catalogue (SPSC) (Sect. 5.4.2) listed in Table 5.3, it is apparent that the completeness limits in the two bands that can be directly compared<sup>8</sup> are distinctly lower for IRAC. This means that in the SPSC we can expect *all* objects of a certain magnitude to be present in the catalogue down to greater faintness than for the WISE catalogue. Conversely, WISE is slightly more

<sup>8</sup>3.4  $\mu\text{m}$  (IRAC 1)/3.6  $\mu\text{m}$  (WISE 1) and 4.6  $\mu\text{m}$  (IRAC 2)/4.5  $\mu\text{m}$  (WISE 2)

## 4 Instruments and surveys

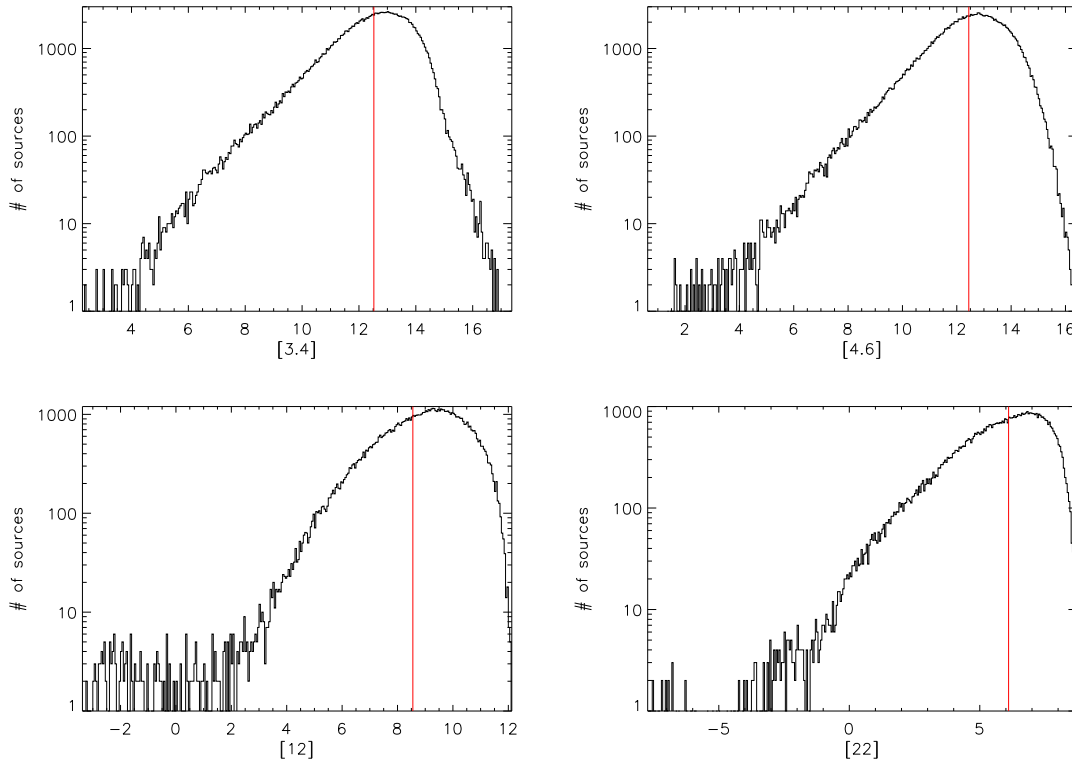


Figure 4.6: Histograms of the measured source magnitudes in the WISE All-Sky Data Release for the environs of the CNC. Red lines mark the completeness limits as listed in Table 4.2.

sensitive for individual sources than IRAC is. Its sensitivity limit lies at  $\approx 40 \mu\text{Jy}$  while that of IRAC is roughly  $100 \mu\text{Jy}$  in those two bands. Thus, we expect fainter sources to be detectable with WISE than with IRAC, but cannot expect the sample to be complete at this point.

These detection limits can be compared to the Baraffe et al. [1998] numerical models of PMS evolution as we do for IRAC in Sect. 5.4.3. Doing so, we found that  $1 M_{\odot}$  stars should be almost completely detectable with WISE in the  $3.4 \mu\text{m}$  and  $4.6 \mu\text{m}$  bands, assuming an age of 1 Ma (Fig. 4.7).

### 4.4 VISTA

Chapter 8 shows NIR images labelled ‘VISTA’ (Figs. 8.10/8.11, Fig. 8.12). The  $H$ -band image of the area around Gum 31 from which they were taken was obtained with the VISTA Infra-Red CAMERA (VIRCAM) [Dalton et al. 2006] in the night of 15 January 2012. It was the first observation of a Visible and Infrared Survey Telescope for Astronomy (VISTA) [Irwin et al. 2004, Emerson and Sutherland 2010] survey of the CNC.<sup>9</sup> These observations are the subject of detailed study by e. g. Zeidler [2013, upcoming publications by Preibisch

<sup>9</sup>ESO run number 088.C-0117(A)

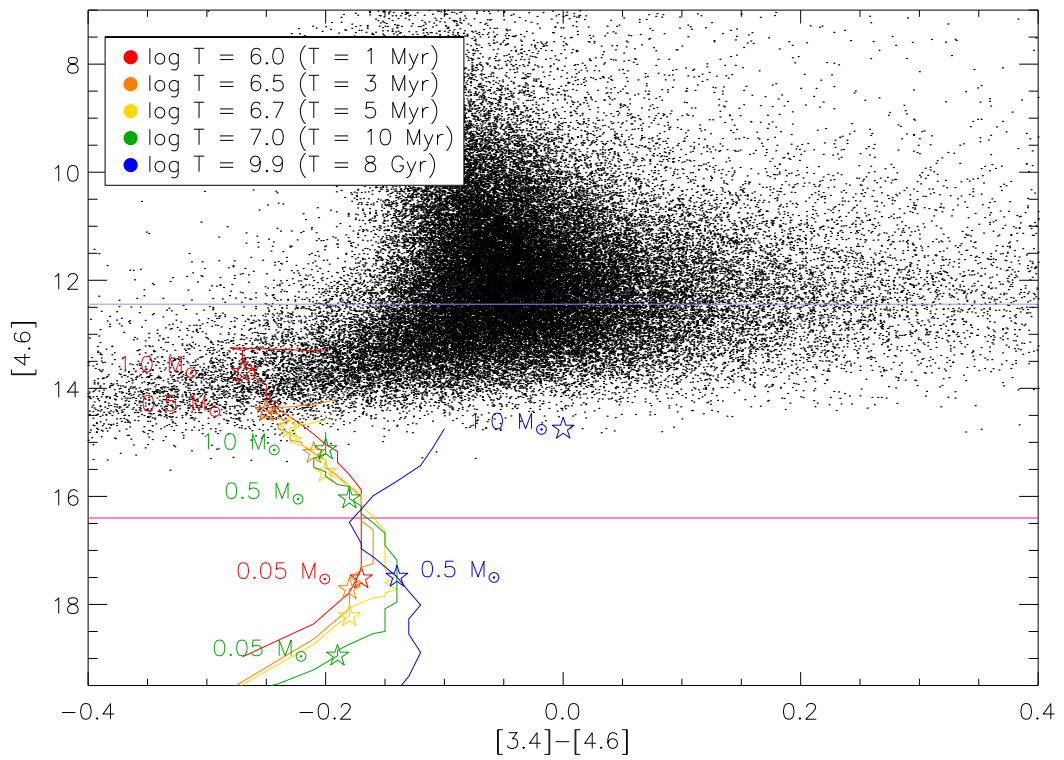
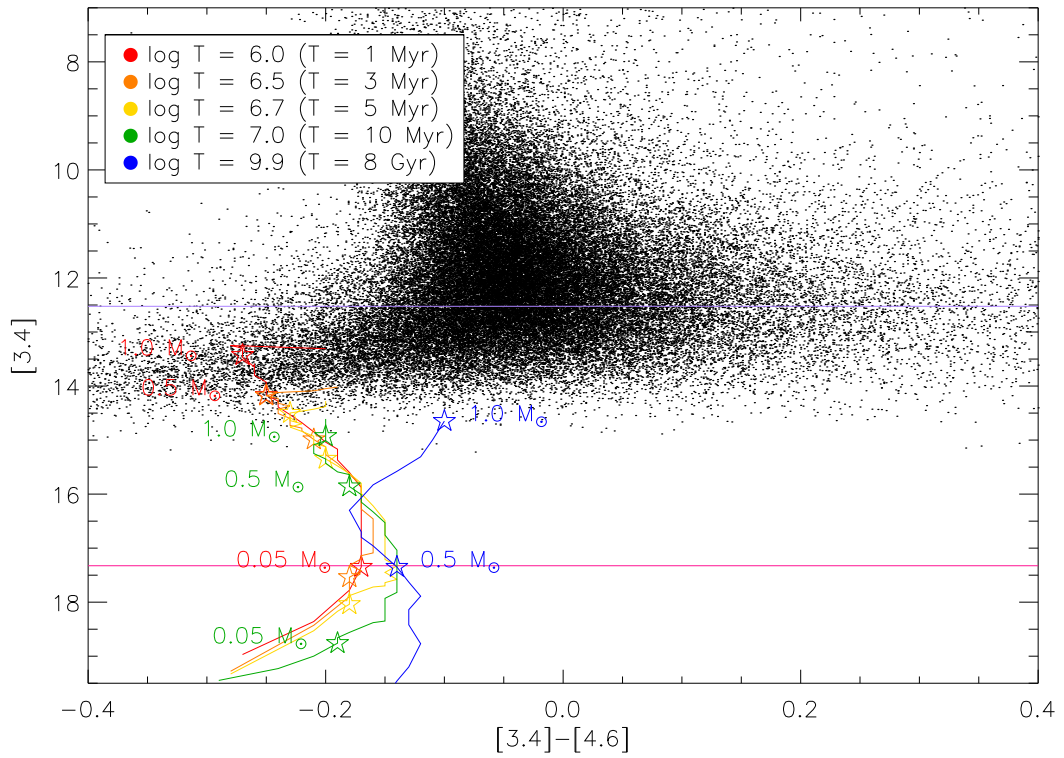


Figure 4.7: Evolutionary tracks according to Baraffe et al. [1998], overplotted on WISE colour-magnitude diagrams. The lavender lines are the completeness limits, the pink lines the sensitivity limits.

et al. and Zeidler et al.]. At the time of performing the analysis on which this work is based, the photometric calibration of these data was still in progress. Therefore, only the image data are used for a (preliminary) scientific analysis here, but no photometric values.

VISTA is a 4-m-class wide-field survey telescope that provides a  $1.3^\circ \times 1.0^\circ$  field of view. The near-infrared camera VIRCAM consists of an array of sixteen individual  $2048 \times 2048$  pixel IR detectors, providing more than 67 million pixels with a nominal pixel size of  $0.339''$  on the sky and sensitive in a wavelength range of  $0.85\text{--}2.4\ \mu\text{m}$ . Because the sixteen chips are non-contiguous they produce a set of sixteen non-contiguous images called a ‘pawprint’. For a contiguous sky coverage six pawprints, offset in x- and y-direction, are combined. The resulting ‘tile’ covers an area of  $1.5^\circ \times 1.2^\circ$  on the sky.

For each of the six pawprints, 27 exposures were obtained at five jitter positions with an integration time of 2 s each. Because the seeing conditions (with an average FWHM of  $\approx 1.7''$ ) did not meet the pre-specified quality criteria, the observations were terminated after this observing block was completed. The observations in the other filters and for the rest of the CN mosaic positions were successfully completed a few months later and were processed by the VISTA data flow system [Irwin et al. 2004] at the Cambridge Astronomy Survey Unit (CASU).

For VISTA as for HAWK-I (see Sect. 4.5 below) the  $H$  band is the most sensitive one, containing the highest number of detections while the  $J$  band is inhibited by extinction and the  $K_s$  band by diffuse nebulosity. A preliminary photometric calibration showed that objects as faint as  $H \approx 18.5$  are clearly detectable in the VISTA image. This is about four magnitudes deeper than the nominal 2MASS survey completeness limit for crowded locations near the galactic plane of  $H \approx 14.5$  [Skrutskie et al. 2006].

## 4.5 HAWK-I

For a part of the CNC (cf. Fig. 4.5),  $JHK_s$  observations are available from the High-Acuity Wide-field  $K$ -band Imager (HAWK-I) on the ESO Very Large Telescope. These provide well-calibrated fluxes with a higher sensitivity than those from the 2MASS survey (Sect. 4.6, cf. Fig. 4.8) and are therefore preferred for SED construction in Chapter 7 where they are available.<sup>10</sup>

The HAWK-I observations of the CNC [Preibisch et al. 2011c] cover a total of  $1280\ \text{arcmin}^2$  in the central CN (see 4.5). They include the South Pillars region and the three clusters Tr 14, Tr 15 and Tr 16. Data acquisition and processing as well as obtaining the catalogue were described in detail by Preibisch et al. [2011a,c]. Data processing and calibration from the 2MASS Point Source Catalog was performed by the CASU. The observations have magnitude limits of 22.4 mag, 20.7 mag and 19.7 mag, which allows detections of stars with masses down to  $0.1 M_\odot$  be complete at ages of 3 Ma [Preibisch et al. 2011a, employing the models of Baraffe et al. 1998].

In total the catalogue contains 600 336 point-like sources [Preibisch et al. 2011c], of which 502 714 were detected in all three filters. However, Preibisch et al. [2011a] estimate around 93% of those to be foreground or background sources. In this study this constriction does not matter: We are only using HAWK-I data to supplement the SEDs of known sources identified from IRAC and *Herschel* observations. If one of these sources is spatially matched to a HAWK-I catalogue source and the data point fits in well with the SED, then (and

<sup>10</sup>Gum 31 is not covered by the observations, so in Chapter 8 HAWK-I is not used.

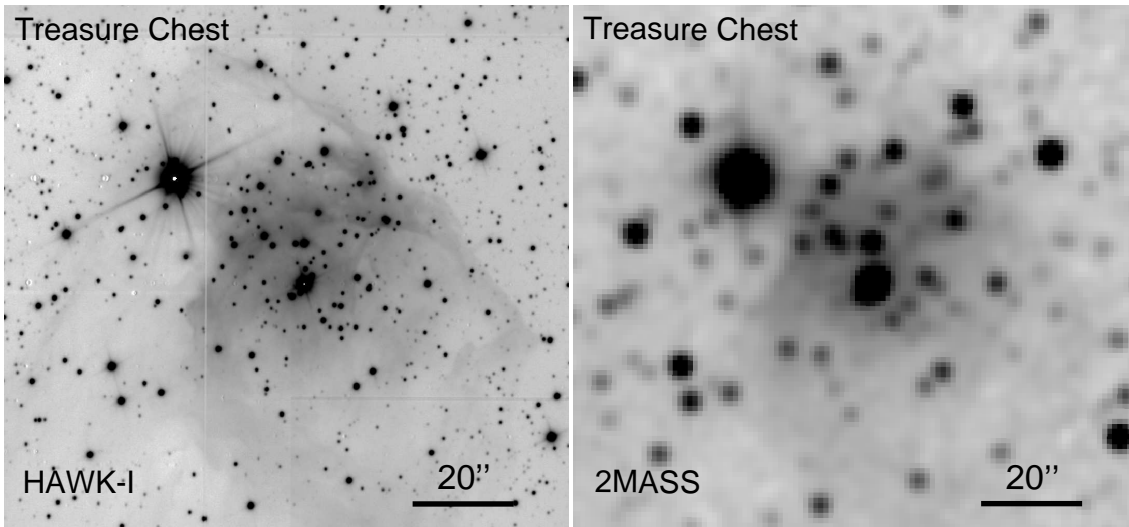


Figure 4.8: This image demonstrates the difference in point-source resolution between HAWK-I and 2MASS. Corresponding details of the Treasure Chest cluster are shown. [Image first published: Preibisch et al. 2011c]

especially if there are similar fluxes observed with 2MASS) we can assume that we are taking the data from a HAWK-I observation of a YSO belonging to the CNC.

## 4.6 2MASS

Where HAWK-I observations were not available, we used the large catalogue provided by the 2MASS survey to obtain fluxes in the NIR. In future studies this function will also be taken up by the VISTA observations, but at the time the analysis presented in Chapters 7 and 8, where SEDs are constructed, was performed, calibrated fluxes for VISTA were not yet available (see above).

The Two Micron All-Sky Survey [Skrutskie et al. 2006] was a large ground-based survey run from 1997 until 2001 [IPAC 2006], with the final All-Sky Data Release published in 2003 [Cutri et al. 2008]. It scanned the entire sky in the NIR  $J$ ,  $H$  and  $K_s$  bands, to a point-source sensitivity of  $\sim 1$  mJy [IPAC 2006]. Covering the full sky was achieved by means of employing two 1.3 m telescopes, one at Mt. Hopkins in the USA to cover the north and one at the Cerro Tololo Inter-American Observatory (CTIO) in Chile to cover the south. Each band was observed with a  $256 \text{ pixels} \times 256 \text{ pixels}$  array of HgCdTe detectors, with pixel sizes of  $2.0''$  [IPAC 2006].

2MASS functions as the calibration reference for point-source positions for many studies, including ours (cf. Sect. 5.4.2). Our large catalogue of *Spitzer*-detected point-like sources was also matched with 2MASS positions to provide NIR data for the MIR detections. Because at the time of writing neither HAWK-I nor VISTA provided coverage of processed data for the entire CNC, consistent values could only be provided by the 2MASS survey. To achieve matching between the catalogues, I simply searched for the closest match to a given IRAC position in the 2MASS catalogue. I excluded any 2MASS data with quality flags X, U, E, or F, i. e. used all detections with reliable fluxes and uncertainties (flags A–D). The closest

match was assigned a counterpart if it lay within a radius of  $0.5''$ . This is the same radius we chose for the IRAC interband matching (Sect. 5.4.2). The root mean square (RMS) of positional deviations between the two catalogues was  $0.22''$ , i. e. considerably smaller.

## 4.7 LABOCA

In Chapter 7, the SEDs of the jet-emitting point-like sources are, if possible, amended by LABOCA data. These were taken from LABOCA observations of the CNC as presented by Preibisch et al. [2011d] and Pektuhl et al. [2013].

The Large APEX BOLometer CAMERA (LABOCA) is mounted at the Atacama Pathfinder Experiment (APEX) in the Chilean Atacama desert. It consists of 295 bolometers that are arranged in nine concentric hexagons, of which around 250–260 are fully usable. It has a bandwidth of 60 GHz, with the bandpass centred on  $870\ \mu\text{m}$  (sub-mm) [345 GHz] and a FWHM of  $19.2''$  [Schuller et al. 2009]. With a single-pixel sensitivity of 40–70 mJy · s, it covers a FOV of  $11.4'$  [Schuller et al. 2009].

The fact that the LABOCA centre wavelength of  $870\ \mu\text{m}$  is far on the long-wavelength side of the *Herschel* observations makes LABOCA data useful to constrain YSO SEDs. A point in the sub-mm beyond the  $500\ \mu\text{m}$  SPIRE can reach constrains the drop-off of the SED towards long wavelengths. This in turn severely constrains the number of models the data can be fitted with (because it determines the overall shape of the SED), which narrows the uncertainty range of the fit (i. e. stellar) parameters (cf. Fig. 7.8).

## 5 Source detection and photometry

Photometry on IRAC data is carried out to obtain the point-source fluxes I use to construct a large catalogue of IRAC point-like sources in the CNC. This catalogue will be the basis for the selection of young stellar objects (described in Chapter 6). It will also be used to obtain the IRAC fluxes we use to construct SEDs of point sources in the analysis presented in Chapters 7 and 8. The full catalogue will be made available online [Ohlendorf et al. 2013b].

Photometry is done in different ways for the different instruments the data of which are used here. In Chapter 4 a short overview is given of photometry for all instruments apart from IRAC. Constructing a catalogue of IRAC photometric data was the main step towards the analysis described in Chapters 7, 8 and 9. Therefore, IRAC photometry will be described in detail in this chapter. I will also describe how and why two slightly different catalogues were obtained from the same basic photometric data and how they were used in further analysis. The main characteristics of the final catalogues will also be described.

### 5.1 MOPEX

The MOsaicker and Point source EXtractor (MOPEX) [Makovoz and Marleau 2005] is a photometry tool provided by the SSC. Its scope is not limited to *Spitzer* data, but it was designed with an emphasis on *Spitzer* photometry and to deal with the corrections uniquely necessary for *Spitzer* observations.

#### 5.1.1 Basic image corrections

The corrections necessary to *Spitzer* data include the slight distortions in the original observations with respect to the world coordinate system (WCS) which are inherent to *Spitzer* data [MOPEX User's Guide v18.4.0, 2010]. Phenomena not exclusive to *Spitzer* data are image artifacts that can be removed by MOPEX, such as radiation hits or dead pixels; these are referred to as outliers. Large IRAC and MIPS pixels leave the point response function (PRF) not well sampled, so that MOPEX has a facility to derive the PRF from the large sample of an entire mosaic, although individual PRF fitting is then performed on the original input images, after they have been corrected for distortions [MOPEX User's Guide v18.4.0, 2010].

We retrieved the Level 1 basic calibrated data (BCD) from the *Spitzer* Heritage Archive. These BCD have already undergone basic data processing, for example some outliers have been flagged at this point. This is done by single frame outlier rejection, relying on the fact that a radiation hit will usually only illuminate a single pixel while a real point source stretches over several pixels. Thus, a detection with an area larger than a defined size and an intensity above a user-defined 'radhit threshold' is rejected.

These raw data as obtained from the SHA are still separated into separate AORS. They will be joined and processed further in the upcoming steps of analysis.

### 5.1.2 Why not perform simple aperture photometry?

In simple aperture photometry, the flux from a source is determined as the flux integrated over all pixels covered by a circle (‘aperture’) of pre-defined size. A constant background may be subtracted. Such a background is typically determined by integrating over the pixels in an annulus surrounding the aperture, either directly around the aperture or detached from it and removed by a certain space to avoid erroneously sampling the tail of the PSF in it. This is a relatively quick and easy method and produces good results in uncrowded fields where point sources are clearly defined and well-separated.

However, in crowded fields as occur in the MIR images on the CNC, aperture photometry serves as a tool for quick-look analysis, but has weaknesses for scientific analysis. If the PSFs of closely neighbouring point-sources overlap, then one will contribute to the flux of the other. This is the case both when a dim point source is located in the halo of a brighter one and when two similarly bright sources are located close to each other. In the first case while the flux of the bright source is only slightly affected, the flux of the dimmer one will be severely distorted by a large contribution from the bright source. In the second case, both flux determinations will suffer severely. Conversely, in PSF/PRF-fitting photometry<sup>1</sup>, the typical spread of the point source as sampled by the detector is taken into account.

## 5.2 Mosaicking

Before further analysis was performed, the narrow strips of observational data constituted by each AOR were combined into an image mosaic on which further analysis could be performed. This was done for each wavelength separately. My experiments showed that MOPEX cannot handle mosaics consisting of four or more AORs for the photometry process. Consequently, the central CNC was divided into three groups of three AORs each which in the following will be called ‘north’, ‘centre’ and ‘south’ (indicated in Table 5.1). These were then processed separately. This also means that the obtained photometric data had to be joined into one single photometry catalogue afterwards (Sect. 5.4).

Furthermore, the mosaics could not be processed for the north group in the IRAC 5.8  $\mu\text{m}$  band and for the south group in the 8.0  $\mu\text{m}$  band. No apparent reason for this behaviour could be determined. For both cases, all further analysis steps were performed separately for all three AORs in the group and the results merged afterwards using the same processes as for the band merging.

It is important to note that in this region we do not have what the MOPEX User’s Guide v18.4.0 [2010] defines as ‘good coverage’: At least ten frames per pixel. Due to the IRAC scanning method, depending on the region each pixel is covered by two to four frames.

To prepare photometry with MOPEX, the following modules (i. e. analysis steps) were performed. (This description relies heavily on the MOPEX User’s Guide v18.4.0 [2010].)

---

<sup>1</sup>The MOPEX User’s Guide v18.4.0 [2010] stresses that the point response function (PRF) and the better-known point-spread function (PSF) are not identical. While the PSF is a function of the point-source image itself, the spread of the light from the source in the image, the PRF is the array created by sampling the PSF on a detector.

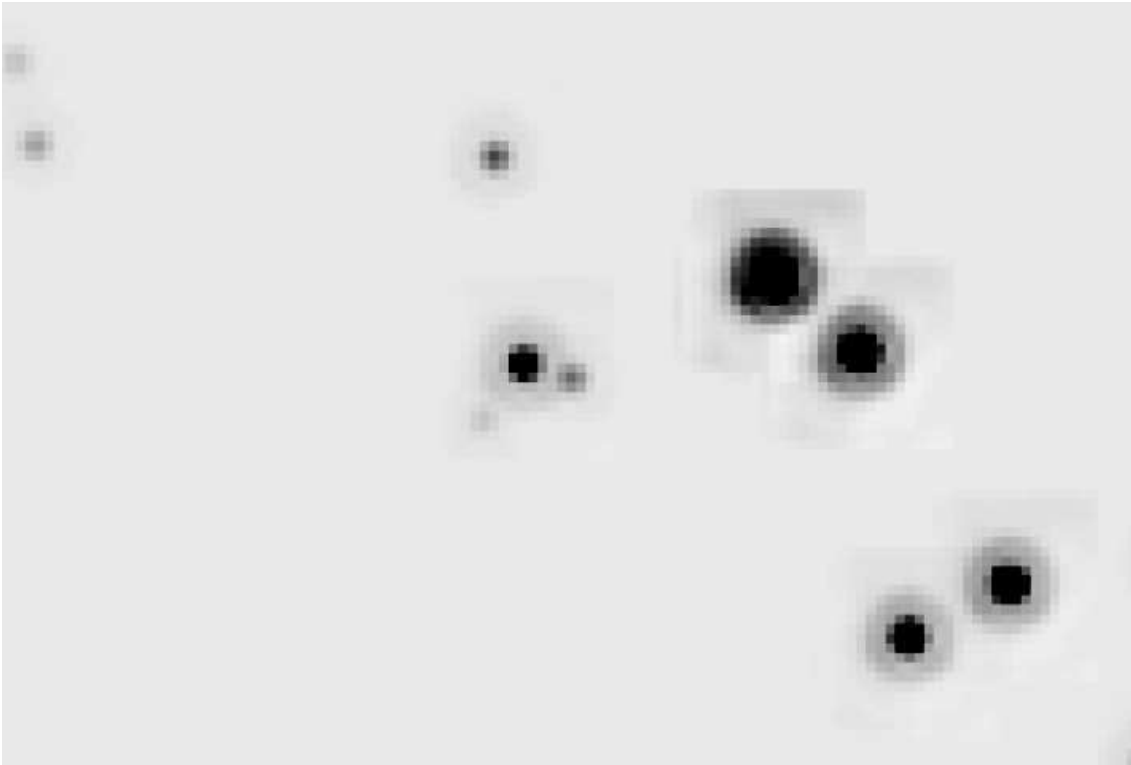


Figure 5.1: This image, drawn from an intermediate step in the StarFinder analysis of the comparatively sparsely populated MIPS field in Gum 31 (cf. Chapter 8), illustrates the problems of aperture photometry in a crowded field. It shows only the StarFinder-detected sources, background removed. The faint source in the centre of the image is placed well inside the PSF of the dominating source to its immediate east. If we were to determine its flux, this would be skewed by the component contributed by the brighter source. In a crowded field, these situations occur far more often.

### 5.2.1 Initial Setup

Three main kinds of files are input into MOPEX: The BCD frames, their uncertainties and a number of bad-pixel masks. These are complemented by the DCE status masks flagging dead pixels and those of permanent detector artifacts (known as PMasks), both provided by the SSC. Different PMasks are provided depending on the observation time. As the data used here were obtained in July 2008 we used the PMasks valid from April 2008 to May 2009. So called RMask masking pixels rejected as outliers can be obtained from the SSC and input into the pipeline or created in the mosaicking process as we chose to do.

In the PMasks, pixels are flagged differently according to their status (e.g. saturated [bit 9], noisy in dark [bit 7] or flatfield [bit 8] images, affected by amplifier glow in the  $5.8\ \mu\text{m}$  and  $8.0\ \mu\text{m}$  bands [bit 10] or dead [bit 14]). The user sets a bit pattern that defines which flagged bits are fatal and lead to rejection of the pixel. We used the default setting ‘18304’ ( $2^7 + 2^8 + 2^9 + 2^{10} + 2^{14}$ ), which includes all these effects. For the RMask, each outlier detection method (see below) sets one bit as described for *Mosaic RMask*.

Table 5.1: *Spitzer* IRAC observations used in this work (cf. Fig. 5.2).

Group	AOR	Start time [UT]		Exposure time
		Date	Time	
North	23708160	19 July 2008	12:12	1.2 s
North	23699200	19 July 2008	13:03	1.2 s
North	23704320	19 July 2008	13:54	1.2 s
Centre	23688192	19 July 2008	14:45	1.2 s
Centre	23701504	19 July 2008	15:37	1.2 s
Centre	23695360	19 July 2008	16:28	1.2 s
South	23696896	19 July 2008	17:19	1.2 s
South	23706368	19 July 2008	18:14	1.2 s
South	23684352	19 July 2008	21:07	1.2 s

**Notes.** These AORs were part of the "Galactic Structure and Star Formation in Vela-Carina" programme observations (PI: Steven R. Majewski, PID: 40791) and were retrieved through the *Spitzer* Heritage Archive.

### 5.2.2 Overlap Settings

As each AOR consists of several observations and we combine several AORs into one data set, the background between the separate images needs to be matched. The *Overlap* pipeline does this and sets the background to a common, non-zero level. This does not affect the source photometry to be performed later [MOPEX User's Guide v18.4.0, 2010]. We combined the *Overlap* and *Mosaic* pipelines into one workflow. This is the standard method to combine both and is according to the design of MOPEX.

### 5.2.3 Fiducial Image Frame

The fiducial image frame (FIF) constitutes a unified coordinate system for all observations within one block of data to be analysed. It is created separately for each run of MOPEX. This means that for each of the three groups analysed here a separate FIF is created by MOPEX, with no regard to the FIFs derived for the other bands and AOR groups.

Consequently, a 'super FIF' was created once from data for all four wavelength bands and the entire region. This was used for all further analysis (i. e. the *Fiducial Image Frame* module removed from the pipeline and the FIF input directly in the setup section) as in this way astrometry will be consistent over all IRAC data. We chose to interpolate to the J2000 equatorial coordinate system, with a pixel size of  $0.000166670''$  ( $\hat{=} 0.6''$ ). For the rotation of the final mosaic, we chose the average orientation of the input images. Apart from the pixel size, this uses the default settings.

### 5.2.4 MedFilter

The *MedFilter* module produces a background-reduced image to be input into the *Detect* module. These background-reduced images are only of temporary value. They are used for the detection and masking of bright objects, but not for the further background matching.

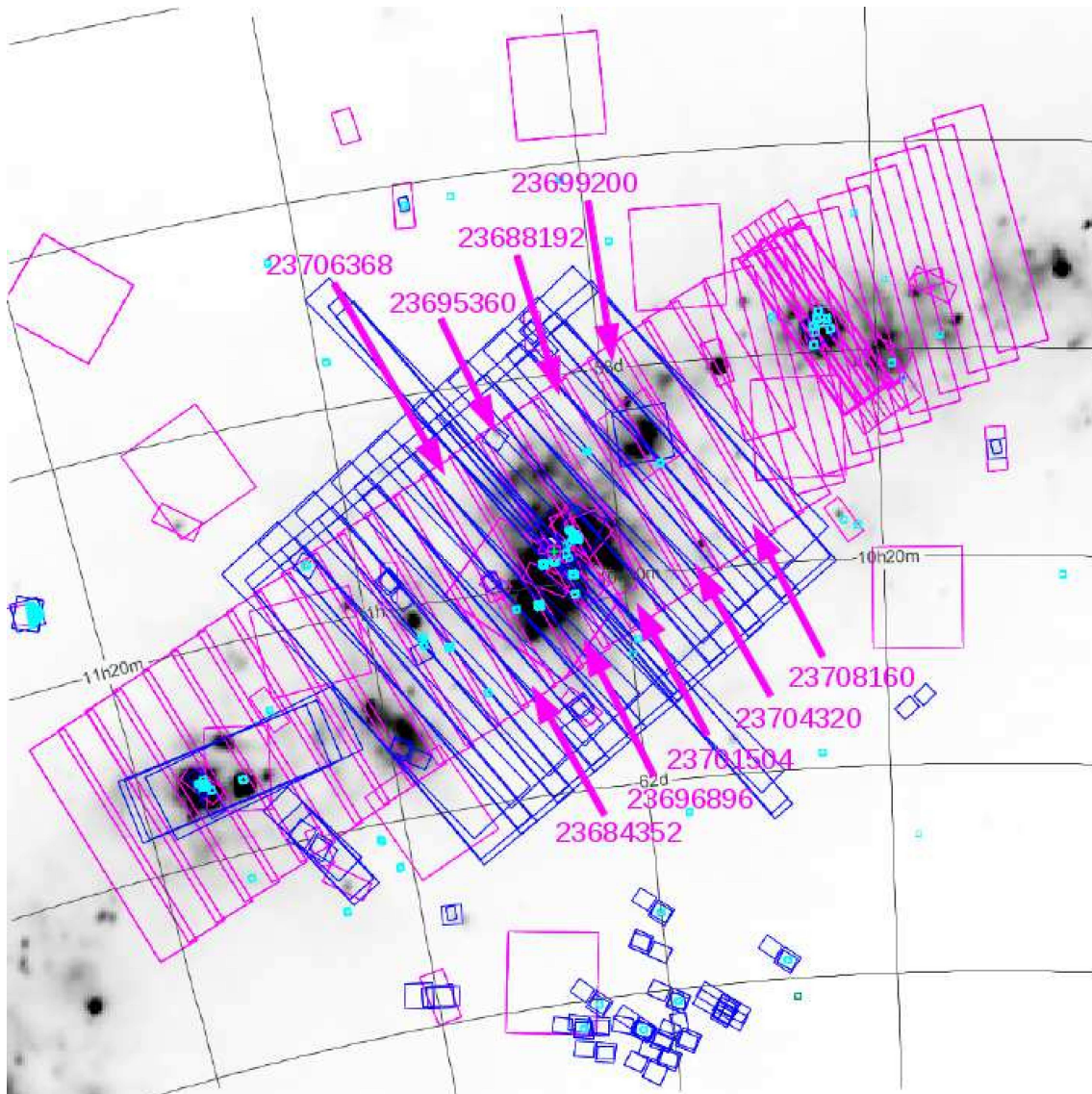


Figure 5.2: Each pink rectangle represents one IRAC AOR, their numbers corresponding to Table 5.1. Those not numbered were not used in this work as they lie beyond the extent of the CNC. Blue rectangles mark MIPS observations as discussed in Sect. 4.1.2. [AOR footprint illustration: SHA]

The background is computed from a  $25 \text{ pixel} \times 25 \text{ pixel}$  window each. For background estimation, we use the SExtractor background estimation method, which works analogously to that employed in the popular SExtractor [Bertin and Arnouts 1996] program for point-source extraction, with a filter size of 3.

### 5.2.5 Detect

In the *Overlap* pipeline, *Detect* is run on the background-subtracted images from the *MedFilter* module to detect bright objects. The module itself is identical to the one used

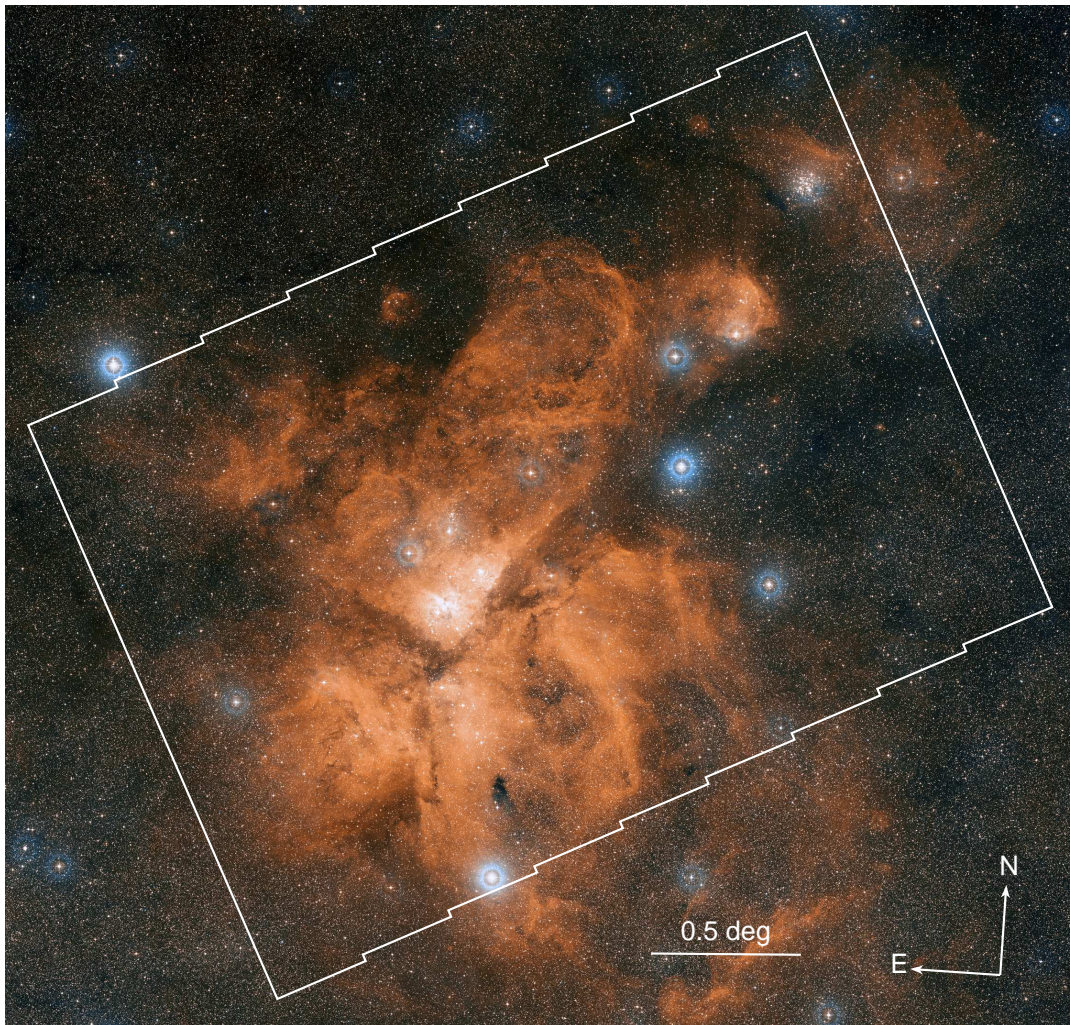


Figure 5.3: The outline of the AORS illustrated in Fig. 5.2 shown on a DSS2 image [Image credit: ESO/Digitized Sky Survey 2. Acknowledgment: Davide De Martin]. The IR band is shown in blue, the  $B$  band in red.

later in the *Mosaic* pipeline (Sect. 5.2.10) and in the APEX pipeline (Sect. 5.3.4) for the detection of point sources.

For all detected pixel clusters, centroids are computed before outlier detection and point-source extraction are performed. All pixels above a certain threshold<sup>2</sup> are marked and the cluster sizes compared to the user-defined minimal and maximal areas. If the cluster is larger than this maximum value, the cluster is either shrunken or split by raising the threshold (cf. Fig. 5.4). This follows a user-defined method, either ‘simple’ (the algorithm tries to recalculate the threshold once, then gives up if the cluster is not split), ‘combo’ (the threshold is recalculated as often as necessary to obtain sub-clusters) or ‘peak’. Here, we

<sup>2</sup>The threshold is defined as the mean signal plus the detection threshold times the standard deviation. The detection threshold here is set to  $3.00$ , i. e. the resulting threshold is three  $\sigma$  above the mean signal.

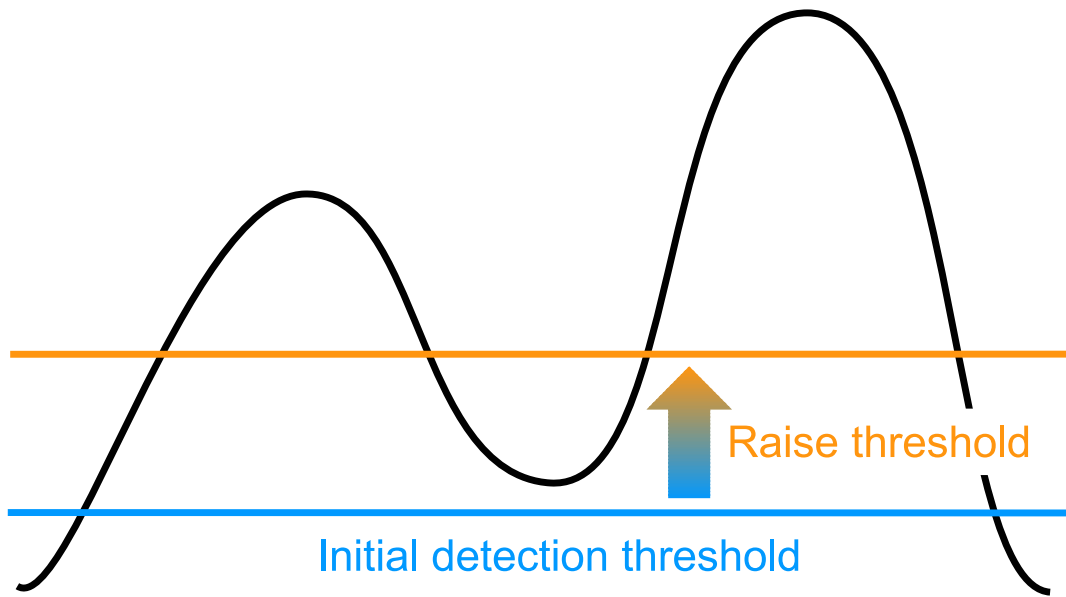


Figure 5.4: Sketch of image segmentation: Cut through the image intensity profile. With the initial detection threshold (blue), a single cluster of pixels is found which splits into two when the detection threshold is raised (orange).

use the ‘peak’ method which in the [MOPEX User’s Guide v18.4.0, 2010] is recommended for point-source detection.

This means that the algorithm not only attempts to split clusters when they are larger than the maximum detection area, but also if they contain more than one ‘peak pixel’, i. e. pixels that have a larger value than any of their neighbouring pixels.<sup>3</sup> For each iteration the new threshold  $T_{cl}$  is determined from the initial threshold  $T_{min}$  and the current lowest peak pixel value  $P_{min}$  by  $T_{cl} = P_{min} - \frac{T_{min}}{seglevel}$ , where  $seglevel \leq 50$  is the level of segmentation, i. e. the number of times the threshold has been moved.

For the *Overlap* pipeline, the clusters detected in this step are used to make masks of bright objects. These masks then serve to exclude the bright objects from the data set used for background matching.

### 5.2.6 Mosaic Interpolate

Image interpolation corrects for the distortions in input images inherent to *Spitzer* data (see above). This means that the output pixel value is interpolated to a user-defined output pixel size. This interpolation is performed to the grid set by the FIF.

In the *Overlap* pipeline I use the simplest algorithm provided by MOPEX, the grid distribution method. The algorithm is fast and provides a resolution good enough for overlap correction, but not for science. In the *Mosaic* pipeline I therefore use a different method, the default setting of pixel overlap integration, which will be explained in the

<sup>3</sup>Because we set the minimum cluster area to 1 pixel and the maximum to 90000 pixels [ $\hat{=}$  infinity] for the *Overlap* pipeline, no cluster splitting would be performed due to size alone.

relevant section.

For the grid distribution computation, a coarse grid is overlaid on the output pixel. Its flux  $O_j$  now is derived from that of the input pixels  $I_i$  it overlaps by applying

$$O_j = \sum_i \frac{n_{ji}}{N_j} I_i \quad \text{with} \quad N_j = \sum_i n_{ji}, \quad (5.1)$$

where  $n_{ji}$  is the number of grid points that fall into the respective input pixel. This is a coarser version of the weighting performed in the pixel overlap integration method.

### 5.2.7 Overlap Correction

In the *Overlap Correction* module, the actual background matching is carried out. For each image, an offset to the common background level is calculated and from this sample outliers are rejected if they deviate more than  $3\sigma$  from the mean value. Outlier rejection at this stage is only performed if at least four (user-defined) images are present. Outliers then are not used for determining the common background level, but a correction is nevertheless applied to them.

### 5.2.8 Mosaic Settings

Because the *Overlap* and *Mosaic* modules are connected, most of the *Mosaic Settings* simply repeat the *Overlap Settings* as the input images, masks, FIF and pixel size are set again here. We add an array-location dependent photometric correction mosaic, however. This is necessary because the photometry varies over the observation area, an intrinsic characteristic of IRAC observations. The array correction frame and the corresponding pixel area frame are available from the SSC for each wavelength.

### 5.2.9 MedFilter

Again, the SExtractor technique is used to make background-removed images. In the *Mosaic* pipeline they are used in the upcoming outlier rejection modules. These images are not used for the mosaicking, but only for the intermediate steps.

### 5.2.10 Mosaic Interpolate and Detect

As described above, the *Mosaic* pipeline incorporates image interpolation like the *Overlap* pipeline, done with the same parameters. Image segmentation, too, is performed again in the *Mosaic* pipeline, with the parameters set to the same values as in the *Overlap* pipeline.

The purpose in this case is, of course, different. *Detect* is run as a prior step to the *Dual Outlier* rejection, providing it with maps of bright objects.

The method used for mosaic interpolation is also different: Here pixel overlap integration is used, as illustrated by Fig. 5.5. This means that the values of the input pixels overlapped by the output pixel to be computed are mapped to the output pixel weighted with the amount of overlap  $a_{ij}$  following the formula

$$O_j = \sum_i \frac{a_{ij}}{A_j} I_i \quad \text{with} \quad A_j = \sum_i a_{ij}. \quad (5.2)$$

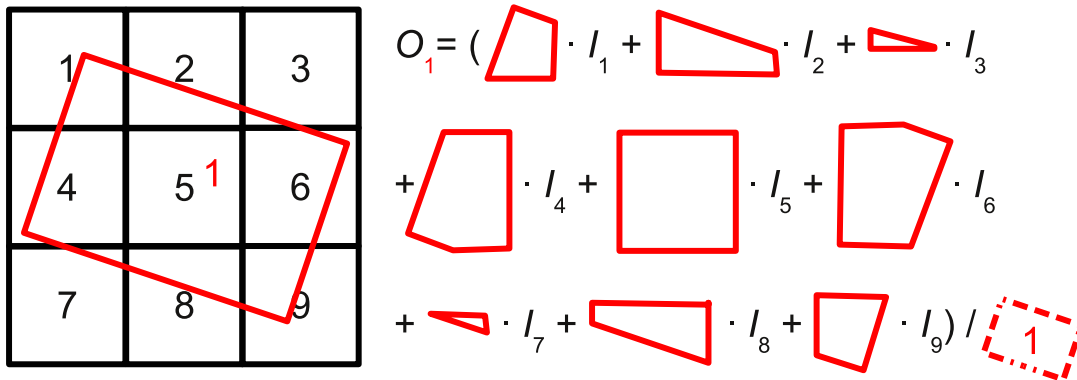


Figure 5.5: Sketch of image interpolation, pixel overlap method: The value  $O_1$  of the output pixel 1 (in red) is computed from the values  $O_{1..9}$  of the input pixels (in black), weighted with the overlap between input and output pixels (drawn as red polygons in the formula). The formula corresponds to Eq. (5.2).

### 5.2.11 Mosaic Projection

The output masks from *Detect* are in the original pixel coordinates. *Mosaic Projection* is run to project them to the WCS using the FIF, to allow them to be applied to the image data.

### 5.2.12 Mosaic Coverage

To minimise memory usage, large mosaics are split into tiles of user-defined size for analysis. The tiles have approximately, but not exactly, the same sizes according to the conditions set by the FIF size and the tile size. We permit tiles to have a size of up to 200 pixels  $\times$  200 pixels.<sup>4</sup> The tiles are later assembled into the final mosaic in the *Mosaic Combiner* module. In the *Mosaic Coverage* module, a preliminary coverage map is assembled to be used in the *Mosaic RMask* module.

### 5.2.13 Mosaic Dual Outlier

*Mosaic Dual Outlier* employs a spatial filtering method first in which clusters of illuminated pixels are identified if their area lies within a user-defined frame and their intensity above a user-defined value. After that, temporal filtering is employed. Multiframe temporal outlier detection only works when coverage of a certain area is good and a number of frames have been obtained for each region. They can be aligned on a common grid and observations can be compared that only differ in the time they were taken. A real point source will not be transient and thus detected in all of them. An outlier, however, will occur only in one of them and not in the other observations taken at different times. A maximum fraction of images for outliers can also be specified. I set it to 0.51, i. e. a detection in less than half of the images is deemed an outlier.

<sup>4</sup>This number was reduced to from 2000 pixels  $\times$  2000 pixels on recommendation of the Ssc Helpdesk. MOPEX appears not to be able to handle larger tiles for our data set.

### 5.2.14 Level

The outliers emerging from the *Mosaic Dual Outlier* module are flagged individually for each pixel. This might result in clusters that contain both pixels appearing to be real detections and those flagged as outliers. In this module, clusters are unified. When in a pixel cluster the majority of pixels are proper detections, a pixel within it flagged as an outlier is deemed to be wrongly marked and lying on the edge of a point source and the entire cluster is set to be a detection. The threshold is set by the user; I set the threshold ratio between flagged and non-flagged pixels to be 0.50 (the default), i. e. a cluster in which less than half the pixels are flagged as outliers is considered to be real, with more it is considered a false detection.

### 5.2.15 Mosaic Outlier

The *Mosaic Outlier* module removes outliers from the images by multiframe temporal outlier detection in a way analogous to that described above for the dual outlier method. As this relies solely on the comparison of data taken for the same area at different points in time, it demands good coverage.

Unfortunately, the coverage in our dataset is extremely sparse (two to four overlapping frames depending on position). Therefore, we deemed the masks created by the *Mosaic Outlier* module to be unreliable. It is, however, not possible to exclude this module from the MOPEX workflow as this will cause the *Mosaic RMask* module to fail. This bug was confirmed by the SSC MOPEX Helpdesk. As a workaround, I allowed the module to build a mask, but set the RMask fatal mask bit pattern in a way that did not include the mask created in the *Mosaic Outlier* module.

### 5.2.16 Mosaic Box Outlier

The box outlier detection follows a statistical method and combines the temporal and spatial outlier detection methods (see above). The MOPEX User's Guide v18.4.0 [2010] recommends this method for poorly sampled regions as in our case.

The module includes the pixels in a 3 pixel  $\times$  3 pixel box around the pixel in question in an analysis analogous to the temporal outlier detection described for the *Mosaic Outlier* module. Pixels from this box are picked for each interpolated image and for them a biased mean with standard deviation is calculated. The deviation of the input pixel value from this mean marks outliers.

### 5.2.17 Mosaic RMask

In the *Mosaic RMask* module, the outliers detected in the *Mosaic Outlier*, *Mosaic Dual Outlier* and *Mosaic Box Outlier* modules are combined into one mask, the so-called RMask. I chose '13' ( $2^0 + 2^2 + 2^3$ ) as the fatal bit pattern, combining *Detect Radhit* [bit 0], *Mosaic Dual Outlier* [bit 2] and *Box Outlier* [bit 3], but excluding the *Mosaic Outlier* module. As described above, this was necessary as a workaround as I discovered a bug in MOPEX which would not allow me to run the pipelines without including the *Mosaic Outlier* module although its use for poorly-sampled data is not recommended. This way, the module is run, allowing MOPEX to complete, but its results are not included in the final RMask. Likewise, including the bit 0 has no effect, as the *Detect Radhit* module is

not run. It would perform single frame outlier rejection, which is applied to the *Spitzer* data in the prior processing to obtain BCDs and therefore does not need to be done again.

It is necessary to define how well-covered a region needs to be to be included in the RMask. For the *Mosaic Outlier* method—not used but run—this is defined as at least four frames, for *Mosaic Dual Outlier* we specify less than 100 frames (i. e. always). The *Box Outlier* output is included in the RMask where at least two frames overlap (this should always be the case).

Note that due to the bug in MOPEX I checked ‘Use outlier for RMask’ as well as ‘Use dual outlier for RMask’ and ‘Use box outlier for RMask’ in this module’s settings. As I set the fatal bit pattern, however, to exclude the *Mosaic Outlier* module, this is irrelevant.

### 5.2.18 Mosaic Reinterpolate

After outlier detection and rejection, the mosaic needs to be re-interpolated onto the FIF. This is done with the same method as explained above. Re-interpolation is only carried out, however, for those pixels included in the new RMask.

### 5.2.19 Mosaic CoAdder and Mosaic Combiner

As described for the *Mosaic Coverage* module, a large mosaic is split into tiles for analysis to avoid memory issues. After all steps in the *Overlap* and *Mosaic* pipelines have been performed, these tiles are co-added. This is done by first setting each pixel to the average of the corresponding interpolated pixel values and weighting it with the exposure time as read from the flexible image transport system (FITS) header (*Mosaic CoAdder*). Finally the individual pixels are combined into a final mosaic (*Mosaic Combiner*). For usage in the Astronomical Point-source Extractor (APEX) pipeline, the co-added tiles are kept together with the assembled mosaic.

## 5.3 Photometry

For these IRAC mosaics I performed photometry using the Astronomical Point-source Extractor (APEX) module of MOPEX for all four IRAC bands (3.6  $\mu\text{m}$ , 4.5  $\mu\text{m}$ , 5.8  $\mu\text{m}$ , and 8.0  $\mu\text{m}$ ) separately. During the process, photometry was carried out individually for each image in the stack and combined internally to provide photometry data for the entire mosaic.

Although mosaicking can be done by APEX, it is preferable to run the mosaic pipeline first because APEX cannot perform outlier rejection (cf. Sect. 5.2). Therefore the photometry pipeline was appended directly to the *Mosaic* pipeline in MOPEX. However, although I used the *Mosaic* and *Overlap* pipelines together from the beginning, I first made sure they ran through and produced consistent results before adding the APEX *Multiframe* pipeline to them and experimenting with this. Eventually, I used the modules described in the following.

### 5.3.1 APEX Multiframe Settings

The APEX multiframe pipeline was used rather than the single frame one because the MOPEX User’s Guide v18.4.0 [2010] recommends this for data where the PRF varies across

the array and where there is an intra-pixel variability. Both conditions are fulfilled for IRAC data [IRAC Instrument Handbook v2.0.2, 2012]. APEX uses the same SSC-provided PRF maps as the *Mosaic* pipeline, but instead of assuming a locally constant PRF as *Mosaic* does (see Sect. 5.2) a map detailing the PRF at every position is given. The original PRF map table provided by the SSC was faulty [probably a spacing issue; SSC Helpdesk, priv. comm.] and caused APEX to fail in the *Source Estimate* module, but a new map from the SSC solved that problem. Additionally, for source detection from the mosaic, a PRF file for the centre of the observation array needs to be provided. As source extraction is not done from the mosaic itself but from the individual input images, it is not important to have a perfect PRF here. The MOPEX User’s Guide v18.4.0 [2010] recommends the centre position of the PRF map for IRAC, which I used (column 129, row 129). Furthermore, a number of files output from the *Mosaic* pipeline are needed as input, such as the coverage map and the tiled images.

### 5.3.2 Detect MedFilter

*Detect MedFilter* performs background subtraction on the input mosaic in preparation to point-source detection. The method is the same as in the *Overlap* and *Mosaic* pipelines. As there, the SExtractor method was used (cf. Sect. 5.2.4).

### 5.3.3 Point Source Probability

For each pixel, the probability of a point source lying in it is estimated. As the method is Bayesian, an a-priori point-source probability needs to be given; here it was set to 0.1. The output of this module is saved in a point-source probability (PSP) image, which is employed for point-source detection in the *Detect* module.

### 5.3.4 Detect

The *Detect* method was described in the *Mosaic* pipeline (Sect. 5.2.5) and was applied analogously here to detect point sources directly from the input images. It uses the point-source probability derived in the *Point Source Probability* module. When point sources overlap, they are fitted simultaneously (‘passive deblending’).

### 5.3.5 Extract MedFilter

Like *Detect MedFilter*, this is a background-removal module, following the same method. This time, however, background minimisation is performed on the input tiles kept from the *Mosaic* pipeline on which PRF-fitting is performed, not the mosaic itself. The background-subtracted images are then used for point-source extraction.

### 5.3.6 Fit Radius

In this module, the fitting area (a box, not a circle) for PRF-fitting to be used later (in the *Source Estimate* module) can be determined individually for each source. Alternatively, the source radius can also be input by the user, which we decided to do (see below).

The input list of point sources to be fit is that produced by *Detect*, the uncertainty image provides the basis for the calculation. The uncertainties are also weighted by the

coverage map from the *Mosaic Coverage* module (by multiplying with the square root of the coverage value). Starting from the pixel listed in the *Detect* table, for each pixel the uncertainty is compared to the pixel value and the pixel added to the fit radius as long as its value is larger than the uncertainty.

### 5.3.7 Select Detect

In the table output by the *Detect* module, large blends of sources can still be present. This, however, can cause problems in the *Source Estimate* module [SSC Helpdesk, priv. comm.], so I included the *Select Detect* module to remove blends consisting of more than 60 sources. This module can be configured individually by the user to purge the detection list of a large number of different kinds of detection types the user deemes unfit. It is only set here to remove very large blends.

### 5.3.8 Source Estimate

*Source Estimate* is the module in which PRF-fitting photometry is done, whereby source fluxes are estimated and the source positions as listed in the *Detect* table are refined. For each point-source candidate, the input image data are fit with a PRF.<sup>5</sup> For the fitting radius, we chose 3 pixels  $\times$  3 pixels. Fitting is regarded as successful when the reduced  $\chi^2$  (divided by the degrees of freedom) is smaller than a user-defined threshold value (here: 2.00). If in the *Detect* module, a cluster of detection pixels was found to be a blend of point sources, those are fitted simultaneously ('passive deblending'). If fitting a source with a single point-source PRF is not successful, up to a number set by the user of point-sources can be fit simultaneously ('active deblending'). I used the default value of one, i. e. effectively switched active deblending off. I also switched off the option of having a background fitted which would be assumed to be constant over the fitting region.

### 5.3.9 Aperture Photometry

In addition to PRF photometry, aperture photometry was carried out as a quick consistency check. Contrary to the former, aperture photometry is done on the mosaicked image, not the original input images. It uses a user-defined circular annulus (here: 4, 6 and 10 pixels). Fractional pixel values are used according to

$$AP = \sum_i a_i I_i \quad \text{with uncertainties} \quad \sigma^2 = \sum_i (\sigma(i))^2. \quad (5.3)$$

The aperture photometry can account for background, which is why in this step the background-subtracted image created in an earlier step is not used in order not to introduce additional uncertainty through relying on the output of an earlier processing step. The individual background is determined from an annulus and subtracted from the photometry result.

### 5.3.10 Select

In the select module, the user sets what is to be written in the final output tables. Finally, those tables containing all photometry results are written. I set set the module to print

---

<sup>5</sup>A detailed description of the algorithm can be found in the MOPEX User's Guide v18.4.0 [2010].

Table 5.2: Numbers of detected sources in the SPSC.

IRAC 1 3.6 $\mu\text{m}$	IRAC 2 4.5 $\mu\text{m}$	IRAC 3 5.8 $\mu\text{m}$	IRAC 4 8.0 $\mu\text{m}$	$\geq 2$ bands	All bands
349 284	338 782	214 144	165 889	244 855	43 458

source identification numbers, coordinates with uncertainties, fluxes with uncertainties,<sup>6</sup> goodness-of-fit parameters ( $\chi^2$ ) and signal-to-noise ratio (SNR), aperture sizes and bad pixels. This constitutes the basic catalogue of IRAC detections in the CNC.

## 5.4 Bandmerging

### 5.4.1 Bandmerge and creation of the Bandmerge Spitzer Catalogue (BSC)

Finally, with the Bandmerge program provided by the SSC, an overall catalogue was created that contained all sources detected with IRAC in the area, their positions and fluxes in all four bands, retaining the information of the detection bands per source. We amended Bandmerge with an IDL program of our own to remove double detections that were caused by the strategy of obtaining photometry for three groups separately and then joining them together. This means that in the overlap regions between the bordering AORs of each group photometry was performed twice on the same source, once in each group. It was necessary to identify these double detections and unify them. In doing this, we followed the simple strategy of always keeping the one detection with the better SNR. The same method was also used to remove double detections when the three separately treated AORs of 5.8  $\mu\text{m}$  north and 8.0  $\mu\text{m}$  south were merged (cf. Sect. 5.2).

Finally, these four photometry tables (i. e. in each wavelength band one table for the entire region) were merged into one, again by using Bandmerge. In the following I will refer to this catalogue as the Bandmerge *Spitzer* catalogue (BSC).

### 5.4.2 Creation of the Spitzer Point-Source Catalogue (SPSC)

Unfortunately, the results of the Bandmerge program turned out to be unreliable. In particular, there were some sources that clearly were counterparts in the different IRAC bands, identifiable by eye, that were split into two or more sources in the final catalogue, i. e. not merged properly.

This prompted the development of an IDL program to merge the sources in a more straightforward way. It consists of a simple matching algorithm, taking the 4.5  $\mu\text{m}$  band as reference. From this point, the closest positional match in each band is searched and, if it is within a radius of 0.5'', this source is chosen as the counterpart. We chose the 4.5  $\mu\text{m}$  band as the reference band because it clearly is the most sensitive one and least likely to be subject to misidentifications (see Sect. 5.4.4). These are common especially in the longest-wavelength bands where random fluctuations in nebulosities are detected as

<sup>6</sup>The uncertainties from the photometry pipeline are formal uncertainties and will underestimate the true values.

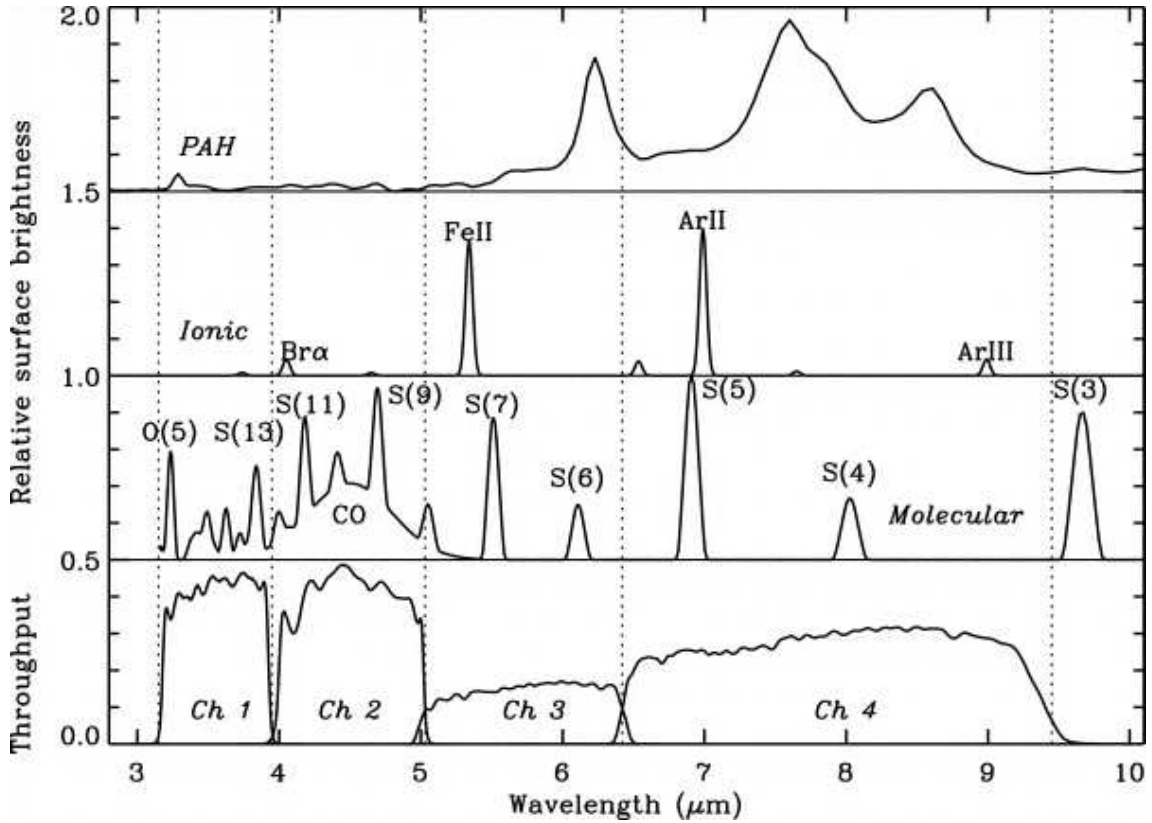


Figure 5.6: The same plot for the IRAC bandpasses as Fig. 4.3a, but comparing those to different line features [image taken from Reach et al. 2006]. The top panel illustrates the PAH emission bands that are present in the 3.6  $\mu\text{m}$  and 5.8  $\mu\text{m}$  band and dominant in the 8.0  $\mu\text{m}$  band, but of which the 4.5  $\mu\text{m}$  band is free. The middle panels show lines from cooling ionised gas behind a fast shock and  $\text{H}_2$  and CO lines, not discussed here.

point-like sources. In consequence of this requirement of detection in the 4.5  $\mu\text{m}$  band, the resulting catalogue is rather conservative. Explicitly, it excludes any object not detected in the 4.5  $\mu\text{m}$  band, even if it were detected in all three other bands (an unlikely scenario). On the other hand, this strategy minimises contamination.

While verifying the consistency of the merged catalogue we noticed a slight misalignment between the *Spitzer* bands. The 3.6  $\mu\text{m}$  band was found to be well aligned with the 2MASS positions. To counteract the offsets measured, the 4.5  $\mu\text{m}$ , 5.8  $\mu\text{m}$ , and 8.0  $\mu\text{m}$  band positions were globally shifted by  $-0.17''$ ,  $-0.1''$  and  $-0.13''$  in declination with regard to the 3.6  $\mu\text{m}$  band. This results in very small spatial deviations between the final IRAC and the 2MASS position with a RMS of  $0.22''$ .

The catalogue created in this way will be called the Spitzer Point-Source Catalogue (SPSC). It contains 338 782 sources detected in at least one band and 244 855 detected in at least two bands (Table 5.2). The full SPSC will be made available online [Ohlendorf et al. 2013b].

## 5 Source detection and photometry

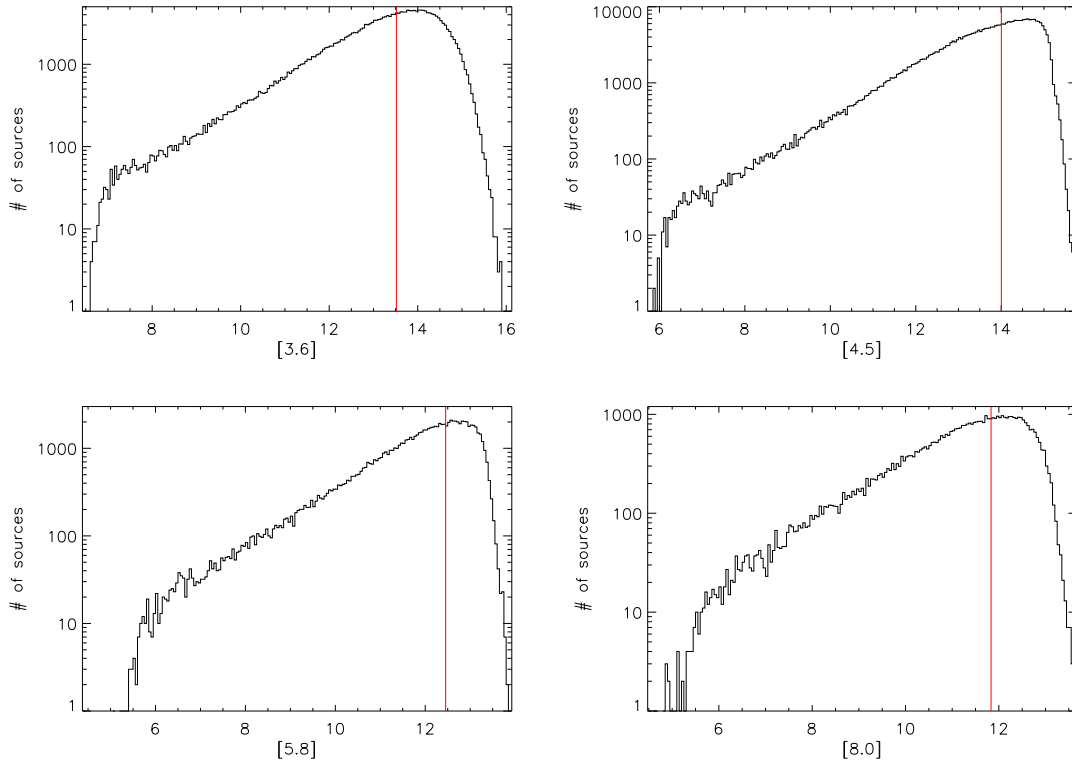


Figure 5.7: Histograms of the measured source magnitudes in the SPSC for the entire CNC. Red lines mark the completeness limits as listed in Table 5.3.

### 5.4.3 Sensitivity and completeness

The one-sigma sensitivity limits for *Spitzer* for a high background as in the present case given in the IRAC Instrument Handbook v2.0.2 [2012] are 34, 41, 180 and 156  $\mu\text{Jy}$  for 3.6  $\mu\text{m}$ , 4.5  $\mu\text{m}$ , 5.8  $\mu\text{m}$  and 8.0  $\mu\text{m}$ . The exact values depend on the background, which within our field varies strongly. Therefore, we try to characterise it individually for our sample. Here I show the values as determined for the full catalogue, a smaller sub-sample (the Gum 31 region) is used and characterised in Sect. 8.2.1. The values obtained for both are very similar, as one would expect if the sub-sample is not remarkably fainter or brighter than the average of the large sample.

Due to the very strong spatial inhomogeneity of the cloud emission in our maps, the sensitivity for IRAC cannot be quantified precisely by a single value. Instead, I characterise it by two typical values, the detection limit and the typical completeness limit. The former is given simply by the faintest sources in the sample. For 3.6  $\mu\text{m}$ , 4.5  $\mu\text{m}$ , 5.8  $\mu\text{m}$ , and 8.0  $\mu\text{m}$  these have fluxes of 100  $\mu\text{Jy}$ , 93  $\mu\text{Jy}$ , 380  $\mu\text{Jy}$  and 250  $\mu\text{Jy}$ .

To estimate the completeness limits, I constructed histograms of the measured source magnitudes and estimated the point where the rise in the source count is no longer well-described by a power-law. Although it is not a formal measure of completeness, the turnover in source count curves can serve as a proxy to show the typical values of the completeness limit across the field. It indicates where the mass (i. e. luminosity) function

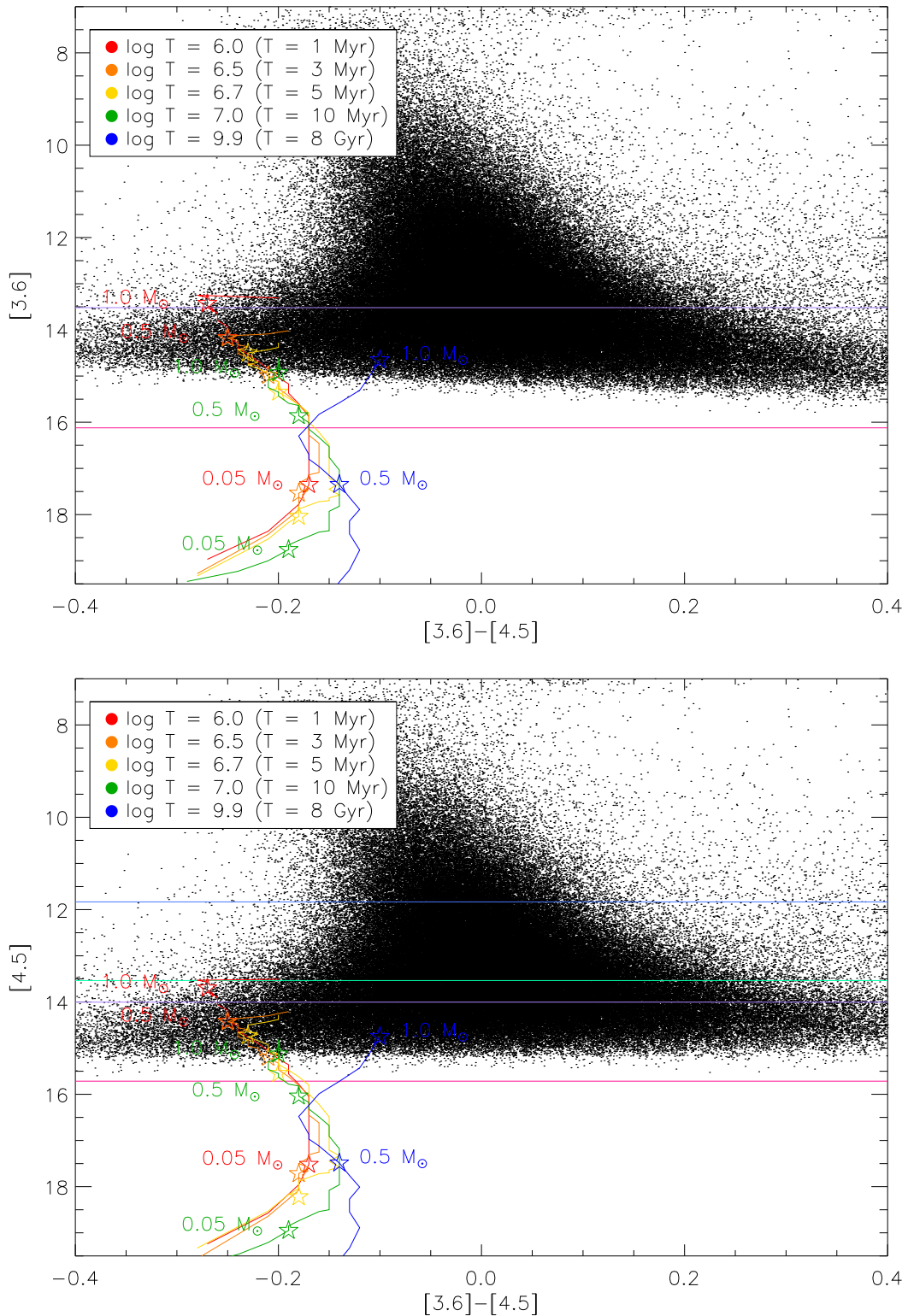


Figure 5.8: Evolutionary tracks according to Baraffe et al. [1998], overplotted on IRAC colour-magnitude diagrams. The lavender lines are the completeness limits, the pink lines the sensitivity limits. The blue and turquoise lines in the bottom diagram are the same for the 8.0  $\mu\text{m}$  band.

Table 5.3: Overview of completeness and sensitivity limits for IRAC observations.

		IRAC 1 3.6 $\mu\text{m}$	IRAC 2 4.5 $\mu\text{m}$	IRAC 3 5.8 $\mu\text{m}$	IRAC 4 8.0 $\mu\text{m}$
Sensitivity limit	[mJy]	0.100	0.093	0.380	0.250
	[mag]	16.1	15.7	13.7	13.5
Completeness limit	[mJy]	1.1	0.45	1.2	1.2
	[mag]	13.5	14.0	12.5	11.8

of the sample deviates from the canonic power-law shape. One would expect this to be continued to lower luminosities. Consequently, where the number of detected sources falls short of the expectation this should be due to detector limitations. Therefore, the ‘bend’ in the function indicates where the sample begins to be less than complete (see the histograms in Fig. 5.7). In this way I estimate completeness limits of  $\approx 1.1$  mJy,  $\approx 0.45$  mJy,  $\approx 1.2$  mJy and  $\approx 1.2$  mJy for 3.6  $\mu\text{m}$ , 4.5  $\mu\text{m}$ , 5.8  $\mu\text{m}$  and 8.0  $\mu\text{m}$ . Comparing the completeness limits to numerical models of pre-main sequence stellar evolution [Baraffe et al. 1998], we find that for an age of  $\sim 1$  Ma the photospheric emission of a  $\sim 0.5 M_{\odot}$  star IRAC detection in the two most sensitive bands (3.6  $\mu\text{m}$  and 4.5  $\mu\text{m}$ )<sup>7</sup> should be almost complete (cf. Fig. 5.8). To obtain a very rough estimate of the detection limit in the longer wavelengths, we assume that  $[4.5] - [8.0] \lesssim 1$  mag [see e.g. Lada et al. 2006, their Fig. 4]. Taking this assumption, we can estimate from Fig. 5.8 that a  $\sim 1$  Ma-old star of  $\sim 1 M_{\odot}$  should still be detectable in the 8.0  $\mu\text{m}$  band. Clearly, the longer-wavelength bands are the limiting factor in the detectability for the YSO selection (Chapter 6), for which we shall require detection in all four bands.

#### 5.4.4 BSC and SPSC

Because the shortcomings of the BSC first became apparent during the analysis summarised in Chapter 7 (as described in Sect. 7.2.1), this chapter is based on the BSC while the analysis done later (Chapters 8 and 9) is based on the SPSC. Both catalogues have their individual merits and shortcomings.

Because it only includes those sources detected at least in the 4.5  $\mu\text{m}$  band, the SPSC is much more conservative than the BSC, which included any source detected in at least one of the four bands, no matter which. On the other hand, the SPSC strategy minimises contamination and eliminates band-split sources. While the BSC has 569 774 point-like sources, the SPSC has only 338 782. This number is limited by the number of detections in the 4.5  $\mu\text{m}$  band, on which the catalogue is based.

The 4.5  $\mu\text{m}$  band is known to be the most reliable one because it has the lowest sensitivity limit and is complete down to fluxes much smaller than for the other three bands (cf. Sect. 5.4.3). Furthermore, it suffers least from contamination through dust and molecular clouds and other extended sources like PAH regions, which are a feature in all three other bands [Cohen et al. 2007, Reach et al. 2006, see Fig. 5.6].

<sup>7</sup>Baraffe et al. [1998] use the  $L'$  band centred at 3.442  $\mu\text{m}$  [Glass 1973, cited following Moro and Munari 2000] and the  $M$  band centred at 5.0  $\mu\text{m}$  [Johnson 1965, cited following Moro and Munari 2000]. These are similar to the IRAC bands.

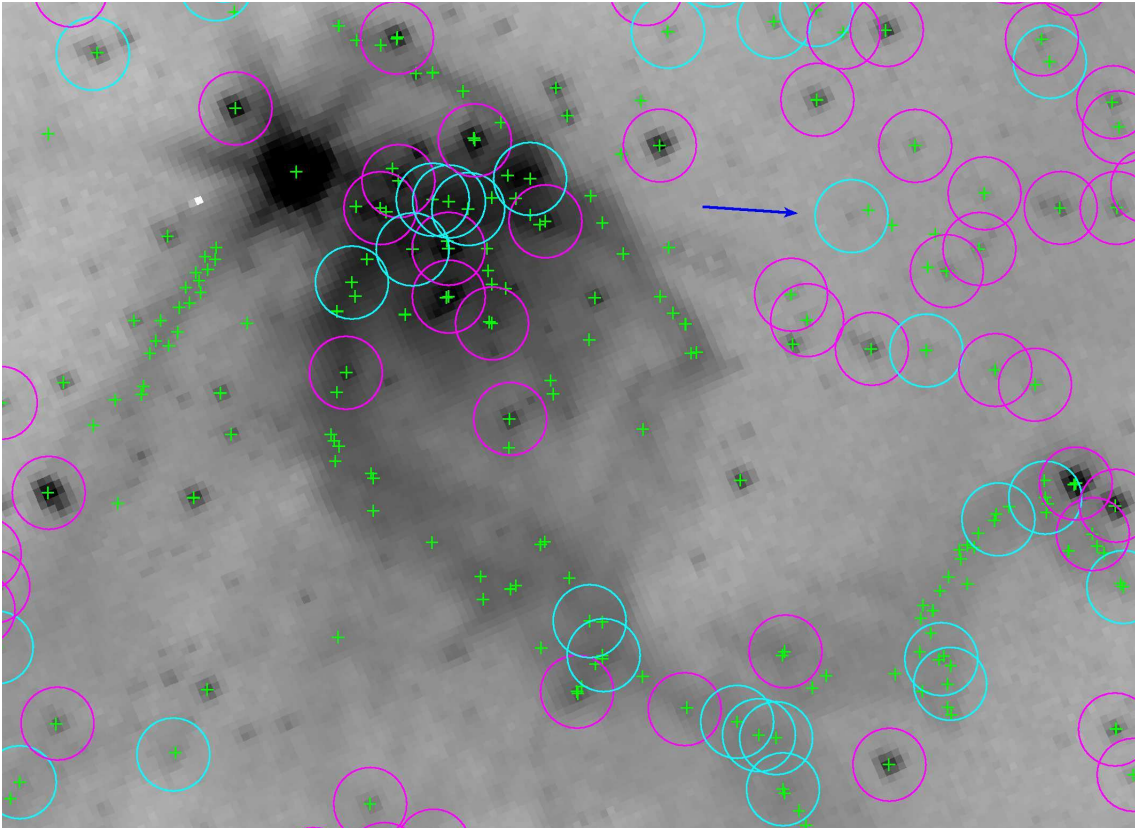


Figure 5.9: The  $4.5\ \mu\text{m}$  IRAC image of the Treasure Chest illustrates the differences between the two catalogues. The BSC (green crosses) picks up many more sources than the SPSC (circles). However, these include very doubtful sources like parts of the emission spikes, e. g. towards the left edge of the image. It also shows that some SPSC sources with only  $4.5\ \mu\text{m}$  detection (cyan) maybe erroneous. Magenta circles mark those SPSC sources detected in two or more bands. The blue arrow illustrates a case where the BSC source position was shifted by Bandmerge.

This strategy excludes many doubtful sources. The BSC, for example, often picks up “point sources” along the spikes of bright sources. As illustrated in Fig. 5.9, this is far less likely to happen in the  $4.5\ \mu\text{m}$  band. The nebulosity surrounding the Treasure Chest cluster, shown in Fig. 5.9, consists of strong PAH emission and is outlined in erroneous “point sources” in the BSC, most of which are not included in the SPSC. The figure also shows that some of the sources that are detected in the  $4.5\ \mu\text{m}$  band only (cyan circles) may have to be treated with caution, too. The highest reliability is provided by those 244 855 sources in the SPSC detected in two or more bands (magenta circles). The blue arrow in Fig. 5.9 points out a case where Bandmerge in the creation of the BSC appears to have merged sources with distinctly different positions in the different bands and thus shifted the source position (green cross) with regard to the  $4.5\ \mu\text{m}$  source (cyan circle). The SPSC retains the  $4.5\ \mu\text{m}$  position as the catalogue position.

## 5 Source detection and photometry

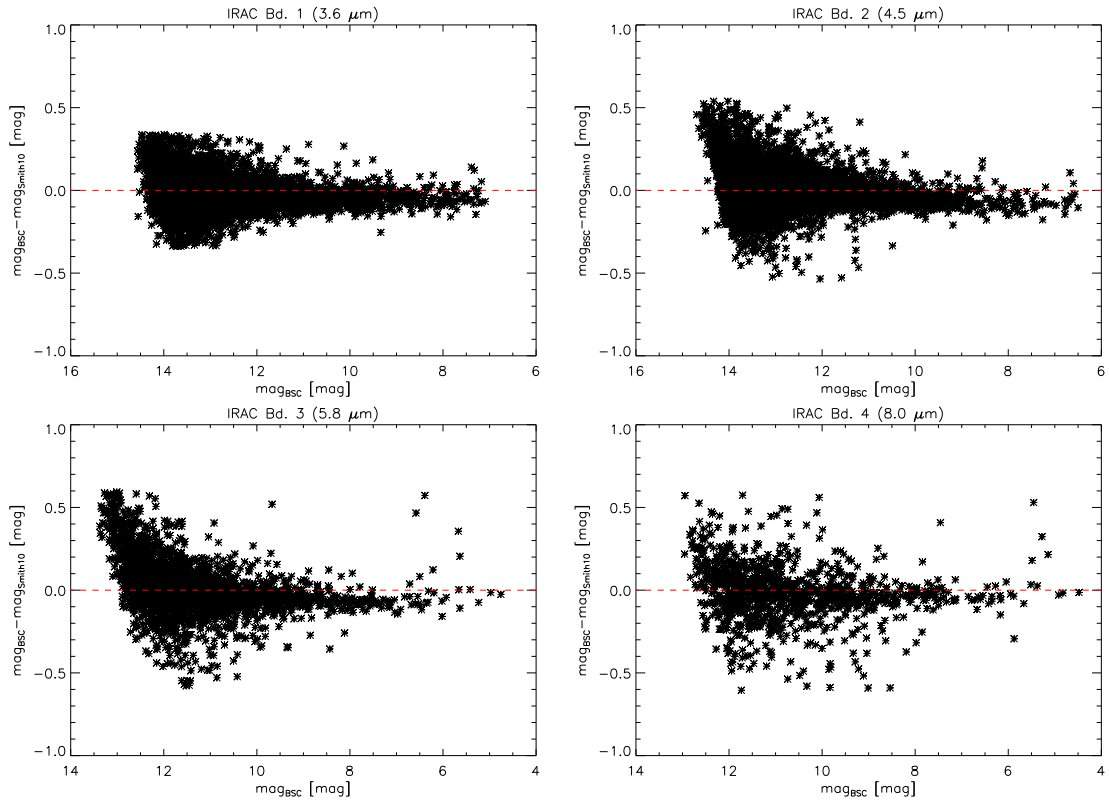


Figure 5.10: Differences in derived magnitude between the BSC and the catalogue by Smith et al. [2010b], plotted against the BSC magnitudes. Sigma-clipping has been employed.

### 5.4.5 Comparison to the catalogue by Smith et al. [2010b]

Smith et al. [2010b] assembled an IRAC point-source catalogue in two fields in the CNC, one centred on the South Pillars, the other one slightly to the west of them, in total encompassing 48 642 sources. Their “west field” contains 9477 sources and agrees well with the BSC within the area where both overlap. Source positions, as well as measured fluxes, are in good concordance between the two catalogues.

A source is considered to have been detected by both if its position does not deviate by more than  $1''$ . For 832 sources this is not the case, the remaining 8645 have a direct counterpart in the BSC. The histogram in Fig. 5.11 shows that in the majority of cases the spatial deviations are much smaller than  $1''$ . The RMS deviation in source position between the two catalogues is  $\sim 0.27''$ . Sigma-clipping was employed, i. e. those sources where the magnitude difference was larger than  $3\sigma$  where removed from the sample as bad matches. Those were 142, 57, 43 and 23 in the four bands. The RMS deviation in magnitudes (Fig. 5.10) is 0.095 mag in the  $3.6\ \mu\text{m}$  band, 0.13 mag in the  $4.5\ \mu\text{m}$  band and 0.17 mag in  $5.8\ \mu\text{m}$  and  $8.0\ \mu\text{m}$ . Comparing to the SPSC instead of the BSC, only 8059 sources have a direct counterpart, whereas the RMS deviations are the same (Fig. 5.12).

In Sect. 6.5, the cYSO subsamples are compared. Additionally, the Spitzer YSO Catalogue in Carina (SYCC) (Chapter 6) is compared to the PCYC of Povich et al. [2011a].

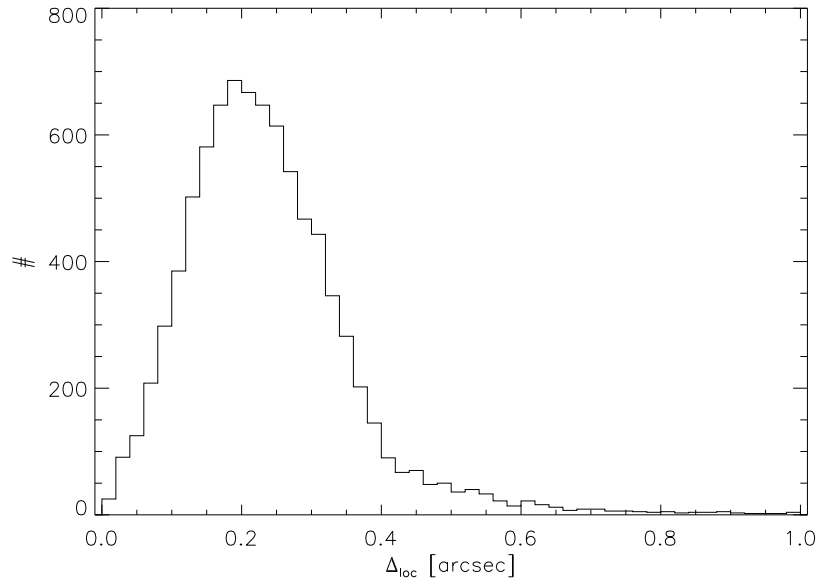


Figure 5.11: Histogram of offsets in source position between the BSC and the catalogue by Smith et al. [2010b]. Sigma-clipping has been employed.

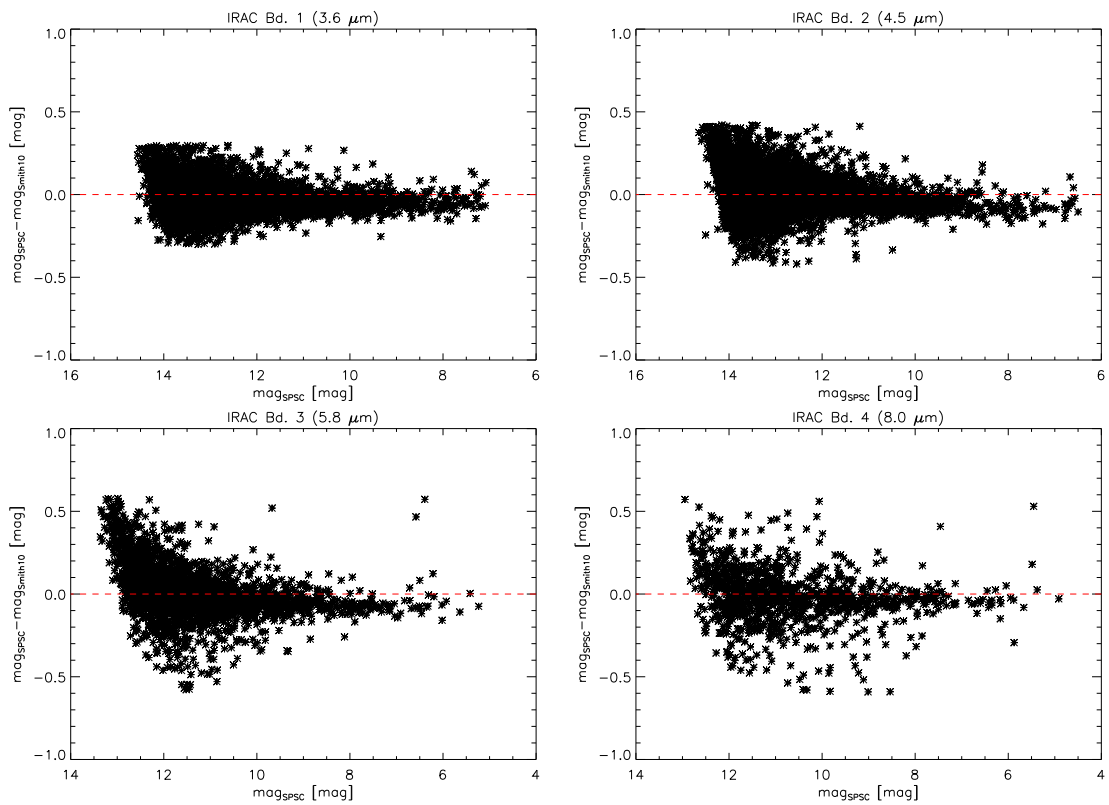


Figure 5.12: Differences in derived magnitude between the SPSC and the catalogue by Smith et al. [2010b], plotted against the SPSC magnitudes. Sigma-clipping has been employed.

## 6 Identifying young stellar objects

Chapter 5 described how to construct a catalogue of point-like sources observed with IRAC in the CNC. In this chapter, only the probable young stellar objects will be selected from this catalogue, the SPSC, to create a cYSO catalogue.

As described in Chapter 3, many studies have been made of the CNC and several of them in the MIR. The studies of Smith et al. [2010b] and Povich et al. [2011a] even used *Spitzer* IRAC data to study the CNC in depth and there are a variety of catalogues of young stars, the PCYC as a large catalogue of IRAC-selected cYSOs among them. This new catalogue will aim at the most careful selection possible to minimise contamination. It also covers an unprecedentedly large part of the CNC, which means that not only parts of the CNC will be studied that have never been studied in detail before (e. g. Gum 31, cf. Chapter 8), but that basic data and data processing will be uniform for all parts of the CNC, allowing direct comparison.

After describing the photometric processes used to derive the source magnitudes in Chapter 5, in Sect. 5.4.4 I already discussed the merits of two different methods of selecting point-like sources. There I showed that the catalogue I will be using for identifying cYSOs here is a comparatively conservative one. It only includes sources that are at least detected in the most reliable band ( $4.5\ \mu\text{m}$ ), which is a different approach than for other surveys. Here, I try not to maximise the number of detected point-like sources but rather to maximise the proportion of real detections among the catalogue. As described in more detail in Sect. 6.4, the likelihood of a cYSO simply to be a contaminant and not a YSO at all is extremely high in the CNC. Again, I opted for conservativeness and tried to exclude as many contaminants as possible, even at the cost of eliminating true YSOs with them. In short, false negatives are preferred over false positives.

This approach lets the new catalogues be much smaller than comparative ones. The PCYC, for example, relying on the same *Spitzer* observations, contains a multiple of sources of the final catalogue of cYSOs, although its survey area is smaller. However, our new catalogue is as free from contaminants as possible, so allows us to draw conclusions from the spatial distribution of the cYSOs. The comparison in Sect. 6.5.2 will show that while the PCYC is much larger than our catalogue, the majority of our sources has a counterpart there. (In Appendix C the differences in selection strategy are illustrated.)

This reliability of YSO selection will be very important especially in Chapter 9. There I will show that the distribution of cYSOs actually shows patterns that agree well with observations of the cloud structure, with other cYSO populations like those derived from *Herschel* and WISE data, and with theoretical predictions. A more complete, but at the same time more contaminated sample would not allow a similar strategy.

## 6.1 A sample of infrared point sources: Which are young?

Young stars exhibit several characteristics that distinguish them from their more evolved companions (cf. Sect. 2.1). Selecting for X-ray emission is a possible technique to sample YSOs; I will be taking another route and filtering the MIR data for stars with an IR excess.

Selecting cYSOs from colour-colour diagrams is a well-tried method and especially for IRAC data has been proven successful repeatedly [e.g. Allen et al. 2004, Winston et al. 2007, Roccatagliata et al. 2011, Fang et al. 2012]. The principle is simply to select those sources that exhibit IR colours that cannot be explained by a reddened photosphere of a main-sequence star. This is a good method for very large samples like ours, where assembling and examining an SED to find the IR slope for classification for each and every source is simply not feasible. However, Winston et al. [2007] find that for their IRAC-observed sample of cYSOs in the Serpens cloud core classification from the SED slope and the colour-colour diagram agree in 86% of cases. Therefore, we feel confident in employing this method for compiling a large catalogue of cYSO for the CNC.

A caution is needed before launching into the details of YSO selection: Strictly speaking, in the following we will be selecting objects that exhibit an IR excess. The reason for this IR excess is not their youthfulness as such, but the fact that they retain a circumstellar disk (Sect. 2.1.1). This dusty disk and not the star itself is the source of the IR excess emission. Therefore, strictly speaking we will not be searching for young stars in the following but for *young stars with disks*. I will be referring to this sample as young stars or YSOs, but the reader will have to keep in mind that we will always be missing those young stars that are diskless. This means that only YSOs of Class 0 to Class II can be seen in this way while most Class III objects remain undetected (cf. Sect. 2.1.2).

Just the same as discussed in Sect. 6.3.1 for the WISE catalogue of cYSOs, contamination is a challenge in the Spitzer YSO Catalogue in Carina (SYCC), too. In short, we need to avoid having other sources observed with IR excess, such as AGN or AGB stars, appear in the catalogue under the guise of YSO. Because the SYCC is one of the main products of this work, contamination needs to be tackled carefully. This will be discussed in detail in Sect. 6.4.

## 6.2 Selection by IRAC colours

With IRAC data only and following the criteria established for a survey of the star-forming region Pismis 24 [Fang et al. 2012, Allen et al. 2004] we can identify IR excess sources by plotting the [3.6] – [4.5] colour against the [5.8] – [8.0] colour. For identification as a cYSO Fang et al. [2012] demand [Eq. (6.1) follows Allen et al. 2004]:

$$\begin{aligned} [3.6] - [4.5] &\geq 0 \quad \text{and} \\ [5.8] - [8.0] &\geq 0.4 \end{aligned} \tag{6.1}$$

$$[3.6] - [4.5] \geq 0.67 - ([5.8] - [8.0]) \cdot 0.67. \tag{6.2}$$

Applying these criteria to the SPSC leaves us with 879 cYSOs. The selection is illustrated in Fig. 6.1. However, it requires that an object be observed in all four IRAC bands to be eligible for the selection process at all. It excludes all those objects which are not observed in at least one out of four bands. As given in Chapter 5, this includes only 43 458 sources out of 338 782 sources in the complete SPSC.

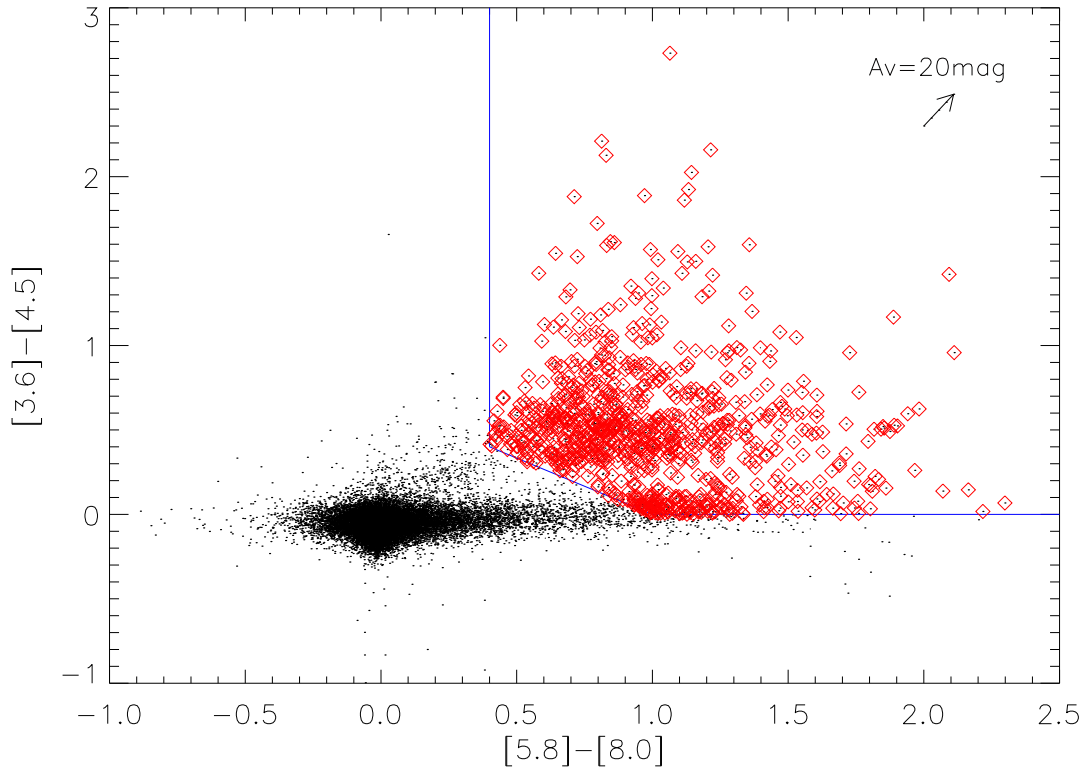


Figure 6.1: Colour-colour diagram using all *Spitzer* IRAC bands. YSOs are marked in red according to the criteria set by Eqs. (6.1) and (6.2).

By plotting the  $[3.6] - [4.5]$  colour against the  $[4.5] - [8.0]$  colour, we can work with a slightly larger sample of 47 810 sources detected in those three bands. To select cYSOs, we demand [Simon et al. 2007]

$$[3.6] - [4.5] > 0.6 \cdot ([4.5] - [8.0]) - 1.0 \quad (6.3)$$

$$[4.5] - [8.0] < 2.8 \quad (6.4)$$

$$[3.6] - [4.5] < 0.6 \cdot ([4.5] - [8.0]) + 0.3 \quad (6.5)$$

$$[3.6] - [4.5] > -([4.5] - [8.0]) + 0.85. \quad (6.6)$$

This leads to the the 1696 cYSOs shown in Fig. 6.2.

Fang et al. [2012] plot their sample in the same colour-colour diagrams. In addition, they use the IRAC spectral index to sort all their cYSOs into Class I and Class II. The separation in the resulting colour-colour diagram forms a straight line which I determined to be defined by

$$[3.6] - [4.5] \geq -1.2 \cdot ([4.5] - [8.0]) + 2.6. \quad (6.7)$$

We can use this result to distinguish between Class I and Class II candidates in our sample (see Fig. 6.2). By applying a strict selection along this line, we obtain 240 cYSOs in the “Class I” section of the colour-colour diagram and 1456 cYSOs in the “Class II” section.

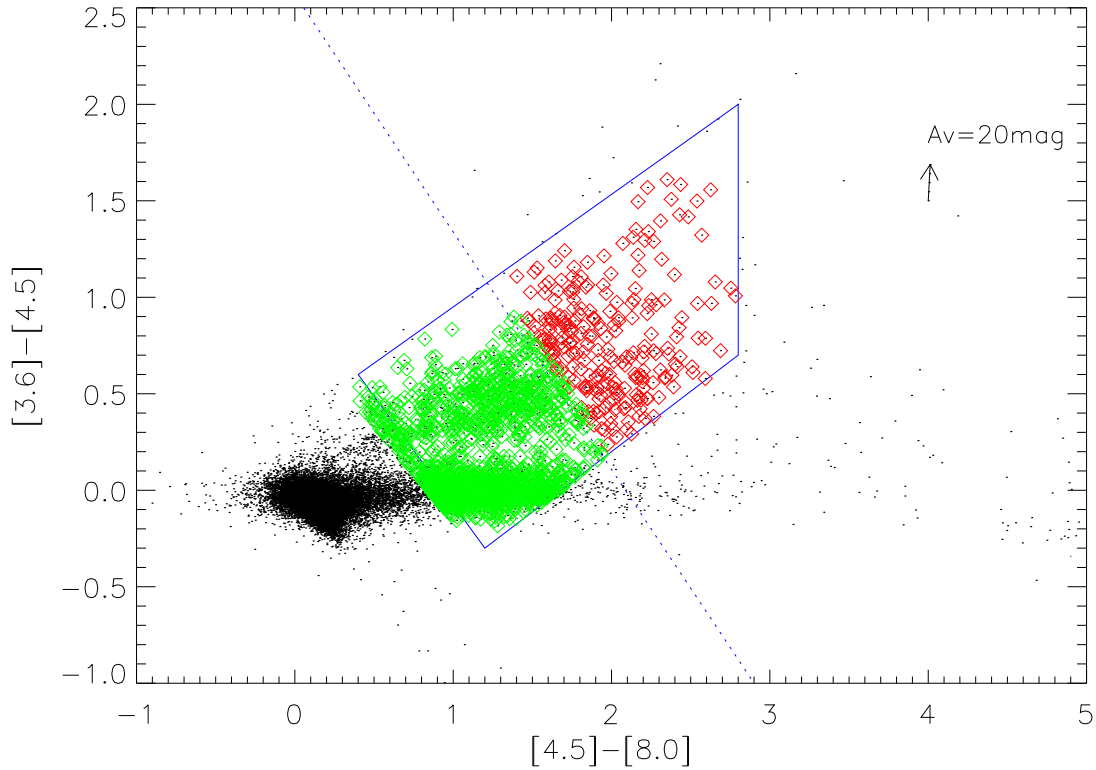


Figure 6.2: Colour-colour diagram using three out of four *Spitzer* IRAC bands. YSOs are contained in the blue box that follows Eqs. 6.3 to 6.6. The blue dotted line marks the separation between Class I and Class II objects (Eq. 6.7), where Class I candidates are plotted in red and Class II candidates in green.

### 6.2.1 The SYCC

Comparing the different samples of cYSOs, we find that the most restrictive identification criterion for YSOs comes from combining selection from different colour-colour diagrams. I combined selection from the  $[3.6] - [4.5]$  vs.  $[5.8] - [8.0]$  diagram with selection from the  $[3.6] - [4.5]$  vs.  $[4.5] - [8.0]$  colour-colour diagram, which allows separating the cYSOs into Class I and Class II objects. Thus, we take only those sources as cYSOs that fulfil Eqs. (6.1) and (6.2) *as well as* Eqs. (6.3) to (6.6).

Including the modifications described in Sect. 6.2.2, we identify 759 objects within the CNC as cYSOs. We find 221 of those to be Class I objects, 538 as Class II objects. Clearly, the  $[3.6] - [4.5]$  vs.  $[5.8] - [8.0]$  diagram is the limiting factor here, yielding half the sources the  $[3.6] - [4.5]$  vs.  $[4.5] - [8.0]$  colour-colour diagram does (879/1696, 52%). This catalogue in the following will be called the *Spitzer* YSO Catalogue in Carina (SYCC).

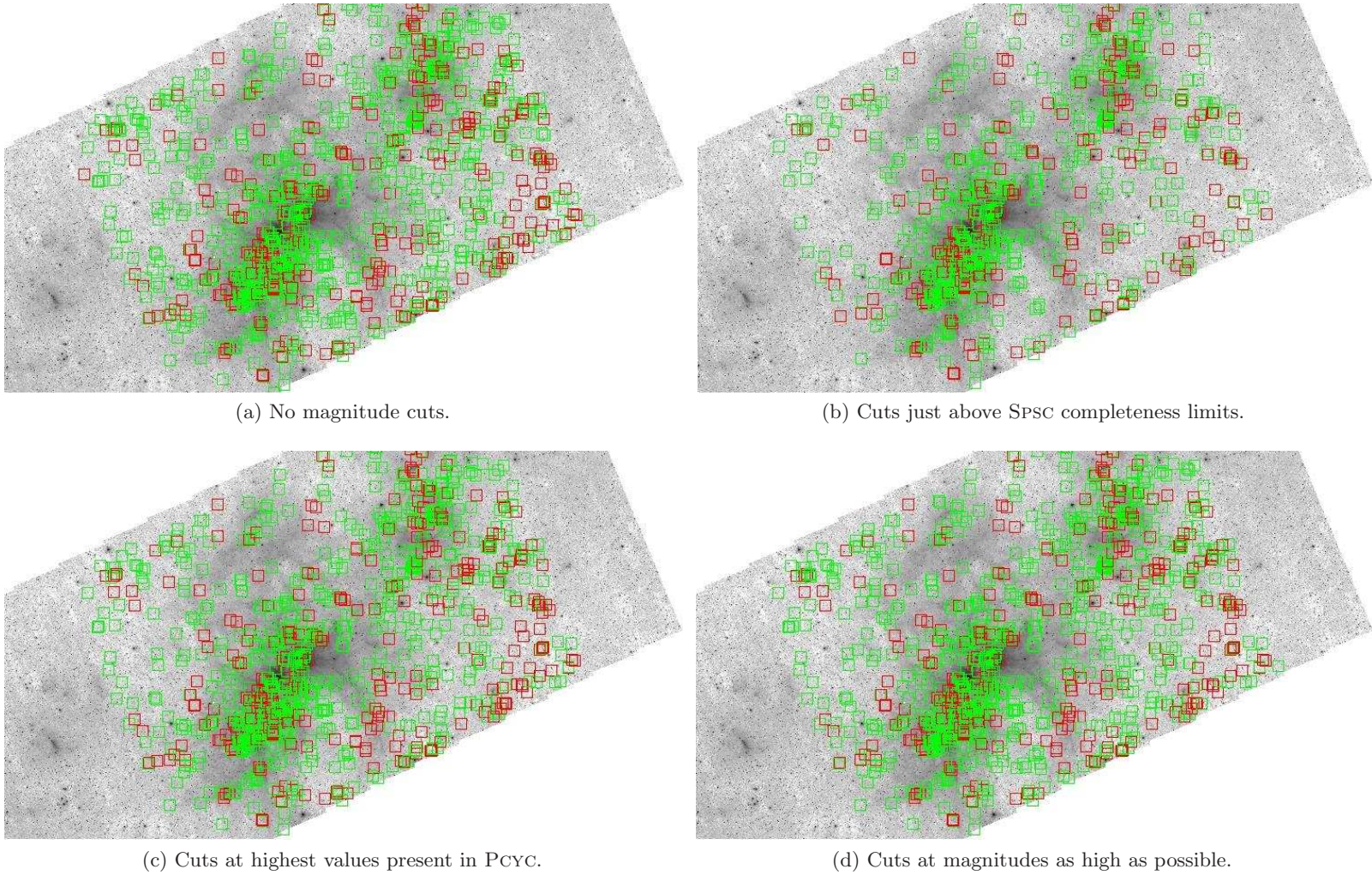


Figure 6.3: Cutting the SPSC at different magnitude levels before assembling the SYCC through colour-colour diagrams.

### 6.2.2 Using the full SPSC?

The four IRAC bands used for assembling the SPSC, as shown in Sect. 5.4.3, have completeness limits around 1 mJy. These values are not universal over the entire catalogue. The detection limits vary according to the nebulosity, which obscures sources where it is strong. This in effect distorts the catalogue because we do not have a consistent cutoff towards faint sources.

To avoid this distortion, the faintest sources are excluded from the catalogue. Figure 6.3 illustrates the different cut levels with which I experimented, with the unmodified catalogue for comparison (Fig. 6.3a). The unmodified catalogue yields 1070 sources. Using only those sources brighter than 13.2 mag, 13.5 mag, 12.5 mag and 11.5 mag in the individual bands (slightly brighter than the completeness limits) for the individual bands (Fig. 6.3b) 759 sources remain.

Because this appears to be a rather severe cut (by 26%), I experimented with other possibilities such as cutting at the faintest magnitudes still present in the PCYC (see Sect. 3.5.3), which are 15.0 mag, 14.0 mag, 13.0 mag and 12.5 mag for 3.6  $\mu\text{m}$ , 4.5  $\mu\text{m}$ , 5.8  $\mu\text{m}$  and 8.0  $\mu\text{m}$  (Fig. 6.3c). This yields 997 sources.

Looking at the magnitude histograms of the SPSC (Fig. 5.7), the faintest magnitude values that can still be justified as a meaningful cutoff (just behind the peak of the distribution) are 14.5 mag, 15.0 mag, 13.2 mag, and 12.7 mag for 3.6  $\mu\text{m}$ , 4.5  $\mu\text{m}$ , 5.8  $\mu\text{m}$  and 8.0  $\mu\text{m}$ . These yield 1030 sources (Fig. 6.3d).

However, if one regards the distribution of cYSOs, there is not much difference in the general aspect of Figs. 6.3a, 6.3c and 6.3d. There is a discernible cluster of cYSOs coincident with the central CN, but an almost uniform distribution around it. Only in Fig. 6.3b, i. e. with cuts just above the completeness limits, there appear to be fewer cYSOs outside the nebulae where one would expect less star formation to take place. Therefore, we use this background-reduced SYCC in the following.

## 6.3 Selection by WISE colours

Because we also obtained the WISE catalogue data for the CNC, the same selection of cYSOs with the aid of colour-colour diagrams is possible. Koenig et al. [2012] in their study of massive star-forming regions developed a set of criteria to identify likely YSOs from WISE four-band photometry which I use.

### 6.3.1 Contaminant removal

As discussed in more detail in Sect. 6.4, any sample of IR-excess selected cYSOs is bound to include a large number of contaminant sources. These contaminants, while exhibiting similar IR colours to the true YSOs, are in reality one of a large range of possible IR excess emitters, like e. g. AGB stars or background galaxies. Because some of them tend to cluster in certain regions of the colour-colour diagram, an attempt at their removal can be made through applying specialised very narrow colour criteria to filter them out.

Using the [3.4] – [4.6] and [4.6] – [12] colours, partly in combination with the [3.4] and [4.6] magnitudes, before the YSO selection, probable background objects are removed from the sample. In particular, these are as follows [Koenig et al. 2012]:

**Background star-forming galaxies** are very red in  $[4.6] - [12]$ . Using this to advantage, they can be removed by applying

$$\begin{aligned}
 [3.4] - [4.6] &< 0.46 \cdot ([4.6] - [12] - 1.7) \\
 [3.4] - [4.6] &> -0.06 \cdot ([4.6] - [12] - 4.67) \\
 [3.4] - [4.6] &< -1.0 \cdot ([4.6] - [12] - 5.1) \\
 [3.4] - [4.6] &> 0.48 \cdot ([4.6] - [12] - 4.1) \\
 [4.6] &> 12 \\
 [4.6] - [12] &> 2.3.
 \end{aligned} \tag{6.8}$$

**Broad-line AGNs** have similar colours as YSOs, but are distinctly fainter. The criteria for their selection are

$$\begin{aligned}
 [4.6] &> 1.9 \cdot ([4.6] - [12] + 3.16) \\
 [4.6] &> -1.4 \cdot ([4.6] - [12] - 11.93) \\
 [4.6] &> 13.5
 \end{aligned} \tag{6.9}$$

or

$$\begin{aligned}
 [3.4] &> 1.9 \cdot ([3.4] - [12] + 2.55) \\
 [3.4] &> 14.0.
 \end{aligned} \tag{6.10}$$

**Resolved PAH emission regions** are redder than the majority of YSOs. They are selected by applying

$$\begin{aligned}
 [3.4] - [4.6] &< 1.0 \\
 [4.6] - [12] &> 4.9
 \end{aligned} \tag{6.11}$$

or

$$\begin{aligned}
 [3.4] - [4.6] &< 0.25 \\
 [4.6] - [12] &> 4.75.
 \end{aligned} \tag{6.12}$$

**Resolved shock emission knots** are removed by demanding

$$\begin{aligned}
 [3.4] - [4.6] &> 1.0 \\
 [4.6] - [12] &< 2.0.
 \end{aligned} \tag{6.13}$$

The colour-colour diagrams which illustrate these steps of contaminant removal are shown in Appendix B.

### 6.3.2 YSO selection

From this cleaned sample the IR excess sources are then selected by demanding [Koenig et al. 2012]:

$$\begin{aligned}
 [3.4] - [4.6] - \sigma_1 &> 0.25 \\
 [4.6] - [12] - \sigma_2 &> 1.0,
 \end{aligned} \tag{6.14}$$

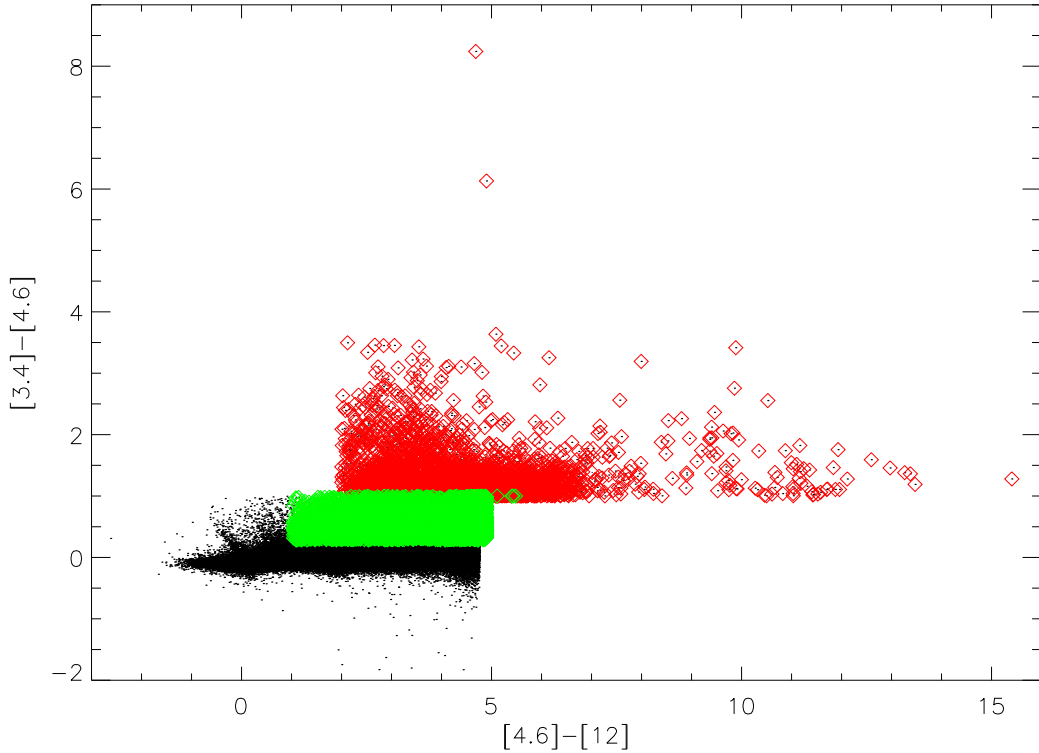


Figure 6.4: Colour-colour diagram using three out of four WISE bands. YSOs are marked in red for Class I and green for Class II according to the criteria set by Eqs. 6.14 and 6.15 [Koenig et al. 2012].

where  $\sigma$  is the quadratically added uncertainty of the respective magnitudes. Class I sources are a subsample of this defined by

$$\begin{aligned} [3.4] - [4.6] &> 1.0 \\ [4.6] - [12] &> 2.0. \end{aligned} \tag{6.15}$$

Because the sample before this step contained only disk-bearing objects (cf. Sect. 6.1), the remainder after Class I objects have been removed must be mainly Class II objects.

The resulting colour-colour diagram after contaminant removal is shown in Fig. 6.4. As before, Class I cYSOs are drawn in red, Class II cYSOs in green. The straight lines in the distribution of the plotted sources that catch the eye are due to the contaminant removal done in Sect. 6.3.1, which relies on straight cuts through the data. Thus, as sources are removed in large numbers along straight lines, the remainder of them will keep the straight cutoff lines.

Overall, the final WISE catalogue of cYSOs contains 7520 cYSOs. 2554 of these appear as Class I, 4966 as Class II.

## 6.4 Possible contaminants

As briefly discussed in the previous sections on cYSO selection, contamination is a major issue for any sample of stars taken from the CNC region and supposed to be part of the CNC. Because the view from the Sun towards the CNC is down the Carina-Sagittarius arm of our Galaxy, a very high number of stars, but also of other objects appearing as point-like sources, is seen in projection with the CNC. Only a few percent of all infrared sources seen in the *Spitzer* and HAWK-I images are actually young stellar objects related to the CNC, while the vast majority are background contaminants [see e. g. the discussion by Smith et al. 2010b, Povich et al. 2011a, Preibisch et al. 2011c]. All due care was taken to remove as many contaminants as possible from our sample. However, as discussed below, a fraction of ‘YSO impostors’ will certainly remain.

A wide variety of sources can exhibit infrared excess emission in the MIR: Variable stars, dusty AGB stars, AGN, unresolved planetary nebulae (PNe) and background galaxies [e. g. Harvey et al. 2007, Mentuch et al. 2009, Rebull et al. 2010, Povich et al. 2011a, Koenig et al. 2012]. AGB stars unfortunately exhibit very similar colours to YSOs and so do background star-forming galaxies. Koenig et al. [2012] estimate the remaining contamination by galaxies in the cYSO population selected with their criteria to be  $\sim 10 \text{ deg}^{-2}$ . Luminous AGB stars are a special problem, as they can be confused with MYSOs [Povich et al. 2011a]. However, AGB stars should not affect our analysis much, as they are few and uniformly distributed [Fang et al. 2012, Koenig et al. 2012]. Classical Be stars can also display weak IR excess, but, being of high masses, they are rare as well [Koenig et al. 2012].

Oliveira et al. [2009] in a spectroscopic survey of objects discovered by the *Spitzer* Legacy Programme “From Molecular Cores to Planet-Forming Disks” (c2d) in the Serpens molecular cloud find a contamination of 25% within their subsample of the brightest objects ( $F_{8.0 \mu\text{m}} > 3 \text{ mJy}$ ). They attribute this high proportion to the closeness of the Serpens cloud to the Galactic plane – something which is also true for the CNC. In their study of the Serpens molecular cloud with c2d data, Harvey et al. [2007] find that AGB stars and galaxies are generally faint at  $\gtrsim 13 \text{ mag}$  in the  $4.5 \mu\text{m}$  band. Since for the SYCC we removed all sources that were fainter than  $13.5 \text{ mag}$ , the vast majority of the interloping AGB stars and galaxies should have been removed by this precaution.

Apart from these rough numbers, I estimate a contamination individually for each analysed region by comparing the number density of point-like sources within it with the number density obtained from comparison regions as far as possible outside the known star-forming regions but with bordering the CN so that the general background (especially through a similar distance to the Galactic plane) is comparable. The results of this are presented with the further data analysis in Sect. 8.4.1 and Sect. 9.1.

Another caveat is that nebular emission in the CNC is strong and strongly variable [cf. also the study of Kobulnicky et al. 2013, who analyse the effect of background emission and source crowding on existing IRAC point-source catalogues]. This influences the sensitivities of especially the IRAC  $8.0 \mu\text{m}$  and MIPS  $24 \mu\text{m}$  bands [Povich et al. 2011a]. In dense cluster centres the IRAC images are also confusion-limited, e. g. in the Treasure Chest cluster [Povich et al. 2011a]. Bright stars, most notably  $\eta \text{ Car}$ , saturate the MIR instruments and thus cause incompleteness in any catalogue derived from them. This especially true for the MIPS  $24 \mu\text{m}$  observations, which are rendered almost unusable in the central CN.

## 6.5 Comparison with other IRAC cYSO catalogues

The SYCC can be compared to two recent other studies that also searched for IR excess sources from IRAC data in subsets of our study region. The studies by Smith et al. [2010b] and Povich et al. [2011a, see Sect. 3.5.3] searched for cYSOs in sub-regions of the SYCC, both using IRAC data.

### 6.5.1 Smith et al. [2010b]

Smith et al. [2010b] observed the South Pillars and a region slightly to the west of them with IRAC (see their Fig. 1). Within these areas (as covered by all four IRAC bands), they detected 48 642 sources. As demonstrated in Sect. 5.4.5, the Smith et al. [2010b] catalogue agrees well with the BSC in our test area of the west field, with  $\gtrsim 90\%$  of the sources in the Smith et al. [2010b] catalogue having a counterpart in the BSC. The restrictive criteria we then applied in assembling the more conservative SPSC reduced the number of remaining sources, so that  $\lesssim 85\%$  of sources have a counterpart in the SPSC. This means that the search for YSOs is carried out on catalogues of different sizes, but that source positions and fluxes between the samples agree well.

Smith et al. fitted the *Spitzer* measurements of their cYSOs, where possible complemented by 2MASS fluxes, with stellar photospheres using the Robitaille et al. [2007] fitting tool to a quality criterion of  $\frac{\chi^2}{\nu} \leq 2$  (where  $\nu$  is the number of data points; cf. our fit-quality criterion described in Sect. 7.4.1). This approach left 1406 objects which could not be fitted with a stellar photosphere. To select the cYSOs from this sample, the authors require

$$[3.6] - [4.5] > \delta ([3.6] - [4.5]) \quad \text{or} \quad |[4.5] - [5.8]| > \delta ([4.5] - [5.8]) \quad (6.16)$$

$$[5.8] - [8.0] > \delta ([5.8] - [8.0]), \quad (6.17)$$

where  $\delta$  denotes the uncertainty of the respective colour. The remaining sources are now fitted with YSO SEDs. Only if more than 67% of the models within a range of  $\chi^2/\nu - \chi_{\text{best}}^2/\nu \leq 2$  agree on an evolutionary stage (cf. Sect. 2.1.2), this is assigned to the source, resulting in 54% of the cYSOs remaining classified as ‘ambiguous’. Of the 1406 objects that cannot be explained by a pure stellar photosphere, this leaves 909 cYSOs, the majority of those (804) in the larger South Pillars field.

It is immediately apparent that this number is larger than that of cYSOs in the SYCC (759 cYSOs in the entire CNC survey region), although the area covered is so much smaller ( $\sim 15\%$  of our survey). This shows again that the selection criteria for the SYCC were chosen to be very restrictive, in all probability also excluding real YSOs, but also keeping contamination to a minimum.

Smith et al. [2010b] find that their cYSOs cluster in the central South Pillars, which is also apparent in the distribution within the SYCC (see Sect. 9.3). They conclude that this region, 17 pc in diameter and surrounded by PAH emission from pillars, is around 1 Ma old. Their evidence for this is that the majority of sources they observe there is of Stage II, with Stage 0/Stage I sources being in the minority. They also find a number of smaller cYSO overdensities, which is also in concordance with our findings from the SYCC (Sect. 9.3). I will discuss the clusters and overdensities in more detail in Sect. 9.5.2.

## 6 Identifying young stellar objects

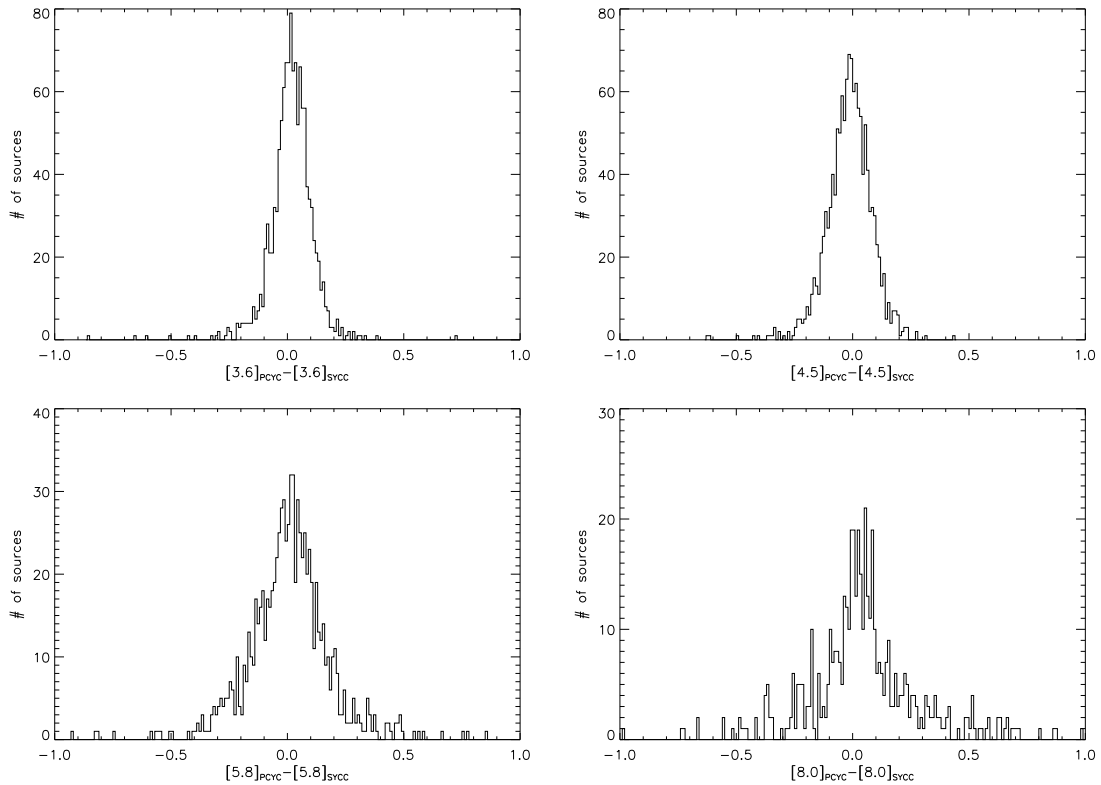


Figure 6.5: Magnitude differences between PCYC and SYCC.

### 6.5.2 Povich et al. [2011a]: The PCYC

Because the PCYC of Povich et al. [2011a, see Sect. 3.5.3] covers part of the region that is also sampled by the SYCC, those two catalogues can be directly compared. Since they rely on the same set of observations they can be expected to be similar, but as the data processing was performed quite differently, this provides a good consistency check for the SYCC.<sup>1</sup>

Figure 6.5 shows histograms of the magnitude differences between the two catalogues for sources detected in both.<sup>2</sup> The vast majority of sources have the same or nearly the same magnitude, with the wings of the distribution spreading out symmetrically to differences of  $\sim \pm 0.5$  mag. The standard deviations are 0.10 mag, 0.10 mag, 0.20 mag, and 0.28 mag for the 3.6  $\mu\text{m}$ , 4.5  $\mu\text{m}$ , 5.8  $\mu\text{m}$ , and 8.0  $\mu\text{m}$  bands. Thus, where we have counterparts in the two catalogues, the fluxes derived agree very well.

This agreement is reassuring, because though the underlying observations are the same, photometry in both cases was performed using completely different programs: the GLIMPSE point-source extractor based on DAOPHOT in the case of the PCYC (cf. Sect. 3.5.3) and MOPEX/APEX here (Chapter 5). It can, accordingly, be ruled out that the differences with respect to the number of cYSOs are due to strongly differing photometry.

<sup>1</sup>Povich et al. [2011a] also provide a small collection of cYSO clusters, extending that of Smith et al. [2010b, Sect. 6.5.1]. These clusters will be discussed in Sect. 9.5.3.

<sup>2</sup>Using the PCYC as reference, I searched a  $0.5''$  radius area around each source for the closest match in the SYCC and treated this as the same source.

## 6.5 Comparison with other IRAC *cYSO* catalogues

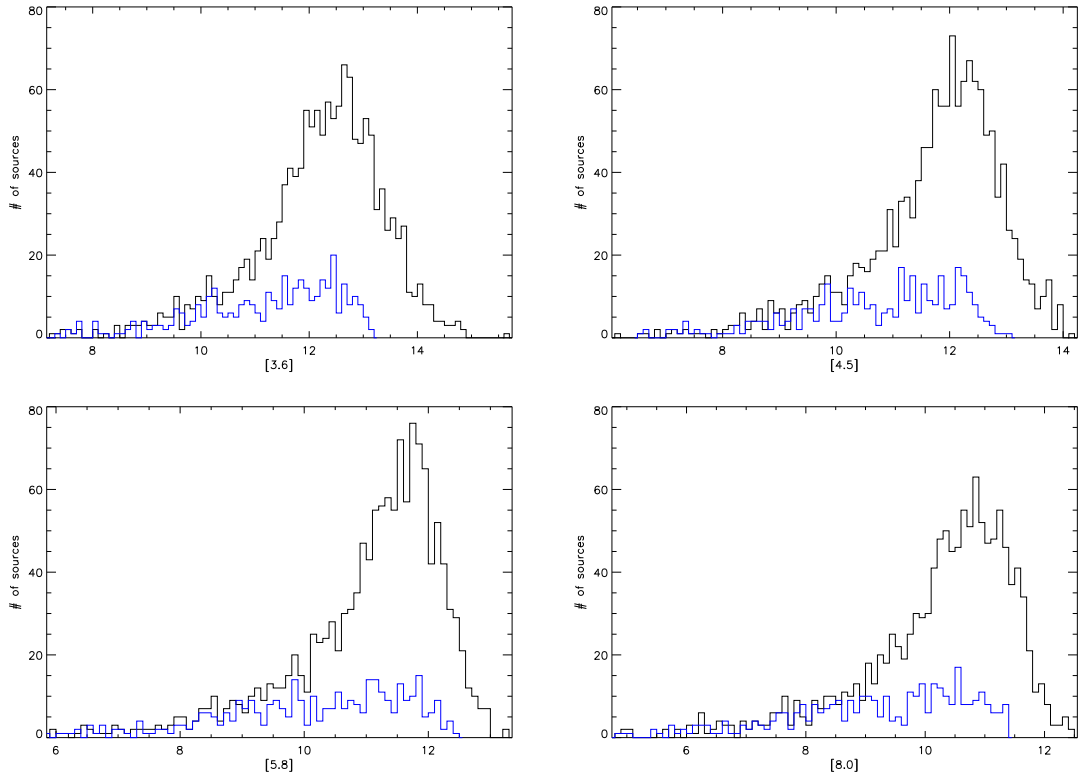


Figure 6.6: Comparing magnitude histograms for PCYC (black) and SYCC (blue).

In the area of the PCYC, the SYCC contains 357 *cYSOs*, the PCYC, however, has a much larger number of 1439 *cYSOs*. With the SYCC as reference, only 22% (78 *cYSOs*) are without a counterpart in the PCYC. The difference in numbers, however, means that 1160 of the 1439 *cYSOs* in the catalogue (81%) are without a counterpart in the SYCC. Thus, though the catalogues seem to agree very well in photometric results, their differing sizes are a reason to look further into their differences.

Plotting magnitude histograms for both PCYC and SYCC, one notices that the distributions are different (Fig. 6.6). The absolute numbers are of course different, but the PCYC also appears to be more sensitive and reach up to higher magnitudes (i. e. smaller fluxes) than the SYCC. As the SYCC was deliberately reduced to include only sources above a certain limit (Sect. 6.2.2), it appears sensible to apply the same magnitude cuts to the PCYC to be able to compare the spatial distributions better. This was done in the process illustrated by Figs. C.1a to C.1d in Appendix C. This reduces the number of *cYSOs* in the PCYC greatly to 1075.

In Fig. 6.8 the two colour-colour diagrams used to identify *YSOs* are shown with the SYCC in blue and the entirety of the PCYC in black.<sup>3</sup> It is apparent here that a large number of sources classified as *YSOs* in the PCYC would not be identified following our selection. To check how large the influence of this effect on the final catalogues is, exactly the same selection of *cYSOs* from colour-colour diagrams I used for constructing the SYCC

<sup>3</sup>Photometric values for the PCYC in VizieR are given in magnitudes and only to one decimal place, so that they appear to be aligned on a grid in the figures.

## 6 Identifying young stellar objects

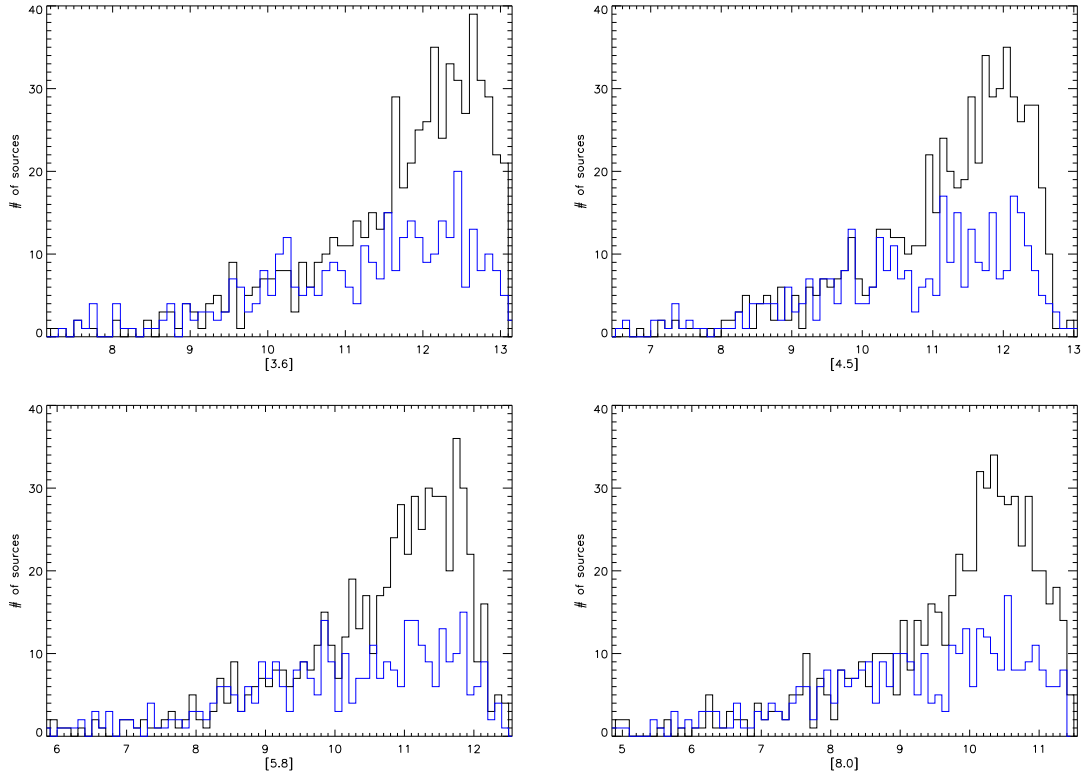
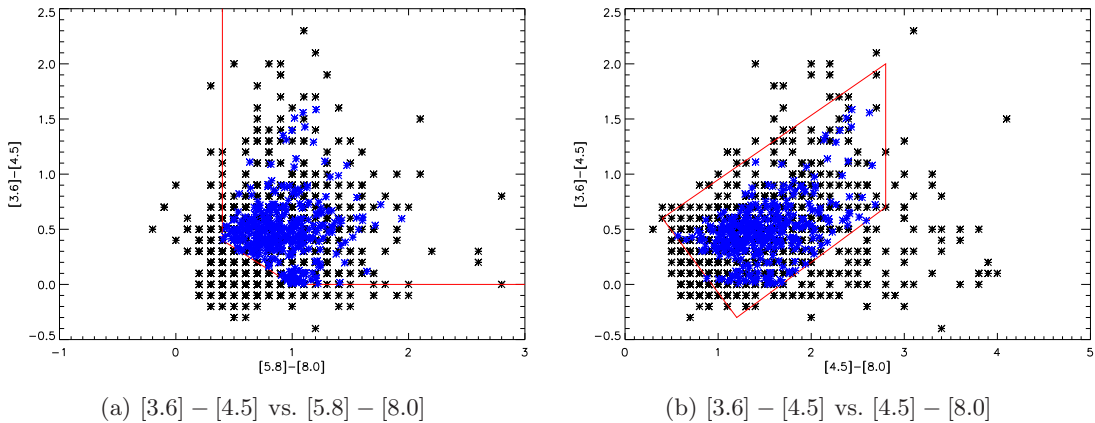


Figure 6.7: Comparing magnitude histograms for PCYC (black) and SYCC (blue) after the PCYC has been subjected to the same selection methods as the SYCC (as described in Appendix C).



(a)  $[3.6] - [4.5]$  vs.  $[5.8] - [8.0]$

(b)  $[3.6] - [4.5]$  vs.  $[4.5] - [8.0]$

Figure 6.8: Comparing colour-colour diagrams for the original PCYC (black) and the SYCC (blue). The red lines are the YSO selection criteria according to Eqs. (6.1) and (6.2) (Fig. 6.8a) and (6.3) to (6.6) (Fig. 6.8b).

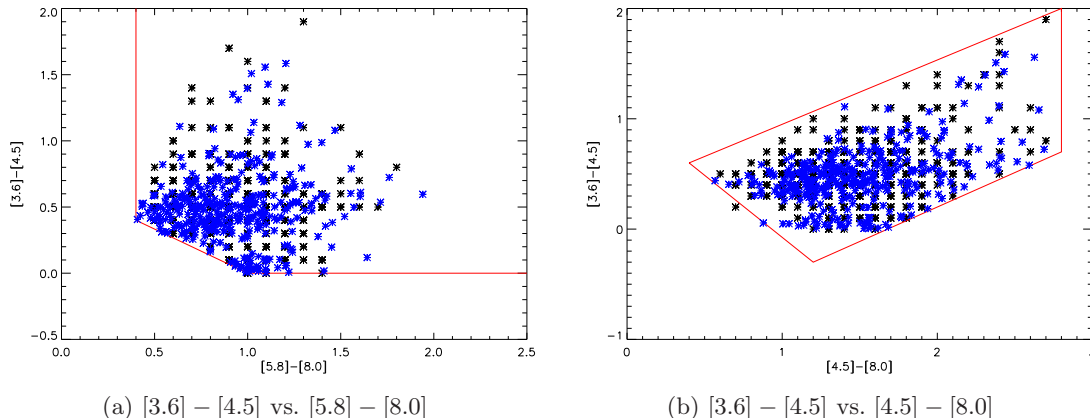


Figure 6.9: Comparing colour-colour diagrams for the reduced version of the PCYC (black) and the SYCC (blue).

was applied to the PCYC (Figs. C.1e to C.1k in Appendix C). The combined effect of the colour-colour diagrams leaves the PCYC with a total of 640 *c*YSOs. After this treatment, the magnitude histograms have changed as shown in Fig. 6.7—that is, they show a much greater similarity.

In Fig. 6.10, the *c*YSO positions within the PCYC before (yellow diamonds) and after reduction (green pluses) are compared to the SYCC (red crosses).<sup>4</sup> It is remarkable that though our stricter selection criteria and the magnitude cuts account for a major part of the *YSOs* that are found in the PCYC but not the SYCC, there are still about twice as many sources left in the PCYC after applying this selection than there are in the SYCC within the same area.

This is due to the different selection methods: The SED selection method used in obtaining the PCYC does not demand detection in all four bands, but due to the combination with 2MASS data, an SED could be assembled with fewer data points. On the contrary, for inclusion in the SYCC, detection in all four IRAC bands is absolutely necessary. Consequently, while nearly all PCYC sources are detected in the SPSC, our conservative *c*YSO selection strategy leaves us with a smaller basic sample. This direct comparison shows that in all probability this leads to false negatives. These sources are picked up in the PCYC. On the other hand, the PCYC due to its inverted selection method has an increased risk of false positives.

<sup>4</sup>Apart from the 78 known *c*YSOs from the SYCC that do not have a counterpart in the PCYC (solitary red crosses), there are a few (28) sources that are listed in the SYCC and the original PCYC, but not the reduced PCYC (yellow diamonds with red crosses). If it is true that the photometry is mainly identical (cf. Fig. 6.5) then this should not happen. However, individual checks on those sources (Appendix D) lead us to believe that these differing classifications are simply due to minor differences in photometry.

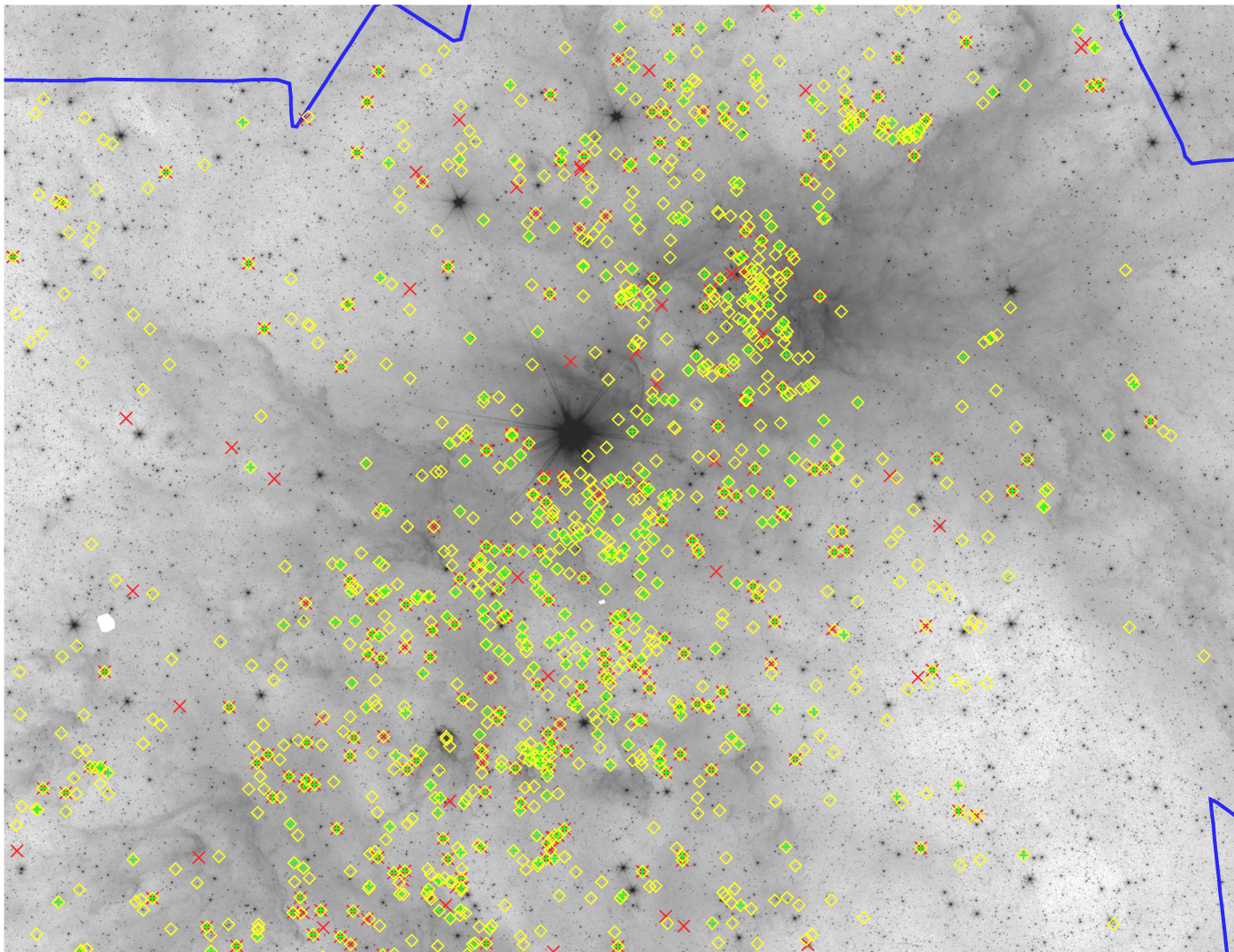


Figure 6.10: Comparing the SYCC and the PCYC. Yellow diamonds represent 1439 cYSO positions in the original PCYC, green pluses those 640 left in the PCYC after subjecting it to the treatment detailed in Appendix C, that is, removing faint sources and applying colour-colour diagram selection criteria. Red crosses mark the 357 cYSOs in the SYCC. The blue outline visible at the edges marks the CCCP field that forms the outline of the PCYC.

# 7 Jet-driving protostars in the Carina Nebula Complex<sup>1</sup>

In this and the following chapters the YSO population of the CNC now catalogued will be analysed and its properties discussed. The study of jets at the centre of this chapter will be extended in the following chapter. Here I concentrate fully on jet-emitting objects in the central CN; the  $\sim 1 \text{ deg}^2$  field of our study is shown in Fig. 7.1. In Chapter 8, where we will study different aspects of the young stellar population of the Gum 31 region outside the central parts of the CN, those HH jets from the study of Smith et al. [2010a] that are not covered here will be inspected for their emitting YSOs.

## 7.1 Motivation

Most stars in the Galaxy are born in massive star-forming regions. As described in Chapter 2, the high-mass stars profoundly influence their environments by their strong ionising radiation and powerful stellar winds that can disperse the natal molecular clouds. However, ionisation fronts and expanding wind-driven superbubbles can also compress surrounding clouds, thereby possibly triggering the formation of new generations of stars. Although this feedback is fundamental for understanding the star-formation processes, the details of the astrophysical processes at work here are still not understood well, mainly because regions with high levels of massive-star feedback are usually too far away for detailed studies.

The CNC, as described in Chapter 3, provides a unique target for studies of massive-star feedback. The feedback of the numerous massive stars has already largely dispersed the original molecular clouds in the central region. A few parsecs from the centre, however, large amounts of rather dense clouds are still present. Infrared images show how these clouds are currently being eroded and shaped by the radiation and winds from the massive stars, giving rise to numerous giant dust pillars, especially in the South Pillars region [Smith et al. 2010b], but also in the clouds northwest of  $\eta$  Car (see Chapter 3). Several very young stellar objects [e. g. Mottram et al. 2007] and a spectacular young embedded cluster [the Treasure Chest; see Smith et al. 2005] have been found in the molecular clouds, providing clear evidence that vigorous star formation activity is going on in these irradiated clouds.

It is thought that the formation of these objects was triggered by the advancing ionisation fronts that originate from the (several Myr old) high-mass stars in the CNC [Smith et al. 2010b, Povich et al. 2011b]. While this scenario appears very reasonable and is supported by recent numerical simulations of the evolution of irradiated clouds [e. g.

---

<sup>1</sup>This chapter is based on a paper published in *Astronomy & Astrophysics* [Ohlendorf et al. 2012] written in close cooperation with Thomas Preibisch, Benjamin Gaczkowski, Thorsten Ratzka, Rebekka Grellmann, and Anna Faye McLeod.

Gritschneider et al. 2010], the existing data cannot provide clear proof of the triggered-star-formation scenario (cf. Sect. 2.3). The alternative explanation that stars form spontaneously everywhere in the clouds (i. e. independent of external influences) and are only revealed by the advancing ionisation fronts (that simply remove the clouds surrounding the newly formed stars) cannot be ruled out. If it were possible to show that star formation is spatially restricted to the irradiated surfaces of the clouds (where the radiation pressure is highest), this would provide a very substantial argument in favour of the triggered star formation scenario.

However, the results so far do not allow drawing strong conclusions about the spatial distribution of the currently forming stars. While the infrared data are deep enough to detect the young stellar objects in the CNC easily, major problems arise from the very high level of field-star contamination that is a consequence of the CNC's location almost exactly on the Galactic plane. Only a few percent of all IR sources seen in the *Spitzer* and HAWK-I images are actually young stellar objects related to the CNC, while the vast majority are background and foreground contaminants. These contamination issues are discussed in Sect. 6.4.

The main challenge in any study of the star-formation process in the CNC thus is not to detect the YSOs, but to discern YSOs in the CNC from background sources. In this context, protostellar jets provide a very good signpost for YSOs, as they point towards objects in the latest generation of the currently forming stars [Bally et al. 2007]. The spatial distribution of jet-driving protostars can thus provide very important information about the regions where star formation presently occurs. These protostars are so young that they are still located very close to their birth site, which means that the jet-driving YSOs trace the spatial location of the currently forming YSO population. For a more detailed description of jet phenomena, see Sect. 2.2.

As described in Sect. 3.5, HST searches of the CNC for jets have been carried out by e. g. Smith et al. [2004, 2010a]. In H $\alpha$  images as obtained with the HST, the jets themselves are clearly visible. It is however impossible to look deeper into the clouds and see the sources of jet emission. With IR images this is possible and *Spitzer* data reveal what is impenetrable to the HST: The nascent stars within the cloud that emit those jets. In Fig. 7.2 this is demonstrated by placing side by side the HST H $\alpha$  and the *Spitzer* image, the probable source of jet emission marked by a red circle in both. It is plain to see that while the H $\alpha$  emission traces the jet, only in the IR image the stars that cause it appear.

In this chapter, the search for jets and their driving protostars will be extended to cover an area  $\sim 1 \text{ deg}^2$  around  $\eta$  Car as shown in Fig. 7.1. This covers the area used in the study of Smith et al. [2010a], with the exception of the Gum 31 region, which will be discussed in more detail in Chapter 8. One EGO slightly north of this area is included in the study.

In the first step, we use the large *Spitzer* IRAC mosaics created from available archive data (cf. Sect. 5.2), which provide a spatially complete coverage of the entire extent of the CNC, to search for more objects with  $4.5 \mu\text{m}$  excess emission, beyond the EGOS (Sect. 2.2.2) already detected by Smith et al. [2010b]. In the second step, we identify the driving sources of the newly detected jets and the known HH jets [from Smith et al. 2010a] and molecular hydrogen emission-line objects (MHOS) [from Preibisch et al. 2011c] in the *Spitzer* images (Sect. 7.3).

Using the tools developed by Robitaille et al. [2006, 2007], we fit the SEDs of the jet sources by combining *Spitzer* photometry with FIR fluxes derived from *Herschel* mapping

and our LABOCA sub-mm study of the CNC. Through this radiative-transfer modelling of the SEDs we derive estimates of the stellar and circumstellar parameters of the jet sources. We investigate the spatial distribution of the jet-driving protostars (Sect. 7.4) to infer information about the star-formation mechanisms currently at work in the CN.

## 7.2 Observational data

We used the following infrared data sets firstly to search for jet sources and secondly to construct their SEDs through radiative transfer modelling as described in Sect. 7.4.1.

### 7.2.1 Spitzer images and photometry

The analysis as described in this chapter is based on the *Spitzer* IRAC images and photometry that were described in detail in Sect. 4.1.1 and Chapter 5. Because at the time this analysis was done and first published the final SPSC had not yet been created, the work in this chapter is based on the Bandmerge *Spitzer* catalogue. The difference between the two catalogues and the incentive for improving over the BSC by constructing the SPSC are explained in Sect. 5.4.

However, we carefully checked photometry for each source and where one source on the sky clearly had been mistakenly split into two separate sources in different bands in the BSC, we put them together by hand for the analysis. This was the first incentive to create a new catalogue to eliminate these misidentifications.

### 7.2.2 Herschel far-infrared fluxes

For further characterisation of the jet sources, we included fluxes extracted from the data of our recent *Herschel* far-infrared survey of the CNC as described in Sect. 4.2.

*Herschel* fluxes were only extracted for cases where a compact, point-like *Herschel* object could be found at the position of the *Spitzer* source. No photometry was performed in cases where strong extended emission shows up in the *Herschel* maps.

Since the angular resolution of *Herschel* with a PSF between  $5''$  and  $36''$ , depending on band, is considerably lower than that of *Spitzer* at a FWHM of the PSF between  $1.5''$  and  $2''$  [Fazio et al. 2004], source detection with *Herschel* is more difficult than it is in *Spitzer* images. In many cases a single point-like source is, however, identified as a counterpart. The remaining cases fall into two different categories: (i) those where the local emission is predominantly uniform, and no compact *Herschel* counterpart to the *Spitzer* point-like source can be detected, and (ii) those for which a counterpart is identified that is a more or less pronounced luminosity increase within a larger structure. Overall, 19 of the 37 *Spitzer*-identified jet sources (51%) do not have a compact *Herschel* counterpart.

### 7.2.3 LABOCA sub-mm fluxes

We complemented the *Herschel* photometry with  $870\ \mu\text{m}$  fluxes extracted from our LABOCA map of the CNC [Preibisch et al. 2011d, cf. Sect. 4.7] whenever a compact source was seen at the location of the *Spitzer*-identified jet sources in the LABOCA map. The source fluxes were extracted from  $\approx 25''$  diameter apertures centred on each object.

### 7.2.4 HAWK-I and 2MASS

We also inspected the 2MASS images and our very deep HAWK-I near-infrared images [Preibisch et al. 2011c, cf. Sect. 4.5] and searched for NIR counterparts of the *Spitzer*-identified jet sources. When an NIR source could be clearly identified with the *Spitzer* source, we used the  $J$ -,  $H$ -, and  $K_s$  band fluxes as given in our HAWK-I photometry catalogue [Preibisch et al. 2011c] or (for sources outside the area of the HAWK-I survey) the 2MASS Point-Source Catalog. The typical completeness limits of the HAWK-I image are  $\sim 21$  mag ( $J$ ),  $\sim 20$  mag ( $H$ ), and  $\sim 19$  mag ( $K_s$ ) [Preibisch et al. 2011a].

## 7.3 Revealing jet sources in the Carina Nebula

Since HH jets and MHOS were detected in other wavelengths, while EGOs and CGOs were identified in the *Spitzer* images themselves, slightly different strategies were employed in searching for infrared sources.

As an example of a case where a *Spitzer* infrared source can be identified while no source can be discerned in the optical HST image, we show HH 903 in Fig. 7.2. Overview figures of optical, NIR, *Spitzer*, and *Herschel* images can be seen in Fig. 7.3 (HH jets), Fig. 7.4 (MHOS), Fig. 7.5 (EGOs), and Fig. 7.7 (CGOs).

A list of all jet objects considered here was compiled in Table 7.1. For all objects studied, it indicates in which wavelength bands they could be detected.

### 7.3.1 The search for sources of the Herbig-Haro jets

The mosaic images created from *Spitzer* data as described in Sect. 5.2 then searched by eye for probable sources of the 20 HH jets and 15 HH jet candidates within our field as identified from HST H $\alpha$  images by Smith et al. [2010a]. For 22 HH jets and HH jet candidates of these 35 objects in our sample, we were able to identify a *Spitzer* point-like source that constitutes a probable jet source, lying on the jet axis or its projection. Eight of them could also be identified with a point-like *Herschel* source. (Two jets were identified with the same source; see Sect. 7.3.1.) In one case, that of HH 900, a *Herschel* source is seen but is probably not associated with a protostar, but rather with the surrounding globule. The remaining twelve jets have neither *Spitzer* nor *Herschel* sources that correspond with them. Some outstanding cases are described below.

#### HH 666

The jet HH 666 emanates from out of a pillarhead and has already been the subject of a detailed analysis in the infrared by Smith et al. [2004]. Prominent in this pillarhead is a very bright *Spitzer* source, which due to its location we identified as the source of the jet. It is also associated with a clear point-like *Herschel* source. For the SED fit we added the optical and NIR fluxes as published by Smith et al. [2004] to our *Spitzer* and *Herschel* fluxes.

#### HH 1004 and HH 1005

Both the jets assigned as HH 1004 and HH 1005 by Smith et al. [2010a] are located towards the tip of the same pillar. Two of the several sources located within this pillar seem to

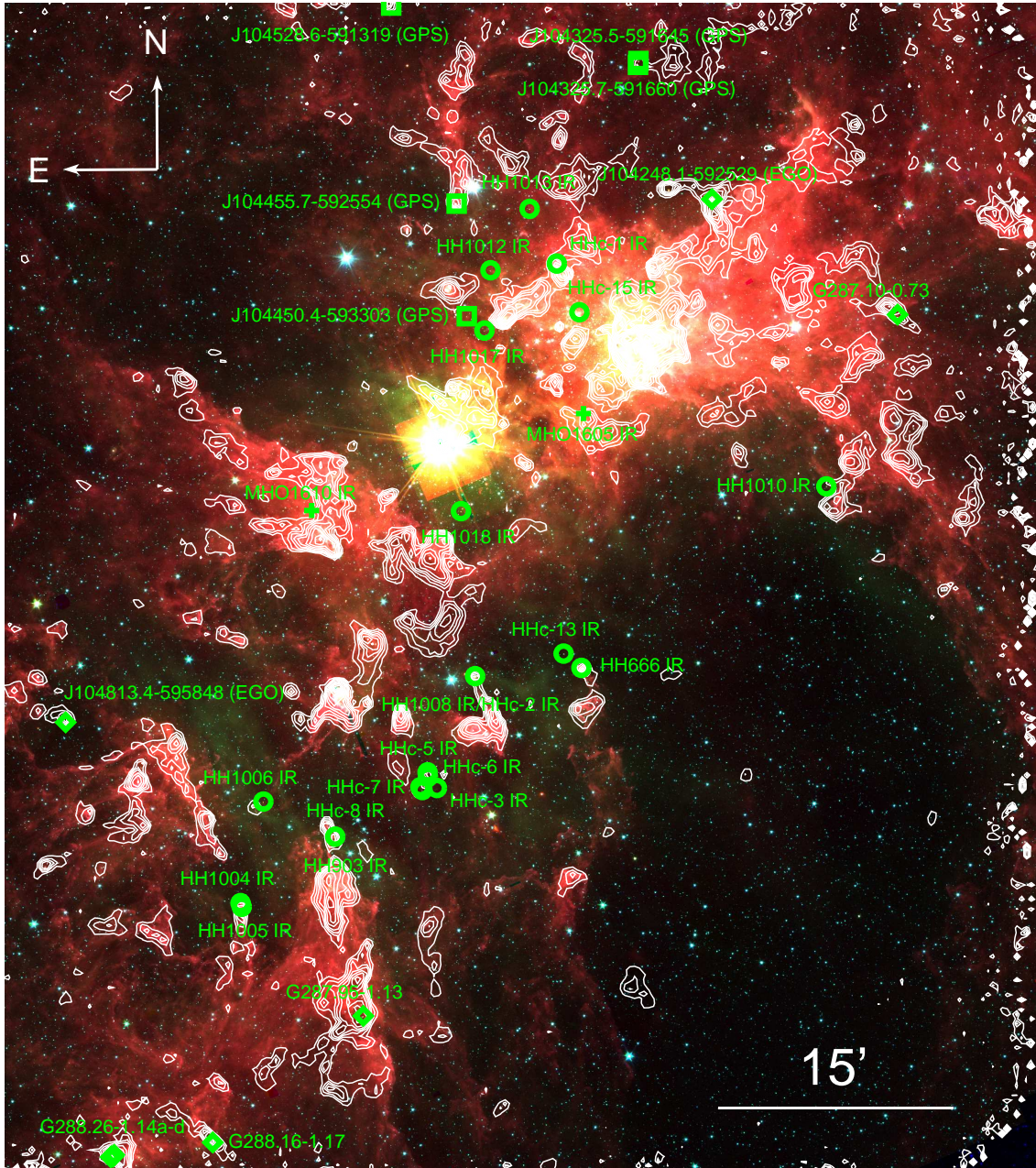


Figure 7.1: *Spitzer* RGB image with overlaid LABOCA 870  $\mu\text{m}$  contours, shown for the same field as in Smith et al. [2010a] for identifying HH jets. The first three contour levels are 0.06, 0.12, and 0.18 Jy/beam, while the further levels increase by a factor of the square root of two. The jet sources in the region are marked in green. Circles indicate sources of HH jets and HH jet candidates, diamonds those of EGOS, and squares CGOS. The sources of MHOs are marked by crosses. [Image first published: Ohlendorf et al. 2012]

7 Jet-driving protostars in the Carina Nebula Complex

Table 7.1: Infrared detections for sources of jet objects within the Carina nebula.

Jet Object	Jet Source	<i>Spitzer</i>	<i>Herschel</i>	2MASS	HAWK-I
HH 666	J104351.5–595521	yes	yes	yes <sup>a</sup>	– <sup>a</sup>
HH 900		no	yes	no	no
HH 901		no	no	no	yes
HH 902		yes	no	no	no
HH 903	J104556.4–600608	yes	yes	no	no
HH 1004	J104644.8–601021	yes	yes	no	no
HH 1005	J104644.2–601035	yes	yes	no	–
HH 1006	J104632.9–600354	yes	no	no	no
HH 1007		no	no	no	–
HH 1008	J104445.4–595555	yes	yes	yes	yes
HH 1009		no	no	no	no
HH 1010	J104148.7–594338	yes	yes	no	–
HH 1011		no	no	no	no
HH 1012	J104438.7–593008	yes	no	no	no
HH 1013	J104419.2–592612	yes	no	no	no
HH 1014	J104545.9–594106	yes	no	no	no
HH 1015		no	no	yes	–
HH 1016		no	no	no	no
HH 1017	J104441.5–593357	yes	no	no	no
HH 1018	J104452.9–594526	yes	no	no	no
HHc 1	J104405.4–592941	yes	no	no	no
HHc 2	J104445.4–595555	yes	yes	yes	yes
HHc 3	J104504.6–600303	yes	no	no	no
HHc 4		no	no	no	no
HHc 5	J104509.4–600203	yes	yes	no	yes
HHc 6	J104509.2–600220	yes	no	no	no
HHc 7	J104513.0–600259	yes	no	no	no
HHc 8	J104512.0–600310	yes	no	no	no
HHc 9		no	no	no	no
HHc 10		no	no	no	no
HHc 11		no	no	no	no
HHc 12		no	no	no	no
HHc 13	J104400.6–595427	yes	no	no	–
HHc 14		no	no	no	no
HHc 15	J104353.9–593245	yes	no	no	no

**Notes.** The HH jets and HH jet candidates are as detected by Smith et al. [2010a], MHOs as identified by Preibisch et al. [2011c], the EGOs bearing a number beginning with *G* as detected by Smith et al. [2010b]. Images of them can be found in the respective source publications. The remaining four EGOs and the CGOs were detected from our *Spitzer* data. For HAWK-I, where neither *yes* nor *no* are indicated the source is located outside the surveyed field.

<sup>(a)</sup> The SOFI *JHK<sub>s</sub>* photometry for HH 666 IR was taken from Smith et al. [2004].

### 7.3 Revealing jet sources in the Carina Nebula

Table 7.1: Continued.

Jet Object	Jet Source	<i>Spitzer</i>	<i>Herschel</i>	2MASS	HAWK-I
EGO	J104040.5–585319	yes	yes	no	–
EGO	J104248.1–592529	yes	yes	yes	–
EGO	J104813.4–595848	yes	yes	no	no
G287.10–0.73	J104114.3–593239	yes	yes	no	–
G287.95–1.13	J104542.0–601732	yes	yes	no	–
G288.15–1.17	J104700.6–602535	no	no	no	–
G288.26–1.14a	J104750.3–602618	yes	yes	no	–
G288.26–1.14b	J104752.1–602627	yes	no	no	–
G288.26–1.14c	J104750.9–602625	yes	no	no	–
G288.26–1.14d	J104751.7–602624	yes	no	no	–
CGO	J104325.5–591645	yes	yes	no	–
CGO	J104325.7–591660	yes	yes	no	–
CGO	J104450.4–593303	yes	no	no	no
CGO	J104455.7–592554	yes	yes	no	no
CGO	J104528.6–591319	yes	yes	yes	–
MHO 1605	J104351.5–593911	yes	no	no	yes
MHO 1606		no	no	no	no
MHO 1607		no	no	no	no
MHO 1608		no	no	no	no
MHO 1609		no	no	no	no
MHO 1610		yes	yes	no	no

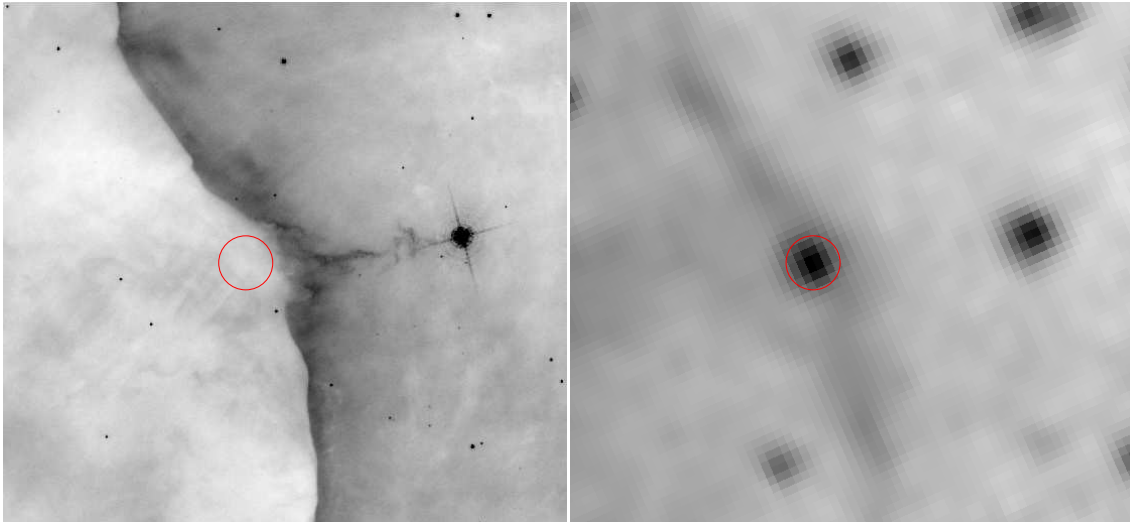


Figure 7.2: HH 903 is clearly visible in the HST H $\alpha$  image (left), but no source for the jet is visible. In the *Spitzer* 4.5  $\mu\text{m}$  image (right), a point-like source (red circle) is revealed that is very likely the source of jet emission. The circle marking the source has a radius of 2". [Image first published: Ohlendorf et al. 2012]

be likely sources for them. The lower part of the clearly two-part structure that is HH 1004 is in line with a faint *Spitzer* point-like source that is associated with a distinct compact *Herschel* source and a HAWK-I point-like source. A second *Herschel* source towards the north of it is coincident with a brighter *Spitzer* source and might be a likely source for the jet HH 1005.

### HH 1008 and HHc 2

HHc 2 is placed right at the top of a thin, elongated pillar, with a very bright *Spitzer* source and a distinct *Herschel* counterpart located inside the pillar head, coincident with a 2MASS point-like source.<sup>2</sup> HH 1008 is bow-shaped and placed to the south-east of the same pillar head. It is probable that it was caused by the same bright source, since it is well aligned with it, and there is no other candidate source in the vicinity.

### HHc 10

HHc 10 is a bow-like structure and, like HH 1008, might have been caused by a source in the nearby head of the pillar close to which it is located. Within this pillarhead, however, there are three distinct *Spitzer* sources while no definite *Herschel* detection can be made. Thus, it remains unclear which, if any, of the *Spitzer* objects might be the source of the HH jet candidate.

### 7.3.2 The search for sources of the molecular hydrogen emission-line objects

A very similar process was applied to the MHOs detected by Preibisch et al. [2011c, see Sect. 3.5] which were searched by eye for probable *Spitzer* point-like sources. Four of the six MHOs are located in regions that are comparatively free of *Spitzer*-detected point-like sources and show no *Spitzer* counterparts themselves. Two of them, MHO 1605 and MHO 1610, however, show a counterpart within the source catalogue. These are the two objects from the sample of six that are located towards the edge of a pillar or globule, both close to or within known clusters (Tr 14 and Tr 16). MHO 1610 also has a *Herschel* counterpart, so its SED could be modelled.

The HAWK-I data cover only a subfield of the one surveyed in this work, so there might be other H<sub>2</sub> sources that could not be detected. For the region surveyed with HAWK-I, where all peculiar features in H<sub>2</sub> emission were described in the study by Preibisch et al. [2011c], no further coincidental detections can be reported.

### 7.3.3 The search for extended green objects and compact green objects

Successively, in the IRAC images we also visually searched for sources with excessive 4.5  $\mu\text{m}$ -band emission, either extended (EGOs) or point-like (CGOs). The RGB images (3.6  $\mu\text{m}$  in blue, 4.5  $\mu\text{m}$  in green and 8.0  $\mu\text{m}$  in red) were scaled freely to obtain the best possible visibility of unusually green objects. However, De Buizer and Vacca [2010] make the valid point that to be able to identify EGOs, the 4.5  $\mu\text{m}$  band usually needs to be scaled up unproportionally high with regard to the red and blue bands. Thus, the weaker emission

---

<sup>2</sup>Smith et al. [2010a] in their Table 3 give coordinates for HHc 2 that are placed within NGC 3324 and identical with those of the jet HHc 2 (3324) (cf. Sect. 8.6) and thus are clearly erroneous. However, from their Fig. 10 we were able to identify the jet marked therein unambiguously.

on the flanks of a relatively extended, bright source might appear to be green only because the scaling was chosen in this way. This is a caveat to be kept in mind when dealing with EGOs surrounding regular point-like sources. Since our EGOs are all well away from bright point-like sources, it is still possible excessively high scaling of the  $4.5\ \mu\text{m}$  band caused them to appear, but care was taken to make sure they were real phenomena.

Care was also taken to check whether especially CGOs were not simply imaging faults and green excess was not caused by faulty pixels in the other bands. It can, however, not be excluded that a minority of the peculiarly CGOs are seen for those reasons and are not real objects. They were selected by visually scanning the processed *Spitzer* images for sources that appeared to the eye to have an excess in the  $4.5\ \mu\text{m}$  (green) band compared to their immediate surroundings. Overall, we found three EGOs and five CGOs within the studied area (Fig. 7.5).

All three new EGOs can clearly be identified with a compact *Herschel* counterpart. Though by nature they are extended in the  $4.5\ \mu\text{m}$  band, for all three of them we can identify a probable *Spitzer* source for which photometry could be obtained. One of them, J104248.1–592529, is also coincident with a 2MASS source, which allowed for photometry in another three bands.

In addition to the three newly discovered objects we included in our study the four EGOs within the CNC identified by Smith et al. [2010b]. They were subjected to the same analysis as the objects identified through the processes described above. The object described by Smith et al. as G288.26–1.14 appears to be a multiple object. It was therefore split into four objects marked *a* to *d* for the analysis. Smith et al. [2010b] note the multiplicity and point out that some of the green objects in this cluster might not be true EGOs; they should thus be treated with caution. Especially as the IRAC RGB images show a greenish hue between clouds comparatively often, it is advisable to be very careful before assigning green objects as astrophysical phenomena. Only for the object designated G288.26–1.14a a compact *Herschel* source is seen, for the other three components no *Herschel* fluxes could be derived.

Likewise, G288.15–1.17 is a composite object. In the *Spitzer* image, it can be recognised as consisting of at least three separate sources (cf. Fig. 7.5), which is also true for the 2MASS image. Thus, though we could identify *Spitzer* sources and also a corresponding compact *Herschel* object, we did not use the photometry for SED fitting, since it would be highly likely to be comprised of different sources. For the other two objects we were each able to identify a compact *Herschel* counterpart.

It is the very nature of compact green objects to be identified with a single *Spitzer* source. Four of them also show a compact *Herschel* counterpart. One, J104450.4–593303, is within a region of diffuse *Herschel* emission, but this is not point-like and could thus not be employed for photometry. For J104528.6–591319, a 2MASS source could be identified and photometry employed for the fitting process.

## 7.4 Characteristics of jet sources

### 7.4.1 Radiative transfer modelling of the SEDs

From the collected data at *Spitzer* and *Herschel* wavelengths, we consecutively constructed SEDs, complemented by the LABOCA, HAWK-I, and 2MASS fluxes, as far as photometry was

available for the respective sources. For SED-fitting we used the online tool of Robitaille et al. [2007]. This tool compares the input observational data with 200 000 SED models for YSOs that were precomputed using a 2D radiative transfer code by Whitney et al. [2003]. These models have a wide parameter space for the properties of the central object and its environment. The important parameters for our study are stellar mass, disk mass, envelope mass, and total luminosity. Because our data sample the peak of the protostar’s SED, they give a good constraint on its total luminosity. Gaczkowski et al. [2013] discuss the relationship between SEDs and stellar parameters for the CNC sample in more detail.

*Herschel*, *Spitzer*, and LABOCA fluxes as listed in Table 7.2, complemented by HAWK-I and 2MASS fluxes where available, were used for the compilation of the SEDs. No fits were performed for sources with only *Spitzer* fluxes or fewer than four data points overall because no reasonable constraints to the model could be obtained in these cases. For the fits, the distance to all objects was assumed to be 2.3 kpc (cf. Chapter 3), and the interstellar extinction range was restricted to  $A_V = 0 \dots 40$  mag. We assumed an uncertainty of 20% for all fluxes. In addition to the best-fit model, we show the range of possible parameters that can be derived from models within the range of  $\chi^2/\nu - \chi_{\text{best}}^2/\nu < 2$  (with  $\nu$  representing the number of data points). These models are shown as grey lines in the plots in Fig. 7.8. The resulting model parameters are listed in Table 7.3. It gives the best-fit value together with the range constrained by the above  $\chi^2$  criterion. The resulting SEDs are shown in Fig. 7.8.

The results of SED fits can be highly ambiguous. Many of the stellar and circumstellar parameters are often poorly constrained because the models show a high degree of degeneracy [e.g. Men’shchikov and Henning 1997]. We therefore restrict our analysis to a few selected parameters that can be determined relatively well from these fits. These are the total luminosity, the stellar mass, and the mass of the circumstellar disk and envelope.

Notably, all the sources in our sample are well modelled by models possessing a circumstellar disk. The masses of the jet-emitting protostars are within a range of  $1 - 10 M_{\odot}$ . Thus, they all are of low masses, with luminosities of the best-fit models varying between 40 and  $1600 L_{\odot}$ . Most of the luminosities are in the lower range below a few hundred  $L_{\odot}$ , with three notable exceptions that exhibit luminosities of more than  $700 L_{\odot}$ .

The source parameters stellar mass and disk mass broken down by type are shown in Fig. 7.6. Sources of CGOs seem to be lower-mass (best-fit values  $\sim 1 - 5 M_{\odot}$ ) than those of EGOs (best-fit values  $\sim 5 - 8 M_{\odot}$ ), while those objects emitting HH jets are of varying masses (best-fit values  $\sim 2 - 7 M_{\odot}$ ). Envelope masses of EGO sources are noticeably higher than most of those for other jet objects. All best-fit envelope masses for EGO sources are at least  $350 M_{\odot}$ , while many of those for the other objects (6 out of 11, 55%) are far below  $100 M_{\odot}$ . However, five of those also range far above that value. There is no distinct pattern recognisable for the disk masses, if any, that HH jet sources have slightly higher disk masses than those of the other jet objects. Still, the smallness of the sample means that these observations of course only have limited statistical value. For MHOs especially, we only have a single specimen so that no qualitative statements are possible.

Table 7.2: Source fluxes as obtained in the *Spitzer* and *Herschel* bands, complemented with photometry from LABOCA and as obtained with HAWK-I or from the 2MASS point-source catalogue.

Part one. IRAC 3.6  $\mu\text{m}$ , 4.5  $\mu\text{m}$ , 5.8  $\mu\text{m}$ , and 8.0  $\mu\text{m}$ .

#	Jet Source		3.6 $\mu\text{m}$ [mJy]	4.5 $\mu\text{m}$ [mJy]	5.8 $\mu\text{m}$ [mJy]	8.0 $\mu\text{m}$ [mJy]
(1)	HH 666 IR	J104351.5–595521	137	238	338	405
(2)	HH 902 IR	J104401.8–593030	–	4.17	29.6	70.0
(3)	HH 903 IR	J104556.4–600608	2.68	6.24	35.4	115
(4)	HH 1004 IR	J104644.8–601021	4.75	6.58	15.2	–
(5)	HH 1005 IR	J104644.2–601035	–	2.50	–	–
(6)	HH 1006 IR	J104632.9–600354	2.57	3.06	10.6	23.1
(7)	HH 1008/HHc 2 IR	J104445.4–595555	44.8	117	326	461
(8)	HH 1010 IR	J104148.7–594338	2.11	3.96	10.8	–
(9)	HH 1012 IR	J104438.7–593008	5.29	5.27	5.92	–
(10)	HH 1013 IR	J104419.2–592612	8.46	11.7	16.7	25.1
(11)	HH 1017 IR	J104441.5–593357	4.98	5.12	–	–
(12)	HH 1018 IR	J104452.9–594526	4.54	5.39	–	10.5
(13)	HHc 1 IR	J104405.4–592941	6.00	–	–	–
(14)	HHc 3 IR	J104504.6–600303	0.611	0.712	2.34	5.02
(15)	HHc 5 IR	J104509.4–600203	20.0	21.1	27.9	41.2
(16)	HHc 6 IR	J104509.2–600220	–	1.29	–	–
(17)	HHc 7 IR	J104513.0–600259	2.25	2.00	–	–
(18)	HHc 8 IR	J104512.0–600310	5.48	8.33	13.2	16.0
(19)	HHc 13 IR	J104400.6–595427	13.2	12.5	13.8	17.1
(20)	HHc 15 IR	J104353.9–593245	274	285	283	239
(21)	EGO	J104040.5–585319	–	13.4	16.3	12.6
(22)	EGO	J104248.1–592529	265	318	440	–
(23)	EGO	J104813.4–595848	5.34	9.52	15.2	14.6
(24)	G287.10–0.73	J104114.3–593239	0.645	1.42	–	–
(25)	G287.95–1.13	J104542.0–601732	–	5.80	–	–
(26)	G288.26–1.14a	J104750.3–602618	2.83	6.70	–	–
(27)	G288.26–1.14b	J104752.1–602627	4.02	14.5	28.8	31.3
(28)	G288.26–1.14c	J104750.9–602625	1.13	1.93	–	–
(29)	G288.26–1.14d	J104751.7–602624	2.25	–	–	–
(30)	CGO	J104325.5–591645	8.99	20.8	44.5	63.0
(31)	CGO	J104325.7–591660	1.60	3.26	6.69	8.22
(32)	CGO	J104450.4–593303	3.18	21.3	9.17	12.0
(33)	CGO	J104455.7–592554	10.6	15.4	–	39.6
(34)	CGO	J104528.6–591319	37.1	52.7	–	–
(35)	MHO 1605 IR	J104351.5–593911	1.27	1.79	8.19	17.9
(36)	MHO 1610 IR	J104608.3–594525	–	1.26	–	–

7 Jet-driving protostars in the Carina Nebula Complex

Table 7.2: Part two. PACS 70  $\mu\text{m}$ , 160  $\mu\text{m}$  and 250  $\mu\text{m}$ , SPIRE 350  $\mu\text{m}$  and 500  $\mu\text{m}$ , LABOCA 870  $\mu\text{m}$ , 2MASS or HAWK-I  $JHK_s$

#	70 $\mu\text{m}$ [Jy]	160 $\mu\text{m}$ [Jy]	250 $\mu\text{m}$ [Jy]	350 $\mu\text{m}$ [Jy]	500 $\mu\text{m}$ [Jy]	870 $\mu\text{m}$ [Jy]	$J$ [mJy]	$H$ [mJy]	$K_s$ [mJy]
(1)	64.6	70.5	43.9	25.6	11.4	–	0.33 <sup>a</sup>	1.9 <sup>a</sup>	12 <sup>a</sup>
(2)	–	–	–	–	–	–	–	–	–
(3)	19.1	55.7	37.9	16.7	8.07	2.03	–	–	–
(4)	10.6	23.9	–	–	–	–	0.0540	0.206	0.624
(5)	14.8	44.4	55.0	26.6	12.0	1.89	–	–	–
(6)	–	–	–	–	–	–	–	–	–
(7)	103	120	59.9	23.2	9.32	1.90	4.71	10.8	22.8
(8)	5.67	12.5	–	–	–	–	–	–	–
(9)	–	–	–	–	–	–	–	–	–
(10)	–	–	–	–	–	–	–	–	–
(11)	–	–	–	–	–	–	–	–	–
(12)	–	–	–	–	–	–	–	–	–
(13)	–	–	–	–	–	–	–	–	–
(14)	–	–	–	–	–	–	–	–	–
(15)	8.12	18.1	–	–	–	–	1.02	3.17	6.52
(16)	–	–	–	–	–	–	–	–	–
(17)	–	–	–	–	–	–	–	–	–
(18)	–	–	–	–	–	–	–	–	–
(19)	–	–	–	–	–	–	–	–	–
(20)	–	–	–	–	–	–	–	–	–
(21)	53.2	79.4	52.7	26.8	12.7	–	–	–	–
(22)	57.3	85.9	65.4	39.4	21.8	5.73	14.0	–	58.1
(23)	33.4	49.8	36.2	19.6	10.5	2.09	–	–	–
(24)	7.36	31.0	32.2	28.3	–	–	–	–	–
(25)	18.4	38.2	51.0	23.8	–	–	–	–	–
(26)	20.0	65.0	–	–	–	–	–	–	–
(27)	–	–	–	–	–	–	–	–	–
(28)	–	–	–	–	–	–	–	–	–
(29)	–	–	–	–	–	–	–	–	–
(30)	1.95	6.93	–	–	–	–	–	–	–
(31)	–	–	10.5	7.10	4.78	–	–	–	–
(32)	–	–	–	–	–	–	–	–	–
(33)	32.7	57.4	48.8	–	–	3.11	0.821	1.64	2.75
(34)	9.96	24.1	17.2	9.46	–	0.923	5.63	14.6	26.1
(35)	–	–	–	–	–	–	–	–	–
(36)	8.68	13.6	10.3	4.80	–	–	–	–	–

**Notes.** The first column indicates the type of the associated jet object: EGO for extended green objects, CGO for compact green objects. The EGOS from Smith et al. [2010b] bear the identifiers given there. For sources of HH jets and HH jet candidates the identifier of the corresponding jet object following Smith et al. [2010a] is given, for the MHOs their catalogue number as assigned by Preibisch et al. [2011c]. For all sources their coordinates are given in the second column.

<sup>(a)</sup> For HH 666 IR we adopted the  $JHK_s$  fluxes measured by Smith et al. [2004] with SOFI.

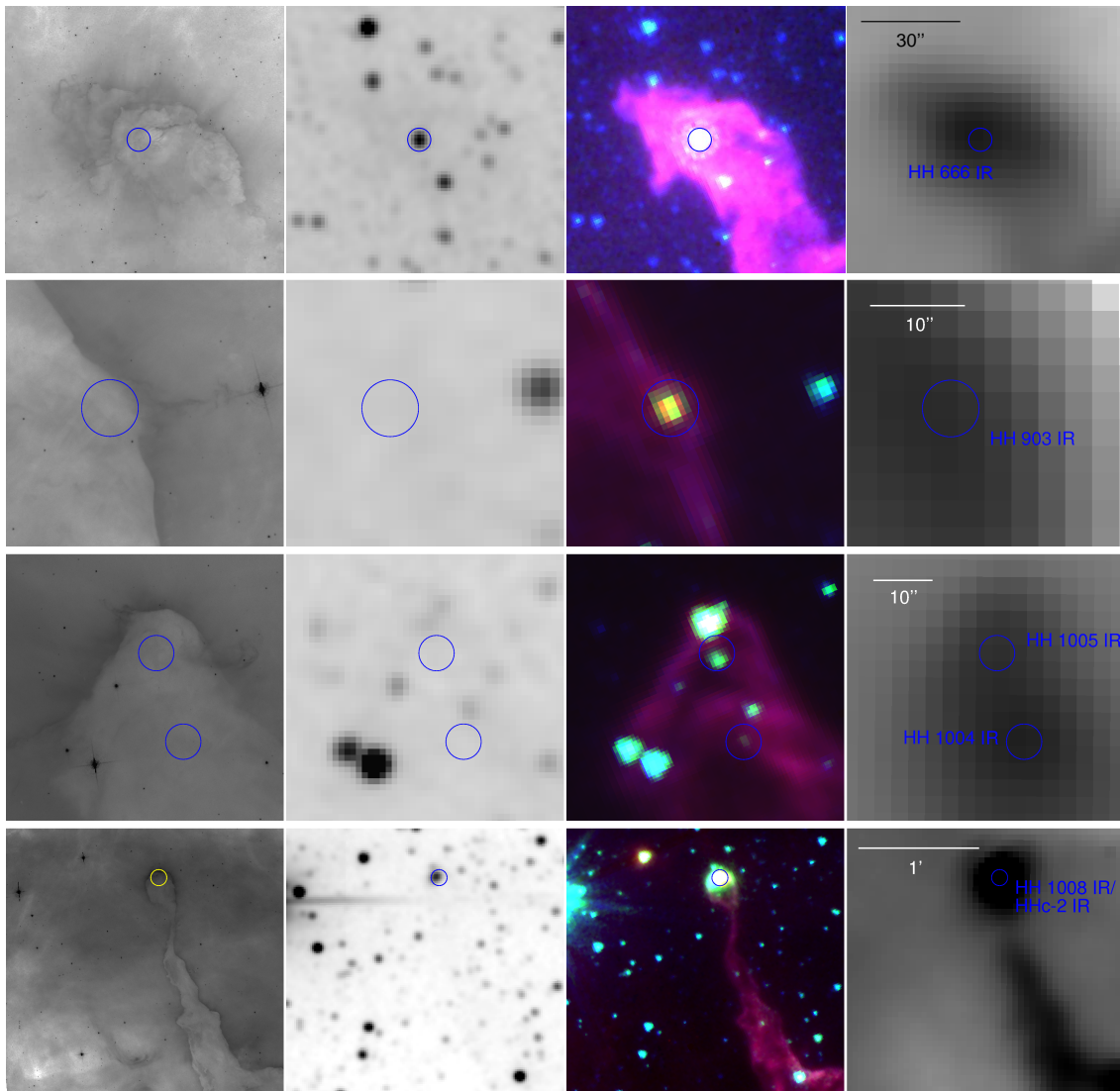


Figure 7.3: The HH jets and HH jet candidates in four different wavelengths. Each row represents from left to right the HST  $H\alpha$  image [Ford and the ACS Science Team 2000, obtained via the Hubble Legacy Archive], the 2MASS  $K_s$  band image [Skrutskie et al. 2006, obtained via the NASA/IPAC Infrared Science Archive], a *Spitzer* RGB image with  $3.6\ \mu\text{m}$  in blue,  $4.5\ \mu\text{m}$  in green and  $8.0\ \mu\text{m}$  in red, and *Herschel* PACS  $170\ \mu\text{m}$  in the rightmost panel. The sources marked with blue circles (partly yellow for better visibility) and labelled in the *Herschel* image are those sources of jet objects that are listed in Table 7.2. Spatial scale was chosen individually and is indicated separately for each row. [Image first published: Ohlendorf et al. 2012]

7 Jet-driving protostars in the Carina Nebula Complex

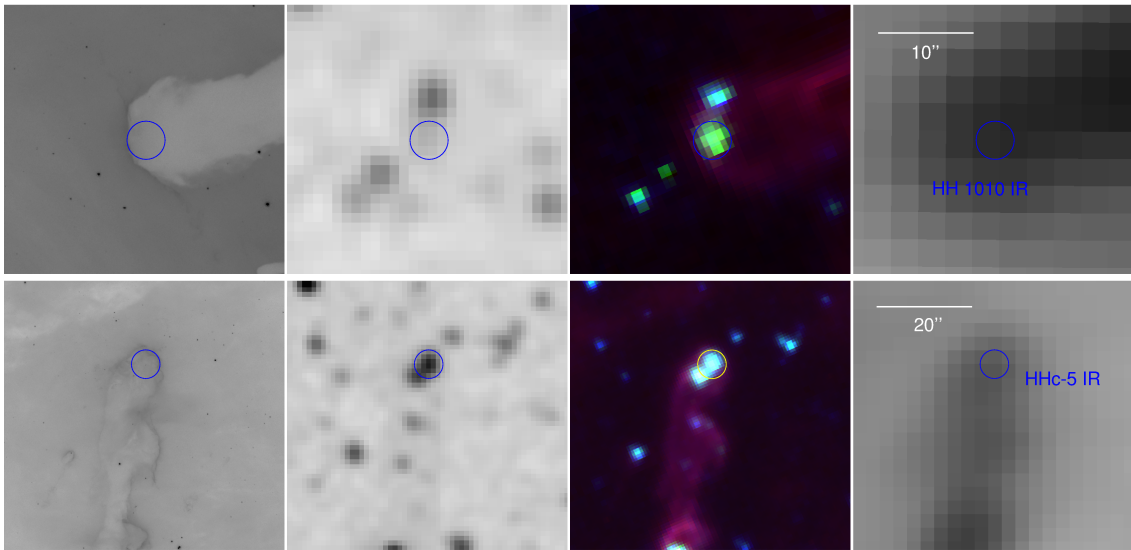


Figure 7.3: Continued.

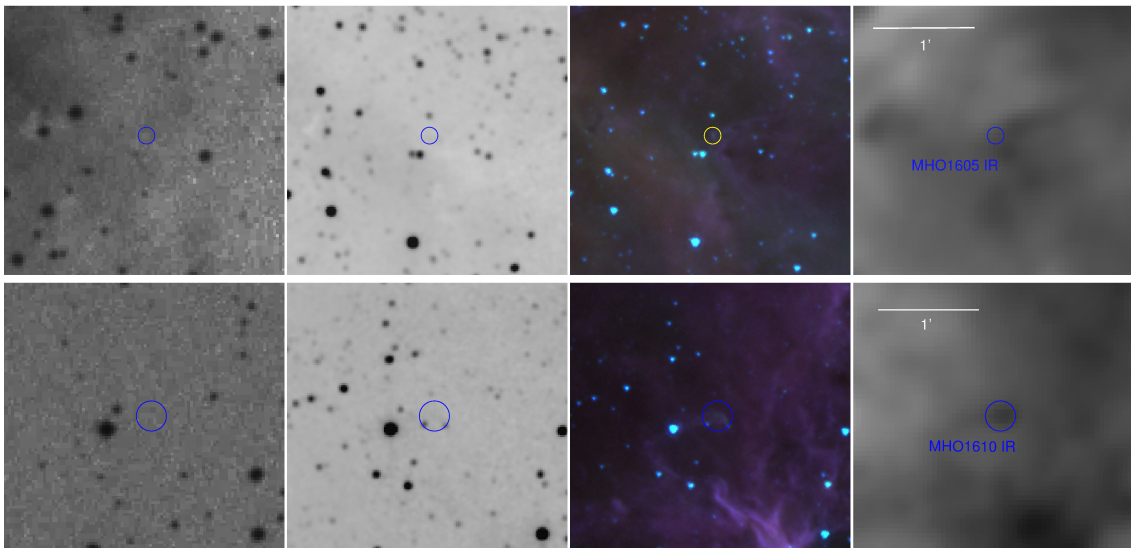


Figure 7.4: As in Fig. 7.3, but showing the two MHOs identified with *Spitzer* sources. Instead of the HST image, the leftmost image in each panel shows the DSS optical image. [Image first published: Ohlendorf et al. 2012]

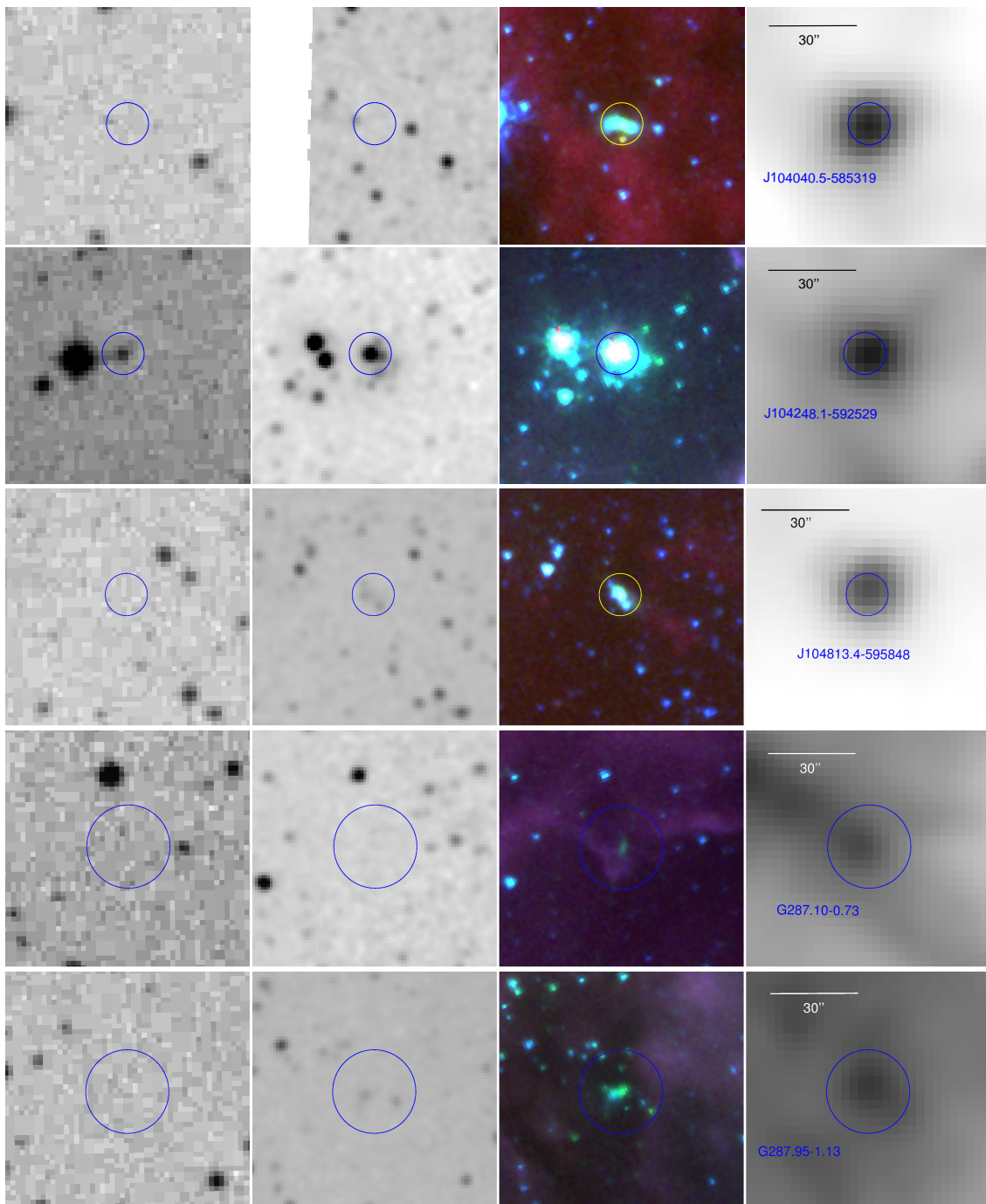


Figure 7.5: As Fig. 7.3, but showing the seven EGOS in our jet source sample. Instead of the HST image, the leftmost image in each panel shows the DSS optical image. [Image first published: Ohlendorf et al. 2012]

7 Jet-driving protostars in the Carina Nebula Complex

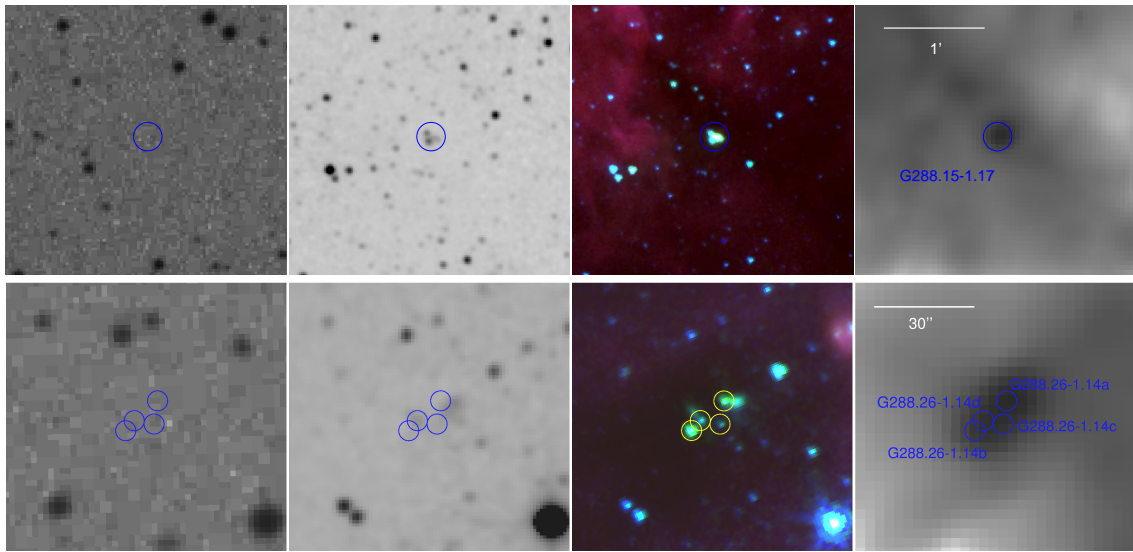


Figure 7.5: Continued.

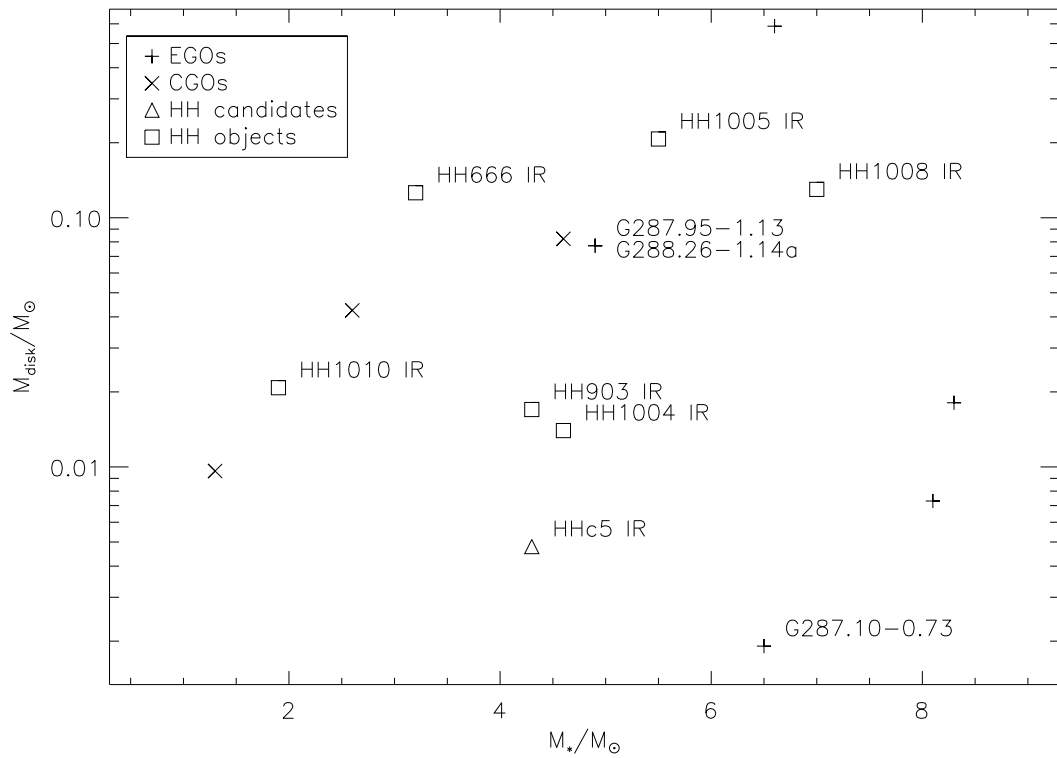


Figure 7.6: Stellar mass and disk mass derived from SED fits, broken down by type.

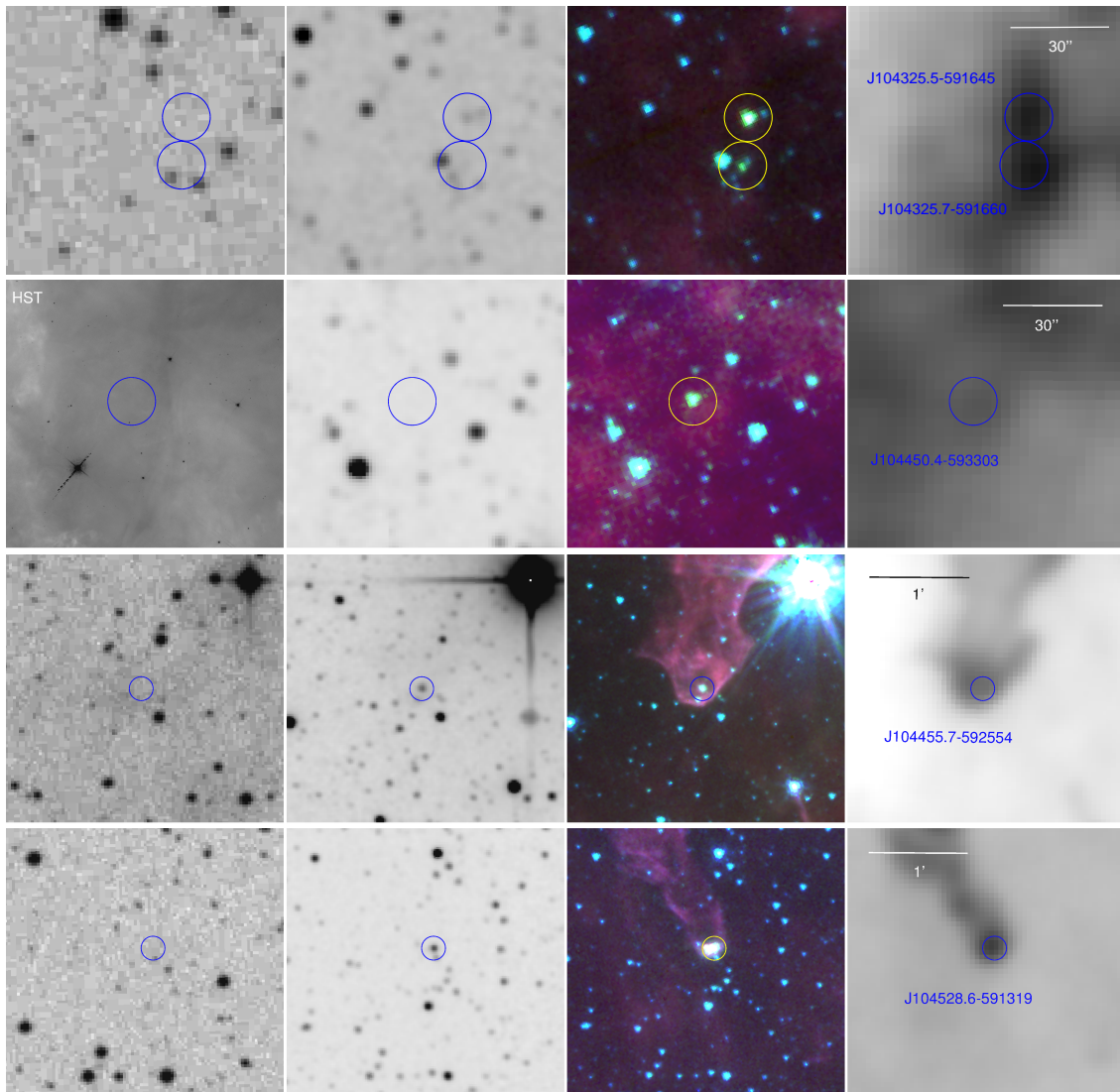


Figure 7.7: As Fig. 7.3, showing the five CGOs in our sample. The leftmost image in each panel is the HST image if indicated by an “HST” in the upper left-hand corner, otherwise it is a DSS image. [Image first published: Ohlendorf et al. 2012]

## 7 Jet-driving protostars in the Carina Nebula Complex

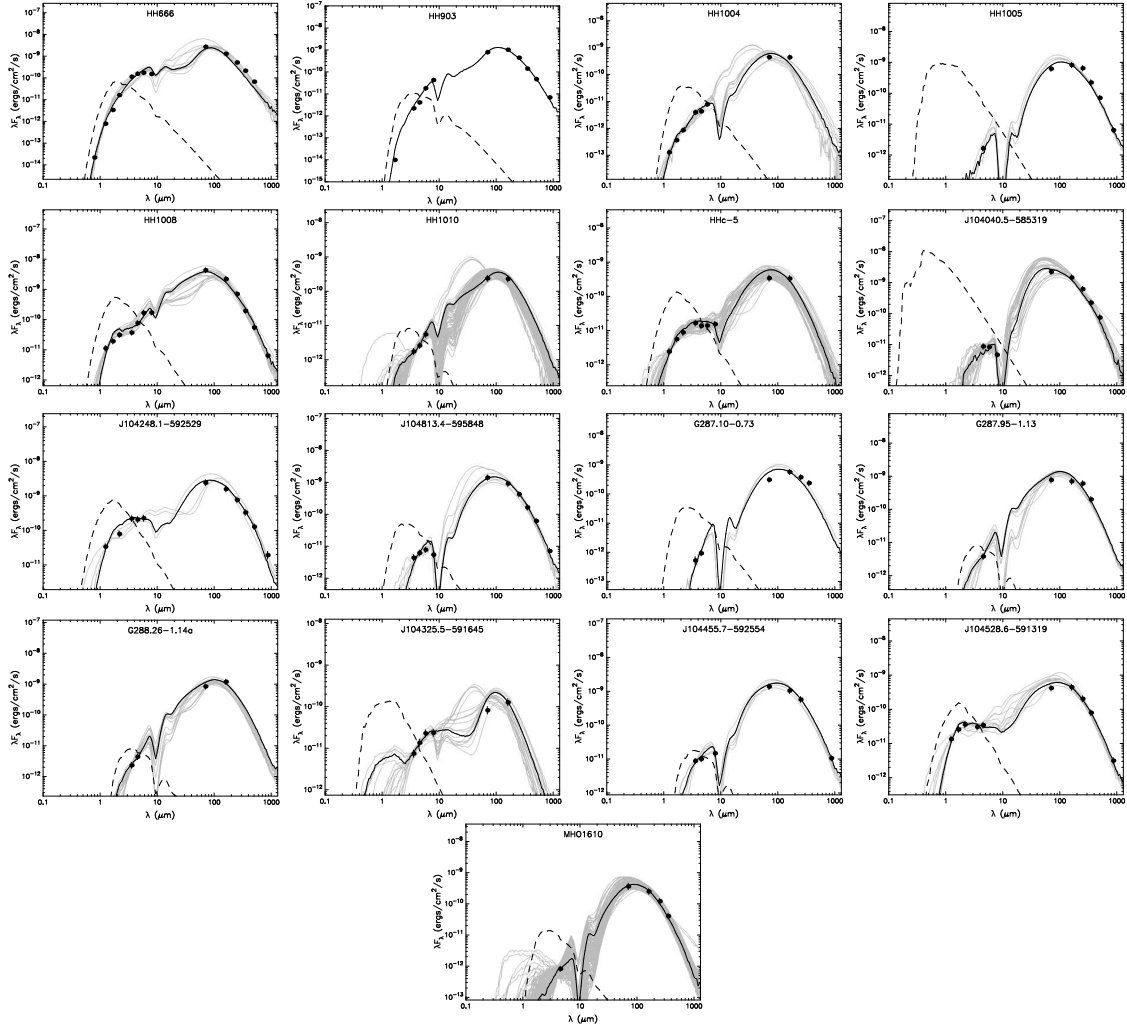


Figure 7.8: Fitted spectral energy distributions of those 17 objects for which we could determine fluxes in at least four bands overall [obtained using the SED fitter of Robitaille et al. 2007]. Filled circles mark the input fluxes. The black line shows the best fit, and the grey lines show subsequent good fits. The dashed line represents the stellar photosphere corresponding to the central source of the best-fitting model, as it would appear in the absence of circumstellar dust (but including interstellar extinction). [Image first published: Ohlendorf et al. 2012]

Table 7.3: Model parameters for the jet sources as obtained from the Robitaille et al. [2007] models.

Jet source	Stellar mass [ $M_{\odot}$ ]		Disk mass [ $M_{\odot}$ ]		Envelope mass [ $M_{\odot}$ ]		Total luminosity [ $L_{\odot}$ ]		Best-fit model
J104040.5–585319	8.3	[1.9 – 10 ]	$1.81 \cdot 10^{-2}$	$[2.73 \cdot 10^{-3} - 6.71 \cdot 10^{-1}]$	350	[ 39 – 1300]	1700	[300 – 3400]	3002514
J104114.3–593239	6.5	[5.5 – 6.5]	$1.91 \cdot 10^{-3}$	$[1.91 \cdot 10^{-3} - 2.07 \cdot 10^{-1}]$	430	[430 – 760]	250	[230 – 250]	3020073
J104148.7–594338	1.9	[1.3 – 6.7]	$2.08 \cdot 10^{-2}$	$[7.76 \cdot 10^{-4} - 2.80 \cdot 10^{-1}]$	77	[6.1 – 250]	64	[40 – 1400]	3008354
J104248.1–592529	8.1	[5.0 – 8.3]	$7.32 \cdot 10^{-3}$	$[7.32 \cdot 10^{-3} - 5.06 \cdot 10^{-1}]$	1500	[200 – 1700]	820	[460 – 1000]	3006025
J104325.5–591645	1.3	[0.8 – 5.7]	$9.63 \cdot 10^{-3}$	$[6.35 \cdot 10^{-5} - 1.86 \cdot 10^{-1}]$	10	[1.9 – 53]	38	[23 – 760]	3002569
J104351.5–595521	3.2	[1.7 – 9.2]	$1.26 \cdot 10^{-1}$	$[1.93 \cdot 10^{-2} - 5.68 \cdot 10^{-1}]$	20	[5.3 – 410]	420	[390 – 1400]	3014036
J104445.4–595555	7.0	[2.1 – 8.1]	$1.30 \cdot 10^{-1}$	$[1.60 \cdot 10^{-3} - 3.42 \cdot 10^{-1}]$	560	[ 94 – 640]	710	[370 – 1000]	3006553
J104455.7–592554	4.6	[4.6 – 7.7]	$8.23 \cdot 10^{-2}$	$[4.79 \cdot 10^{-2} - 5.87 \cdot 10^{-1}]$	1200	[550 – 1200]	310	[230 – 570]	3000552
J104509.4–600203	4.3	[1.4 – 6.4]	$4.79 \cdot 10^{-3}$	$[2.10 \cdot 10^{-4} - 2.73 \cdot 10^{-1}]$	43	[3.9 – 350]	130	[56 – 310]	3019527
J104528.6–591319	2.6	[1.5 – 4.8]	$4.25 \cdot 10^{-2}$	$[1.05 \cdot 10^{-3} - 2.16 \cdot 10^{-1}]$	270	[ 65 – 300]	100	[94 – 200]	3003259
J104542.0–601732	4.9	[3.0 – 7.3]	$7.72 \cdot 10^{-2}$	$[2.77 \cdot 10^{-3} - 5.87 \cdot 10^{-1}]$	540	[300 – 550]	250	[190 – 420]	3014735
J104556.4–600608	4.3	[4.3 – 4.3]	$1.74 \cdot 10^{-2}$	$[1.74 \cdot 10^{-2} - 1.74 \cdot 10^{-2}]$	490	[490 – 490]	250	[250 – 250]	3018560
J104608.3–594525	3.6	[1.4 – 6.4]	$1.34 \cdot 10^{-3}$	$[2.52 \cdot 10^{-4} - 2.71 \cdot 10^{-1}]$	80	[9.3 – 250]	110	[52 – 260]	3004022
J104644.2–601035	5.5	[5.5 – 7.3]	$2.07 \cdot 10^{-1}$	$[4.25 \cdot 10^{-3} - 5.87 \cdot 10^{-1}]$	760	[480 – 760]	230	[230 – 440]	3013239
J104644.8–601021	4.6	[2.6 – 7.0]	$1.40 \cdot 10^{-2}$	$[7.32 \cdot 10^{-3} - 2.26 \cdot 10^{-1}]$	20	[4.9 – 250]	150	[81 – 1600]	3016324
J104750.3–602618	4.9	[3.0 – 6.6]	$7.72 \cdot 10^{-2}$	$[2.77 \cdot 10^{-3} - 5.87 \cdot 10^{-1}]$	540	[ 66 – 550]	250	[190 – 380]	3014735
J104813.4–595848	6.6	[3.6 – 8.3]	$5.87 \cdot 10^{-1}$	$[2.77 \cdot 10^{-3} - 5.87 \cdot 10^{-1}]$	550	[250 – 750]	330	[220 – 2500]	3013941

**Notes.** For each model parameter, the best-fit value is given in the respective first column, followed by a range defined by the minimum and maximum values obtained from models constrained by a  $\chi^2$  criterion (see Sect. 7.4.1). The last column gives the identifier of the best-fit model.

## 7.5 Discussion

We surveyed 55 jet objects and found corresponding point-like driving sources for 36 of them. For three of the CGOs and seven of the EGOs we were able to derive the SEDs of the newly identified IR sources. Out of 35 HH jets and HH jet candidates, we could identify sources for 22 of them and model SEDs for seven. Out of the six MHOS within the HAWK-I field – which is smaller than the entire field surveyed here – we could only identify sources for two and find an SEDs model for one.

It is important to note that this study is not able to identify all the jet objects in the CNC. The majority of jets are just too faint and fall below the sensitivity limits of our data. Consequently, out of the members of the CNC that are currently undergoing jet-emitting phases, we can only observe a low percentage of the most luminous ones. This explains why out of the very large number of young stars within the surveyed region only so few jets are detected.

The stellar-mass estimates derived from SED fitting are in the range  $\sim 1 M_{\odot}$  to  $\sim 10 M_{\odot}$ . This range agrees very well with the expectations in the following sense: The lower mass limit of  $\sim 1 M_{\odot}$  is probably a consequence of the detection limit. Although the *Spitzer* images are deep enough to detect stars below this mass limit, one has to keep in mind that it is necessary to detect emission from the jet, too. That the mass flow rates of jets and outflows from YSOs are roughly correlated to the stellar luminosity [and thus also to the stellar mass; e.g. Reipurth and Bally 2001] explains why we do not detect jets from YSOs of lower masses. The upper mass limit is more interesting, since there is no reason why the jets from high-mass protostars should not be observable, if such jets were present. The absence of jet-driving high-mass ( $M \gtrsim 20 M_{\odot}$ ) protostars therefore suggests that no such objects are present. This agrees with the conclusion derived from the analysis of the sub-mm data of the cloud structure by Preibisch et al. [2011d] that the clouds present today in the Carina Nebula are not dense and massive enough for high-mass star formation. This suggests that the currently ongoing star formation process in the CNC is qualitatively different from the processes that led to the formation of dozens of very high-mass stars [ $M \gtrsim 50 M_{\odot}$ , e.g. Smith 2006a] in the CNC a few million years ago.

Further conclusions about the star-formation process can be drawn from the properties of the jets and the jet-driving protostars. The first interesting result is found by comparing the number of jets detected in the infrared images to the number of HH jets detected in the optical HST images. For a quantitative analysis, we consider the  $\approx 1.0^{\circ} \times 1.3^{\circ}$  region investigated by Smith et al. [2010a, their Fig. 1]. Their (mostly non-contiguous) HST pointings cover  $\approx 15\%$  of this area and have led to the detection of 34 HH jets and HH jet candidates. If the full area had been observed by HST, the number of detected jets in this area would very likely be larger, perhaps<sup>3</sup>  $\sim 70$ .

The number of jets detected in the infrared images of the same area is 20 (9 EGOs, 5 CGOs, and 6 MHOS), i.e. substantially smaller. We are confident that this is not an effect of the cloud extinction, because the sub-mm observations [Preibisch et al. 2011d] have shown that the column densities and the extinction of almost all clouds in the region are rather low, generally  $A_V \lesssim 15$  mag. The clouds are therefore largely transparent for light

---

<sup>3</sup>We have to consider that the positions of the individual HST pointings were targeted on particularly promising locations and the true spatial distribution of HH jets is presumably not perfectly homogeneous; thus, the number of jets is presumably smaller than an estimate based simply on the area-filling factor of  $\approx 15\%$ .

in the *Spitzer* bands, so that we do not expect to miss a significant number of jets due to cloud extinction.

For comparing the number of optical HH jets to the IR jets one has to keep in mind that these two groups are intrinsically different: The optical HH objects trace jets moving in the atomic gas outside the molecular clouds and originate in protostars located close to the surfaces of clouds. The IR jets, on the other hand, trace molecular material inside the clouds [e. g. Elias 1980]. Since almost all clouds should be essentially transparent at *Spitzer* wavelengths, one expects to see considerably more IR jets than optical jets, assuming that the jet-driving sources are distributed in a spatially homogeneous way throughout the entire volume of the clouds. In many observations of nearby star-forming clouds, this expectation is confirmed [see e. g. Gutermuth et al. 2008, for the case of the NGC 1333 cloud].

In the case of the CNC, however, we see the opposite trend, i. e. the number of infrared jets is smaller than the number of optical jets. This suggests that most jet-driving protostars are located at the surfaces of the clouds, rather than in the inner cloud regions.

## 7.6 Conclusions

Our search for jets in wide-field *Spitzer* IRAC mosaic images of the CNC led to the detection of three new EGOs and five CGOs in and immediately around the area studied previously with the HST by Smith et al. [2010a]. We also identified sources for 23 of the 34 HH jets in this area. Combining *Spitzer* and *Herschel* photometry with complementary LABOCA and HAWK-I/2MASS data, we obtained the SEDs of the jet sources through radiative transfer modelling [Robitaille et al. 2006, 2007] to estimate basic stellar and circumstellar parameters for 17 sources overall, where photometry in at least four bands could be obtained.

We find that the jet-driving protostars generally have low to intermediate masses ( $\sim 1 - 10 M_{\odot}$ ), which corroborates the notion that there is no current formation of high-mass stars in the CNC and that the present star formation epoch is thus different from the epoch that formed the present  $\sim 70$  high-mass stars in Carina [Preibisch et al. 2011d]. More optical jets, which come from sources close to the cloud surfaces, than IR jets from more deeply embedded sources, are seen in the region, showing that presently forming stars predominantly lie near the surfaces of clouds.

# 8 Discovering young stars in the Gum 31 region<sup>1</sup>

The new catalogue of cYSOs extends beyond the conventionally studied central area of the Carina Nebula. It therefore allows us to study adjacent regions of equal importance to research. The analysis in Chapter 9 will clearly show that the Gum 31 region is a prominent hotbed of star formation, similar to the South Pillars. This chapter demonstrates that it is an outlying part of the CNC and analyses its young stellar population in detail. Furthermore, we will also extend the study of jet-emitting YSOs begun in Chapter 7 to Gum 31.

## 8.1 Motivation

As described in Sect. 3.3, the bubble-shaped H II region Gum 31 around the young stellar cluster NGC 3324 is located  $\approx 1^\circ$  north-west of the CN. While numerous observations of the Carina Nebula (CN) have been performed in the last few years and provided comprehensive information about the stellar populations as well as the cloud properties [Yonekura et al. 2005, Smith and Brooks 2007, Kramer et al. 2008, Smith et al. 2010a,b, Townsley et al. 2011b, Preibisch et al. 2011a,c,d, 2012, Salatino et al. 2012], the Gum 31 region has not received much attention. Despite its interesting morphology and the publicity of HST images of its western rim (Hubble News Release STScI-2008-34), the H II region and its stellar population remain rather poorly studied until today. This seems to be related to its celestial position: the closeness to the extremely eye-catching CN has always overshadowed Gum 31.

The physical relation between NGC 3324 and the CNC is still unclear, though recent distance determinations of Gum 31 and NGC 3324 imply that the NGC 3324/Gum 31 region is located at the same distance as the CN (cf. Sect. 3.3).

In this paper, we are aiming to characterise the protostellar and young stellar population of the stellar cluster, the surrounding H II region and its environs. Our study is based on *Spitzer*, WISE, *Herschel*, and VISTA data, which provide much better sensitivity and angular resolution than the previously existing data sets.

We will describe the data sets we used in Sect. 8.2. In Sect. 8.3, we will describe the general morphology of the infrared clouds in and around the Gum 31 region and its implications for our work. Detections of cYSOs from the IR data, including the identification method, and their spatial distribution will be described in Sect. 8.4. Furthermore, we have analysed point-like sources as detected with both *Herschel* and *Spitzer* and derived

---

<sup>1</sup>This chapter is based on a paper published in *Astronomy & Astrophysics* [Ohlendorf et al. 2013a] written in close cooperation with Thomas Preibisch, Benjamin Gaczkowski, Thorsten Ratzka, Judith Ngoumou, Veronica Roccatagliata, and Rebekka Grellmann.

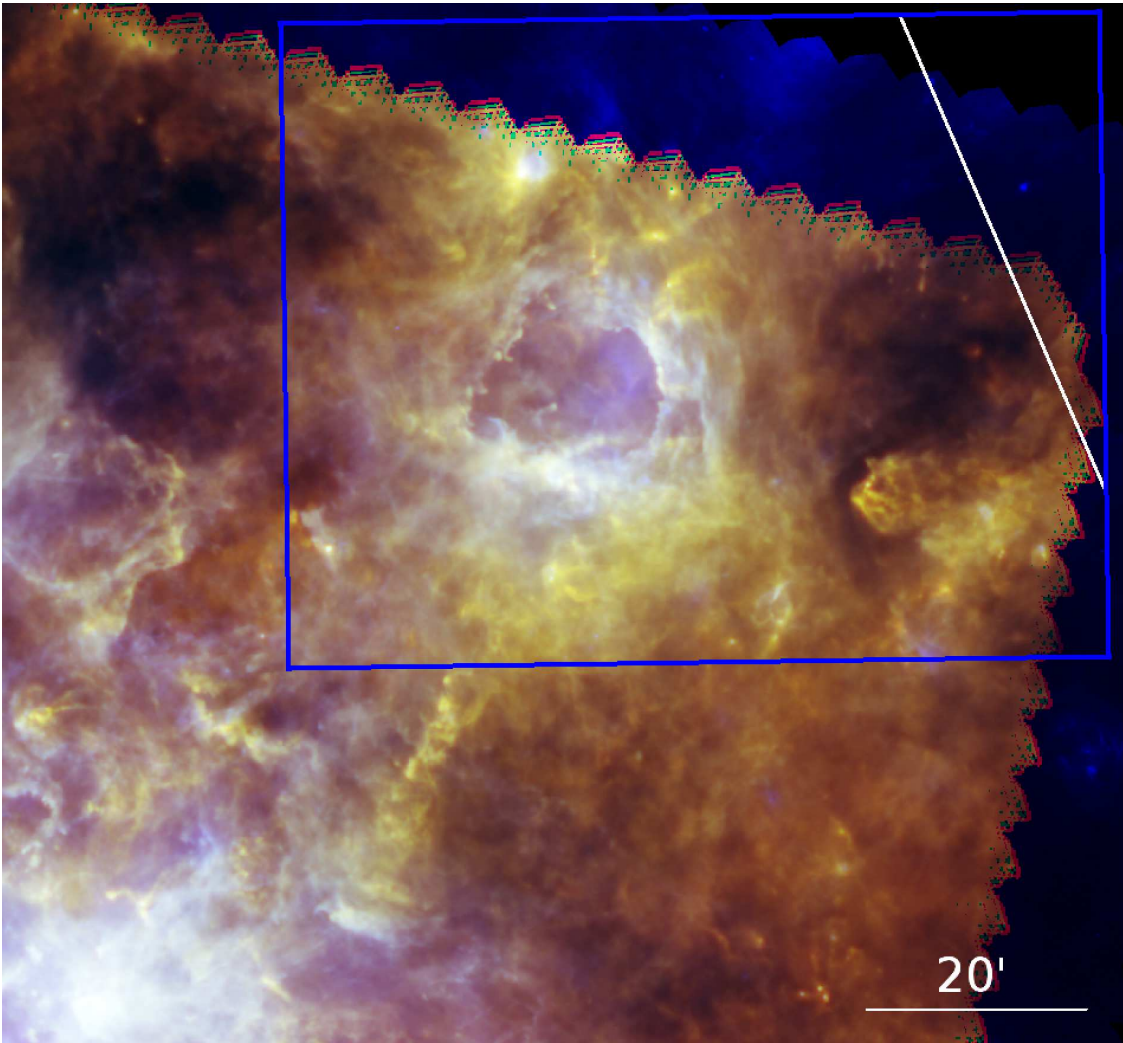


Figure 8.1: The Gum 31 region and its connection to the central CN, seen in a *Herschel* RGB image, with the PACS 70  $\mu\text{m}$  image in blue, SPIRE 250  $\mu\text{m}$  in green, and SPIRE 500  $\mu\text{m}$  in red. The blue box marks the  $1.0^\circ \times 1.1^\circ$  area used for analysis here. The diagonal white line marks the area covered by IRAC. [Image first published: Ohlendorf et al. 2013a]

their SEDs (Sect. 8.5). We have also identified likely sources to two previously detected Herbig-Haro jets (Sect. 8.6). Inferences will be discussed in Sect. 8.7.

## 8.2 Observational data

This chapter uses data taken with *Spitzer* (see Sect. 4.1), *Herschel* (see Sect. 4.2) and an image taken by VISTA (no photometry, cf. Sect. 4.4) as well as catalogue data from WISE (Sect. 4.3) and 2MASS (Sect. 4.6). An overview of the observations for which data reduction and photometry was done (i. e. *Spitzer* and *Herschel*) can be found in Table 8.1.

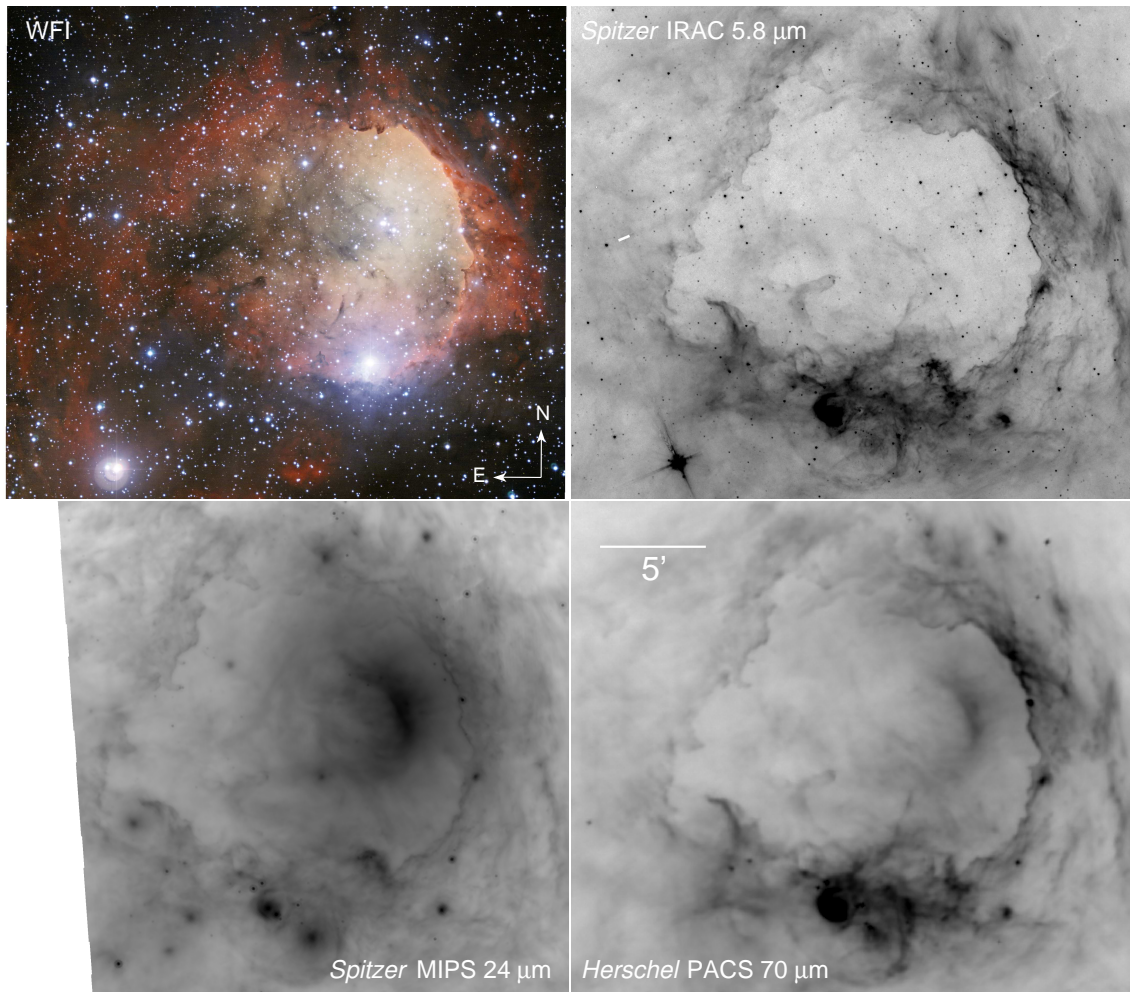


Figure 8.2: An overview of the Gum 31 region in the optical, MIR, and FIR. The WFI optical image [ESO image release eso1207] shows the  $V$  band in blue,  $R$  band in yellow, O III 501 nm emission in green, and  $H\alpha$  in red. [Image first published: Ohlendorf et al. 2013a]

## 8.2.1 Spitzer images and photometry

### IRAC

From the complete data set which is described in Sect. 4.1 and Chapter 5, we use only a  $1.0^\circ \times 1.1^\circ$  area corresponding to the Gum 31 region and a small region to the west of it. This complements the area as described by Gaczkowski et al. [2013] to complete the area surveyed with our *Herschel* observation programme (cf. Sect. 8.2.2).

In this chapter we use the SPSC as described in Sect. 5.1. The total number of point-like sources detected in at least one band in the sampled area is 57 828. 6739 of those were detected in all four IRAC bands. In the way described in Sect. 5.4.3 we estimate completeness limits of  $\approx 1.5$  mJy,  $\approx 0.7$  mJy,  $\approx 1.2$  mJy and  $\approx 1.6$  mJy (13.2 mag, 13.5 mag, 12.5 mag, and 11.5 mag) for  $3.6 \mu\text{m}$ ,  $4.5 \mu\text{m}$ ,  $5.8 \mu\text{m}$ , and  $8.0 \mu\text{m}$ . For reference, the histograms used are shown in Fig. 8.3. The detection limits, as quantified by the faintest sources in our

Table 8.1: Overview of observations with *Spitzer*, *Herschel* and VISTA used in this chapter.

Instrument	AOR	Obs. mode	Time	Date [UT]	PI
<i>Spitzer</i> IRAC	23708160	IRAC map	3301 s	19 Jul 2008	S. R. Majewski
<i>Spitzer</i> IRAC	23699200	IRAC map	3057 s	19 Jul 2008	S. R. Majewski
<i>Spitzer</i> IRAC	23704320	IRAC map	3070 s	19 Jul 2008	S. R. Majewski
<i>Spitzer</i> IRAC	23688192	IRAC map	3082 s	19 Jul 2008	S. R. Majewski
<i>Spitzer</i> IRAC	23701504	IRAC map	3086 s	19 Jul 2008	S. R. Majewski
<i>Spitzer</i> IRAC	23695360	IRAC map	3086 s	19 Jul 2008	S. R. Majewski
<i>Spitzer</i> IRAC	23696896	IRAC map	3087 s	19 Jul 2008	S. R. Majewski
<i>Spitzer</i> IRAC	23706368	IRAC map	3088 s	19 Jul 2008	S. R. Majewski
<i>Spitzer</i> IRAC	23684352	IRAC map	3312 s	19 Jul 2008	S. R. Majewski
<i>Spitzer</i> MIPS	15054080	MIPS phot	9469 s	12 Jun 2006	J. Hester
<i>Herschel</i> PACS	1342211615	SpirePacsParallel	11889 s	26 Dec 2010	T. Preibisch
<i>Herschel</i> PACS	1342211616	SpirePacsParallel	12863 s	26 Dec 2010	T. Preibisch
<i>Herschel</i> SPIRE	1342211615	SpirePacsParallel	11889 s	26 Dec 2010	T. Preibisch
<i>Herschel</i> SPIRE	1342211616	SpirePacsParallel	12863 s	26 Dec 2010	T. Preibisch
VISTA VIRCAM	586281	<i>H</i> filter	270 s	16 Jan 2012	T. Preibisch

sample, are  $100 \mu\text{Jy}$ ,  $100 \mu\text{Jy}$ ,  $330 \mu\text{Jy}$ , and  $280 \mu\text{Jy}$  (16.7 mag, 15.7 mag, 13.9 mag, and 13.4 mag) for  $3.6 \mu\text{m}$ ,  $4.5 \mu\text{m}$ ,  $5.8 \mu\text{m}$ , and  $8.0 \mu\text{m}$ .

Comparing these to numerical models of stellar evolution [Baraffe et al. 1998], we find that for an age of  $\sim 3 \text{ Ma}$  the photospheric emission of a  $1 M_{\odot}$  star is well above the detection limit for WISE in the  $3.4 \mu\text{m}$  and  $4.6 \mu\text{m}$  bands while for IRAC the sensitivity extends down to  $\sim 0.5 M_{\odot}$ . For younger stars this boundary shifts towards lower masses so that with WISE 1 Ma old  $0.5 M_{\odot}$  stars are still detectable while with IRAC we could reach down to  $\sim 0.25 M_{\odot}$ . If we compare the completeness limits to the RADMC model [Dullemond and Dominik 2004] which provides calculations of continuum radiative transfer in axisymmetric circumstellar dust distributions around a central illuminating star, we find that disk masses as low as  $0.013 M_{\odot}$  would still be detectable for a  $1 M_{\odot}$  YSO.

## MIPS

For the detailed analysis in Sect. 8.5 the IRAC data were complemented by photometry on the MIPS  $24 \mu\text{m}$  map described in Sect. 4.1.2<sup>2</sup>. The MIPS images were searched by eye for point-like sources coinciding with the previously identified IRAC and *Herschel* (Sect. 8.2.2) sources. Because this field is only sparsely populated with point-like sources in the  $24 \mu\text{m}$  band, they were easily found by eye.

Source detection and PSF photometry were then performed with StarFinder as described in Sect. 4.1.2. In this way, the sub-sample of MIPS point-like sources defined by IRAC and *Herschel* detection is analysed from the brightest ( $4570 \text{ mJy}$ ) to the faintest ( $5 \text{ mJy}$ ) objects and background-corrected fluxes derived.

<sup>2</sup>“*Spitzer* Follow-up of HST Observations of Star Formation in HII Regions” programme; principal investigator (PI): Jeff Hester, programme identification number (PID): 20726; June 2006

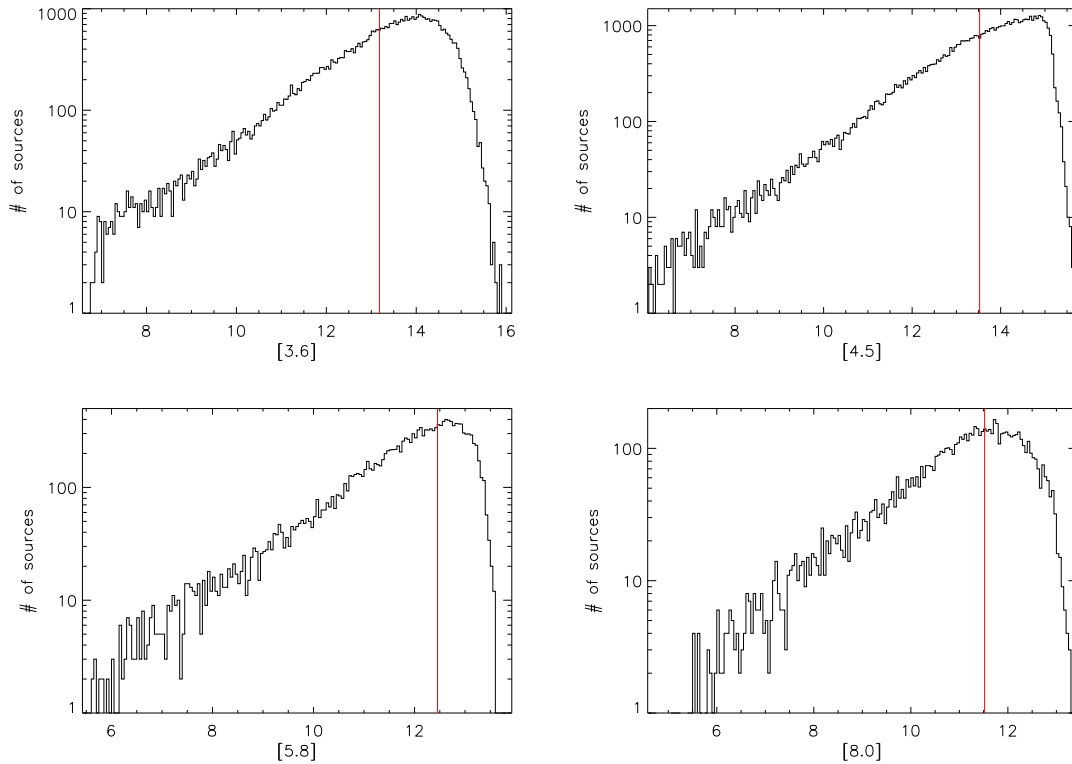


Figure 8.3: Histograms of the measured source magnitudes in the SPSC for the Gum 31 region. Red lines indicate the completeness limits.

### 8.2.2 Herschel far-infrared maps

We analysed the Gum 31 region using data from our recent *Herschel* far-infrared survey of the CNC<sup>3</sup> as described in Sect. 4.2.

As any source catalogue based on maps with strong and highly spatially inhomogeneous background emission, our *Herschel* source lists will miss some faint sources and at the same time contain a small number of spurious detections. To improve the reliability of the source catalogue, we restricted our analysis to those sources that are detected (independently) in at least two *Herschel* maps and for the SED construction in Sect. 8.5 even to those detected in at least three bands. For this, the point-like sources detected in each individual *Herschel* band were matched. The matching process was described by Gaczkowski et al. [2013].

In the Gum 31 area, we detect 91 point-like sources in at least two bands and 59 in at least three bands. For each of them we checked coincidence with IRAC-identified point-like sources. We excluded all cases where either the spatial coincidence of *Herschel* and IRAC source was not clear or where more than one IRAC source appeared as a possible counterpart. This results in the 17 sources identified both in *Herschel* and in IRAC wavelengths that are subject to the analysis in Sect. 8.5.

The detection limit can be approximated by the fluxes of the faintest detected sources; this is in the range of  $\approx 1$  Jy to  $\approx 2$  Jy in our maps. An estimate for the ‘typical’

<sup>3</sup>PI: Thomas Preibisch, PID: OT1-tpreibis-1; December 2010

completeness limit (i. e. the limit above which we can expect most objects in the survey area to be detected) can be derived from the histograms of the fluxes similar to those shown in Sect. 8.2.1. The corresponding limits are at  $\sim 10$  Jy,  $\sim 15$  Jy,  $\sim 10$  Jy,  $\sim 10$  Jy, and  $\sim 6$  Jy for  $70\ \mu\text{m}$ ,  $160\ \mu\text{m}$ ,  $250\ \mu\text{m}$ ,  $350\ \mu\text{m}$ , and  $500\ \mu\text{m}$  [cf. Gaczkowski et al. 2013].

### 8.2.3 VISTA near-infrared images

We use the  $H$ -band image of the area around Gum 31 obtained with the VISTA Infra-Red CAMERA (VIRCAM) in the night of 15 January 2012 as the first observation of our VISTA survey of the CNC (Sect. 4.4).<sup>4</sup> At the time of writing the photometric calibration of these data was still in progress. Therefore, we use only the  $H$  band image data taken in January 2012 for a (preliminary) scientific analysis here, but no photometric values.

### 8.2.4 WISE

We used catalogue data from the WISE [Wright et al. 2010] All-Sky Data Release [Cutri and al. 2012] as described in Sect. 4.3. In our survey area the catalogue contains 20 739 point sources with detection in at least one band. In way parallel to the way described in Sect. 4.3, we estimate the detection limits to be  $90\ \mu\text{Jy}$ ,  $70\ \mu\text{Jy}$ , and  $700\ \mu\text{Jy}$  (16.3 mag, 15.9 mag, and 11.6 mag) for  $3.4\ \mu\text{m}$ ,  $4.6\ \mu\text{m}$ , and  $12\ \mu\text{m}$  (for the analysis described in Sect. 8.4.1 we do not use the  $22\ \mu\text{m}$  band). Analogously, we estimate completeness limits of  $4\ \text{mJy}$ ,  $3\ \text{mJy}$ , and  $24\ \text{mJy}$  (12.1 mag, 11.9 mag, and 7.7 mag) for  $3.4\ \mu\text{m}$ ,  $4.6\ \mu\text{m}$ , and  $12\ \mu\text{m}$ .

## 8.3 Morphology

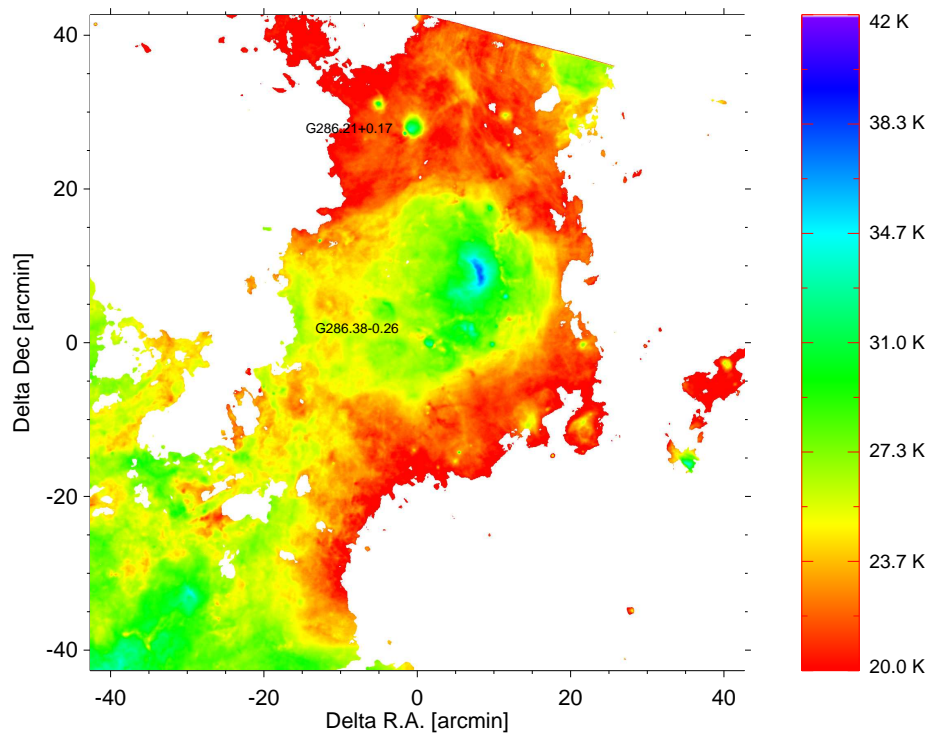
Figure 8.1 shows the FIR morphology of the Gum 31 bubble and its environs. In both wavelength ranges, the cavity of the HII region is clearly delineated. Figure 8.2 contrasts optical and infrared images of the Gum 31 bubble. Near the centre of the bubble a cluster of stars is just discernible in the IRAC  $5.8\ \mu\text{m}$  image. This is NGC 3324. In the MIPS  $24\ \mu\text{m}$  and PACS  $70\ \mu\text{m}$  images the warm dust surrounding the stars of NGC 3324 forms an arc-like structure that follows the shape of the inner bubble wall.

Several pillar-like structures extend from the edge of the bubble into its inner part, especially from its southern rim. Notably, some but not all optical pillars coincide with those seen in the infrared. The photo-dissociation regions that very sharply delineate the edge of the bubble are well-observable in the IRAC  $5.8\ \mu\text{m}$  image where their fluorescence under the influence of UV radiation can be seen, but also in the MIPS  $24\ \mu\text{m}$  image that shows the emission from the dust grains within.

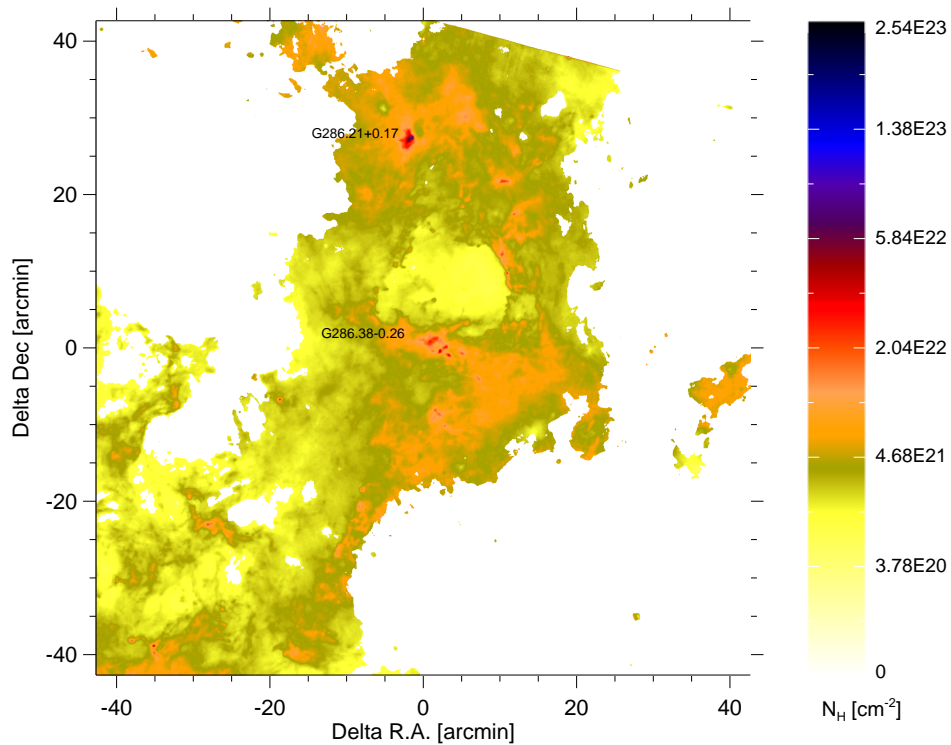
Figure 8.4a shows a colour temperature map for the larger Gum 31 region, extending downwards into the central CNC. It was derived from the ratio of the PACS  $70\ \mu\text{m}$  and  $160\ \mu\text{m}$  emission as detailed by Preibisch et al. [2012]. It shows the temperatures for the HII region being comparatively high ( $\approx 30$ – $40$  K), while those of the surrounding clouds are considerably cooler down to 20 K. The warm dust in NGC 3324 is clearly seen as an outstandingly blue ( $\approx 40$  K) patch inside the bubble.

---

<sup>4</sup>Eso project number 088.C-0117(A)



(a) Colour-temperature map.



(b) Map of hydrogen column density.

Figure 8.4: Colour-temperature map and hydrogen column-density map derived from *Herschel* data. They show the cloud structure in and around the Gum 31 nebula and the connection to the central parts of the Carina Nebula (just outside the lower left edge of the maps). [Image first published: Ohlendorf et al. 2013a]

The G286.21+0.17 cluster (cf. Sect. 8.4.3) also stands out. It is about 8 K warmer than its immediate surroundings. It is also much denser, as can be seen from Fig. 8.4b, which shows the hydrogen column-density derived from the colour temperatures as described by Preibisch et al. [2012]. We see that the column density inside the bubble is relatively low compared to its surroundings at a few  $10^{20} \text{ cm}^{-2}$  and rises steeply by more than one order of magnitude at the ionisation front. Other than G286.21+0.17, we see some more dense clumps scattered within the bubble rim and beyond it. A notable feature is the cluster G286.38–0.26 (cf. Sect. 8.4.3) which has a column density of around  $3 \cdot 10^{22} \text{ cm}^{-2}$ . In sharp contrast to the unusually warm clump G286.21+0.17, in Fig. 8.4a G286.38–0.26 is seen to be cooler than its surroundings, down to  $\approx 20 \text{ K}$ .

The integrated cloud mass of the whole region derived by Preibisch et al. is  $186\,700 M_{\odot}$ . They derive this value by integrating over the same column density map that we show here, but for a region around Gum 31 slightly differently defined than the one here.

In the longer IRAC-wavelength emission and especially in the *Herschel* image, a ‘bridge’ of filamentary structure can be seen to extend from Gum 31 downwards in the direction of the central Carina Nebula, forming a connection. The column density map (Fig. 8.4b), too, shows that the clouds surrounding Gum 31 are connected to the clouds in the more central parts of the CN. Forte [1976] remarks that in the deep optical plates of Lyngå and Hansson [1972] a filamentary structure connecting the H II region H-31 [ $\hat{=}$  Gum 31; Hoffleit 1953] to NGC 3372, the central Carina Nebula, can be seen.

According to Yonekura et al. [2005], the radial velocities of their  $\text{C}^{18}\text{O}$  clumps Nos. 2–6, which surround the Gum 31 bubble, range from  $V_{\text{LSR}} = -20.0 \text{ km s}^{-1}$  to  $V_{\text{LSR}} = -24.1 \text{ km s}^{-1}$ . The  $\text{C}^{18}\text{O}$  clumps in the central and northern part of the CN (Nos. 8–12) have radial velocities in the  $V_{\text{LSR}} = -25.8 \dots -19.9 \text{ km s}^{-1}$  range. This good agreement of the radial velocities suggests that the clouds around Gum 31 and the CN are connected and actually part of the same complex. As was argued by Preibisch et al. [2012] and in Sect. 8.1, we will therefore assume a distance of 2.3 kpc towards Gum 31, the same as to the CNC. This number also agrees well with recent distance determinations with independent means (see Sect. 8.1).

## 8.4 Young stellar objects in the Gum 31 region

### 8.4.1 Identification of YSO candidates

The selection of cYSOs in the following sections is based on the detection of infrared excesses. It follows, therefore, that only those YSOs exhibiting excess IR emission can be detected with this method (cf. also Sect. 8.4.2). These are only those objects that still retain their disks. This means that only YSOs of Class 0 to Class II are the subject of this analysis while Class III objects must mostly remain undetected.

#### Selection by Spitzer colours

We applied the selection by colour-colour diagram as described by Fang et al. [2012] and outlined in Sect. 6.2 to the Gum 31 sample of the SPSC by plotting them into a diagram constrained by Eq. (6.1) and Eq. (6.2). Doing this, we are able to identify 304 infrared excess sources from the total sample of 6739 point-like sources detected in all four bands.

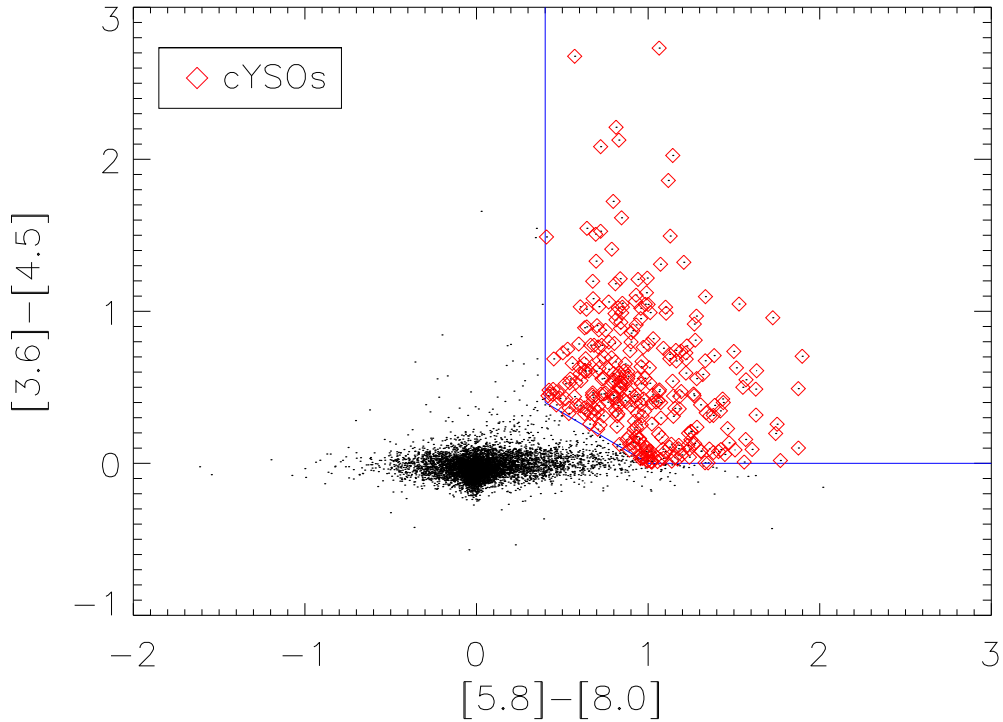


Figure 8.5: Colour-colour diagram using all *Spitzer* IRAC bands. The criteria adopted for YSO identification follow Fang et al. [2012] and Allen et al. [2004] and are described in more detail in Chapter 6.

The resultant colour-colour diagram, showing the  $[3.6] - [4.5]$  colour against the  $[5.8] - [8.0]$  colour is displayed in Fig. 8.5.

Within these samples, it is certain that there are contaminants masking as YSOs for any sample of cYSOs taken from a colour-colour diagram. Because of the closeness of Gum 31 to the Galactic plane ( $b_{\text{Gum 31}} \approx 0.2^\circ$ ), we expect a high contamination especially by background AGB stars (see Sect. 6.4). We can also estimate the contamination based on the criteria of Winston et al. [2007] for the selection of contaminants from the  $[5.8] - [8.0]$  vs.  $[4.5] - [5.8]$  and  $[4.5] - [8.0]$  vs.  $[3.6] - [5.8]$  diagrams. This yields an estimated contamination in the IRAC-selected sample of  $\lesssim 10\%$ .

Checking the spatial distribution of these cYSOs, it is noticeable that their distribution throughout Gum 31 and outside it is almost uniform. This is suspicious. We thus conclude that the contamination within this sample due to fore- and background sources is high and thus do not use this sample for further analysis.<sup>5</sup>

<sup>5</sup>Note that this analysis was done separately from the assembly of the SYCC, which was improved in reliability above the sample described here.

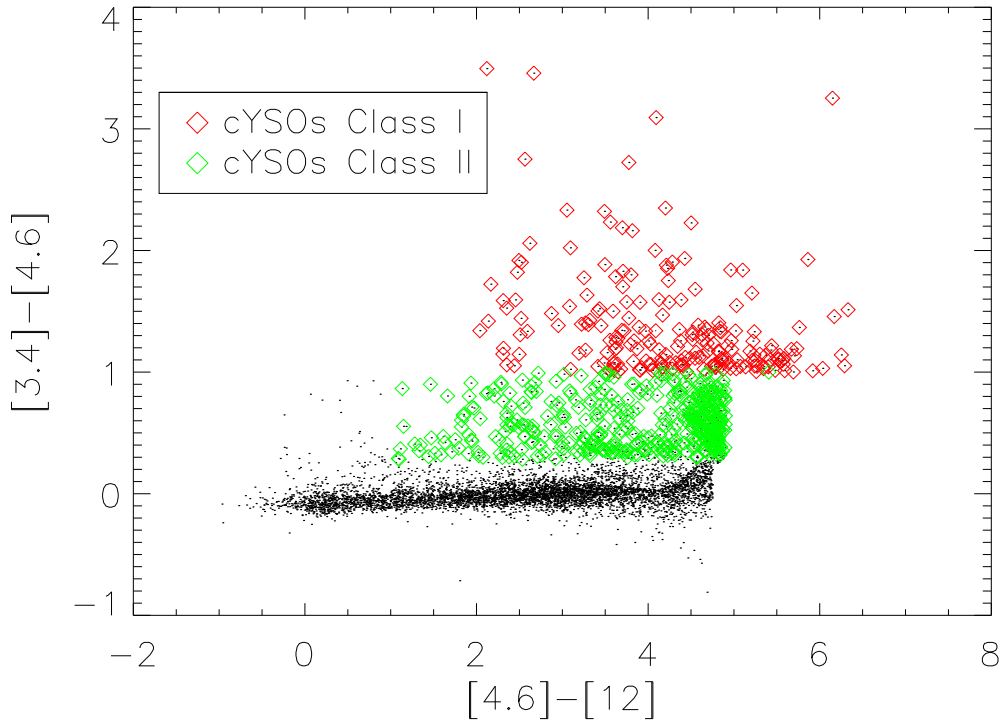


Figure 8.6: Colour-colour diagram using three out of four WISE bands. The criteria adopted for YSO identification follow Koenig et al. [2012]. cYSOs are marked in red for Class I sources and in green for Class II. [Image first published: Ohlen-dorf et al. 2013a]

### Selection by WISE colours

We used WISE catalogue data to search for infrared excess sources. To identify those, we used the criteria of Koenig et al. [2012] described in Sect. 6.3 and applied Eq. (6.15) and Eq. (6.14) to a  $[3.4] - [4.6]$  vs.  $[4.6] - [12]$  colour-colour diagram. From this analysis we excluded any data point from the catalogue that did not have an SNR of 5 or better as well as applied the background elimination strategy outlined in Sect. 6.3. Fig. 8.6 shows the  $[3.4] - [4.6]$  vs.  $[4.6] - [12]$  colour-colour diagram, constructed after probable contaminants had been removed (cf. Sect. 6.3.1). The total sample before this removal were 10 128 sources. After removal of probable contaminants, 6669 sources remained. These were plotted in Fig. 8.6. Class I sources identified from these selection criteria are drawn in red in the figure, while Class II sources are drawn in green. The same colour-coding is used in Fig. 8.8, which shows the spatial distribution of the 661 cYSOs. Of these 207 are Class I candidates and 454 are Class II candidates.

The distribution of WISE-selected cYSOs follows the cloud structure as expected. Koenig et al. [2012] estimate the remaining contamination of the cYSO population selected with their criteria by galaxies to be  $\sim 10 \text{ deg}^{-2}$  which in our  $1.2^\circ$  field leads to an estimate of  $\sim 12$ . However, in a region projected onto the Galactic disk as the Carina Nebula Complex

is we expect a high level of contamination mainly from background and foreground stars. To estimate the total contamination as described in Sect. 6.4 we compared the number density of sources here to two circular areas of  $30'$  radius well outside the CN (i. e. regions that we expect to be relatively free of YSOs). One of them is centred around  $\alpha_{2000} = 10:51:52.5$ ,  $\delta_{2000} = -59:14:30$ , the other around  $\alpha_{2000} = 10:25:10.7$ ,  $\delta_{2000} = -58:52:00$ . They were chosen as having a similar proximity to the Galactic plane as Gum 31 ( $b = 0.15$  and  $b = -1.18$ ; Gum 31:  $b = -0.17$ ). Furthermore, we carefully selected fields that were as free of CO and H $\alpha$  emission as possible and appeared as empty as possible in the IRAS  $100\ \mu\text{m}$  images.

In those fields we find a mean cYSO density of  $97\ \text{deg}^{-2}$ ; with the cYSOs spread homogeneously. In the Gum 31 region we determine a cYSO density of  $550\ \text{deg}^{-2}$ . This leads us to expect a contamination of around 18% ( $\sim 120$  cYSOs) for the Gum 31 cYSO sample. For the IRAC data we were not able to conduct a similar comparison as we do not have photometry data for the full study area around Gum 31 and none for regions outside the central CN.

We therefore deem the WISE-selected sample to be more reliable and base our conclusion in the following sections predominantly on this sample, although we will occasionally describe a classification with IRAC. Those should, however, be regarded carefully.

#### 8.4.2 Identification of protostars from Herschel data

With the methods described in Sect. 8.2.2 and in more detail by Gaczkowski et al. [2013], a point-source catalogue for the *Herschel* data was obtained. Although we consider only ‘point-like’ *Herschel* sources in the following, it is important to keep in mind that the relatively large PSF corresponds to quite large physical scales at the 2.3 kpc distance of Gum 31. In the PACS  $70\ \mu\text{m}$  map, all objects with an angular [spatial] extent of up to  $\approx 5''$  [ $0.056\ \text{pc}$ ] are compact enough to appear ‘point-like’. For the SPIRE  $250\ \mu\text{m}$  map, this is true for sources of up to  $\approx 18''$  [ $0.20\ \text{pc}$ ]. This shows immediately that (pre-stellar) cloud cores, which have typical radii of  $\lesssim 0.1\ \text{pc}$ , cannot be (well) resolved in the *Herschel* maps and may appear as compact ‘point-like’ sources. This implies that YSOs in all their evolutionary stages can, in principle, appear as point-like sources in the *Herschel* maps. However, the possibility to detect an object in a specific stage depends strongly on its properties: As described by Gaczkowski et al. [2013], many pre-stellar cores ( $\gtrsim 1\text{--}2\ M_{\odot}$ ) and embedded protostars ( $\gtrsim 1\ M_{\odot}$ ) will be easily detectable, while most of the more evolved PMS stars with disks should remain undetected. In this last case the detection limit depends on the disk mass; as shown by Gaczkowski et al. a  $1\ M_{\odot}$  YSO is still detectable if it has a disk mass of  $\gtrsim 0.5\ M_{\odot}$ , this is reduced to  $\gtrsim 0.1\ M_{\odot}$  for a  $3\ M_{\odot}$  YSO and  $\gtrsim 0.01\ M_{\odot}$  for a  $6\ M_{\odot}$  YSO.

This means that while with IRAC we find mainly Class II YSOs and a number of Class I YSOs, with *Herschel* the emphasis is on Class 0 protostars, with some Class I stars. This also implies that the overlap between both is relatively small (cf. Sect. 8.5). Ragan et al. [2012] presented radiative transfer models of starless cores and protostellar cores and investigated the detectability of these classes of objects. Their models showed that the SEDs of starless (i. e. pre-stellar) cores typically peak around  $200\text{--}300\ \mu\text{m}$  and drop very steeply towards shorter wavelengths. Their model fluxes at  $70\ \mu\text{m}$  (scaled to the distance of the CNC) are several orders of magnitudes below our detection limits. Protostellar cores, on the other hand, have much stronger fluxes at PACS wavelengths. Guided by

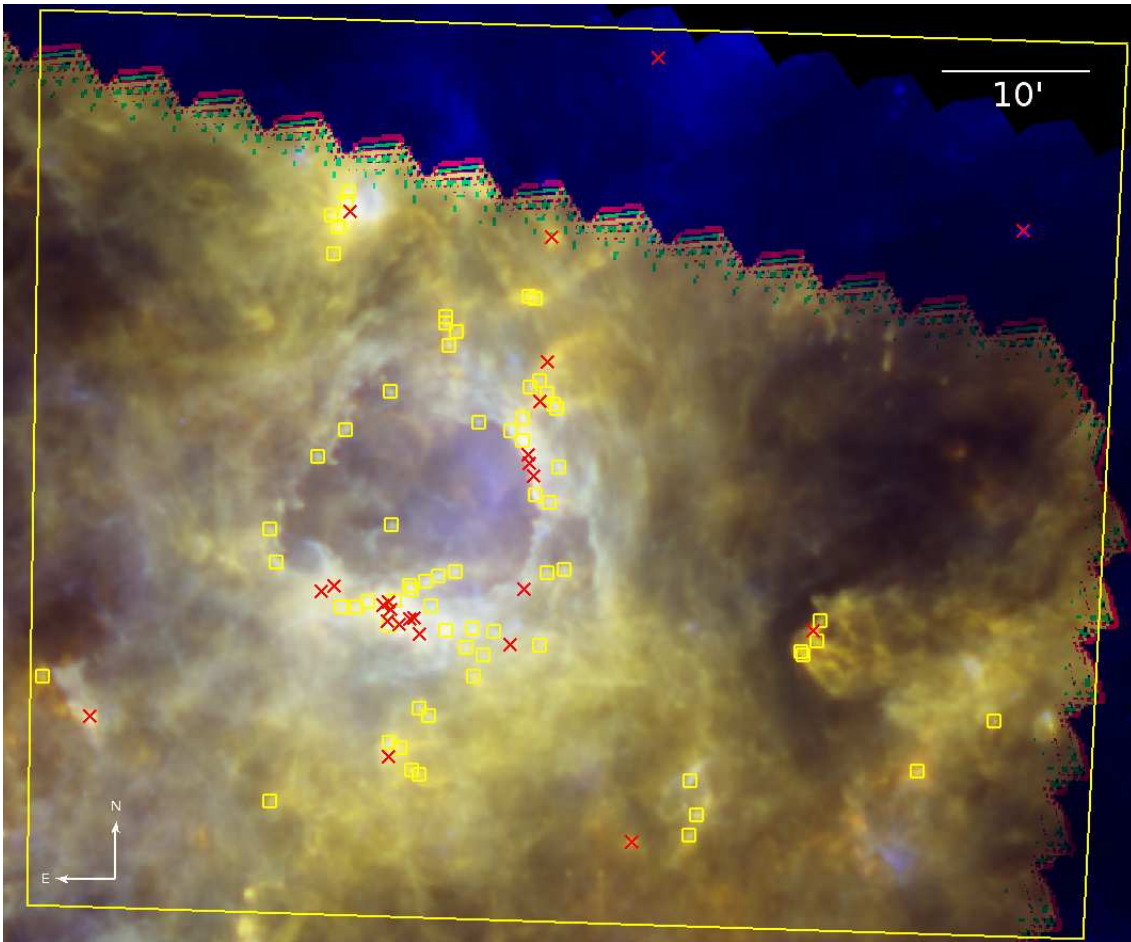


Figure 8.7: *Herschel* RGB image (red: 500  $\mu\text{m}$ , green: 250  $\mu\text{m}$ , blue: 70  $\mu\text{m}$ ) with positions of all *Herschel* point-like sources detected in at least two bands overlaid. Red crosses show the position of protostellar, yellow boxes those of prestellar cores. The yellow rectangle marks the borders of the region analysed. [Image first published: Ohlendorf et al. 2013a]

these results, we can take a detection at 70  $\mu\text{m}$  as an indication for the protostellar nature of the source, whereas *Herschel* sources without 70  $\mu\text{m}$  detection would then be pre-stellar cores. In Fig. 8.7 these two classes are indicated separately.

Gaczkowski et al. [2013] argue that in a sample of *Herschel* point-like objects in the CN it is very unlikely for contamination by evolved stars or extragalactic objects to occur. The same reasoning applies to Gum 31. The photometric data for those sources that fall within the Gum 31 area can be found in the publication by Gaczkowski et al. [2013].

### 8.4.3 Spatial distribution of the candidate young stellar objects

It is notable that both Class I and Class II sources are found predominantly within the interior of the Gum 31 bubble or along its rim. They tend to occur in clusters and in their distribution are often correlated with the Yonekura et al. [2005] molecular cloud

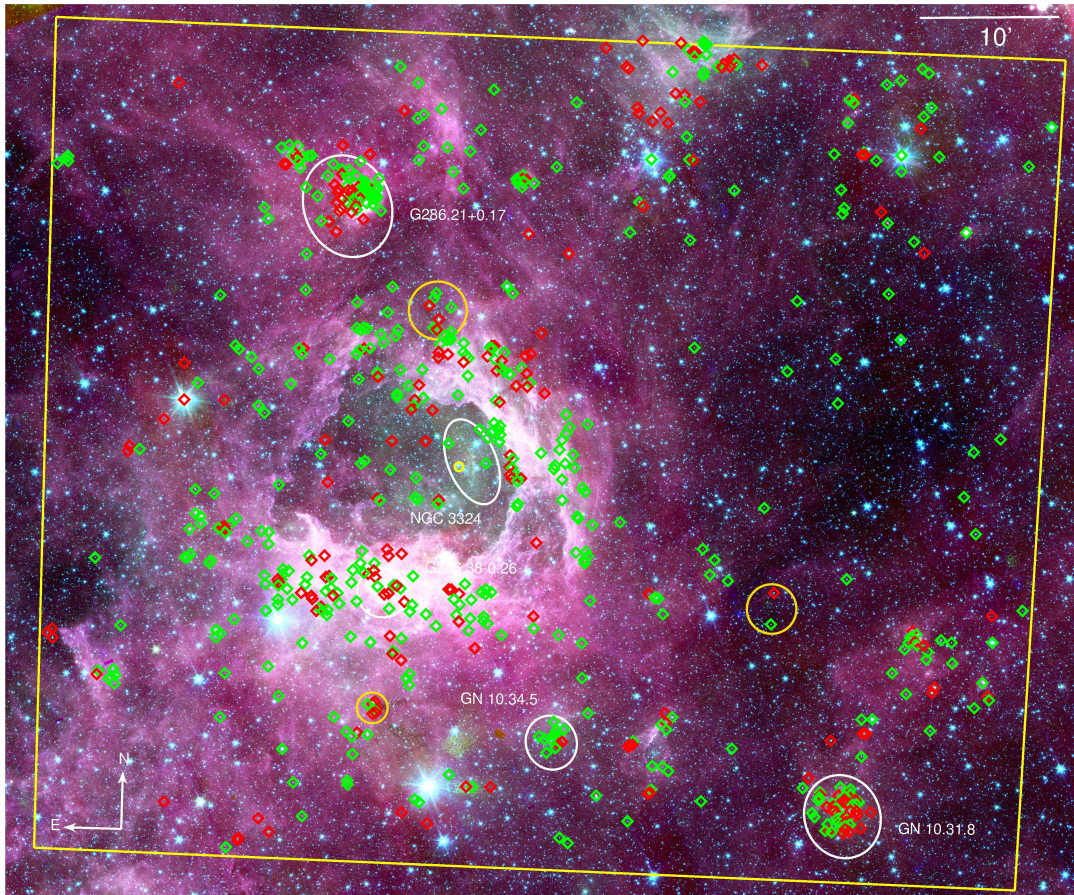


Figure 8.8: *Spitzer* IRAC RGB image (red:  $8.0\ \mu\text{m}$ , green:  $4.5\ \mu\text{m}$ , blue:  $3.6\ \mu\text{m}$ ) with positions of WISE-identified cYSOs overlaid. Class I sources are marked by red diamonds, Class II in green. The white ellipses represent the clusters discussed in Sect. 8.4.3, the orange circles mark the smaller clusters described in Sect. 8.4.3. The yellow rectangle marks the borders of the region analysed. [Image first published: Ohlendorf et al. 2013a]

clumps (see below). When in the following we refer to a cYSO with a number preceded by ‘[CNA2008]’ this source was classified as a cYSO by Cappa et al. [2008].

### NGC 3324

The cluster NGC 3324 appears prominent in the *Spitzer* images, containing  $\approx 200$  point-like sources. Within the cluster itself, we identify only a single cYSO with WISE, J103706.9–583710 at the western edge of the cluster (Class II). From the  $[3.6] - [4.5]$  vs.  $[5.8] - [8.0]$  diagram (IRAC) we identify half a dozen cYSOs coincident with the cluster NGC 3324 and distributed about  $40''$  towards the north-east of the cluster centre. The very small fraction of stars with detectable infrared excess ( $\approx 0.5\%$ ) supports previous age estimates of  $\gtrsim 3\text{ Ma}$ —the typical disk lifetime [e. g. Lada and Lada 1995]—for this cluster.

### cYSOs in the rim of the bubble

Numerous cYSOs are found lined up along the ionisation front of the Gum 31 bubble to the west of NGC 3324. A dozen cYSOs are found right at the edge of the ionisation front. Among them are J103653.9–583719, J103653.3–583754, and J103652.4–583809, three Class I candidates that are found along the ridge traced in IRAC and *Herschel* images at the very edge of the bubble, neighbouring NGC 3324. Two of them, J103653.9–583719 and J103652.4–583809, will be discussed in Sect. 8.6 as possible sources of Herbig-Haro jets.

Behind this ‘first row’ of Class I candidates, there is a ‘second row’ of five Class II candidates, all lined up about  $19''$  behind the ionisation front. Further northwards along the rim there are four more Class II candidates, one behind the front and three along it.

In Fig. 8.8 it is evident that a major part of the cYSOs is located along the bubble edges, similar to what is observed in comparable bubbles associated with H II regions [e.g. Dewangan et al. 2012]. Their distribution follows its circular shape and their number sharply goes down outside the cloud structure that is traced in the IRAC  $8.0\ \mu\text{m}$  band and thus appears magenta in the image. This is suggestive of triggered star-formation in a ‘collect and collapse’ scenario as described by Whitworth et al. [1994].

With analytical models, we can derive approximate bubble sizes for a stellar population equivalent to the one observed in Gum 31. To estimate the mechanical luminosities emitted by the three most massive stars in NGC 3324 we used values from Smith [2006a] (and the erratum [Smith 2006b]) for stars with the same spectral types (Luminosity class V) observed in the CN. Following analytical models for this scenario, a stellar wind bubble produced by three massive stars with spectral types O6.5, O6.5 and O9.5 could reach a radius of approximately 9–11 pc in 1.5–2.0 Ma assuming initial cloud densities in a range of  $500\text{--}1000\ \text{cm}^{-3}$ . The radius at which fragmentation occurred would then vary between 7 pc and 11 pc. The  $\sim 15'$  diameter of the Gum 31 H II region corresponds to 10 pc at a distance of 2.3 kpc, which agrees very well with the values derived from the model. The fact that we also find numerous embedded cYSOs in and near the rim of the bubble is consistent with star-formation according to the ‘collect and collapse’ model.

### cYSOs in pillars

In the southern and eastern part of the bubble edge we find a number of small pillars extending into the bubble interior. They can be seen in the optical and infrared in Fig. 8.2 and a closeup of the IR pillars is shown in Fig. 8.9. Within four of them we find cYSOs in their very tips, reminiscent of what is observed in the central CN (e.g. the South Pillars region). One of them, J103806.6–584002, coincides with a *Herschel* point-like source (cf. Sect. 8.5.1) and is therefore most probably a protostar. This suggests that radiative triggering is at work, very similar to the processes seen in the South Pillars [Smith et al. 2010b, Gaczkowski et al. 2013].

### G286.21+0.17

The cloud clump G286.21+0.17 ([DBS2003] 127, BYF73) is located about  $12'$  north of the rim of the Gum 31 bubble (cf. Fig. 8.8). The structure of this clump was recently studied in several molecular lines by Barnes et al. [2010]. They determined a diameter of  $\sim 0.9$  pc, a luminosity of  $\sim 2\text{--}3 \cdot 10^4 L_{\odot}$ , and estimated a clump mass of about  $20\,000 M_{\odot}$ . This estimated clump mass value is about forty times as large as the previous mass estimate based

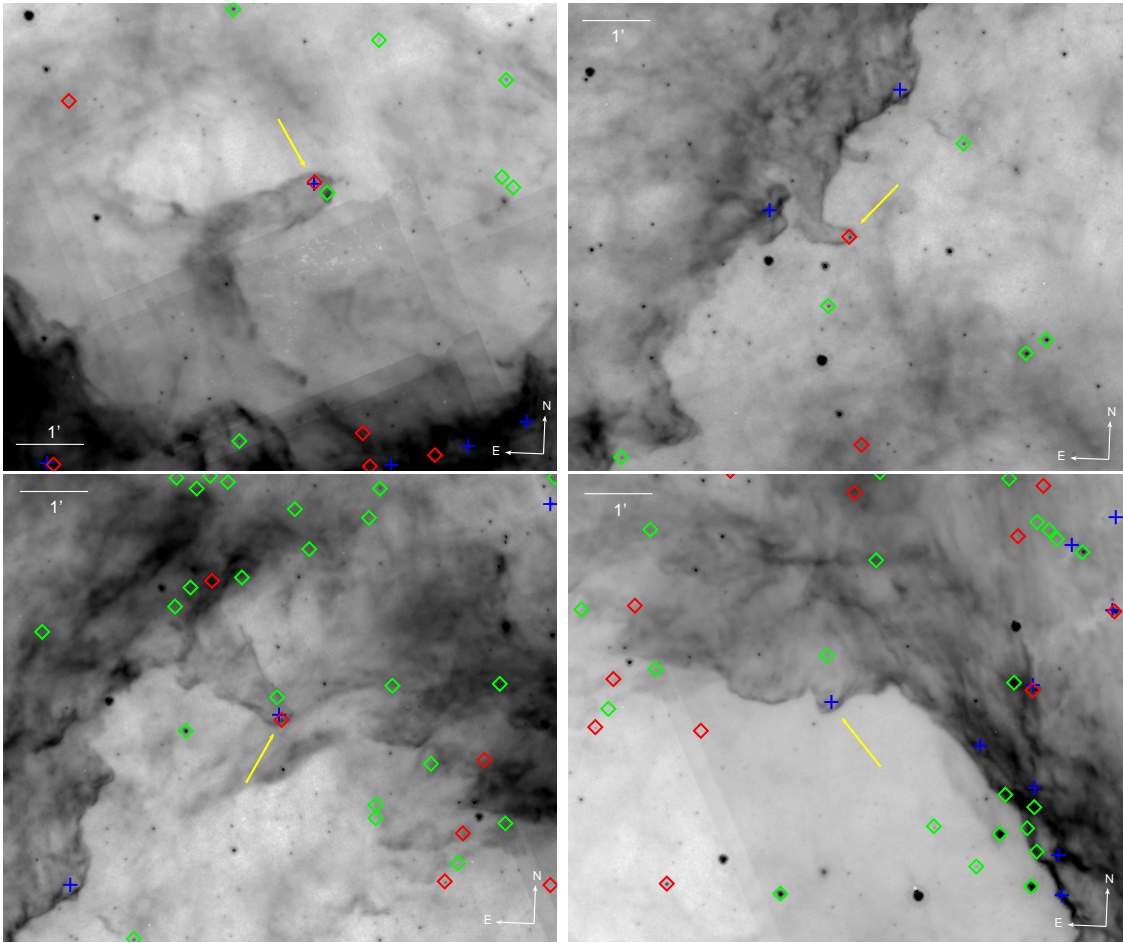


Figure 8.9: In a *Spitzer* IRAC 8.0  $\mu\text{m}$  image, the yellow arrows mark the positions of four remarkable cysos found in the very tips of pillars. Positions of WISE-identified cysos are overlaid as in Fig. 8.8: Class I sources are marked by red diamonds, Class II sources in green. Blue crosses mark *Herschel* point-like sources detected in at least two bands. [Image first published: Ohlendorf et al. 2013a]

on millimetre data by Faúndez et al. [2004]. The mass infall rate of  $\sim 3.4 \cdot 10^{-2} M_{\odot} \text{a}^{-1}$  derived by Barnes et al. [2010] would be the highest mass infall rate yet seen, if confirmed. These properties make this cloud a particularly interesting site of possible massive-star formation.

In our *Herschel* maps, this clump appears as a very bright and prominent compact feature. In Fig. 8.11, its morphology in the *Herschel* FIR bands (PACS 70  $\mu\text{m}$  and SPIRE 350  $\mu\text{m}$ ) can be compared to a NIR image from our VISTA data and a *Spitzer* MIR image. As already discussed by Barnes et al. [2010], a young stellar cluster, surrounded by diffuse nebulosity, is located immediately north-west of the clump. This cluster appears very prominent in Fig. 8.8 as well. We find it to contain  $\sim 45$  cysos. In the centre of the clump itself, the *Spitzer* images show two bright point sources with an angular separation of 7.6'' (Fig. 8.11). They can be identified with the 10  $\mu\text{m}$  point sources J103832.08–581908.9 and J103832.71–581914.8. These two MIR sources were detected as counterparts of the

MSX/RMS massive cYSO G286.2086+00.1694, for which Mottram et al. [2007] determined a bolometric luminosity of  $7750 L_{\odot}$ .

The VISTA *H*-band image shows very faint diffuse nebulosities at the location of these two MIR sources (see the close-up in Fig. 8.10). This is consistent with the idea that these two objects represent deeply embedded YSOs in the protostellar evolutionary phase. With WISE the two sources are not resolved but run into one that we classify as a Class I candidate.

The peak of the *Herschel* PACS  $70 \mu\text{m}$  emission is centred on the MIR source J103832.0–581908. A two-dimensional Gaussian fit to the  $70 \mu\text{m}$  emission yields a FWHM size of  $13.6'' \times 11.3''$ , which is clearly larger than the FWHM size of  $10'' \times 10''$  measured for several isolated point-like sources in the same map. With an angular distance of  $7.6''$ , the emission of the two MIR sources cannot be resolved in the *Herschel* maps, but the measured direction of the elongation towards J103832.71–581914.8 suggests that both contribute to the observed FIR emission.

Another cYSO is found in the south-east of the clump, at the projection of the line connecting J103832.08–581908.9 and J103832.71–581914.8. It probably corresponds to the IRAC-identified source at  $\alpha_{2000} = 10:38:33.6$ ,  $\delta_{2000} = -58:19:22$ . There is another cYSO, situated at the very edge of the clump, at  $\alpha_{2000} = 10:38:35.0$ ,  $\delta_{2000} = -58:18:44$ . These three are the only cYSOs identified in the clump itself with WISE, while in the immediately adjoining cluster of stars visible in the IRAC images a large number of cYSOs is found with WISE. There are  $\sim 45$  overall, with a slight majority of Class II sources over Class I sources. If there is any trend in their spatial distribution, Class I are found with slight emphasis to the south-east, while Class II sources tend to be located to the north-west.

Our colour-temperature map (Fig. 8.4a), constructed from the *Herschel*  $70 \mu\text{m}$  and  $160 \mu\text{m}$  maps, shows that the cloud temperatures range from  $\lesssim 20$  K at the edge of the clump to  $\sim 25$ – $30$  K in the clump centre, and up to  $33$  K in the nebulosity surrounding the stellar cluster north-west of the clump.

In our *Herschel* column-density map (Fig. 8.4b), the level  $N_{\text{H}} = 2 \cdot 10^{22} \text{ cm}^{-2}$  traces the shape of the clump. This agrees very well with the morphology as seen in the  $1.2 \text{ mm}$  map shown by Faúndez et al. [2004]. The peak value of the column density is found to be  $1.4 \cdot 10^{23} \text{ cm}^{-2}$  and corresponds to a visual extinction of  $A_{\text{V}} \approx 70$  mag. From our column density map we determined the mass of the clump by integrating over a  $200'' \times 200''$  ( $2.23 \text{ pc} \times 2.23 \text{ pc}$ ) box around the clump and subtracting the local background level. This yields a clump mass of  $2105 M_{\odot}$ . This value is nearly five times as large as the  $470 M_{\odot}$  derived by Faúndez et al. [2004], but a factor of ten smaller than the  $20000 M_{\odot}$  estimated by Barnes et al. [2010]. This suggests that this clump might not be as extreme as suspected.

Its FIR fluxes as derived from our *Herschel* data using elliptical apertures for photometry with the Graphical Astronomy and Image Analysis tool (GAIA) are  $1661 \text{ Jy}$ ,  $2261 \text{ Jy}$ ,  $1293 \text{ Jy}$ ,  $653 \text{ Jy}$  and  $297 \text{ Jy}$  for  $70 \mu\text{m}$ ,  $160 \mu\text{m}$ ,  $250 \mu\text{m}$ ,  $350 \mu\text{m}$  and  $500 \mu\text{m}$ , respectively, which results in an integrated FIR luminosity ( $70 \mu\text{m}$  to  $1.3 \text{ mm}$ ) of  $L_{\text{int}} \approx 9000 L_{\odot}$ .

This is clearly one of the most luminous clumps in the CNC. Its mass is rather high, but probably not as high as previously suggested. It may form stars with  $\lesssim 10 M_{\odot}$ , but is probably not massive enough for the formation of high-mass stars with  $M_{*} \gtrsim 20 M_{\odot}$ .

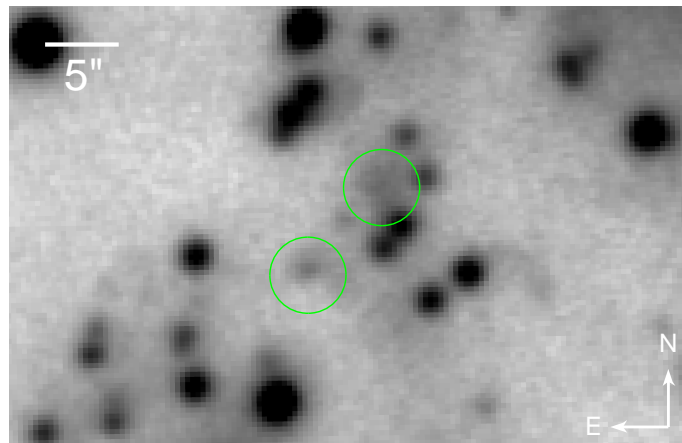


Figure 8.10: Close-up of the VISTA *H*-band image (Fig. 8.11) around the two bright IRAC sources (green circles) within the cluster G286.21+0.17. [Image first published: Ohlendorf et al. 2013a]

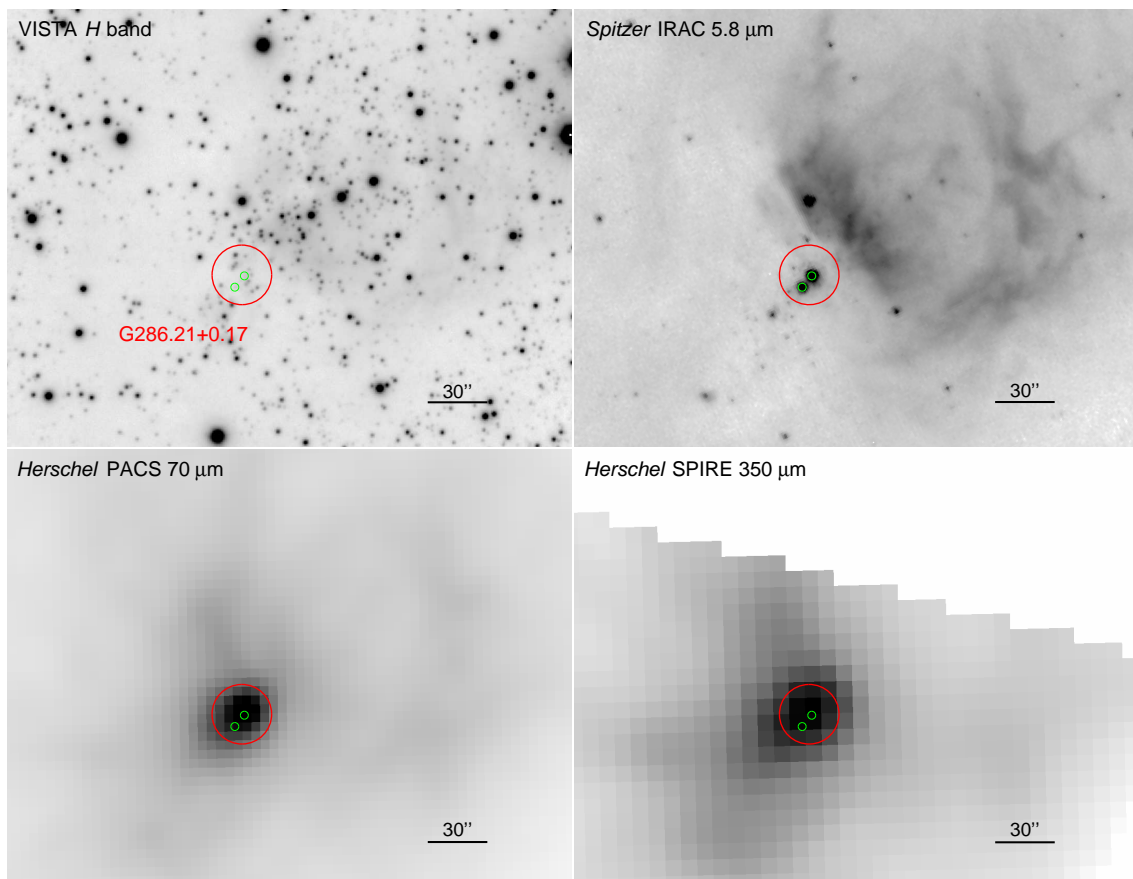


Figure 8.11: Cluster G286.21+0.17 (red circle; cf. Sect. 8.4.3) and its immediate surroundings from NIR to FIR. The two green circles mark the two bright *Spitzer*-resolved sources within it. (A close-up of the VISTA *H*-band image is shown in Fig. 8.10.) [Image first published: Ohlendorf et al. 2013a]

**G286.38–0.26**

The *Spitzer* IRAC images show a prominent dense cluster of several dozen stars at the southern edge of the Gum 31 bubble, which is surrounded by bright diffuse nebulous emission (Fig. 8.12). This cluster is listed as [DBS2003] 128 by Dutra et al. [2003]. It is spatially coincident with the extended ( $r = 2$  pc)  $C^{18}O$  clump<sup>6</sup> No. 6 [Yonekura et al. 2005].

The nebulosity around the stellar cluster displays a remarkable arc-like shape at the eastern edge. Projecting it into a full circle, it would have around  $42''$  diameter in IRAC images and  $62''$  in *Herschel* images. The centre of this circle would be around  $\alpha_{2000} = 10:38:03$ ,  $\delta_{2000} = -58:46:19$ . The star J10380461–5846233, cYSO [CNA2008] 21, is found close ( $\sim 11''$ ) to this central position of the arc. In the *Spitzer* bands, this cYSO shows strongly increasing brightness with wavelength. In the MIPS  $24\ \mu\text{m}$  image, it is the brightest point source in the cluster. It was detected as a MIR source by MSX and is listed as G286.3773–00.2563 in the MSX6C catalogue. With WISE data we classify it as a Class II cYSO. The star is not detected in any of our *Herschel* FIR images. Using USNO-B optical catalogue data, 2MASS, IRAC, MIPS, and WISE photometry and *Herschel* upper limits we employed the online SED fitter by Robitaille et al. [2007] to construct an SED and thus estimate the (proto-) stellar parameters. The stellar mass is estimated to be  $\approx 5.8 M_{\odot}$  for the best-fit model, the luminosity  $\approx 238 L_{\odot}$ . Within the arc three further WISE Class I cYSOs are seen, J103805.8–584542, J103758.4–584648, and J103800.7–584654.

The optically brightest star in the cluster is HD 303094, for which a spectral type A2 is given by Nesterov et al. [1995]. It is located about  $17''$  south of J10380461–5846233 and the centre of the arc. According to the Pickles and Depagne [2010] survey of all-sky spectrally matched Tycho-2 stars it may be a foreground star (distance: 886 pc).

Strong far-IR emission from the region of this cluster was detected with IRAS (point source IRAS 10361-5830). Our *Herschel* maps resolved this FIR emission into ten point-like sources in the area of the clump. The only *Herschel* source with an MIR counterpart is J103801.4–584641. The IRAC image at this point is dominated by strong nebular emission. There is extended emission in a confined region a few arcseconds east of the *Herschel*-identified point-like source, but since it is not well-resolved and the identification with the *Herschel*-identified source is not unambiguous, we do not include it in the sample studied in Sect. 8.5. The two *Herschel*-identified point-like sources north-east of the arc-like nebula that are also detected as bright sources in the MIPS maps are J103810.2–584527 and J103807.2–584511, both have no clear NIR counterparts. A similar case is J103754.0–584614, which has a very faint nebulous NIR counterpart in the VISTA image. All three are also detected as point-like sources in our IRAC images. They are included in Table 8.2, but only for J103807.2–584511 we obtained the model parameters listed in Table 8.3 as for the others the quality of the SED fit was not sufficient. Additionally, all three sources described are classified as Class I sources from WISE data.

In the south-western part of this extended  $C^{18}O$  clump, Yonekura et al. [2005] detected a compact ( $r = 0.27$  pc)  $H^{13}CO^+$  clump (their clump No. 2); with a central density of  $n(H_2) = 6.8 \cdot 10^4\ \text{cm}^{-3}$  this is the densest of all the clumps they detected in their survey of the CNC. The *Herschel*-identified point-like source J103750.8–584718 coincides with this

---

<sup>6</sup>We note that Yonekura et al. [2005] denoted these structures as ‘cores’; however, according to the definition that *cores* are very compact clouds (with typical sizes of  $\sim 0.1$  pc or less), out of which individual stellar systems form, these clouds are better characterised as *clumps* (i. e. relatively large dense clouds linked to the formation of small stellar clusters).

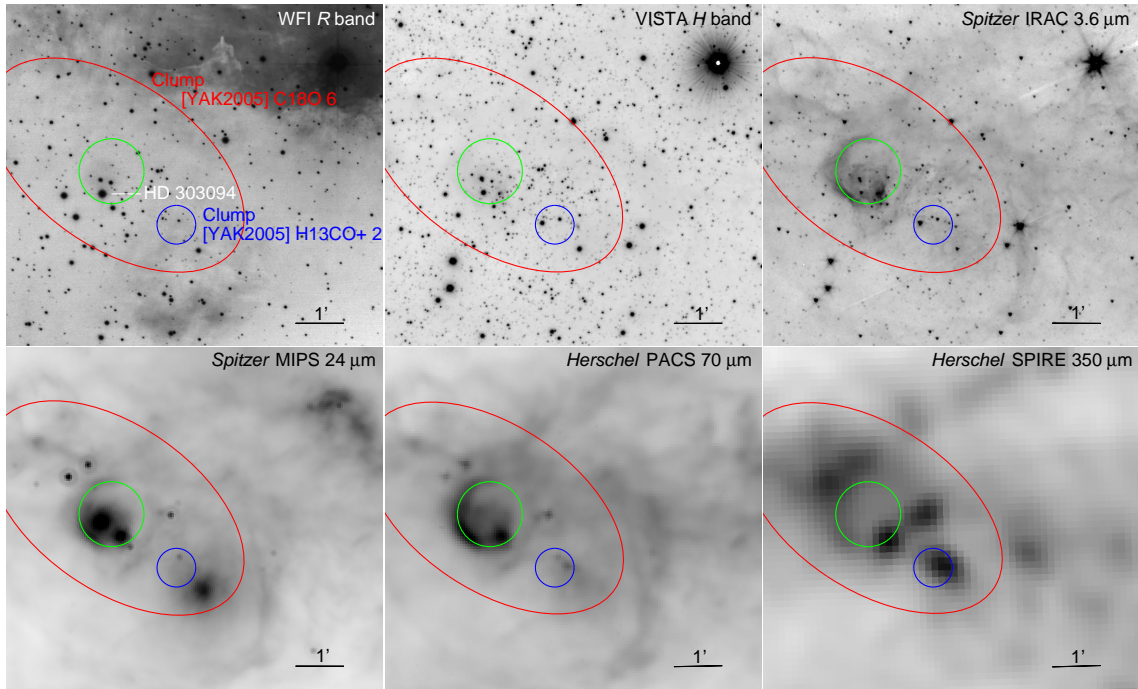


Figure 8.12: Cluster G286.38–0.26 from NIR to FIR. The large red ellipse marks the approximate outline of the  $C^{18}O$  clump No. 6 ([YAK2005] C18O 6; Yonekura et al. 2005). The blue circle marks  $H^{13}CO^+$  clump No. 2 ([YAK2005] H13CO+ 2), the green circle indicates the shape of the arc-like nebulosity visible in the *Spitzer* IRAC images. [Image first published: Ohlendorf et al. 2013a]

clump. With IRAC, there are several small point-like sources seen to be coincident with it and an identification is therefore impossible. An IRAC-detected source slightly to the south-west of it, J103749.3–584722, is identified as a Class I WISE cYSO.

This area also contains the A0 supergiant HD 92207. This star has a strong NIR excess, was detected as a  $12\ \mu\text{m}$  source with IRAS (IRAS 10355-5828), and is seen as a point-like source surrounded by nebulosity in the MIPS  $24\ \mu\text{m}$  image. Neither the star nor the surrounding nebulosity can be seen in the *Herschel* images.

### Other structure

Towards the south-west of the Gum 31 shell, two nebulae are found, GN 10.34.5 and GN 10.31.8 (both are marked with white ellipses in Fig. 8.8). Both are very clearly delineated by cYSOs and coincide with two of the most conspicuous clusters in our field of view. GN 10.34.5 is visible in the *Spitzer* RGB image (especially the  $4.5\ \mu\text{m}$  band) and seen in projection with a dozen cYSOs. GN 10.31.8, on the other hand, is both larger in angular extent and coincident with four times the number of cYSOs. It, too, is very conspicuous in the  $4.5\ \mu\text{m}$  band.

There also is a smaller cluster of about two dozen IRAC point-like sources centred at  $\alpha_{2000} = 10:38:03$ ,  $\delta_{2000} = -58:55:09$  within the Gum 31 shell. Immediately to its west there lies molecular cloud No. 7 of Yonekura et al. [2005]. It is accompanied by emission visible in the *Herschel* bands and a peculiarly green point-like feature in the IRAC RGB

image, that is, strong emission in the IRAC 4.5  $\mu\text{m}$  band.

In the distribution of IRAC-identified cYSOs there is another notable cluster consisting of 12 candidates to the west of the H II region around  $\alpha_{2000} = 10:34:27$ ,  $\delta_{2000} = -58:46:45$ . This region is devoid of MIR emission but is coincident with C<sup>18</sup>O clump No. 1 of Yonekura et al. [2005] and FIR emission as traced by *Herschel*. The cYSOs are aligned along the western ridge of the FIR cloud as seen in the *Herschel* image and even follow the shape of its filaments, broadly in the shape of an arrowhead pointing eastwards. The northern part is better aligned with the filament shape while the southern part is more randomly distributed around the filament itself. The border is also traced by the Yonekura et al. [2005] <sup>13</sup>CO intensity contours. With the WISE classification, however, there is nothing remarkable about that region. We find Class I candidate J103423.7–584531 to the north and Class II candidate J103424.6–584749 to the south, but no appearance of clustering.

North of the Gum 31 bubble, around  $\alpha_{2000} = 10:37:36$ ,  $\delta_{2000} = -58:26:36$ , there is a cluster of stars clearly discernible in the IRAC image. It lies about 2' to the south-west of Yonekura et al. [2005] C<sup>18</sup>O clump No. 4. Around three dozen stars are seen within this group in projection and it is also associated with a number of *Herschel*-identified point-like sources. Two of them, J103739.6–582756 and J103741.7–582629, are part of the sample analysed in Sect. 8.5. Few stars within or around this cluster are identified as cYSOs with WISE. J103736.3–582655 and J103741.9–582556 are the brightest stars in the IRAC images of the cluster and both identified as Class I candidates with WISE. There is one more Class I candidate and five Class II candidates distributed fairly evenly over the cluster.

There are several more minor clusters of  $\sim 5$  cYSOs. Notably, these are always coincident with local maxima in the Yonekura et al. [2005] C<sup>18</sup>O maps.

Table 8.2: Source fluxes as obtained in the *Spitzer* and *Herschel* bands, complemented with photometry from the WISE All-Sky Data Release and as obtained from the 2MASS All-Sky Catalog of Point Sources.  
Part One. 2MASS *J*, *H* and *K<sub>s</sub>* band, WISE 3.4  $\mu\text{m}$ , and IRAC 3.6  $\mu\text{m}$  and 4.5  $\mu\text{m}$ .

Source	F <sub>J</sub> [mJy]	F <sub>H</sub> [mJy]	F <sub>K<sub>s</sub></sub> [mJy]	F <sub>3.4 <math>\mu\text{m}</math></sub> [mJy]	F <sub>3.6 <math>\mu\text{m}</math></sub> [mJy]	F <sub>4.5 <math>\mu\text{m}</math></sub> [mJy]
J103427.3–584611	–	–	–	0.939 $\pm$ 0.015	0.902 $\pm$ 0.033	2.395 $\pm$ 0.033
J103557.6–590046	8.624 $\pm$ 0.069	13.35 $\pm$ 0.11	12.380 $\pm$ 0.082	16.095 $\pm$ 0.061	8.902 $\pm$ 0.037	–
J103643.2–583158	–	–	0.796 $\pm$ 0.025	–	1.585 $\pm$ 0.026	1.226 $\pm$ 0.030
J103645.9–584258	2.245 $\pm$ 0.019	2.112 $\pm$ 0.018	1.352 $\pm$ 0.026	–	–	0.336 $\pm$ 0.034
J103652.4–583129	–	–	0.843 $\pm$ 0.030	4.629 $\pm$ 0.046	14.790 $\pm$ 0.030	67.070 $\pm$ 0.030
J103700.9–583237	–	–	–	8.596 $\pm$ 0.067	5.908 $\pm$ 0.030	17.420 $\pm$ 0.026
J103703.6–584751	0.711 $\pm$ 0.020	2.610 $\pm$ 0.036	5.281 $\pm$ 0.036	5.753 $\pm$ 0.077	20.540 $\pm$ 0.029	28.310 $\pm$ 0.031
J103726.7–584809	–	–	–	–	–	0.359 $\pm$ 0.024
J103737.3–584700	–	0.580 $\pm$ 0.021	0.873 $\pm$ 0.022	–	1.925 $\pm$ 0.026	6.835 $\pm$ 0.029
J103739.6–582756	–	–	–	–	–	3.464 $\pm$ 0.026
J103741.7–582629	–	–	–	–	–	0.659 $\pm$ 0.030
J103754.0–584614	–	–	0.876 $\pm$ 0.031	5.03 $\pm$ 0.15	9.175 $\pm$ 0.029	44.960 $\pm$ 0.030
J103804.9–585533	–	–	–	30.11 $\pm$ 0.17	50.610 $\pm$ 0.024	158.300 $\pm$ 0.033
J103806.6–584002	–	1.119 $\pm$ 0.033	4.066 $\pm$ 0.039	8.316 $\pm$ 0.047	9.277 $\pm$ 0.024	13.320 $\pm$ 0.035
J103807.2–584512	–	–	8.309 $\pm$ 0.065	92.87 $\pm$ 0.31	82.700 $\pm$ 0.025	129.100 $\pm$ 0.032
J103810.2–584527	–	–	–	7.343 $\pm$ 0.073	12.330 $\pm$ 0.024	50.940 $\pm$ 0.029
J103842.1–584437	–	2.376 $\pm$ 0.026	12.26 $\pm$ 0.074	51.46 $\pm$ 0.19	–	68.850 $\pm$ 0.030

**Notes.** The given uncertainties are the individual photometric measurement uncertainties only, as derived (for IRAC and MIPS) or as obtained from the catalogue (for 2MASS and WISE). For *Herschel* we did not obtain an uncertainty from photometry, but use an estimated total uncertainty of 20%.

Table 8.2: Part Two. WISE 4.6  $\mu\text{m}$ , IRAC 5.8  $\mu\text{m}$  and 8.0  $\mu\text{m}$ , WISE 12  $\mu\text{m}$  and 22  $\mu\text{m}$ , and MIPS 24  $\mu\text{m}$ .

Source	F <sub>4.6 <math>\mu\text{m}</math></sub> [mJy]	F <sub>5.8 <math>\mu\text{m}</math></sub> [mJy]	F <sub>8.0 <math>\mu\text{m}</math></sub> [mJy]	F <sub>12 <math>\mu\text{m}</math></sub> [mJy]	F <sub>22 <math>\mu\text{m}</math></sub> [mJy]	F <sub>24 <math>\mu\text{m}</math></sub> [mJy]
J103427.3–584611	5.173 $\pm$ 0.023	2.84 $\pm$ 0.13	2.21 $\pm$ 0.11	–	188.04 $\pm$ 0.42	–
J103557.6–590046	15.002 $\pm$ 0.051	–	70.36 $\pm$ 0.13	177.29 $\pm$ 0.27	344.38 $\pm$ 0.46	–
J103643.2–583158	–	–	–	–	–	–
J103645.9–584258	–	–	–	–	–	–
J103652.4–583129	64.47 $\pm$ 0.19	162.60 $\pm$ 0.12	197.00 $\pm$ 0.11	77.32 $\pm$ 0.39	623.2 $\pm$ 1.9	755.35 $\pm$ 0.14
J103700.9–583237	26.02 $\pm$ 0.10	–	–	486.49 $\pm$ 0.48	1171.2 $\pm$ 1.3 <sup>a</sup>	395.42 $\pm$ 0.14
J103703.6–584751	10.379 $\pm$ 0.070	35.55 $\pm$ 0.15	25.51 $\pm$ 0.13	–	257.42 $\pm$ 0.61	181.70 $\pm$ 0.13
J103726.7–584809	–	–	–	–	–	–
J103737.3–584700	–	17.14 $\pm$ 0.14	27.08 $\pm$ 0.11	–	631.3 $\pm$ 2.6	149.17 $\pm$ 0.14
J103739.6–582756	4.411 $\pm$ 0.026	7.78 $\pm$ 0.13	5.47 $\pm$ 0.13	–	164.83 $\pm$ 0.38	245.81 $\pm$ 0.14
J103741.7–582629	–	–	–	–	–	–
J103754.0–584614	67.63 $\pm$ 0.24	113.80 $\pm$ 0.13	135.80 $\pm$ 0.13	134.2 $\pm$ 1.4	1146.7 $\pm$ 2.4	858.43 $\pm$ 0.14
J103804.9–585533	211.13 $\pm$ 0.52	309.70 $\pm$ 0.14	364.000 $\pm$ 0.099	81.48 $\pm$ 0.80	2197.1 $\pm$ 1.2	–
J103806.6–584002	12.363 $\pm$ 0.059	17.23 $\pm$ 0.12	18.75 $\pm$ 0.14	60.29 $\pm$ 0.34	158.6 $\pm$ 2.2	–
J103807.2–584512	186.10 $\pm$ 0.46	286.30 $\pm$ 0.15	526.00 $\pm$ 0.14	664.2 $\pm$ 1.1	2409.2 $\pm$ 1.9	1436.24 $\pm$ 0.14
J103810.2–584527	50.23 $\pm$ 0.16	151.40 $\pm$ 0.13	245.00 $\pm$ 0.15	276.9 $\pm$ 1.1	843.8 $\pm$ 1.9	1814.13 $\pm$ 0.14
J103842.1–584437	112.14 $\pm$ 0.29	111.60 $\pm$ 0.11	146.40 $\pm$ 0.14	269.07 $\pm$ 0.88	714.2 $\pm$ 1.4	505.00 $\pm$ 0.13

**Notes.** The given uncertainties are the individual photometric measurement uncertainties only, as derived (for IRAC and MIPS) or as obtained from the catalogue (for 2MASS and WISE). For Herschel we did not obtain an uncertainty from photometry, but use an estimated total uncertainty of 20%.

<sup>(a)</sup> The extremely high 22  $\mu\text{m}$  flux compared to the 24  $\mu\text{m}$  flux is probably due to the source’s close proximity to a much brighter point source the contribution of which might not fully have been removed in the WISE All-Sky Data Release.

Table 8.2: Part Three. PACS 70  $\mu\text{m}$  and 160  $\mu\text{m}$ , and SPIRE 250  $\mu\text{m}$ , 350  $\mu\text{m}$  and 500  $\mu\text{m}$ .

Source	F <sub>70 <math>\mu\text{m}</math></sub> [Jy]	F <sub>160 <math>\mu\text{m}</math></sub> [Jy]	F <sub>250 <math>\mu\text{m}</math></sub> [Jy]	F <sub>350 <math>\mu\text{m}</math></sub> [Jy]	F <sub>500 <math>\mu\text{m}</math></sub> [Jy]
J103427.3–584611	15.8	11.0	10.7	12.2	4.47
J103557.6–590046	4.03	7.63	6.09	–	–
J103643.2–583158	–	22.6	14.4	21.2	–
J103645.9–584258	–	–	9.50	8.54	2.69
J103652.4–583129	21.3	13.9	11.2	–	11.2
J103700.9–583237	–	19.1	19.9	11.2	6.96
J103703.6–584751	1.32	6.72	10.8	6.32	2.89
J103726.7–584809	–	12.2	11.6	9.68	7.10
J103737.3–584700	–	31.4	28.1	29.8	18.4
J103739.6–582756	–	7.68	14.1	12.0	5.68
J103741.7–582629	–	11.1	11.4	9.05	6.68
J103754.0–584614	9.03	35.8	79.6	40.7	32.4
J103804.9–585533	5.91	19.8	11.8	9.01	6.23
J103806.6–584002	–	10.6	13.1	5.70	2.09
J103807.2–584512	15.2	35.1	26.8	–	–
J103810.2–584527	6.32	23.6	43.0	46.2	54.2
J103842.1–584437	24.1	14.8	15.4	10.2	5.63

**Notes.** The given uncertainties are the individual photometric measurement uncertainties only, as derived (for IRAC and MIPS) or as obtained from the catalogue (for 2MASS and WISE). For Herschel we did not obtain an uncertainty from photometry, but use an estimated total uncertainty of 20%.

## 8.5 SED modelling for sources with both Herschel and Spitzer counterparts

Using our *Herschel* and *Spitzer* catalogues, we were able to identify those sources that are detected as point-like sources in both wavelength ranges. For *Herschel* we applied the restriction that the sources had to be detected in at least three of the five bands, bringing the total number down from 91 sources detected in at least two bands to 59. This results in 17 sources overall that can be identified in at least three *Herschel* bands and at least one of the IRAC bands. We then compared these identifications to the MIPS image and performed photometry as described in Sect. 8.2.1 for those nine sources where we could identify a MIPS counterpart.

To extend the wavelength range of our observations, we additionally matched the point sources analysed here with sources from the 2MASS [Skrutskie et al. 2006] All-Sky Catalog of Point Sources [Cutri et al. 2003]. This was performed applying the same strategy as for the inter-band matching within the IRAC sources (Sect. 5.4.2), using only sources with quality flags A to D. We then repeated this process with the WISE catalogue, where we selected only those sources that had a SNR larger than 5. A detailed overview of all photometric data assembled is given in Table 8.2. WISE 22  $\mu\text{m}$  and MIPS 24  $\mu\text{m}$  fluxes show some incongruity, however, there is no underlying pattern as to what in the environs

## 8.5 SED modelling for sources with both *Herschel* and *Spitzer* counterparts

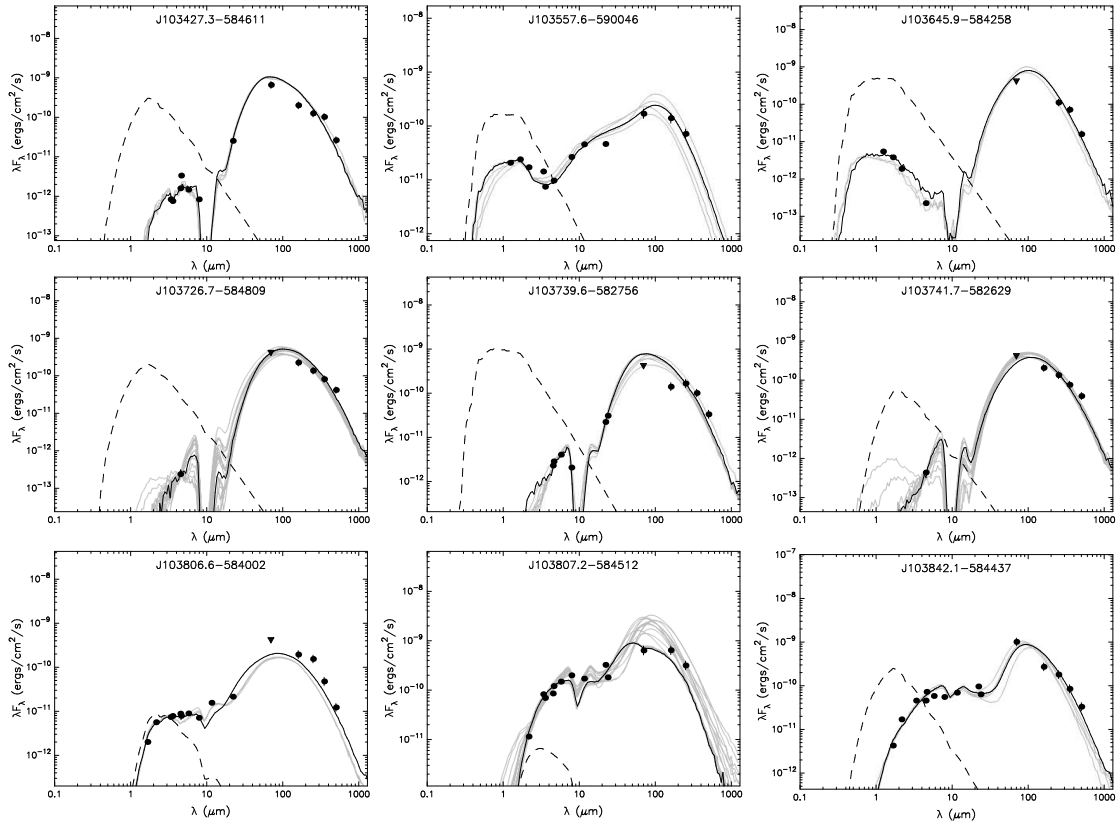


Figure 8.13: Spectral energy distributions of those objects for which we could determine fluxes with at least three *Herschel* and one *Spitzer* IRAC band. Filled circles mark the input fluxes. The black line shows the best fit, and the grey lines show subsequent good fits. The dashed line represents the stellar photosphere corresponding to the central source of the best fitting model, as it would appear in the absence of circumstellar dust (but including interstellar extinction). [Image first published by Ohlendorf et al. 2013a]

of the source may have influenced the photometry. This does not, however, influence the findings from the SED fits. In the two cases where the  $22\ \mu\text{m}$  flux appears unduly high compared to the  $24\ \mu\text{m}$  flux and an SED fit is performed, leaving out one or the other from the fit has little or no influence on the best-fit model.

### 8.5.1 Modelling of the SEDs

For SED-fitting we used the online tool of Robitaille et al. [2007].<sup>7</sup> This tool compares the input observational data with 200 000 SED models for YSOs that were precomputed using a 2D radiative transfer code by Whitney et al. [2003]. These models have a wide parameter space for the properties of the central object and its environment.

For the fits, the distance to all objects was assumed to be 2.3 kpc (cf. Sect. 8.3), and the interstellar extinction range was restricted to  $A_V = 0 \dots 40$  mag. We assumed an

<sup>7</sup><http://caravan.astro.wisc.edu/protostars/sedfitter.php>

uncertainty of 20% for all *Herschel* fluxes. For 2MASS, *Spitzer* and WISE fluxes in addition to the individual photometric measurement uncertainty as given in Table 8.2 we assumed a further systematic uncertainty of 10% due e. g. to the reliability of flux calibration. For IRAC, photometry varies by up to 10% due to the position of the point-like source within the detector array and though appropriate corrections were applied in the process, this is an additional source of uncertainty.

In addition to the best-fit model, we show the range of possible parameters that can be derived from models within the range of  $\chi^2/N - \chi_{\text{best}}^2/N < 2$  (with  $N$  representing the number of data points). These models are shown as grey lines in the plots in Fig. 8.13. The resulting model parameters are listed in Table 8.3. It gives the best-fit value together with the range constrained by the above  $\chi^2$  criterion. The resulting SEDs are shown in Fig. 8.13. We only use fits where  $\chi^2/N$  for the best-fit model is smaller than or equal to 10.0.

### 8.5.2 Results of SED modelling

As explained in Sect. 7.4.1 we restrict our analysis to a few selected parameters that can be determined relatively well from the fits. These are the total luminosity, the stellar mass, and the mass of the circumstellar disk and envelope.

The best-fit masses as listed in Table 8.3 are between  $1.7 M_{\odot}$  and  $6.6 M_{\odot}$  and even the extremes of the ranges do not exceed  $1.2 M_{\odot}$  to  $7.3 M_{\odot}$ . The majority of luminosities are to be found in a range of  $\sim 100\text{--}300 L_{\odot}$ , with two notable exceptions well below that at  $38 L_{\odot}$  and  $42 L_{\odot}$ , respectively, and one exceptionally luminous source at  $890 L_{\odot}$  best-fit value, corresponding with the highest best-fit stellar mass in our sample. Whereas four of the ten sources sampled here exhibit best-fit envelope masses of  $190 M_{\odot}$  or higher, three are at  $\leq 100 M_{\odot}$  and two lower than  $50 M_{\odot}$ . The disk masses span a range of about one order of magnitude between  $\sim 0.01 M_{\odot}$  and  $\sim 0.1 M_{\odot}$ . The highest-mass star in the sample is the notable exception with a disk mass of  $\sim 0.001 M_{\odot}$ .

In a large-scale view it is immediately noticeable that all but two of the sources for which *Herschel* counterparts to *Spitzer* point-like sources are detected are to be found within the Gum 31 bubble. Although the field of our study stretches further out especially to the west, only two sources are found outside the bubble. These are J103557.6–590046 and J103427.3–584611.

J103806.6–584002 is remarkable in that contrary to the vast majority of objects it is not located in the rim of the bubble but within the bubble itself, being the only specimen in our sample. It is placed in the very head of a pillar-like filament that extends from the southern rim of the bubble into it (cf. Fig. 8.9). With the methods employed in Sect. 8.4 we classify it as a WISE Class I candidate and an IRAC cYSO. In the *Herschel* images the filament is rather faint, but J103806.6–584002 itself is clearly visible as a point-like source.

Table 8.3: Model parameters for the sources in Gum 31 as obtained from the Robitaille et al. [2007] models.

Source	Stellar mass [ $M_{\odot}$ ]		Disk mass [ $M_{\odot}$ ]		Envelope mass [ $M_{\odot}$ ]		Total luminosity [ $L_{\odot}$ ]		Best-fit model	$\frac{\chi^2}{N}$
J103427.3–584611	5.8	[5.8 – 7.3]	$1.02 \cdot 10^{-1}$	$[4.30 \cdot 10^{-3} - 1.02 \cdot 10^{-1}]$	110	[110 – 170]	320	[320 – 400]	3003596	6.9
J103557.6–590046	1.7	[1.2 – 2.0]	$3.91 \cdot 10^{-2}$	$[1.76 \cdot 10^{-3} - 3.91 \cdot 10^{-2}]$	27	[4.2 – 60]	42	[27 – 68]	3015149	5.5
J103645.9–584258	4.2	[3.9 – 5.2]	$9.61 \cdot 10^{-2}$	$[1.09 \cdot 10^{-3} - 9.61 \cdot 10^{-2}]$	46	[18 – 46]	160	[140 – 190]	3006782	8.2
J103726.7–584809	6.0	[2.6 – 6.0]	$2.64 \cdot 10^{-2}$	$[1.05 \cdot 10^{-3} - 1.53 \cdot 10^{-1}]$	310	[160 – 310]	190	[94 – 190]	3008699	2.6
J103739.6–582756	5.8	[3.9 – 6.9]	$2.92 \cdot 10^{-2}$	$[2.21 \cdot 10^{-3} - 2.16 \cdot 10^{-1}]$	190	[140 – 410]	240	[160 – 360]	3009009	4.8
J103741.7–582629	3.4	[2.6 – 6.0]	$9.53 \cdot 10^{-2}$	$[1.62 \cdot 10^{-3} - 1.53 \cdot 10^{-1}]$	250	[160 – 310]	94	[94 – 190]	3005296	2.8
J103806.6–584002	1.7	[1.7 – 2.6]	$4.57 \cdot 10^{-2}$	$[1.34 \cdot 10^{-2} - 4.57 \cdot 10^{-2}]$	120	[52 – 120]	38	[38 – 58]	3016199	8.8
J103807.2–584512	6.6	[1.7 – 7.3]	$6.77 \cdot 10^{-4}$	$[6.77 \cdot 10^{-4} - 5.06 \cdot 10^{-1}]$	130	[5.3 – 310]	890	[220 – 890]	3010777	7.8
J103842.1–584437	3.5	[1.7 – 3.9]	$1.03 \cdot 10^{-2}$	$[6.45 \cdot 10^{-3} - 1.97 \cdot 10^{-1}]$	220	[13 – 220]	170	[130 – 190]	3011717	6.6

**Notes.** For every model parameter the best-fit-value is given in the respective first column, followed by a range defined by the minimum and maximum value obtained from models constrained by a  $\chi^2$  criterion. The second-to-last and last columns give the identifier of the best-fit model and its reduced  $\chi^2$  ( $\chi^2/N$ , with  $N$  representing the number of data points).

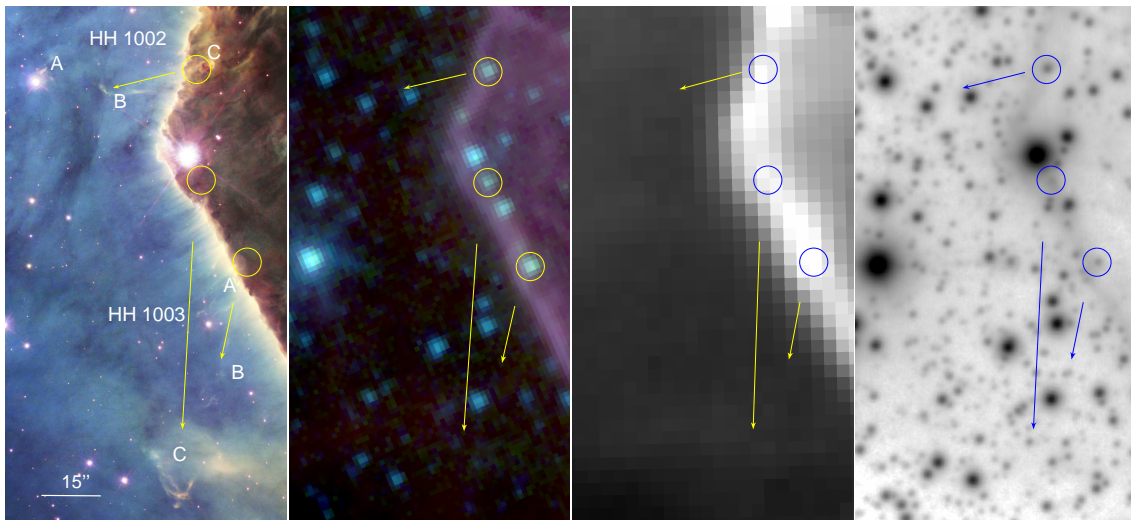


Figure 8.14: The known HH jets and their probable sources as seen in four different wavelengths. From left to right: HST RGB image (red: WFPC 2 SII filter (673 nm), green: ACS H $\alpha$  +NII filter (658 nm), blue: WFPC 2 O III filter (502 nm); image credit: NASA/ESA/Hubble Heritage Team (STScI/AURA)), *Spitzer* IRAC RGB image with 3.6  $\mu$ m in blue, 4.5  $\mu$ m in green, and 8.0  $\mu$ m in red, *Herschel* PACS 170  $\mu$ m image and VISTA *H*-band image. The yellow or blue arrows indicate the broad shape and direction of the outflow in question, white letters mark their features as described by Smith et al. [2010a]. The probable IR-identified sources are marked at their *Spitzer* coordinates with circles in yellow or blue. [Image first published: Ohlendorf et al. 2013a]

## 8.6 Sources of HH jets

In Chapter 7 we traced a number of HH jets identified in the CNC by Smith et al. [2010a] back to their protostellar sources. Smith et al. [2010a] also identify two HH jets and two HH jet candidates in the Gum 31 bubble. It should be remarked that the HST images on which the Smith et al. [2010a] study is based cover only a very small area of the entire Gum 31 region. A search for jet objects like MHOS as done in Chapter 7 was not possible here because the HAWK-I data do not extend so far out of the central CN. Due to the small sample size and its very limited spatial dimensions, we cannot draw any conclusions about the distribution or likely number of all jet-driving protostars within the region.

As can be seen in Fig. 8.14, the jet HH 1002 is almost perpendicular to the ionisation front. It shows a number of distinct features, marked by Smith et al. [2010a] as A, B and C and labelled thus in our figure. Smith et al. [2010a] remark that in the 2MASS images they detect a very likely source located at  $\alpha_{2000} = 10:36:53.9$ ,  $\delta_{2000} = -58:37:19$ . This matches almost exactly with the location of the object identified in IRAC images that is most likely to be the source of the jet: J103654.0–583720, which we classified as being a cYSO through its WISE and IRAC infrared excesses in Sect. 8.4.1. The *Herschel* observations trace the ionisation front well, but show no point-like source to be coincident with J103654.0–583720. Therefore it could not be included in the SED-based analysis in Sect. 8.5.

HH1003 has a more complicated structure and Smith et al. [2010a] discuss it as possibly being a two-part object, made out of two jets in close association. Tracing back the direction of the bow shocks in Fig. 8.14, we find two point-like sources in the IRAC images that are very probably the sources of two different jets. One of them, J103652.4–583809, associated with features A and B, is identified as a cYSO from the WISE and IRAC colour-colour diagrams, while the other is an IRAC cYSO. Both are coincident with faint sources in the 2MASS images. Again, the *Herschel* image shows no point-like sources.

The two candidate outflows, HHC 1 and HHC 2 (not to be confused with HHC 1 and HHC 2 within the extent of the central CN which were included in the study in Chapter 7, could not be traced back to any IR sources within the scope of our study. Following the axes of the jets, we cannot identify any likely emitting sources within their immediate surroundings.

## 8.7 Discussion

In this chapter we analysed *Spitzer*, WISE, and *Herschel* data to investigate the cloud structure and the young stellar population in and around the Gum 31 nebula. These data provide considerably better sensitivity and spatial resolution than the data sets previously available.

The *Herschel* FIR maps show that the bubble surrounding the Gum 31 nebula is connected to the central parts of the CN. This adds strong direct support to the assumption that Gum 31 is actually part of the CNC, as is also suggested by the matching C<sup>18</sup>O radial velocities measured by Yonekura et al. [2005] and other recent distance determinations (cf. Sect. 8.1).

The bubble itself has a very sharp western edge, where the column density derived from *Herschel* measurements rises abruptly by at least an order of magnitude. The dust temperatures range from  $\lesssim 20$  K in the dark clouds surrounding the H II region to  $\approx 30$  K in the H II region and up to  $\approx 40$  K near the location of the O stars.

The very small excess fraction seen for the MIR sources in the central stellar cluster NGC 3324 ( $\approx 0.5\%$ ) suggests that it is at least several Ma old already. For the whole Gum 31 region, the *Spitzer* and WISE data reveal about 300/660 cYSOs. These objects are most likely Class I protostars or Class II sources of solar to intermediate mass. The 59 FIR point-like sources revealed by the *Herschel* data are either pre-stellar cores or embedded (Class 0) protostars. This means that they trace a younger population of currently forming stars. The spatial distribution of the cYSOs is highly non-uniform. We expect a contamination of around 18%, so most of the widely distributed YSO population we see is probably due to back- and foreground stars. Those unrelated stars would be expected to be distributed homogeneously. Many cYSOs are found in rather compact clusterings. A considerable number of them, on the other hand, is found at the inner edge of the dusty bubble surrounding the H II region. The *Herschel*-identified point-like sources in particular trace the edge of the bubble.

This led us to assume a ‘collect and collapse’ scenario driven by the O stars within the cluster [Whitworth et al. 1994], resulting in an expected bubble size of 9–11 pc for an age of 1.5–2.0 Ma. This agrees very well with the  $\sim 10$  pc diameter observed. We find four cYSOs in the very tips of small pillars extending from the bubble rim (cf. Fig. 8.9), suggesting radiative triggering processes very similar to what is observed in the South Pillars [Smith et al. 2010a, Gaczkowski et al. 2013].

We conclude that two different modes of triggered star-formation occur simultaneously in the Gum 31 region: ‘collect and collapse’, as evidenced by the bubble size and the cYSOs in its rim, and radiative triggering, as evidenced by cYSOs in the heads of pillars.

We construct the NIR to FIR SEDs of 17 cYSOs and estimate basic stellar and circumstellar parameters by comparison to radiative-transfer models with good-quality fits for nine of them. All these cYSOs are of moderate luminosity ( $L \lesssim 900 L_{\odot}$ ), clearly suggesting that they are low- or intermediate-mass objects ( $M \lesssim 7 M_{\odot}$ ). This agrees with the results from our analysis of the cYSOs in the central parts of the CNC [Gaczkowski et al. 2013], where we found that no high-mass stars are currently forming.

We identify the driving sources of two Herbig-Haro jets in the western rim of the Gum 31 bubble. These sources are also identified as cYSOs by applying colour-selection criteria to IRAC or WISE photometry data.

From the total number of cYSOs observed and the IMF [Kroupa 2002] we can estimate a total young stellar population for the Gum 31 region. Our detection limit for cYSOs is about  $1 M_{\odot}$  and following the IMF there should be eight times as many stars below this mass ( $> 0.1 M_{\odot}$ ) as above it. Correcting the number of cYSOs given in Sect. 8.4.1 for the contamination estimated there, this gives a number of  $\sim 5000$  young stellar objects in the region.

A more detailed investigation of the star-formation history in this area requires a reliable identification of the individual young stars. While the infrared data presented here can reveal protostars and young stars with circumstellar disks, most of the slightly older ( $\gtrsim 2$  Myr old) stars cannot be detected by infrared excesses. Our very recent *Chandra* X-ray observations of the Gum 31 region, NIR observations with VISTA and other ongoing observations will allow us to finally identify these stars, too. This will constitute the basis for a comprehensive multi-wavelength study of this interesting region, in a way similar to the recent studies of the young stellar populations in the central parts of the CN [see Townsley et al. 2011b, Preibisch et al. 2011a, Wang et al. 2011, Wolk et al. 2011, Feigelson et al. 2011].

# 9 Clustering properties of the young stellar population of the Carina Nebula Complex<sup>1</sup>

The cYSOs catalogue assembled from IRAC observations in Chapter 5 and Chapter 6, the SYCC, has not been fully analysed in Chapter 7 and Chapter 8, which each concentrated on a specialist topic and a sub-sample of the young stars in the region. It has thus not been used to its full potential.

Compared to other *Spitzer* MIR studies of the CNC [e. g. Smith et al. 2010b, Povich et al. 2011a], this is the first large study encompassing all the CNC, including Gum 31 and the adjacent fields. Previous studies, in the MIR as well as in other wavelength ranges, usually concentrated on a small region within the CN, such as the South Pillars. We compiled *Spitzer* data of the entire region, especially stretching out towards the underrated Gum 31 region, and thus are able to complement those in-depth studies with a large-scale overview that shows up the patterns of star-formation in the complex and also allows the comparison of observations with other instruments (e. g. the comparison to the cYSOs derived from the WISE catalogue) and in other wavelengths. The latter can only be touched in this work but is done in depth within our research group, by comparing new data from instruments as different as *Chandra* [Preibisch et al. 2011a], HAWK-I [Preibisch et al. 2011b,c], VISTA [e. g. Zeidler 2013, and upcoming publications by Preibisch et al. and Zeidler et al.], *Herschel* [Preibisch et al. 2012, Gaczkowski et al. 2013, Roccatagliata et al. 2013], and LABOCA [Preibisch et al. 2011d, Pekruhl et al. 2013] and combining these with observational data obtained from catalogues and archive data, such as is done here for *Spitzer* and WISE. The work presented here is an integral part within this larger frame.

In this chapter, we will use the SYCC to analyse the large-scale YSO population of the CNC and explore its clustering properties. We can compare this to previous studies of YSO clusters and make inferences about the young stellar population itself.

## 9.1 How many cYSOs are indeed YSOs?

As described in Sect. 6.4 and Sect. 8.4.1, we expect a high degree of contamination for our sample of cYSOs. For Gum 31 we estimated it to be  $\sim 18\%$  for the WISE-selected YSO sample. To be able to work reassuredly with the SYCC, we need to estimate its contamination in order to assess its trustworthiness.

We perform a similar comparison with the full SYCC as we did in Sect. 8.4.1 for the WISE-selected sample. To this end, we use the same region that we also used in Sect. 8.4.1: Circular with a diameter of  $30'$  and centred at  $\alpha_{2000} = 10:51:52.5$ ,  $\delta_{2000} = -59:14:30$ . The second region we identified as suited to the analysis in Sect. 8.4.1, i. e. as free of IR sources,

---

<sup>1</sup>Major parts of this chapter are contained in a paper submitted to *The Astronomical Journal* [Ohlen-dorf et al. 2013b] written in close cooperation with Thomas Preibisch, Veronica Roccatagliata and Thorsten Ratzka.

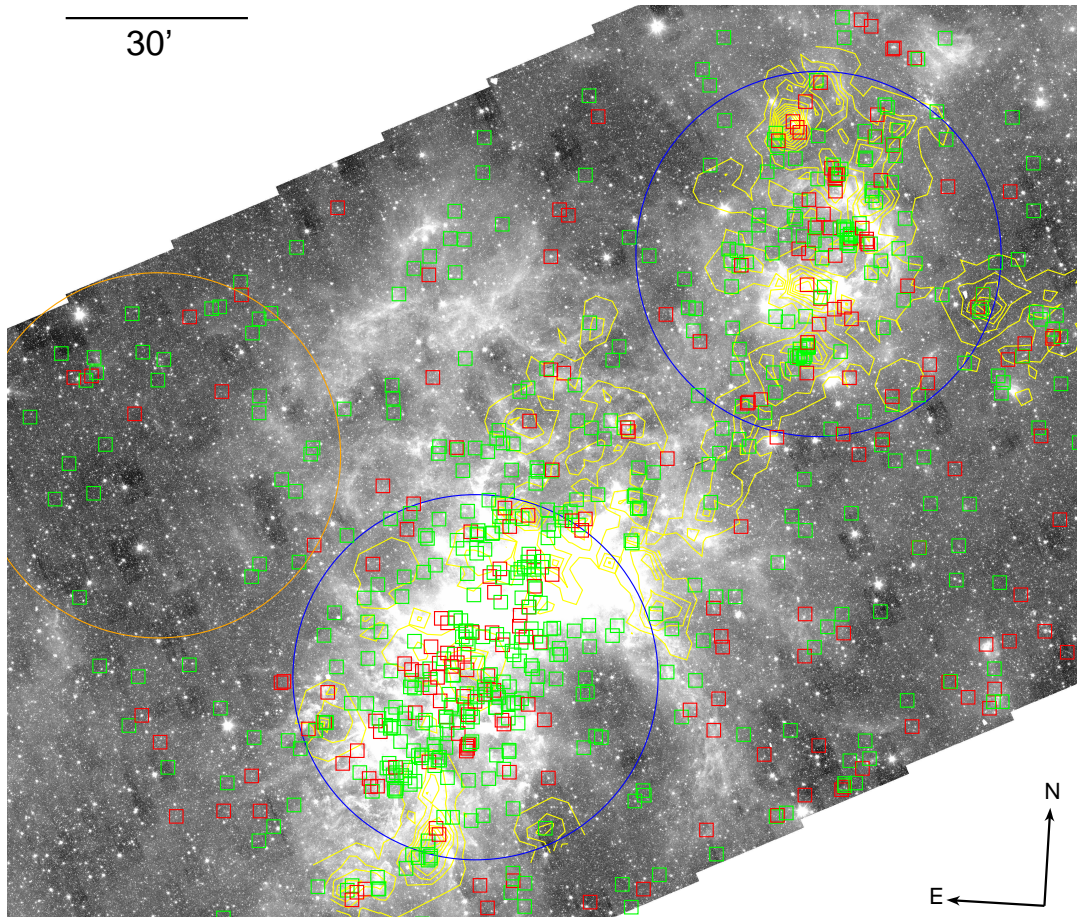


Figure 9.1: Comparison regions to correct for YSO catalogue contamination. The orange circle shows the region which we define as ‘contaminants only’ and against which we tested. The blue circles are the central CN (below) and Gum 31 (above). The red (Class I) and green (Class II) boxes are the SYCC. In yellow we show the  $C^{18}O$  contours of Yonekura et al. [2005]; the background image is an IRAC  $4.5\ \mu\text{m}$  image.

$H\alpha$  and CO emission, is unfortunately almost entirely outside the area of the SYCC. Within the circle defined above we count  $N = 35$  cYSOs in an area of  $A = 2827.4$  arcmin<sup>2</sup>. This results in a cYSO density  $\frac{N}{A} = 0.0124$  arcmin<sup>-2</sup>  $\approx 45$  deg<sup>-2</sup>.

In the entire catalogue region,  $N = 759$  cYSOs are found in an area of  $A = 24840$  arcmin<sup>2</sup> ( $2.3^\circ \times 3.0^\circ$ ), thus yielding  $\frac{N}{A} = 0.0306$  arcmin<sup>-2</sup>  $\approx 110$  deg<sup>-2</sup>. This would mean a background contamination of around 40%. This number seems very high, but one has to consider that this is averaged over the entire region, containing those fields with very high background (expected outside the nebular regions) as well as those where a high YSO density is indeed expected. It even encompasses the test region which we defined as containing only contaminants just now.

If we limit the test region to an area where we expect a high degree of star formation

to be taking place—that is, the central Carina Nebula region including the clusters Tr 14 and Tr 16—things look very different. We chose a circle of 30′ diameter centred on  $\alpha_{2000} = 10:45:01.1$ ,  $\delta_{2000} = 59:51:01$  in which 274 cYSOs are found. This yields  $\frac{N}{A} = 0.0969 \text{ arcmin}^{-2} \approx 349 \text{ deg}^{-2}$  and thus an estimated contamination of only  $\sim 13\%$ . This is, of course, an extreme case, but it shows well how strongly the contamination factors vary over the CNC.

For a 30′ circle around Gum 31 centred on  $\alpha_{2000} = 10:37:54.0$ ,  $\delta_{2000} = 58:40:02$ , we find 165 cYSOs, which results in  $\frac{N}{A} = 0.0584 \text{ arcmin}^{-2} \approx 210 \text{ deg}^{-2}$ . Assuming that no real YSOs are placed in the test region sample, this yields an estimated contamination of  $\sim 21\%$ .

Averaging over Gum 31 and the central CN yields  $\sim 16\%$  ( $0.0776 \text{ arcmin}^{-2} \approx 280 \text{ deg}^{-2}$ ). Comparing those to the  $\sim 18\%$  derived for the WISE-selected YSO sample in Sect. 8.4.1, it seems that the methods for cleaning and restricting the SYCC described in Sect. 6.2 have indeed yielded a catalogue that in its reliability is comparable to the catalogue of YSOs selected from the WISE catalogue.

## 9.2 Combining the MIR-selected samples with a *Herschel* sample of prestellar objects and protostars

The *Herschel* study of Gaczkowski et al. [2013] has been heavily relied upon in Chapters 7 and 8. It revealed the very young stars and protostars in the CNC. As described in Sect. 8.4.2, we accept a point-like source as a protostar if it has a detection in the 70  $\mu\text{m}$  band, otherwise we regard it as a pre-stellar object. So far, we have used the *Herschel* data for the Gum 31 region for which it was first presented by Ohlendorf et al. [2013a, cf. Chapter 8], but the field covered by *Herschel* maps is much larger. Together with the cYSOs selected by their IR excesses detected by IRAC and WISE, I will use the full sample of Gaczkowski et al. [2013] in this chapter to describe the young stellar population of the CNC.

In Fig. 9.2 the *Herschel*-identified point-like sources are contrasted with the SYCC cYSOs from IRAC observations. It is clear that both studies trace different populations. This is not surprising, since the *Herschel* point-like sources are systematically younger than those selected from the *Spitzer* catalogue. As explained in Sect. 4.2.1, this is due to the shape of the SEDs of pre- and protostellar cores, which have their peaks in the FIR while being faint in the MIR. Consequently while *Herschel* detects the very young objects, even before the cores form stars, *Spitzer*, as shown in Sect. 2.1, traces predominantly Class I and Class II YSOs.

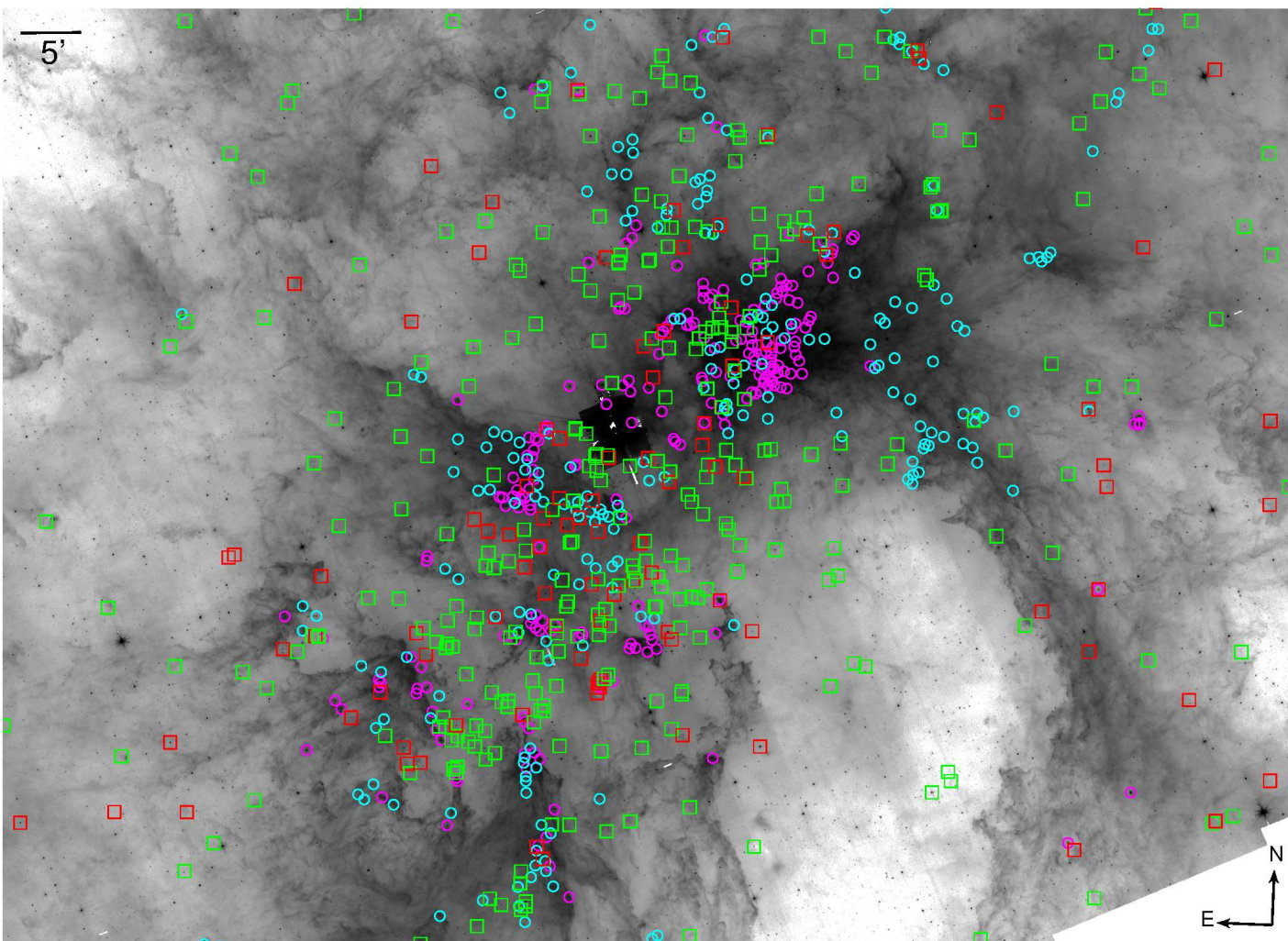


Figure 9.2: SYCC cysos (boxes) and *Herschel*-identified pre- and protostellar objects (circles). The figure shows the central part of the CN in  $8.0\ \mu\text{m}$ . The red boxes are Class I candidates, the green boxes Class II candidates from the SYCC. Circles in cyan mark pre-stellar objects and circles in magenta protostellar objects identified with *Herschel*.

## 9.3 Finding clusters

### 9.3.1 How to identify YSO clusters?

Although just looking at the distribution of YSOs on the sky gives a broad idea of where clusters occur, it of course an extremely biased and subjective method. As shown in the following, an unbiased search for clusters reveals structure that would otherwise have been overlooked.

Clustering studies of stellar populations are a staple of analysis [for the CNC cf. e.g. Rathborne et al. 2004, Feigelson et al. 2011] and there are a number of tools to perform it with. Here I choose two conceptually very similar methods to determine the cYSO density: A simple density computation within a rectangular area that I dubbed the ‘box’ method and a more sophisticated nearest-neighbour algorithm.<sup>2</sup> The study of Schmeja [2011] showed that both densities from star counts (the ‘box’ method) and nearest-neighbour searches are apt for showing up clusters of lower densities. A low density is indeed what we can expect, owing to our small sample. The authors recommend both methods for a case like the CNC because they did not find general differences in performance. Computing time in our study is not an issue due to the small number of sources and as Schmeja [2011] suggested, I compared the methods for our individual case to make a choice.

#### The ‘box’ method

To employ the ‘box’ method, a user-defined grid ( $N_{\text{RA}} \times N_{\text{Dec}}$  steps in right ascension and declination) is overlaid on the sample area. On each of the grid points, the cYSO density is computed within a user-defined box centred on the grid point. This is then mapped onto a contour plot. In this way, density maps on different spatial scales can be derived. There is, however, no smoothing employed and consequently the ‘boxy’ shape of the contours shines through. Furthermore, the results depend very strongly not only on the box size chosen but also on the grid employed, as can easily be seen by comparing Fig. 9.3 and Fig. 9.4. Both parameters need to be matched carefully to yield a meaningful plot.

As the equatorial coordinate system is a spherical system, equal distances in right ascension at different declinations do not map into equal distances on the sky. Therefore, this method of density estimation would introduce a slight error if the boxes were kept the same throughout. The distances between the grid points are not equal at the lowest and the highest declinations and neither would be the sizes of the density integration boxes. This is accounted for in the maps shown by scaling the size of the density integration box appropriately with the current declination.

#### The nearest-neighbour method

These shortcomings are avoided using the nearest-neighbour method that is one of the standard methods in clustering analysis. For each source, the distance to its neighbours is determined and the distance to the  $n$ -th neighbour, with  $n$  chosen by the user, is used as the reference for density calculations. Here I choose the fifth-nearest neighbour throughout. Thus, the density at the point of each cYSO is calculated from four objects<sup>3</sup> within a circle

<sup>2</sup>Both were implemented using Interactive Data Language (IDL) programs.

<sup>3</sup>The fifth-nearest neighbour itself and the centre are disregarded [Casertano and Hut 1985].

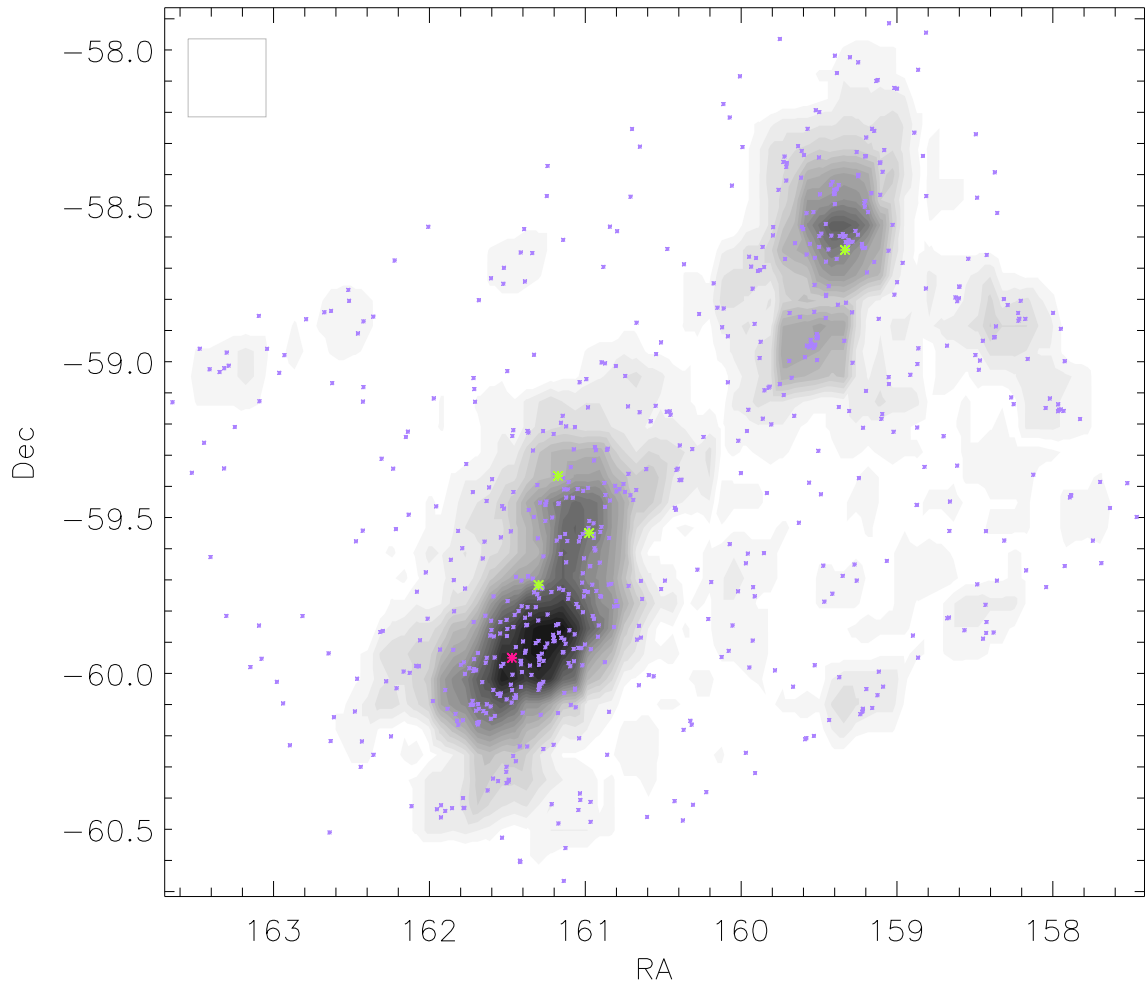


Figure 9.3: Density of SYCC cysos in the CNC, derived on a large scale. The method used to derive this image was the ‘box’ method (grid intervals  $80 \times 35$ , box size  $0.25^\circ \times 0.25^\circ$ ). The central coordinates of the clusters Tr 14, Tr 15, Tr 16, and NGC 3324 are marked in green for orientation. The pink marker shows the position of the Treasure Chest cluster and therefore roughly the centre of the South Pillars region.

with the radius of the distance of the fifth-nearest neighbour. The relevant formula is

$$\mu_j = \frac{j-1}{\pi s_j^2}, \quad (9.1)$$

where  $s_j$  is the distance to the  $j$ -th neighbour and  $\mu_j$  is the resulting surface density estimator [Casertano and Hut 1985].

For a smoother plot, a Gaussian distribution with the distance to the  $n$ -th neighbour as the standard deviation was overlaid on each cysos position. The nearest-neighbour method is far less dependent on parameter choice and, with the additionally applied Gaussian smoothing, yields smoother maps than the box method.

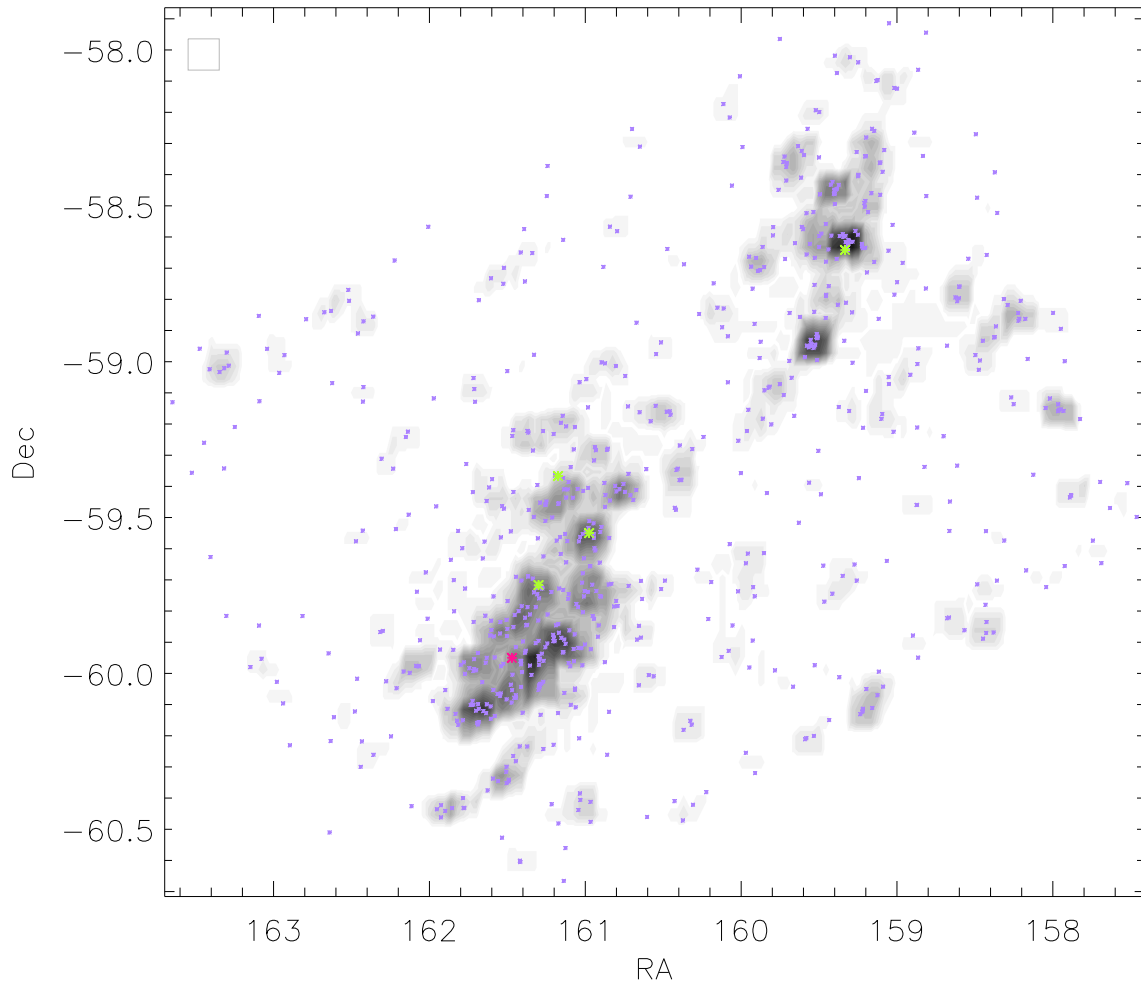


Figure 9.4: Density of SYCC cYSOs in the CNC, derived on a small scale using the ‘box’ method. The figure is identical to Fig. 9.3, but a smaller box was employed to derive the density (grid intervals  $150 \times 66$ , box size  $0.1^\circ \times 0.1^\circ$ ). The green and pink markers are for the central coordinates of Tr 14, Tr 15, Tr 16, NGC 3324, and the Treasure Chest cluster as in Fig. 9.3.

### 9.3.2 YSO density maps

#### The ‘box’ method

By varying the parameters of the box method two fundamentally different kinds of maps can be retrieved: A large-scale overview that shows the basic structure of the CNC well and a small-scale map that allows a more detailed view on the individual cYSO clusters.

A large-scale map is obtained by choosing a broad-spaced grid ( $80 \times 35$  steps) and a large density integration box ( $0.25^\circ \times 0.25^\circ$ ). This map is shown in Fig. 9.3. It shows the overall structure of the Carina Nebula Complex very well: There is one concentration of cYSOs corresponding to the main Carina Nebula and associated with the known stellar clusters Tr 14, Tr 15 and Tr 16. It is apparent from this map that the barycentre of the cYSO distribution is clearly placed in the South Pillars region.

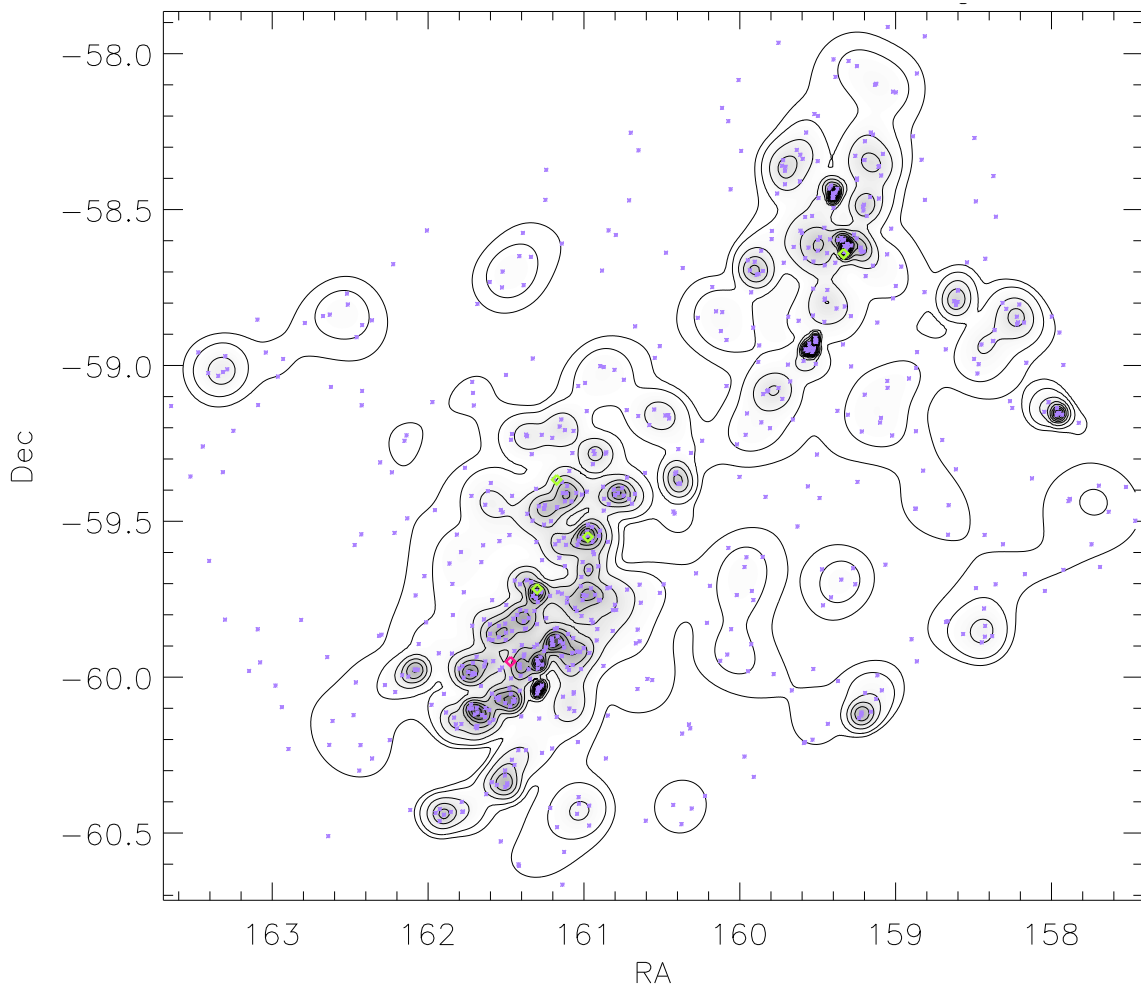


Figure 9.5: Density of cYSOs derived by a nearest-neighbour algorithm searching for the fifth-nearest neighbour. The grid was  $500 \times 222$  steps and the contours were smoothed employing a Gaussian. The green and pink markers are for the central coordinates of Tr 14, Tr 15, Tr 16, NGC 3324, and the Treasure Chest cluster as in Fig. 9.3.

The second focus of cYSO distribution is Gum 31. As described in Chapter 8, the barycentre is not coincident with the cluster NGC 3324, but slightly displaced from it towards the north-east. The maximum density of cYSOs in Gum 31 is slightly lower than in the South Pillars, but it appears as a prominent centre of star formation.

Outside these two main centres of star formation there are some further pockets spreading out towards the edges of our study field. More detailed descriptions of these outlying clusters can be found in Sect. E.2 in Appendix E.

A map with a much finer scale is obtained with a more finely spaced grid ( $150 \times 66$  steps) and a smaller density integration box ( $0.1^\circ \times 0.1^\circ$ ). This map, shown in Fig. 9.4, yields much more detail than the one shown in Fig. 9.3. The trend of the distribution is of course the same: A large clustering around the South Pillars and another in the region of Gum 31.

### The nearest-neighbour method

The nearest-neighbour method produces a map that is strikingly similar to the one yielded by the box method with small box and fine grid, which means that both methods confirm each other. Shown in Fig. 9.5, it is the reference map for the detailed investigation of the clustering properties of the sample below.

#### 9.3.3 Defining clusters

From those maps, we now need a method to define stellar clusters. This method must be objective and neutral for all of the region. By drawing a histogram of the YSO density as shown in Fig. 9.6a, the differing densities within the map can be demonstrated visually. The density computation is evaluated at the position of each known SYCC star, thus giving a YSO density estimate for the environs of the object.

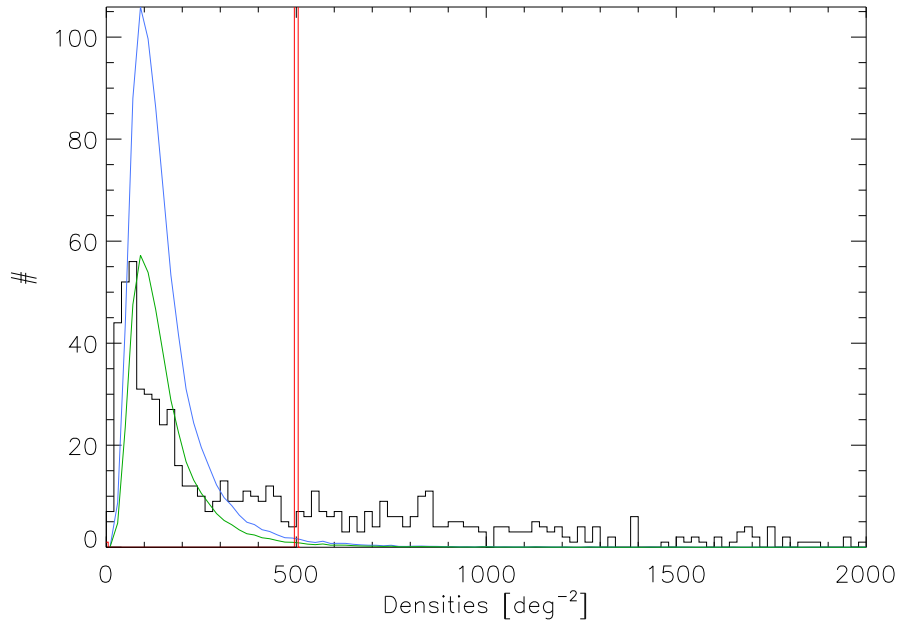
The alternative assumption to a clustering behaviour of stars of course would be a uniform distribution, where sources are placed randomly within the study field. This can be easily simulated numerically and produces a steep rise and decline in the density histogram. The histogram compiled from the real-life situation in the CNC shows essentially the same behaviour up to a certain density, but above this number exhibits many measurements of much higher density.

Contrasting the distributions as in Fig. 9.6a allows to define a density that serves as the distinctive value above which we define clusters to lie. A conservative choice for the case in hand, as illustrated by Fig. 9.6a, is  $500 \text{ deg}^{-2}$ . At this point, we no longer expect a contribution by any underlying random distribution. As we wish to have a reliable list of clusters, we choose this conservative cutoff point even though values as low as  $300 \text{ deg}^{-2}$  could probably have been argued for. At those low values, however, a contribution from the spread-out population cannot be excluded even though it probably is low.

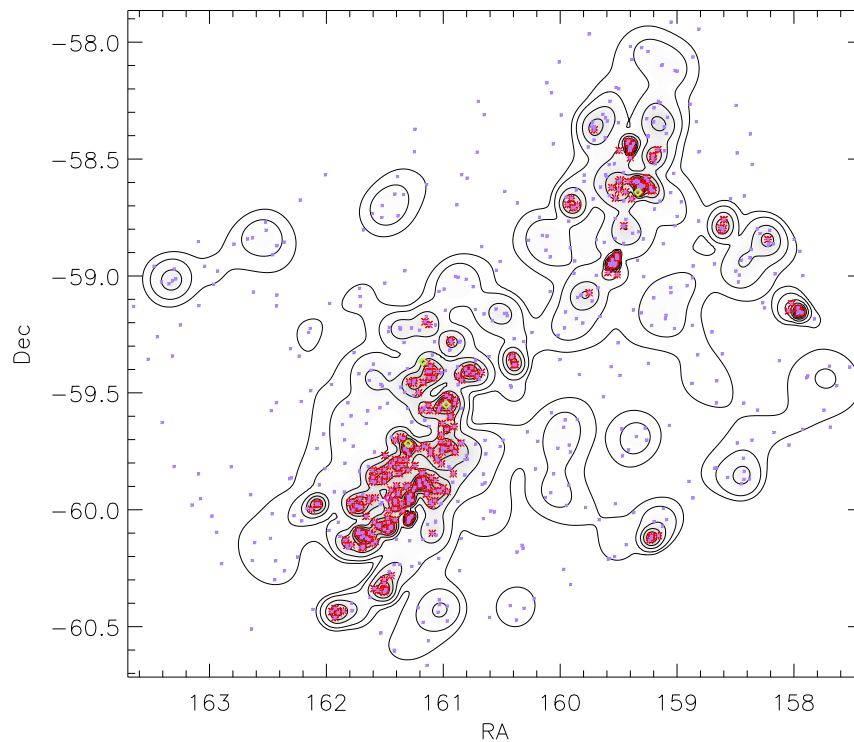
The cysos identified as having a density above the cluster limit are shown in Fig. 9.6b in red. We find 301 of those, clearly outlining the South Pillars on the one hand and Gum 31 on the other hand. There are a number of small clusters outside these areas, most notably Cluster No. 7 described in Sect. 9.4.1. Typically, these clusters consist of a few stars only. Compared to other studies, e.g. the one by Feigelson et al. [2011], where there are mostly between 30 and 100, and up to 1378, stars per cluster, these numbers are very small. This is due to the conservatively selected YSO catalogue that forms its basis and has a low overall density of stars to begin with.

We find  $\sim 40\%$  of the cysos ( $301/759$ ) to occur in clusters. The distributed population includes  $\sim 50\%$  of the cysos. Their position in the histogram (Fig. 9.6a) is well in agreement with those drawn randomly from a uniform distribution. The remaining  $\sim 10\%$  lie between the intersection point of the curves ( $\sim 300 \text{ deg}^{-2}$ ) and the cluster limit ( $500 \text{ deg}^{-2}$ ). These are, as per our definition, not in clusters; but roughly half of them also lie above the amount expected from a distributed population. Within our uncertainties (e.g. boundary effects due to stars that *cannot* have close neighbours because they lie at the boundaries of the field), these remain in an ambiguous position.

We demand for a cluster to contain three or more sources with densities above the cluster limit. The clusters are often well-delimited by their spatial position alone (e.g. Clusters No. 9, 10 or 23 in Fig. 9.8). They appear as close conglomerations in the map in Fig. 9.6b and the density contours encircle them, clearly marking them as local density



(a) The histogram does not show densities of more than 2000 deg<sup>-2</sup>, which excludes 69 sources. For comparison, the blue line shows the same number of stars as randomly drawn from a uniform distribution. The green line shows the same distribution, but scaled down to meet the peak of the real distribution. The red vertical line drawn at 500 deg<sup>-2</sup> illustrates the cutoff we define for clusters.



(b) The plot, similar to Fig. 9.5, shows the SYCC stars with density contours. The stars highlighted in red are those for which the local density exceeds 500 deg<sup>-2</sup>, i. e. those defined as belonging to a cluster.

Figure 9.6: Identifying YSO clusters from the positions of the SYCC stars using the nearest-neighbour method.

maxima. In some cases, matters are slightly more complicated. The contours suggest a density minimum between two maxima, but it does not appear to be so deep as to present two clearly distinct clusters. In these cases, the decision of keeping them as one cluster (as for Cluster No. 15) or splitting them in two (as for Clusters No. 3 and 4) is taken by the spatial layout of the stars and by their context. In the case of Cluster No. 15, it is associated with the known cluster Tr 15. It is sensible to assume that the YSOs, as long as they show no explicit deviation, also exhibit one single cluster. In the case of Clusters No. 3 and 4 we also see Cluster No. 4 associated with NGC 3324, while Cluster No. 3 is situated in the interior of the Gum 31 bubble.

The South Pillars present a challenge in this respect. Here, a high number of density maxima is found in close conjunction. Again, the selection of clusters is done carefully by the spatial distribution of the cYSOs. Some clusters, like Cluster No. 25, clearly stand out while for example the separation of the long line of stars marked in red in the north-east of the South Pillars is more challenging. In this case, Tr 16 can be seen to constitute Cluster No. 16 while two separate conglomerations, Clusters No. 13 and 17, can be identified to its south. Cluster No. 26 from its spatial appearance alone might be deemed as two clusters, a larger one in the north-west and a smaller one in the south-east. Our density contours, however, show no strong drop-off of density between those two entities, which is why we assigned only a single cluster here.

In Table 9.1 the cYSOs clusters are listed. Because the contours are not a reliable source for it owing to our low numbers of cYSOs per cluster, the size of the cluster was then determined by the smallest circle that could encompass all cluster members. The table lists the centres and radii for the clusters which we consequently defined always to be circular. It also gives the number of SYCC sources found strictly within this circular region. This strict definition might exclude physical cluster members, but provides us with the only objective criterion to define cluster membership obtainable within the scope of this study.

In Figs. 9.7 and 9.8 the positions of the clusters are shown on an IRAC image. In the following sections we will refer to the numbers given to the clusters in the images and table to enable orientation for the reader.

## 9.4 Investigation of the clusters

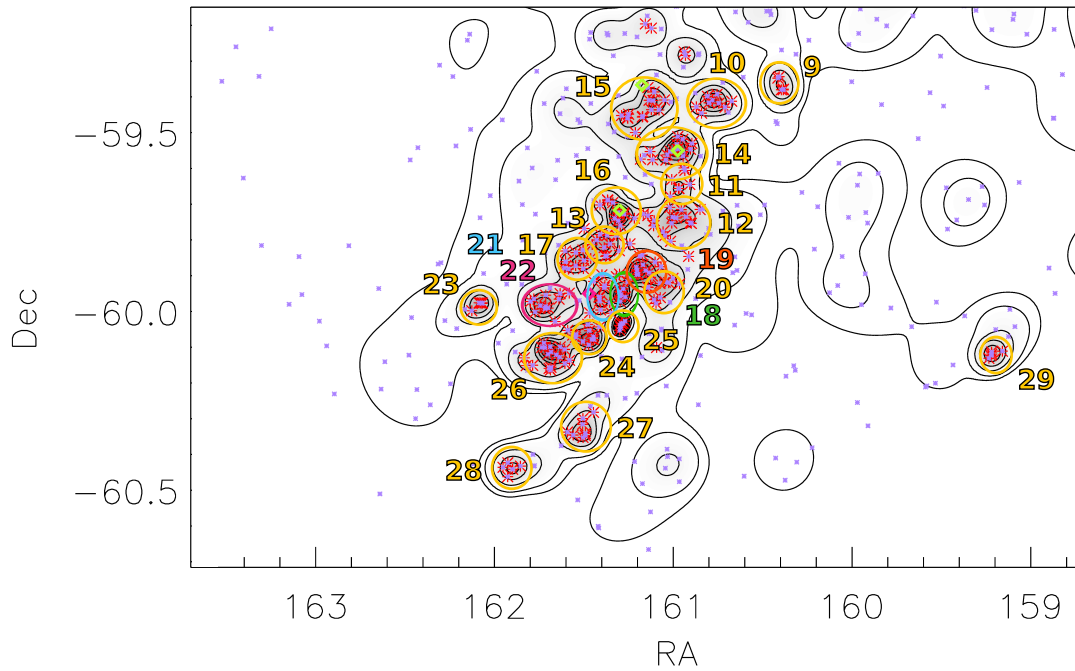
### 9.4.1 The Gum 31 region

The Gum 31 HII bubble and its environs have already been discussed at length in Chapter 8. Despite their having been largely neglected by researchers in past years, as Fig. 9.3 shows they are a prominent star-forming region. Apart from the significant clusters described here, there is also a number of small overdensities associated with the region. A more detailed description of those can be found in Sect. E.1 in Appendix E.

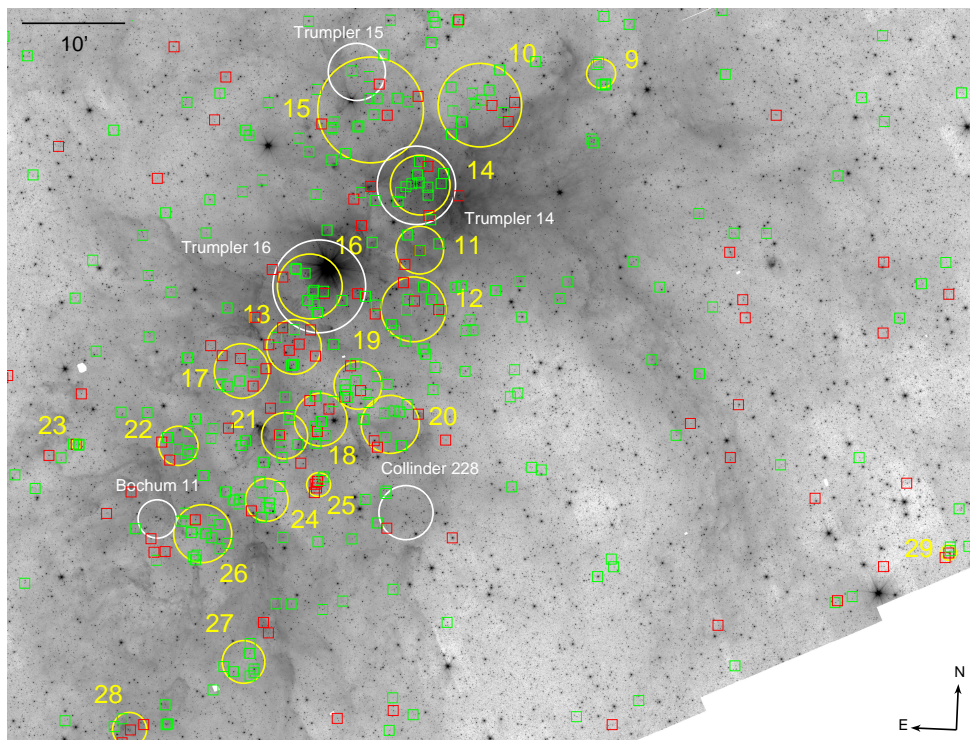
An overview over the SYCC cYSOs in the region is given in Fig. 9.9, which is analogous to Fig. 8.8 showing the WISE-identified cYSOs in the region. The SYCC cYSOs are overlaid on an IRAC RGB image. The WISE-identified cYSOs are also plotted as red (Class I) and green (Class II) diamonds in Fig. 9.9, for comparison to the SYCC sample shown as squares in the same colours.

While there are similarities, the two distributions appear different in a number of ways.

9 Clustering properties of the young stellar population of the Carina Nebula Complex

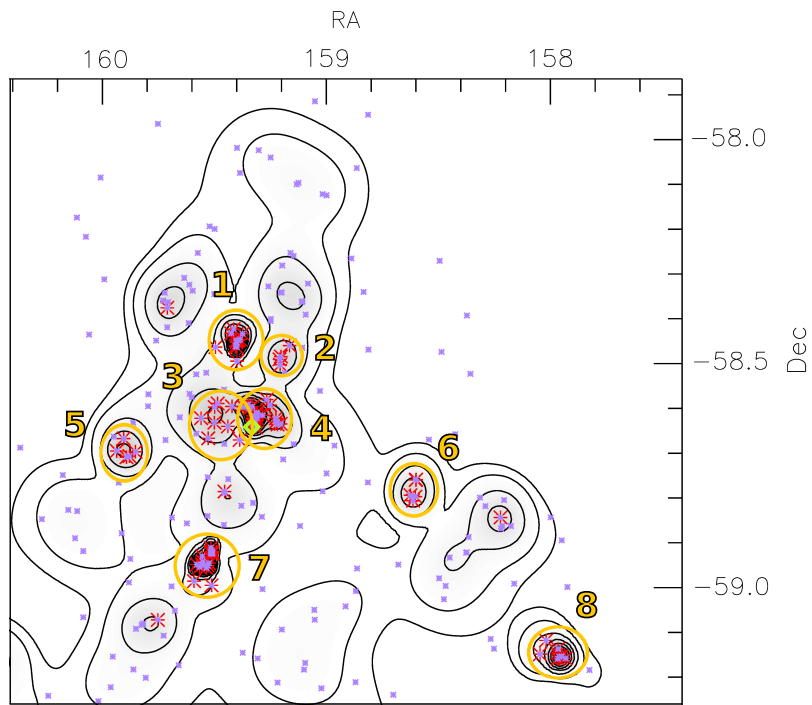


(a) Schematic. The plot is based on Fig. 9.6b, highlighting the clusters.

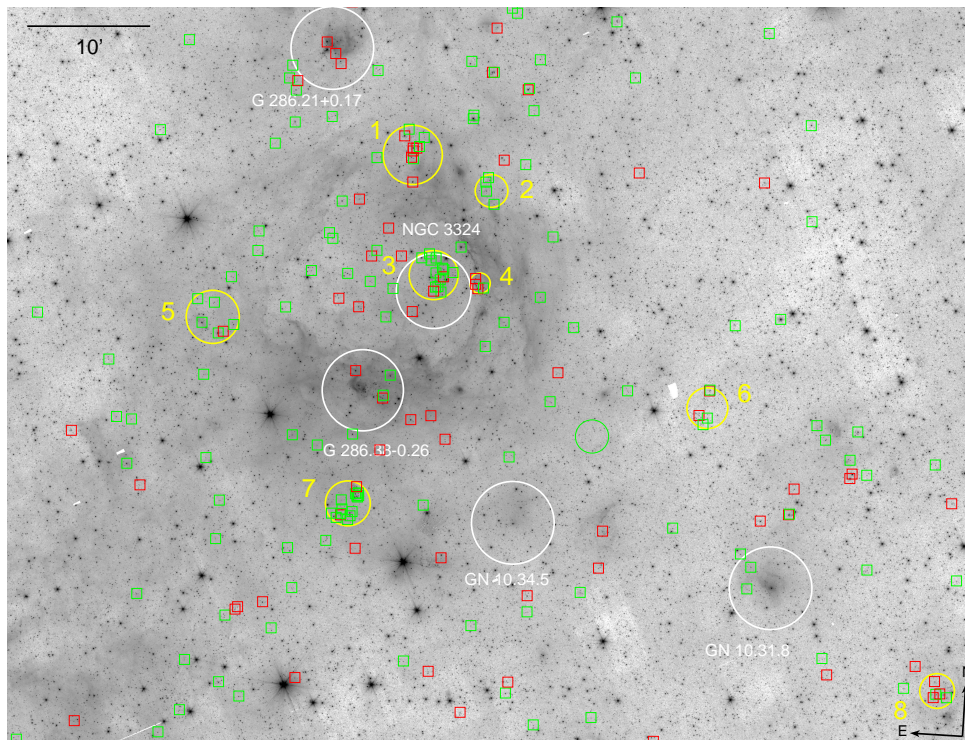


(b) Observation. The background image is IRAC 4.5 μm and the white circles mark the nominal positions of the known clusters in the region.

Figure 9.7: The cYSO clusters in the CNC as they are listed in Table 9.1 (yellow circles; Clusters Nos. 9–29).



(a) Schematic. The plot is based on Fig. 9.6b, highlighting the clusters.



(b) Observation. The background image is IRAC 4.5  $\mu\text{m}$  and the white circles mark the nominal positions of the known clusters in the region.

Figure 9.8: The CYSO clusters in the Gum 31 region as they are listed in Table 9.1 (yellow circles; Clusters Nos. 1–8).

9 Clustering properties of the young stellar population of the Carina Nebula Complex

Table 9.1: Clusters of IRAC cYSOs.

No.	Cluster centre		Radius [arcsec]	# of sources	Known clusters		
	RA	Dec			X-ray <sup>b</sup>	IR <sup>c</sup>	
1	10:37:41.5	-58:27:35	140	11	–	–	–
2	10:36:44.8	-58:28:50	90	4	–	–	–
3	10:37:51.5	-58:38:21	190	8	–	–	–
4	10:37:08.1	-58:36:51	175	19	–	–	–
5	10:39:34.3	-58:41:21	85	5	–	–	–
6	10:34:26.0	-58:46:56	89	5	–	–	–
7	10:38:08.3	-58:57:11	160	16	–	–	–
8	10:31:56.8	-59:08:42	115	7	–	–	–
9	10:41:35.1	-59:21:43	75	5	–	–	–
10	10:43:05.1	-59:25:08	185	9	g4?, g7?	P, Q?	–
11	10:43:52.3	-59:39:25	125	5	–	–	–
12	10:44:00.1	-59:46:01	335	17	–	–	–
13	10:45:29.3	-59:48:59	150	10	c14	G?	–
14	10:44:09.1	-59:33:18	280	17	c1	–	Tr 14
15	10:44:39.1	-59:26:19	240	14	c7, c8? g15?, g19?	–	Tr 15
16	10:45:14.8	-59:43:11	190	11	c12	–	Tr 16
17	10:46:09.9	-59:51:23	150	10	–	–	–
18	10:45:10.1	-59:56:01	145	10	c13?	F	–
19	10:44:34.3	-59:52:31	145	12	–	D	–
20 <sup>a</sup>	10:44:12.5	-59:56:15	170	10	–	B?	–
20a	10:44:12.6	-59:55:44	165	7	–	–	–
20b	10:44:21.1	-59:58:04	45	3	g13?	B?	–
21	10:45:41.6	-59:57:22	155	8	g21?, g22	J?	–
22	10:46:44.4	-59:58:22	210	12	–	–	–
23	10:48:23.4	-59:59:09	75	5	–	–	–
24	10:45:59.2	-60:02:54	175	13	c16?	K?	–
25	10:45:08.4	-60:02:23	65	7	–	–	–
26	10:46:49.5	-60:08:10	230	18	g29?	–	–
27	10:46:02.5	-60:18:53	170	8	–	–	–
28	10:47:36.4	-60:26:24	95	5	–	O	–
29	10:36:47.5	-60:07:10	85	5	–	–	–

**Notes.** For the known clusters, a question mark denotes those cases where the cluster appears to lie within the boundaries of our cluster, but their centres differ.

(<sup>a</sup>) The X-ray clusters of Feigelson et al. [2011, see Fig. F.1 in Appendix F] suggest that our Cluster No. 20 might consist of two clusters, dubbed Cluster No. 20a and Cluster No. 20b here.

(<sup>b</sup>) Feigelson et al. [2011], *c* denotes clusters (their Table 1), *g* groups (their Table 2)

(<sup>c</sup>) Smith et al. [2010b], their Table 4, and Povich et al. [2011a]

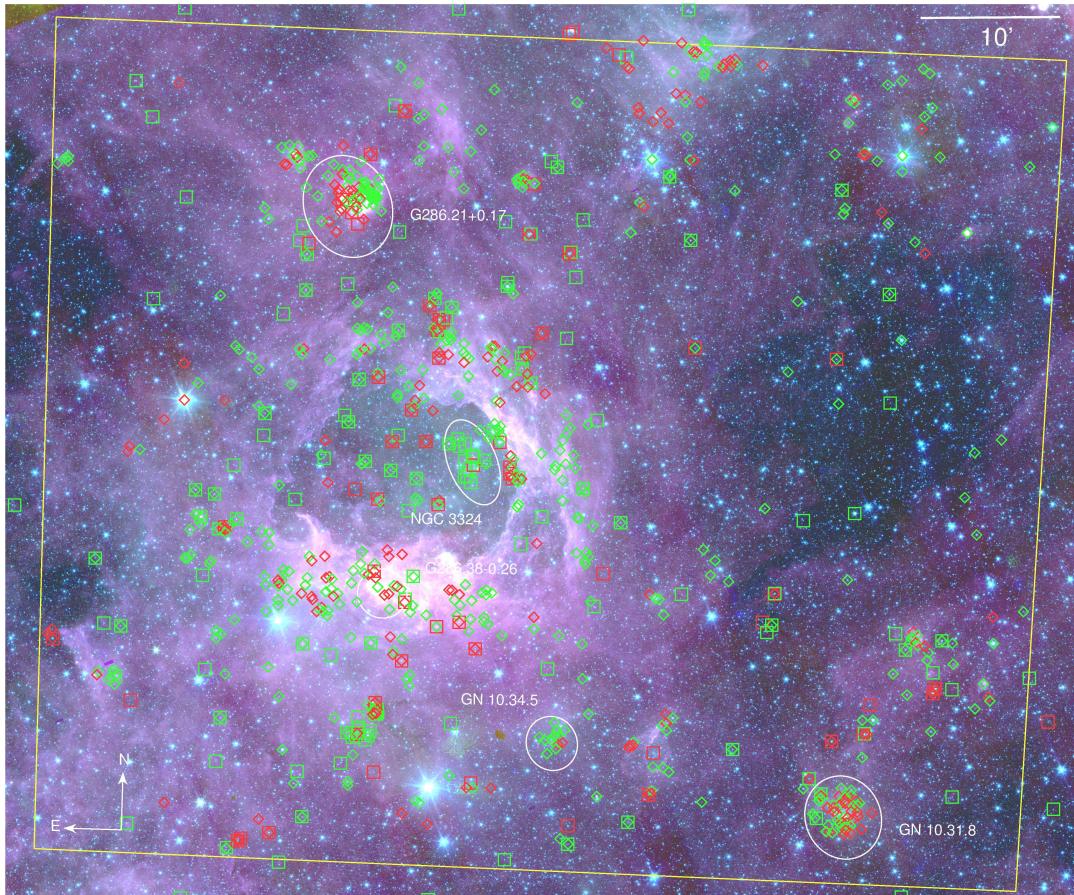
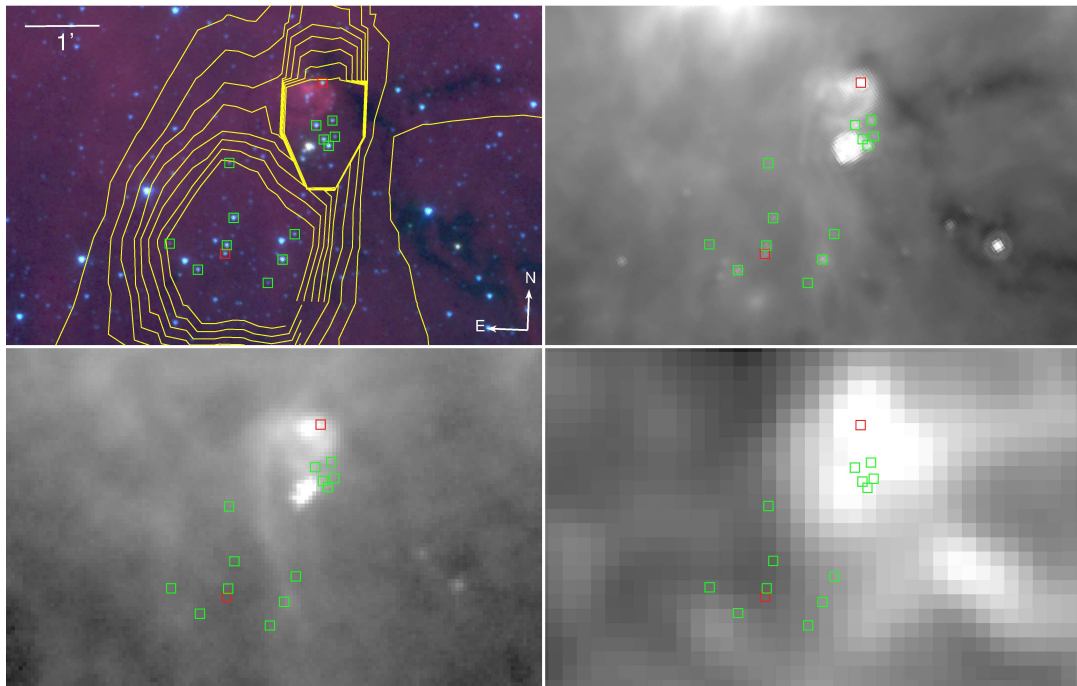


Figure 9.9: cYSOs in the Gum 31 region. This figure is analogous to Fig. 8.8 and shows an IRAC RGB image. The red (Class I) and green (Class II) diamonds are the WISE-identified cYSOs (cf. Sect. 8.4.1), the squares are the cYSOs from the SYCC. In both cases, Class I sources are red, Class II sources are green.

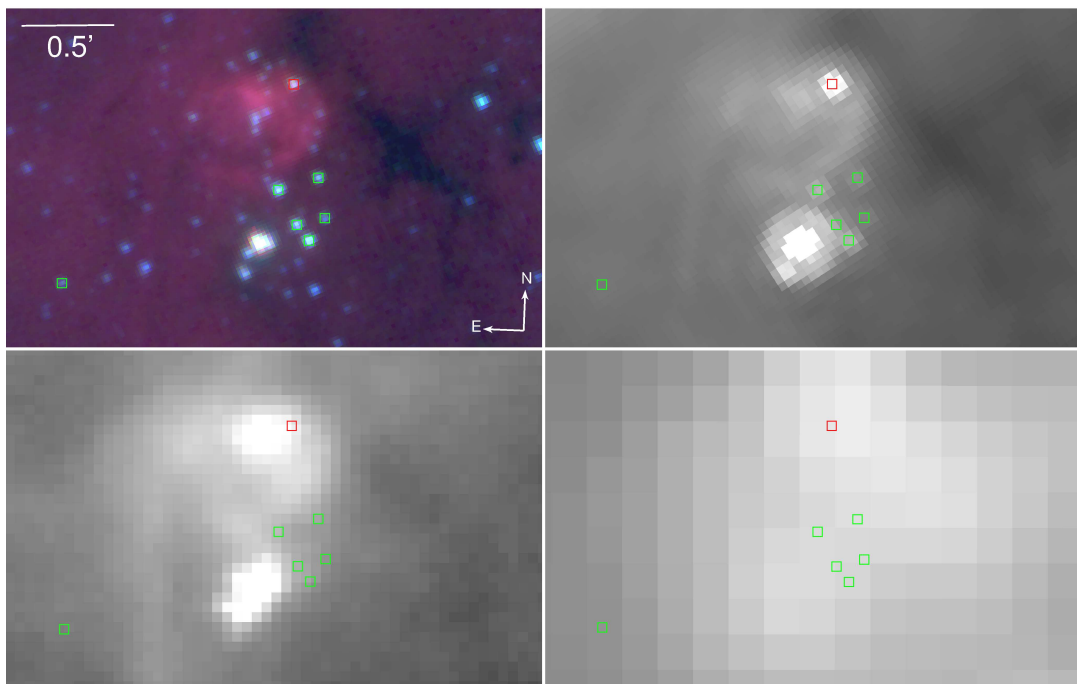
The WISE-identified cYSOs, for example, closely follow the edge of the bubble as described in Sect. 8.4.3. In contrast to that, the SYCC cYSOs are more broadly distributed and show less of a tendency to align with strong nebulosity. One striking point is that the cluster NGC 3324 itself, which in Sect. 8.4.3 was described as being remarkably devoid of cYSOs, stands out clearly as a cluster of SYCC cYSOs. It is described in more detail in Sect. 9.4.1. Just the same as with the WISE-selected cYSOs, we find a population of SYCC cYSOs aligned with the western rim of the bubble. There are, however, fewer sources in the IRAC selection than the WISE selection. WISE has  $\sim 14$ , IRAC only six.

The two nebulae GN 10.34.5 and GN 10.31.8 that appear as clear clusters in the WISE-selected cYSO sample (cf. Sect. 8.4.3) are not conspicuous at all in the SYCC sample. In fact, GN 10.34.5 does not contain a single SYCC source.

9 Clustering properties of the young stellar population of the Carina Nebula Complex



(a) Larger region.



(b) Close-up on the “question mark” structure.

Figure 9.10: Cluster No. 7. Upper left: *Spitzer* IRAC RGB image (red:  $8.0\ \mu\text{m}$ , green:  $4.5\ \mu\text{m}$ , blue:  $3.6\ \mu\text{m}$ ), upper right: *Spitzer* MIPS  $24\ \mu\text{m}$  image. Lower left: *Herschel* PACS  $70\ \mu\text{m}$  image, lower right: *Herschel* SPIRE  $500\ \mu\text{m}$  image. The cyso are marked by boxes, red for Class I, green for Class II. The yellow contours are identical to those in Fig. 9.5.

### The “Question Mark” cluster

The most apparent of the newly-discovered details in the region is Cluster No. 7 in the outskirts of the distributed IR emission region associated with Gum31, which appears as the very dark ( $\hat{=}$  dense) feature south of Gum31 in Fig. 9.8a. On visual inspection it appears unobtrusive and only came to our special attention in the clustering analysis presented here. It clearly separates from the broad distribution associated with Gum31 and has a cYSO density comparable to that of the South Pillars. It was noted in our dedicated survey of the region (Sect. 8.4.3).

On closer inspection this cluster of cYSOs is associated with an intriguing IR feature. The cYSO distribution falls into two sub-clusters: One broadly delineating the shape of an anchor towards the south-east of the IR feature and one directly associated with it. The former is coincident with an overdensity of NIR point-like sources seen in the shorter-wavelength IRAC images (Fig. 9.10a). In the MIPS 24  $\mu\text{m}$  image a semi-circular shape can be made out along which the southernmost five of the YSOs appear to be aligned and which is also visible in the PACS 70  $\mu\text{m}$  image. In the SPIRE 500  $\mu\text{m}$  image the same shape is visible, but shifted southwards compared to the lower-wavelength images. The remaining four YSOs, on the contrary, are aligned along a dark streak in the far IR. All but one cYSOs in this ‘anchor’ are classified as Class II with IRAC, six—the potential Class I YSO among them—can be identified with a MIPS point-like source. With WISE, only three of these sources are detected. Notably, the IRAC Class I candidate and its neighbour 7'' to the north, a Class II candidate, appear to be unresolved with WISE, which finds a single Class I at an intermediate position.

The northern condensation of cYSOs is coincidental with a conspicuous IR feature that exhibits broadly the shape of a question mark. The ‘dot’ of the question mark is a very bright point-like source, visible from 3.6  $\mu\text{m}$  through 500  $\mu\text{m}$ . Both here and especially in the 24  $\mu\text{m}$  image it is the brightest source by far in the vicinity. With *Herschel* it is classified as a protostar and it is also a WISE Class I candidate. In its immediate vicinity there are five cYSOs in a tight bunch, four clearly corresponding to a MIPS point-like source, the fifth ‘drowning’ in the bright source’s PSF at 24  $\mu\text{m}$ . The sixth source is the only one classified as Class I and appears as a bright point-like source in the 24  $\mu\text{m}$  image. It is embedded in a bow-shaped feature (the ‘question mark’) that begins to be conspicuous at 8.0  $\mu\text{m}$  and is visible into the FIR. In the 500  $\mu\text{m}$  image it is still very bright but not resolved any more.

### The vicinity of NGC 3324

The other outstandingly dense cluster of cYSOs associated with the Gum31 region appears right inside the H II bubble, in close vicinity to the stellar cluster NGC 3324 (Fig. 9.11). It is listed as Cluster No. 4 in Table 9.1.

Twelve cYSOs are found associated with the cluster. Only one of the SYCC cYSOs in the NGC 3324 cluster was classified as a young star with WISE and there is one other WISE cYSO in the vicinity, both Class II. The SYCC cYSOs are also classified as Class II, with one exception right at the centre of the cluster. This shows that the catalogues derived from IRAC and WISE observations seem to sample two different groups of cYSOs. Evidence to this effect is also found in other parts of the CNC.

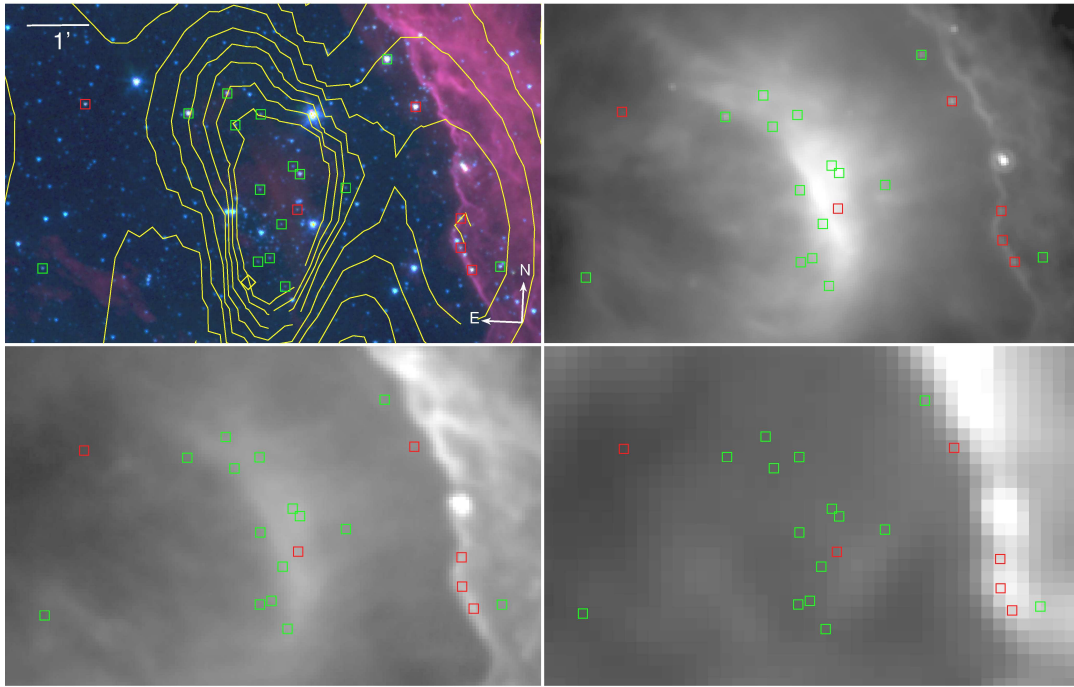


Figure 9.11: Cluster No. 4, associated with NGC 3324. Image wavelengths, contours and symbols are the same as in Fig. 9.10. The yellow diamond is placed at the approximate position of NGC 3324.

Part of Cluster No. 4 (six cYSOs) is found in front of and just behind the ionisation front. All but one of the sources were also classified as cYSOs with WISE, too, notably as the same class but for one exception. The extended emission seen in the 24  $\mu\text{m}$  image was described in Sect. 8.3 (cf. Fig. 8.2).

The cYSO population within the inside of the Gum 31 bubble that is not associated with NGC 3324 (east of it) also shows up as a loose cluster in the density map (Cluster No. 3). It is also interesting to note that of the three WISE-identified cYSOs found in the heads of pillars in the cavity (cf. Fig. 8.9), two are also classified as cYSOs using IRAC (both Class I in both samples) and one is not.

### G286.21+0.17

The cloud clump G286.21+0.17 was described in detail in Sect. 8.4.3, where we discussed the cYSO cluster associated with it found from the WISE data. Just at the edge of the WISE and *Herschel* SPIRE survey areas, it also appears as a slight overdensity in the SYCC. This can also be seen in Fig. 9.13. Only one star in the group is over our cluster limit density so that we do not define this group as a cluster. The number of cYSOs within the group is a lot lower than for the cluster observed from WISE data as the comparison in Fig. 9.9 shows.

The clump itself harbours no SYCC sources. The two bright IRAC sources that we described in Sect. 8.4.3 as WISE and MSX cYSOs are not included in the SYCC. Together

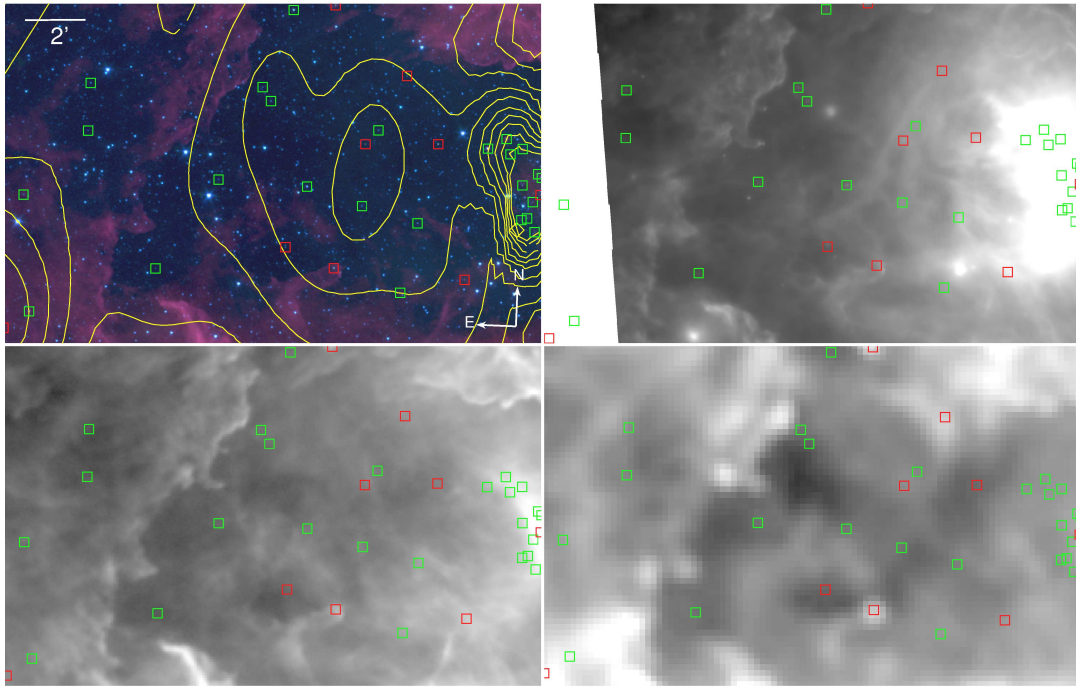


Figure 9.12: cYSOs inside the Gum 31 bubble (Cluster No. 3). Image wavelengths, contours and symbols are the same as in Fig. 9.10.

they are identified as a *Herschel* protostar candidate and neither of the aforementioned studies was able to resolve the two sources, which means that all classed them as one cYSO. *Spitzer* can provide the necessary resolution but does not detect an IR excess for either.

SYCC cYSOs are exclusively found in the young stellar cluster associated with the clump. The central cluster is probably constituted by seven cYSOs, broken up into two distinct structures: Three Class I candidates lining up along the ridge formed by warm dust as seen in the IRAC  $8.0\mu\text{m}$  images (red in the upper left quarter of Fig. 9.13) on the one hand and a group of four cYSOs to the south-west of it on the other hand. This latter group is associated with faint  $8.0\mu\text{m}$  emission, but not with colder structures. The area around it is devoid of any FIR emission.

### G286.38–0.26

G286.38–0.26 is embedded in the southern rim of the Gum 31 bubble as described in Sect. 8.4.3. While we described around ten WISE cYSOs found associated with the cluster in Sect. 8.4.3, in the SYCC there are only four sources related to it. Only one of those is above the density limit for clusters, so G286.38–0.26 is not defined as a cluster in our study.

### A cYSO cluster north of Gum 31: Cluster No. 1

A denser cluster to the north of Gum 31 is much more prominent than G286.21+0.17 or G286.38–0.26. We assigned it Cluster No. 1; in our dedicated study of the region it was

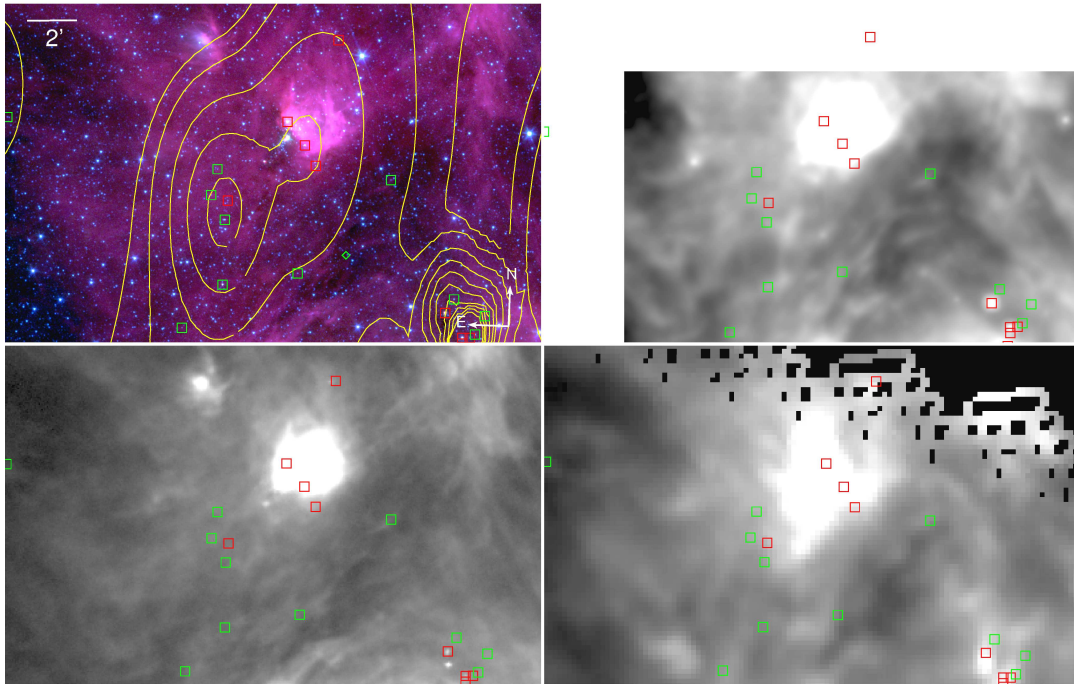


Figure 9.13: cYSOs associated with G286.21+0.17. Cluster No. 1 can be seen in the lower right corner. Image wavelengths, contours and symbols are the same as in Fig. 9.10.

noticed (Sect. 8.4.3). It is associated with a small cluster of stars in the IRAC RGB image not previously described that can be seen in Fig. 9.14. A  $C^{18}O$  clump [No. 4 of Yonekura et al. 2005] is found about  $70''$  to the north-east of this cluster.

The cYSOs themselves are located primarily to the south-west of the cluster of older stars, although three cYSOs are found scattered to its north. Clearly there is no cluster of WISE-selected cYSOs here, although six of the SYCC sources are classified in the same way from WISE data.

#### 9.4.2 The central Carina Nebula

As a centre of star formation the CN itself is of course historically better studied than Gum 31. As described in Chapter 3 and seen in Fig. 9.3, star formation is offset from the three dominating stellar clusters Tr 14, Tr 15 and Tr 16 toward the region known as the South Pillars. In Fig. 9.5 one can easily see that the densest parts are found near the Treasure Chest cluster within the South Pillars.

##### Tr 14, Tr 15 and Tr 16

The cluster Tr 14 is clearly discernible as Cluster No. 14 in the cYSO density map. Seventeen SYCC cYSOs are found in conjunction with the cluster. These cYSOs are predominantly Class II objects and consequently among the oldest objects that our study can detect. The region also is completely devoid of *Herschel* pre- or protostars. This points to a

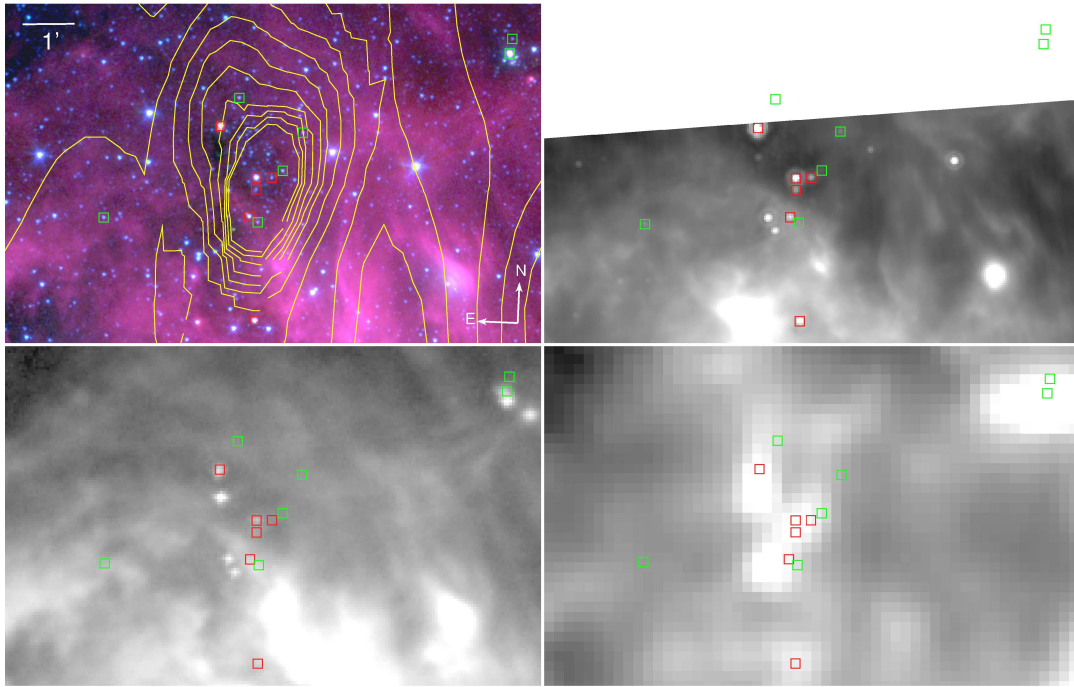


Figure 9.14: Cluster No. 1, north of Gum 31. Image wavelengths, contours and symbols are the same as in Fig. 9.10.

comparatively old population of YSOs for Tr 14. Furthermore, from the WISE sample, no cYSOs are found in conjunction with Tr 14. This is another strong hint that the WISE-detected sample is different from the IRAC-detected one and probably comprises younger stars.

Between Tr 14 and Tr 15 there is a cluster of nine cYSOs, Cluster No. 10, that is placed in the cavity between two ‘arms’ of the nebulosity of the central CN. There are a few *Herschel* pre- and protostars associated with this cluster, in contrast to the surrounding area that is comparatively free of dust and young stars. The cluster appears coincident with C<sup>18</sup>O clump No. 9 of Yonekura et al. [2005].

Contrary to Tr 14, Tr 15 is not associated with a single cluster of cYSOs. Instead, in Fig. 9.17 it is apparent that there are two smaller aggregations of cYSOs.<sup>4</sup> The first one consists of three Class II candidates that are clustered within 80'' immediately in front of a pillar, pointing slightly east of  $\eta$  Car, and a Class I candidate slightly off-centre to those three (see Fig. 9.17). The tip of the pillar contains three *Herschel*-identified protostars and there are two pre-stellar objects found further along the pillar. This finding would be in support of the theory of an age sequence in the objects left behind by an eroding pillar.

The second cluster is more dispersed, with a density peak west of the aforementioned pillar. The majority are Class II, there are just two Class I sources in the cluster.

The cluster Tr 16 in all *Spitzer* images, IRAC as well as MIPS, is outshone by the bright  $\eta$  Car. This makes analysis in this region more difficult than farther away from the star. However, there is a cluster of cYSOs directly to the south-east of  $\eta$  Car (Cluster No. 16)

<sup>4</sup>In Table 9.1, nevertheless, they appear together as Cluster No. 15.

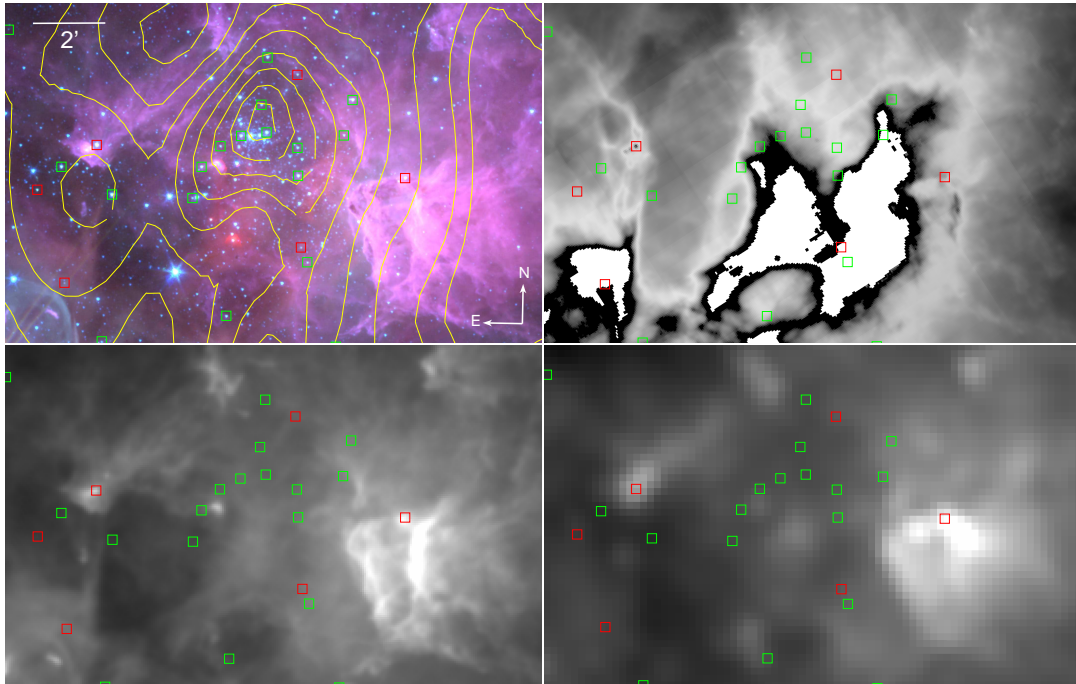


Figure 9.15: cYSO cluster in Tr 14 (Cluster No. 14). Image wavelengths, contours and symbols are the same as in Fig. 9.10. The MIPS image is saturated in large parts, which is why it is dominated by a black-bordered white region that is simply an instrumental effect.

seen in Fig. 9.18. It comprises eleven cYSOs, predominantly Class II candidates. None of them is associated with any distinguishable features in the MIR and FIR images.

The image also shows a cYSO overdensity to its south, Cluster No. 13, better seen in the top right of Fig. 9.19, where ten (six Class I, four Class II) cYSOs are found. This might correspond to the heavily obscured cluster in connection with Tr 16 that Smith et al. [2010b] report in this place (cluster G in their Fig. 13).

To the west of Tr 16 there is a cavity beneath a bright pillar almost triangular in appearance. This appears to be filled with cYSOs, as seen in Fig. 9.19. Ten SYCC sources are found here (Cluster No. 17), five of them also exhibiting an infrared excess detected by WISE. The pillar itself is filled with *Herschel* point-like sources, twelve of them, all but one protostars. There are also two Class II WISE cYSOs in the pillar, but no SYCC sources. This general pattern appears to be observable in a number of cases: While the *Herschel* and WISE cYSOs trace the clouds and especially pillars, IRAC cYSOs tend to be found in cavities, outside the densest clouds and *in front* of pillars.

### The South Pillars

As described in Sect. 3.5.1, the South Pillars are the most prominent star-forming region in the CN. This is also how they appear in our study. Looking at the overview in Fig. 9.5, the region appears as the densest overall part of the figure, consisting of several smaller clusters in close spatial association. In Fig. 9.20, which shows Clusters Nos. 18–21 and

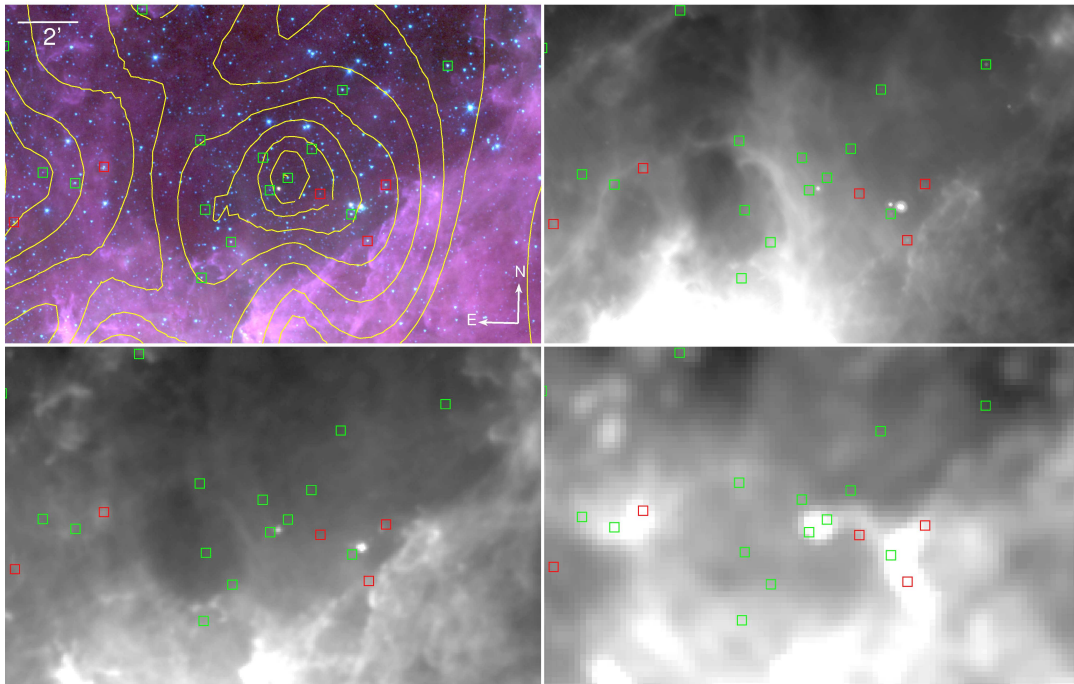


Figure 9.16: Cluster No. 10 between Tr 14 and Tr 15. Image wavelengths, contours and symbols are the same as in Fig. 9.10.

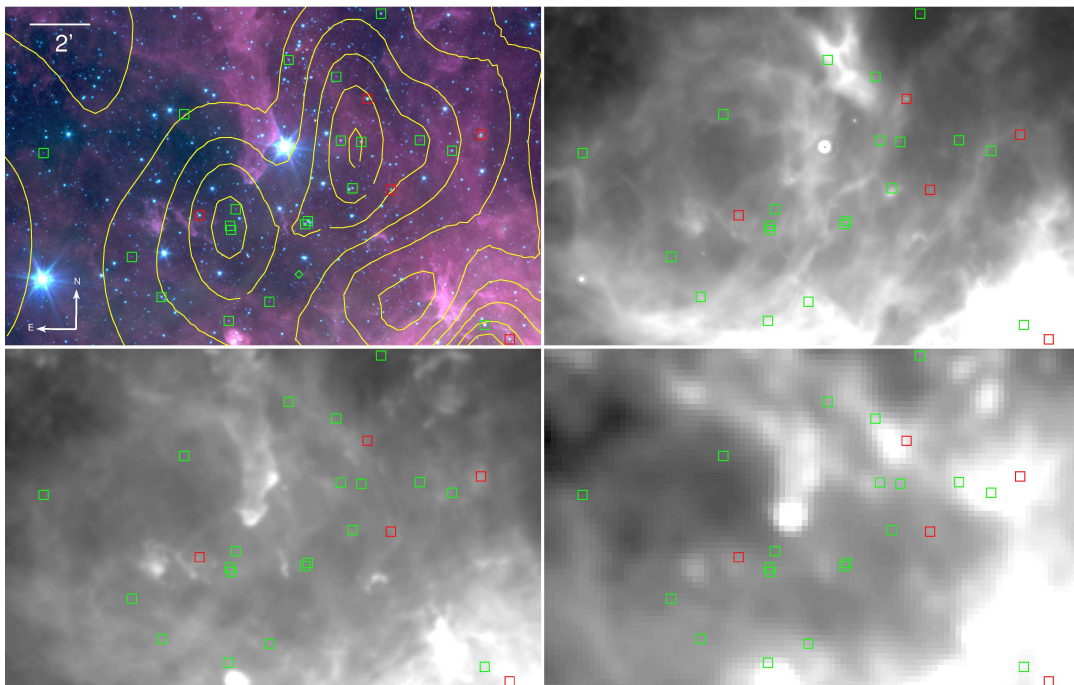


Figure 9.17: Cluster No. 15, associated with Tr 15. Image wavelengths, contours and symbols are the same as in Fig. 9.10.

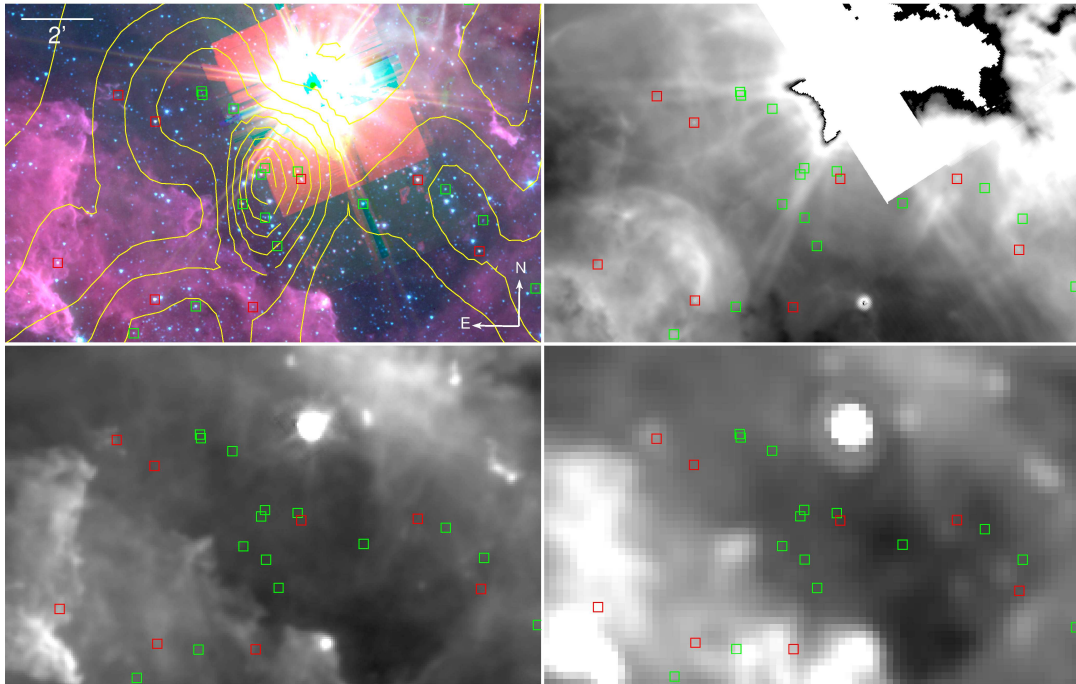


Figure 9.18: Cluster No. 16, associated with Tr 16. Image wavelengths, contours and symbols are the same as in Fig. 9.10.  $\eta$  Car is saturated in both IRAC and MIPS images, leading to the artifacts in the upper right corner of both.

Cluster No. 25 (cf. Fig. 9.21), this clustering effect can be seen.

There is a pillar on the right side of Fig. 9.20 that harbours a cYSO its head. This source is a Class I candidate with both IRAC and WISE and also a *Herschel* protostar candidate. It corresponds to MSX source G287.57–0.91 of Rathborne et al. [2004]. Another, very small, pillar is found to the west of the very bright nebular emission that is associated with the Treasure Chest. This pillar has two cYSOs at its tip, one each of Class I and Class II. In fact, the Class II candidate is not embedded in the pillar, but placed right outside it, immediately next to the Class I candidate that sits right in the pillar head.

There are at least two other pillars in the image, neither of which appears to be associated with a cYSO. There is a possibility, though, that the ‘line’ of three Class II and one Class I candidates which appears towards the upper centre of the image might be associated with the pillar in the centre of Fig. 9.20. Those four cYSOs seem to extend the pillar direction towards the north, i. e. the bright clusters and especially  $\eta$  Car. It is therefore possible that this is a group of young stars left behind by the erosion of this pillar.

In Fig. 9.21 a close-up of Cluster No. 25 is displayed. It shows a very narrow ( $\lesssim 8''$ ) pillar of dust. It is remarkable in that four Class I cYSOs are aligned along it, with one other close beside it and two Class II candidates around  $16''$  and  $43''$  in front of it, roughly in the direction in which the head points. Two of the Class I candidates are found in this head. The pillar itself is faintly seen in the  $24\ \mu\text{m}$  MIPS image and appears stronger again in the FIR, clearly visible in the  $70\ \mu\text{m}$  image with the same general outline as in the IRAC RGB image. At roughly the same position a source is seen in the  $500\ \mu\text{m}$  image.

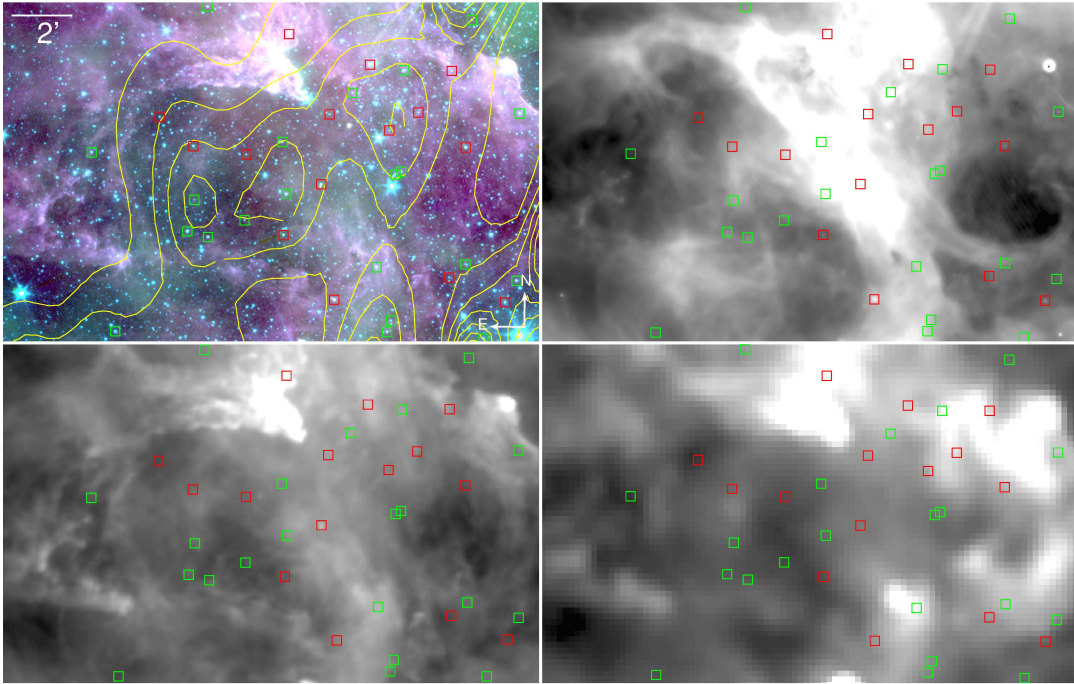


Figure 9.19: Clusters No. 13 and 17 near Tr 16. Image wavelengths, contours and symbols are the same as in Fig. 9.10.

It is notable that the slightly peculiar (having an unusual reddish halo) point-like source J104613.5–595831 shown in Fig. 9.22 directly to the south-east of the Treasure Chest is not in the SYCC, but a WISE IR excess source and a *Herschel* protostar. It probably corresponds to MSX IR excess source G287.86–0.82 detected by Rathborne et al. [2004]. We note, however, that while the source appears to have a red (i. e.  $8.0\ \mu\text{m}$ ) halo here, Rathborne et al. [2004] contrarily see “*weak  $8\ \mu\text{m}$  emission*”.

At first sight, the cavity between the clouds shown in Fig. 9.22 is a typical example of the ‘greenish hue between clouds’ in IRAC RGB images described in Sect. 7.3.3 as potentially wrongly identified EGOS. It is, however, far more extended than this and, more revealing, the  $4.5\ \mu\text{m}$  structures coincide with those seen at  $24\ \mu\text{m}$  and  $70\ \mu\text{m}$  and even  $500\ \mu\text{m}$ . The morphology is the same in all cases—compare especially the ‘kink’ in the top centre of the image. That it is seen at so many wavelengths, from  $4.5\ \mu\text{m}$  to  $500\ \mu\text{m}$  (but not in  $8.0\ \mu\text{m}$ ), might be an indication that it is not a feature caused by shocks or similar, where one would expect a few lines. Harvey et al. [2006] observed areas of green diffuse emission in their IRAC study of the Serpens Cloud, too. These, however, appear to be on much smaller scales than the emission seen here, especially regarding that this cloud is at a lower distance than the CNC.

Therefore it is likely that the extended green emission is mainly a scaling effect and not indeed a physical feature. It may only seem very bright in the  $4.5\ \mu\text{m}$  band because the  $4.5\ \mu\text{m}$  band tends to be scaled quite highly compared to the other IRAC bands [e. g. De Buizer and Vacca 2010]. It is, indeed, possible by extreme choices of the scaling for the blue  $3.6\ \mu\text{m}$  band to cause the region to appear blue-green. It appears certain, though,

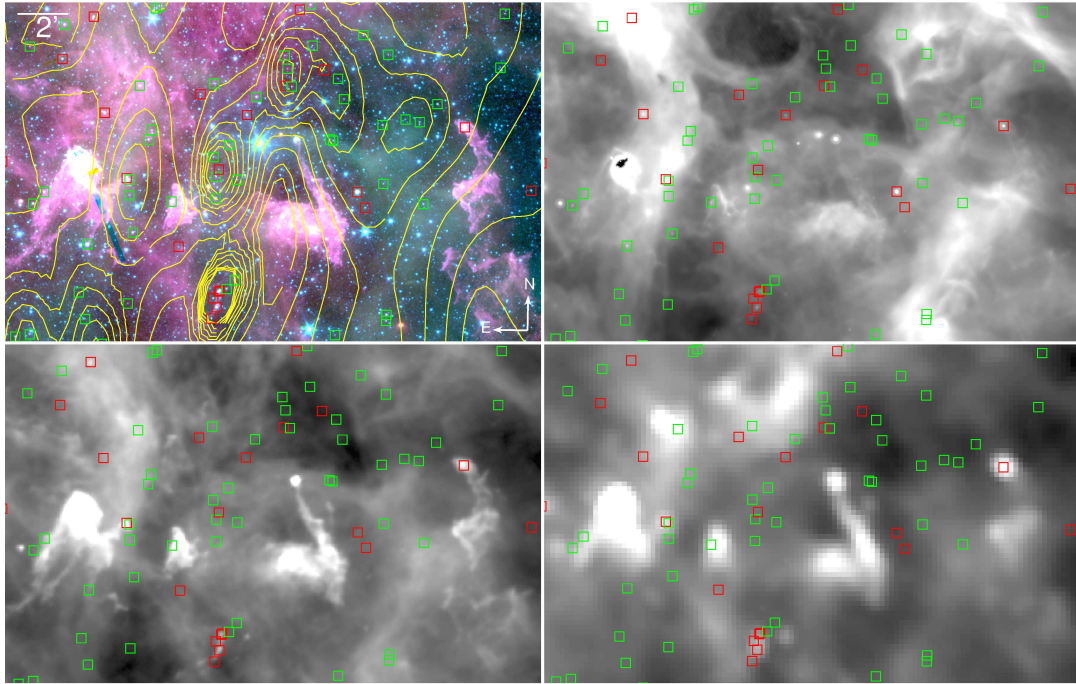


Figure 9.20: cYSO clusters inside the South Pillars region. The very bright nebulosity to the left of the image that is seen from MIR to FIR is the Treasure Chest cluster. Image wavelengths, contours and symbols are the same as in Fig. 9.10.

that whatever scales one chooses, the  $8.0\ \mu\text{m}$  band does not show these structures.

For the SYCC cYSOs there clearly is a cluster, Cluster No. 22, centred on the  $4.5\ \mu\text{m}$  emission stripe. The region is, however, completely devoid of *Herschel* point-like sources (cf. Fig. 9.2) and of WISE-identified cYSOs, too. Those are found towards the west, in and around the Treasure Chest cluster and to the east, in the cloud front seen to the left of Fig. 9.22. Possibly this cloud front, clearly outlined in very young, *Herschel*-identified sources, currently is being eroded and thus forming pillars.

The cluster shown in Fig. 9.23, Cluster No. 23, is peculiar because within a very small area ( $23''$ ) three Class II candidates and one Class I candidate cluster. This small stellar group is also clearly coincident with  $\text{C}^{18}\text{O}$  clump No. 14 of Yonekura et al. [2005]. All four cYSOs are placed roughly in a straight line that points in the same direction as a short, wide pillar  $\sim 40''$  from the closest cYSO. Within the pillar head a *Herschel*-detected pre-stellar source is found. Another *Herschel* protostar is found following the projection of the line described by the pillar and the cYSOs. Unlike in other examples described in this section, we thus do not clearly see an age sequence.

The cluster in the centre of Fig. 9.24, Cluster No. 26, might correspond to the X-ray group No. 29 of Feigelson et al. [2011, cf. Fig. F.1]. Its position is slightly offset to the north-east of the density peak seen here. The nearby group No. 31 of Feigelson et al. [2011], however, agrees very well with the small Class I-dominated eastern subset of Cluster No. 26. The rightmost part of Cluster No. 24, seen on the right in Fig. 9.24, coincides with the X-ray cluster No. 16 of Feigelson et al. [2011].

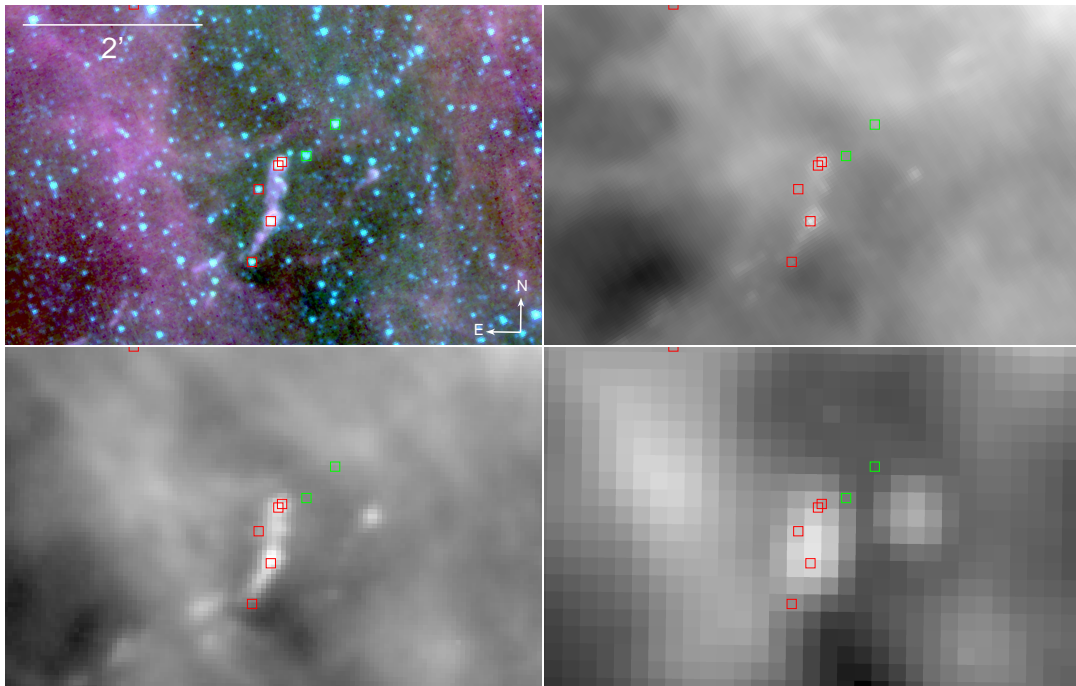


Figure 9.21: A close-up of Fig. 9.20 on Cluster No. 25. The IRAC, MIPS, PACS and SPIRE images are arranged as there.

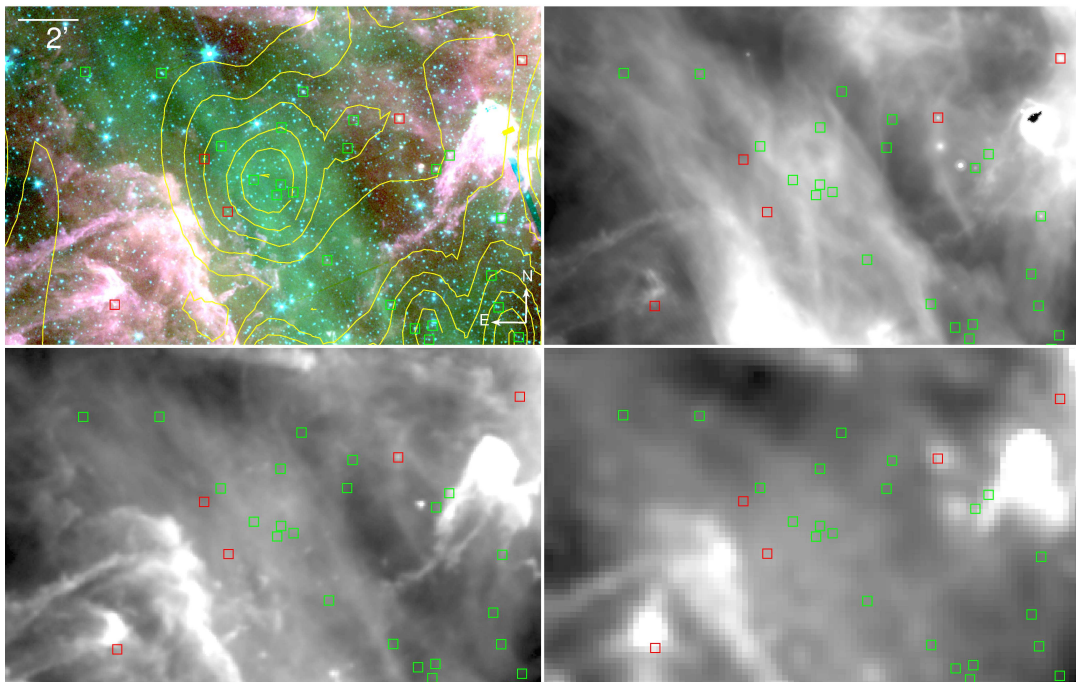


Figure 9.22: Cluster No. 22, north of the South Pillars. Image wavelengths, contours and symbols are the same as in Fig. 9.10.

9 Clustering properties of the young stellar population of the Carina Nebula Complex

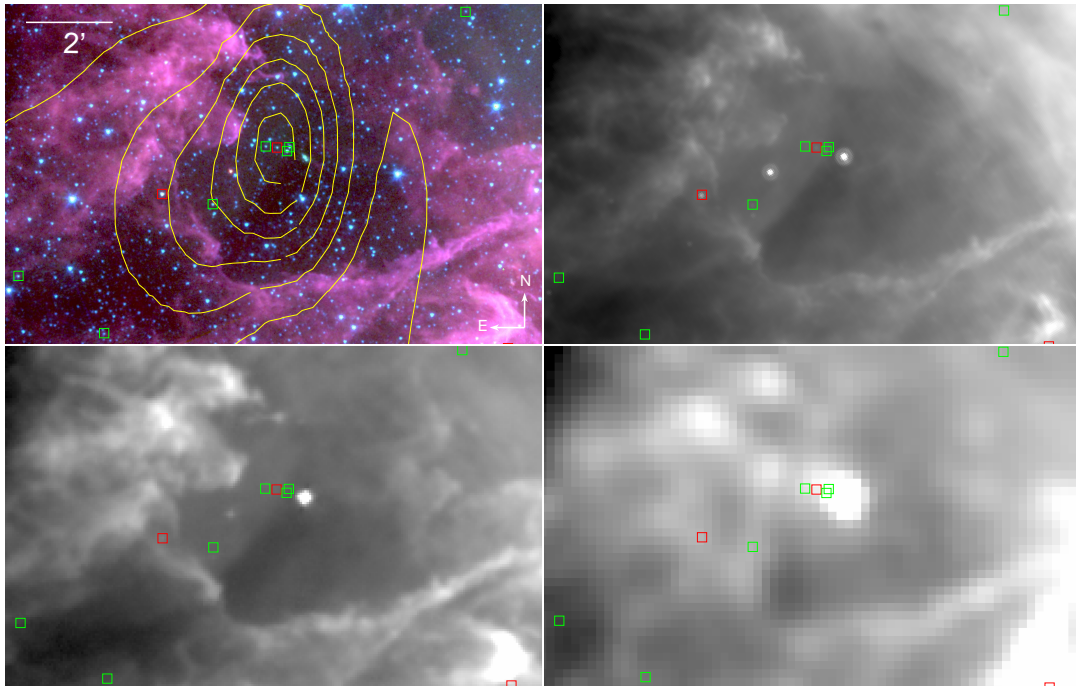


Figure 9.23: Cluster No. 23, to the east of the South Pillars. Image wavelengths, contours and symbols are the same as in Fig. 9.10.

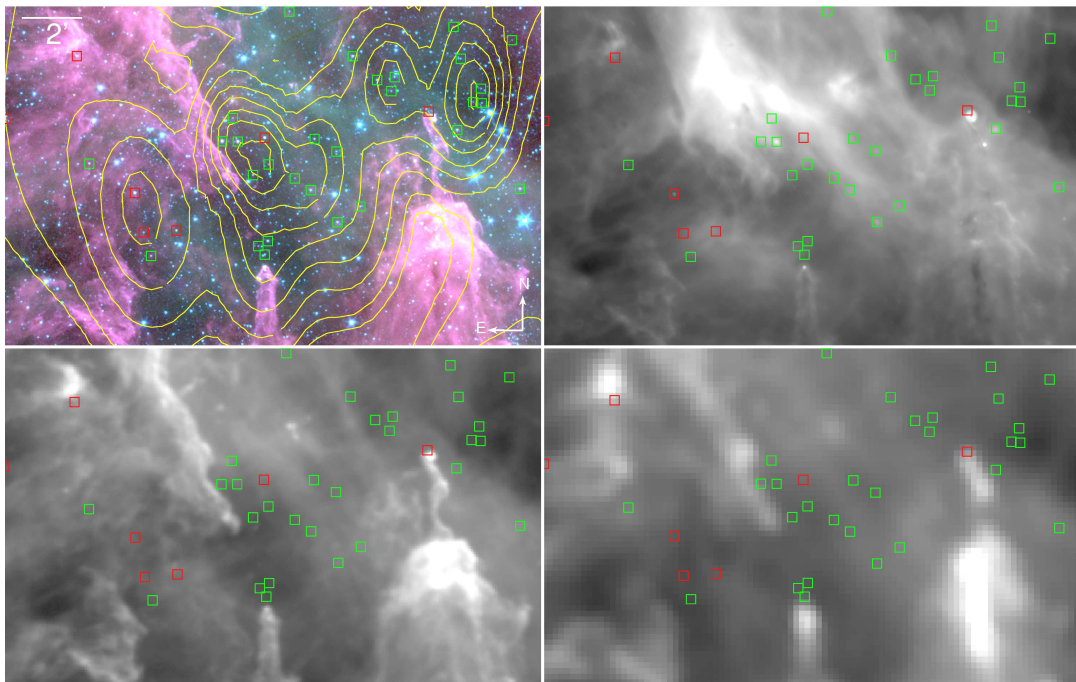


Figure 9.24: Cluster No. 26 within a cavity in the South Pillars. Image wavelengths, contours and symbols are the same as in Fig. 9.10.

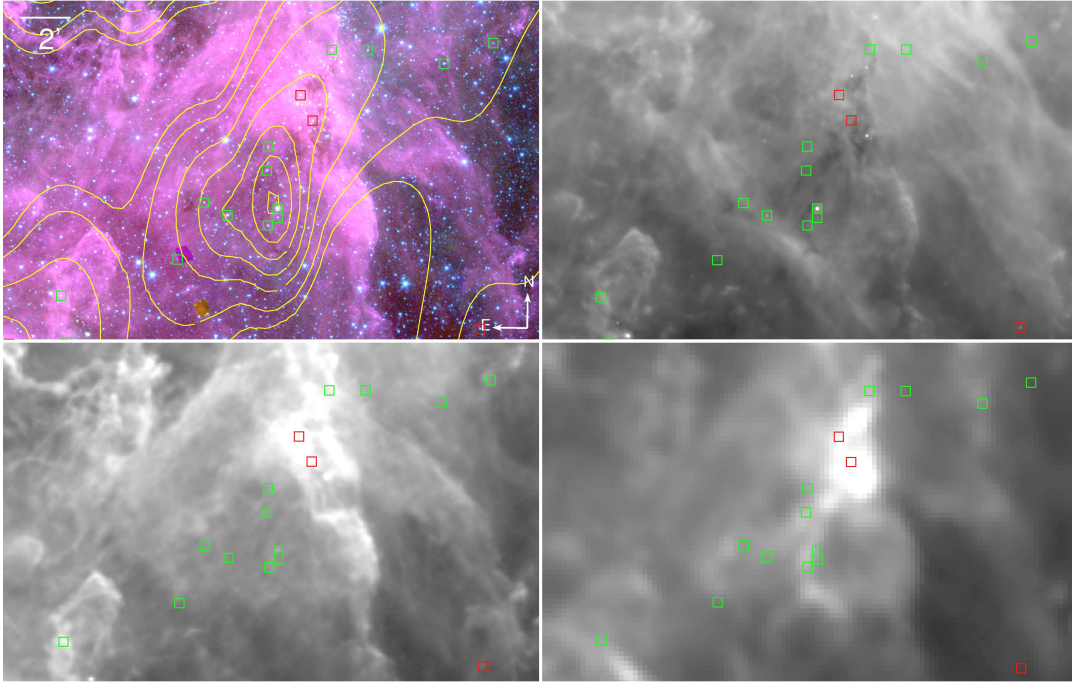


Figure 9.25: Cluster No. 27 in the foot of the Giant Pillar. Image wavelengths, contours and symbols are the same as in Fig. 9.10. Compare also Fig. 9.27.

One pillar is very prominent in Fig. 9.24, poking up from the bottom centre. It has a bright  $24\mu\text{m}$  point-like source in its tip that is, however, not identified as a cYSO. Right in front of the pillar, though, there is a compact group of three Class II candidates, clustered together within  $22''$  of each other. Especially as their immediate surroundings are comparatively devoid of other cYSOs, it is highly likely that these three sources are connected to the pillar. Within the pillar head itself, there have two protostars been detected with *Herschel*, which is again indicative of an age sequence: The older, Class II YSOs lie in front of the pillar while the younger objects are still embedded in its head.

A similar structure is seen in the thin, winding pillar towards the right edge of Fig. 9.24. It has three *Herschel* candidate protostars distributed evenly along its length and one IRAC Class I candidate right outside the head. One of the *Herschel* protostars, the one immediately in the pillar head is seen as a bright point-like source also in MIPS and IRAC images, but is not identified as a YSO by its infrared excess. This thin pillar might, however, be called a sub-pillar as it is only part of a larger structure known as the Giant Pillar, the top of which can be seen to the right in Fig. 9.24.

### The Giant Pillar

This Giant Pillar, seen in Fig. 9.25, is one of the dominant structures in the South Pillars. It has a length of roughly  $11'$  ( $\approx 7\text{pc}$ ), which makes it far larger than any other pillar found in the CNC. In its foot, Cluster No. 27 with eight cYSOs is found. Two of the sources, associated with the brightest emission in the FIR, are Class I, the rest Class II. The cluster is placed in the ‘hollow’ of the pillar foot, where the dominant nebulosity is

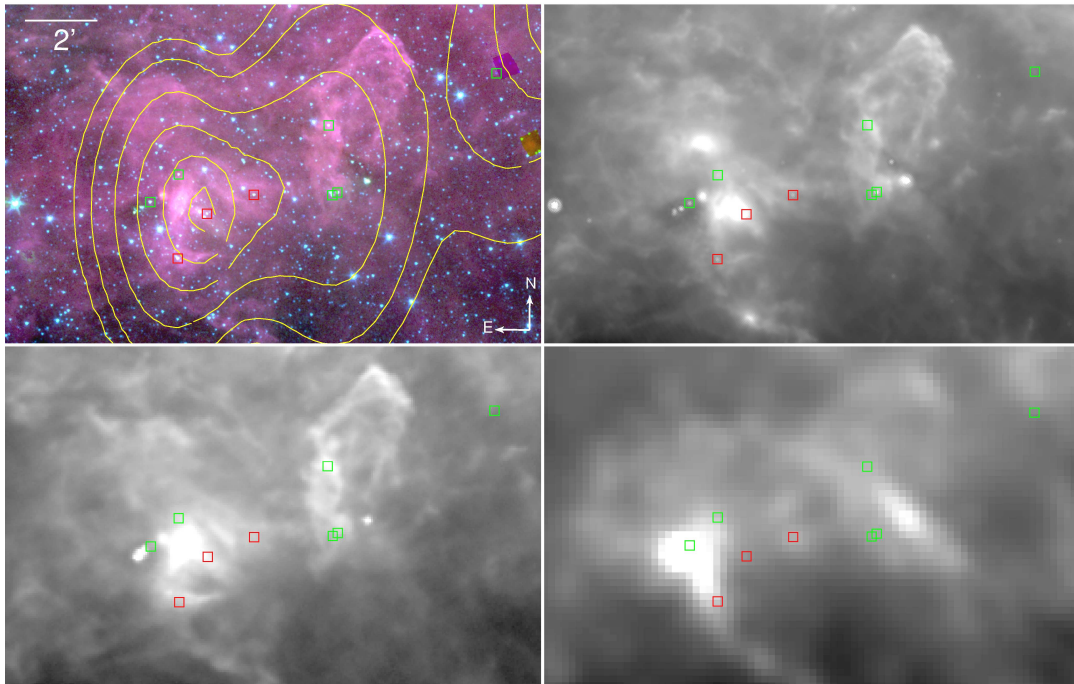


Figure 9.26: Cluster No. 28 to the south-east of the Giant Pillar. Image wavelengths, contours and symbols are the same as in Fig. 9.10.

much less pronounced than around it. The foot of the pillar is also coincident with  $C^{18}O$  clump No. 13 of Yonekura et al. [2005]. Its peak density is, however, offset to the north-west from the peak of the  $\gamma$ SO density by about  $22''$ . About 15 WISE cYSOs are found at this position, together with the two Class I candidates from the SYCC and eight pre- and protostellar sources as identified with *Herschel*.

WISE-identified cYSOs are positioned very differently from the SYCC sample. The majority are found in the interior of the pillar, where the two IRAC-identified Class I sources (classed likewise with WISE) are located. They very prominently delineate the western edge of the pillar. Sixteen of them are found arrayed along the pillar edge on a line of about  $45''$  length (cf. Fig. 9.27). This seems indicative of there being another source of irradiation apart from the one that shaped the pillar. The direction from which this hypothetical irradiation might originate points directly to the stellar cluster Collinder 228. This cluster,  $16'$  away from this line of cYSOs, contains the O8.5V star CD-593274 and several B and A stars, so appears to be a likely source.

The *Herschel* point-like sources appear to corroborate this view. Those that are found in the base of the pillar along with IRAC and WISE cYSOs are spatially coincident with these and show a predominance of protostars to the north-west, together with and behind the front of WISE cYSOs and of prestellar objects in the south-east. The orientation of all young objects is peculiarly in a broad strip running diagonally through the foot of the Giant Pillar between north-west and south-east, as seen in Fig. 9.27. The fact that the edge of the pillar is so clearly outlined in WISE cYSOs while the IRAC cYSOs are found behind them in the foot of the pillar is another indication that WISE selection traces a

slightly younger population than the IRAC selection does (Sect. 9.6).

The upper part of the pillar seems to possess its own population. It does not coincide with an officially listed  $C^{18}O$  clump from the study of Yonekura et al. [2005], however, their contours show a minor peak clearly at this position. While there are numerous *Herschel* and WISE young objects within the pillar head and also along the thin ‘sub-pillar’ described above, it is entirely devoid of SYCC sources. Feigelson et al. [2011] place their cluster No. 19 here, which we can corroborate from the young *Herschel* and WISE sources.

This two-part structure found in the cYSO population is in very good accordance with the structure that Roccatagliata et al. [2013] see from their *Herschel* observations of the cloud material: Two overlaid pillars, one running in north-south direction (their pillar B), the other running across it from the north-west to the south-east (their pillar A). The latter shows up especially clearly in their temperature map, where the across-running pillar exhibits lower temperatures than the surrounding foot of the north-south one.<sup>5</sup>

Cluster No. 24, as described above, might conceivably be associated with the Giant Pillar: It is coincident with X-ray cluster No. 16 of Feigelson et al. [2011]. The Class I candidate in the head of the wispy top of the Giant Pillar might also be considered part of the cluster.

Towards the south-east of the Giant Pillar, Cluster No. 28 is found. It appears as a clear overdensity in our SYCC density map, but, uncharacteristically, is also a dense cluster of WISE-selected cYSOs. The  $C^{18}O$  clump No. 15 of Yonekura et al. [2005] is found slightly to the north-west of the density peak of both IRAC and WISE cYSO distributions. This region clearly deserves special mention as it is not only a SYCC cluster, but also a cluster of WISE cYSOs and in the catalogues of Smith et al. [2010b] and Povich et al. [2011a] (Sect. 9.5.2). It also harbours the EGO G288.26–1.14 (Sect. 7.3.3).

## 9.5 Comparison to other studies of YSO clusters

The clustering properties of the YSOs in the CNC have been studied before, but never on a sample comprising as large an area as ours does. The study of clusters has often been the by-product of broader analysis, while other studies as that of Feigelson et al. [2011] were explicitly designed to study clusters in more depth.

In Table 9.1 the clusters we numbered are compared to the X-ray clusters of Feigelson et al. [2011] and the MIR cYSO clusters of Smith et al. [2010b]. The identification is not always unambiguous mainly because the number densities in the catalogues are different. This may skew the position of the cluster centre for low numbers (i. e. the SYCC), so that I also included those clusters which might conceivably be associated with SYCC clusters but where the clusters appear so different that this cannot be clearly stated.

### 9.5.1 The CCCP X-ray clusters of Feigelson et al. [2011]

The study by Feigelson et al. [2011] is based on the CCCP X-ray survey of the CN (cf. Sect. 3.5). They defined a spatially complete subsample of the full CCCP data set, which was then subjected to a statistical study of clustering properties.

<sup>5</sup>Roccatagliata et al. [2013] find that the centres of the pillars are always the coolest and at the same time the densest part.

To find clusters, they smoothed their sample with Gaussian kernels. Contrary to our smoothing process, which utilises the individual distance to the specified neighbour, they use a standard deviation of  $30''$  (0.3 pc at the distance of the CN) for all cases. Parameters such as the density threshold defining a cluster were set subjectively, thus making the study as observer-influenced as ours is. Preibisch et al. [2011a] find that 19 of their 20 main stellar clusters are also identifiable as clusters in the HAWK-I image (apart from cluster 19 which may be highly obscured, yielding HAWK-I non-detection). Consequently, these clusters are clusters of cYSOs, which should be comparable to the SYCC clusters discussed above. Apart from clusters Feigelson et al. also identified what they called ‘groups’, i. e. aggregates of X-ray stars of smaller numbers than what they dubbed clusters. Fig. F.1 in Appendix F shows a comparison between the clusters found in each study.

We find corresponding clusters to their clusters No. 1 (Tr 14, Cluster No. 14), No. 7 (Tr 15, Cluster No. 15), No. 12 (Tr 16, Cluster No. 16) and No. 14 (Cluster No. 13). We see possible matches for their clusters No. 8 (Tr 15, Cluster No. 15), No. 13 (Cluster No. 18) and No. 16 (Cluster No. 24). As small overdensities, not clusters as per our definition, we detect clusters No. 5 (immediately east of Tr 14, seen in Fig. 9.15) and No. 6 (the ‘nose’ to the right of Fig. 9.18). Of their 31 smaller groups outside clusters, we see group No. 22 identified with Cluster No. 21 and possible matches for seven more: Groups No. 4 and 7 (Cluster No. 10), No. 13 (Cluster No. 20 [20b]), No. 15 and 19 (Tr 15, Cluster No. 15), No. 21 (Cluster No. 21) and No. 29 (Cluster No. 26). Those 31 groups, though, show clustering on a much smaller scale than we typically observe in the SYCC (because the CCCP catalogue is much denser than the SYCC).

### 9.5.2 Spitzer cYSO clusters of Smith et al. [2010b]

In their *Spitzer* study of the CN, Smith et al. [2010b] (see Sect. 6.5.1) describe 16 overdensities of cYSOs which they subjectively picked. They expressly state that they only included the most obvious clusters in this list because the identification method is so subjective. The clusters are smaller in spatial extent than those we detect and the number of cYSOs tends to be slightly larger (except for the Treasure Chest, which is considerably larger). Most identifications between the two studies are not unambiguous because of this difference in size.

Three of their 16 clusters we unambiguously identify as SYCC clusters: *Spitzer* D, F (both in Fig. 9.20), and O. The cluster *Spitzer* O deserves a special mention, as it is identified by Smith et al., us (Cluster No. 28, Fig. 9.26), and Povich et al. [2011a] (see below) and harbours the four-part EGO G288.26–1.14 discovered by Smith et al. and described in Sect. 7.3.3.

### 9.5.3 The ‘butterfly collection’ of Povich et al. [2011a]

Povich et al. [2011a] in their paper describing the PCYC (Sect. 3.5.3) also present a ‘butterfly collection’ of “*intriguing YSO sub-clusters*”. This includes the cluster *Spitzer* O, which, as stated in Sect. 9.5.2, we also identify. The obscured X-ray cluster No. 18 of Feigelson et al. [2011] they report associated with IR source G287.9186–01.2913 is not seen to correspond to a cYSO cluster in either the Povich et al. [2011a] study or ours. However, the IR source is a cYSO in PCYC and SYCC and seen to have an IR excess with WISE.

Their clusters *Spitzer* P and *Spitzer* Q<sup>6</sup> appear to correspond to our Cluster No. 10. Probably Cluster No. 10 corresponds mainly to Q, while P is better matched by the WISE cYSOs that appear to cluster around 50'' in front of the cloud front there. Here, again, IRAC and WISE cYSOs appear to separate into two different populations. Cluster *Spitzer* R, however, is associated with a single cYSO each in the IRAC and WISE-based catalogues and, quite to the contrary, is a particularly *empty* region in both surveys. There are, however, four *Herschel* point-like sources clustered at the position of *Spitzer* R, which might indicate that a potential cluster could be young.

The cluster Cr 232 is not seen as a cluster in either sample of cYSOs, but does constitute a very minor overdensity, causing a very slight bulk in our density contours. Four SYCC sources, one WISE cYSO and three *Herschel* protostars are found here.

## 9.6 Discussion and conclusions

### Different populations

It is known that the *Herschel*-selected prestellar objects and protostars are, as such, a younger population than those cYSOs selected from IRAC data, which are predominantly Class I and Class II. This has been utilised for the analysis in Chapter 8 already and is also very apparent in the comparison done in this chapter. It also appears, however, that the WISE-selected sample traces an intermediate population, older than the *Herschel* point-like sources, yet younger than the majority of the SYCC sources. Though the two MIR studies often agree and select the same sources, there are several regions in the CN where the WISE-selected cYSOs clearly form a separate population from those selected with IRAC.

Maybe the most striking example is Gum 31 with its cluster NGC 3324. In Chapter 8, which focussed on the WISE sample, we declared NGC 3324 to be an old cluster because of its lack of cYSOs. Yet, in Sect. 9.4.1 we discussed the SYCC population of the cluster—twelve cYSOs clearly associated with the cluster, in sharp contrast to the WISE population. A possible explanation for this disparity would of course be that the SYCC sources are simply older than the WISE ones. In Chapter 8, it has also been shown that the WISE-detected cYSOs lie predominantly in the bubble rim. Figure 9.9 shows both populations in direct comparison and it can clearly be seen that no such tendency can be attested for the SYCC sources. On the contrary, they fill the interior of the bubble, where WISE cYSOs are scarce. This, too, might indicate that the sources found inside the bubble were left behind by the advancing ionisation front while those outside it were more recently triggered by the front at its current position.

In this scenario, we would expect some WISE cYSOs from the ‘front’ and ‘back’ of the bubble projected into its interior, too. These, indeed, are there. On the other hand, following the same logic it is feasible that the SYCC sources are *projected* where they are found from the wall of a bubble oriented towards us. However, if a population uniformly distributed on a spherical surface was projected onto our view direction, we would still expect to see a majority of sources towards the side walls. This is observed for the WISE-identified cYSOs, but not for the SYCC sources.

---

<sup>6</sup>This nomenclature extends the clusters *Spitzer* A to *Spitzer* O employed by Smith et al. [2010b] (Sect. 9.5.2).

WISE reaches longer wavelengths compared to IRAC ( $12\ \mu\text{m}$  in the colour-colour diagram compared to  $8.0\ \mu\text{m}$ ). Because a protostar's SED is especially steep in this region, this small difference can make a large difference in detectability. As IR excess in longer wavelengths traces colder material and thus younger stellar objects, WISE has higher chances of detecting the younger objects.

Sensitivity might also be an issue, where the greater sensitivity of IRAC compared to WISE (cf. Sect. 8.2.1) enables us to detect sources with weaker IR excess. As this excess diminishes over the life of a developing star, this means that stars losing their excess remain detectable with an instrument that reaches deeper in sensitivity. Consequently, older stars could stay detectable with IRAC when they are already too faint to be detected with WISE.

## Clusters

Generally, the cYSO sample is widely distributed. In a low-resolution overview, however, it is clear to see that firstly young stars are found in connection with the dust and clouds in the CNC and secondly that there are two distinct centres: The South Pillars on the one hand and Gum 31 on the other hand. This lends additional weight to the detailed analysis of Gum 31 performed in Chapter 8 as we have undoubtedly shown that it is a sadly neglected part of the complex that warrants more attention than it is currently given.

The more detailed analysis of the clusters has also shown that while some of them are associated with well-known clusters such as Tr 14, there are many more, some not much smaller in numbers, that are distributed all over the CNC. Clustering analysis has also helped entirely unknown clusters to surface that will surely be rewarding targets for further study. A prime example is Cluster No. 7 described in Sect. 9.4.1, which only came to our special attention when a detailed search for YSO clusters was performed. Many more such objects may still be hidden within the region.

In general, all cYSO clusters observed in the region led us to some interesting feature. Some were associated with nebulosity, while others pointed to small stellar clusters as yet unstudied. A large number, however, also exhibit a behaviour that appears to be a 'smoking gun' for the theory of triggered star formation in the South Pillars: They are found in connection with the dust pillars that abound there. In some cases, SYCC sources are found in the heads of such pillars. Yet there are more cases to be observed where the IRAC cYSOs are found immediately *outside* pillars. This is a behaviour that would be expected if young stars were left behind by a receding pillar in a radiatively triggered star-formation process. The distribution of the (younger) *Herschel* point-like sources reinforces this argument: They exhibit a clearly different distribution from the SYCC sources and line the cloud edges and the pillars. *Herschel* sources are rarely found outside those encasings. We have shown several examples of pillars, most prominently the Giant Pillar described in 9.4.2, that illustrate this age structure well.

We find a number of clusters that have not been described before, for two reasons. The obvious first reason is that we searched for YSO clusters in regions where this had not been done before. This includes the entire Gum 31 region with our Clusters Nos. 1–8. The same is true for Clusters No. 9, 11, 12, 14, 15 and 16, which lie outside the region surveyed by Smith et al. [2010b] (but not that of Feigelson et al. [2011]). Cluster No. 29 lies outside this region as well as the one surveyed by Feigelson et al. [2011] and is only covered by

our exceptionally large study field.

Clusters No. 18, 19 and 28 do lie inside the area covered by Smith et al. [2010b] and are also detected in that study. Clusters No. 13, 20 [20b], 21 and 24 may be co-detections by both studies, but cannot be positively identified as the same clusters. We also find Clusters No. 13, 14, 15 and 16 to coincide with clusters identified by Feigelson et al. [2011], which in the case of Clusters No. 14, 15 and 16 is not entirely unsuspected as these correspond to the clusters Tr 14, Tr 15 and Tr 16. Furthermore, Clusters No. 11, 18, 20 [20b], 21, 24 and 26 are possible co-detections with this study of X-ray clusters.

The second category of prior non-detections is the scientifically more interesting one: Clusters we identify where earlier studies have not detected clusters. In the case of the study by Feigelson et al. [2011] this of course may easily be due to the different nature of YSOs with X-ray excess and those with IR excess. In the case of the *Spitzer* study by Smith et al. [2010b], differing selection of cYSOs and clustering criteria may be the reason. The clusters not detected by Smith et al. [2010b] are Clusters No. 10, 17, 20a, 22, 23, 25, 26, and 27. Feigelson et al. [2011] do not detect Clusters No. 9, 11, 12, 17, 19, 20a, 22, 23, 25, 27 and 28. In conclusion this means that our Clusters No. 9, 11, 12, 17, 20a, 22, 23, 25 and 27 represent clusters to our knowledge never detected in prior surveys of the same area.

### Spread-out population

Another notable observation is that not all cYSOs in Carina are found in clusters. There is quite a substantial spread-out population as well. Referring back to the discussion of contamination in Sect. 9.1, we can conclude that the level of cYSOs we observe outside the clusters is above contamination and that therefore both variants can be observed in the CNC: cYSOs concentrated in dense clusters and those in a loose, spread-out population.

Up to  $\sim 60\%$  of the cYSOs in the region surveyed are found outside clusters<sup>7</sup>, which makes this quite a substantial population. We can conclude that neither spread-out nor clustered population dominate the CNC, but that both contribute to the total stellar population in the area equally. This is in agreement with the results of Feigelson et al. [2011] and Preibisch et al. [2011c], who find that about 50% of the young stars in the CN are found outside clusters.

### Total stellar populations

In the field covered by the CCCP, Feigelson et al. [2011] estimate a total young stellar population of 104 000 YSOs. Within this area, we count 366 cYSOs. Extrapolating this to the complete  $2.3^\circ \times 3.0^\circ$  area of the SYCC and the 759 cYSOs found there, we would expect a total young stellar population about twice the number of Feigelson et al. [2011], amounting to  $\sim 200\,000$  YSOs. About a third of cYSOs in clusters are found in the northern part of the CNC. This demonstrates that studies that concentrate on the central parts of the CNC miss a large number of young stars that are situated outside the most popularly studied parts of the complex.

---

<sup>7</sup>In Sect. 9.3.1 301 cYSOs out of the 759 cYSOs studied were found to have a density above our clustering level, of which 9 are isolated and not part of clusters.

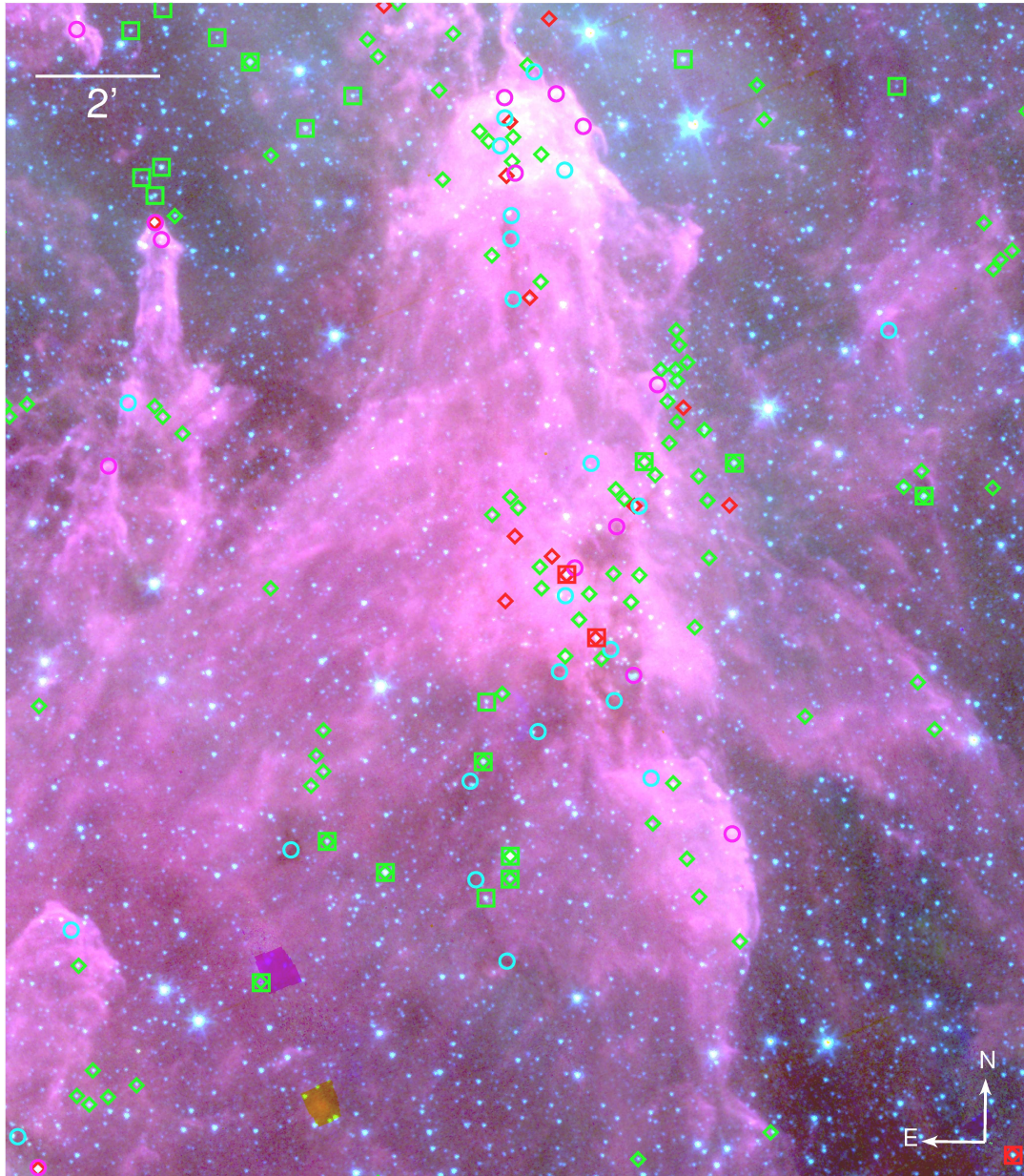


Figure 9.27: cYSOs in the Giant Pillar, overlaid on a *Spitzer* IRAC RGB image (red:  $8.0 \mu\text{m}$ , green:  $4.5 \mu\text{m}$ , blue:  $3.6 \mu\text{m}$ ). The circles are *Herschel* point-like sources (magenta for protostars, cyan for pre-stellar objects). The boxes are SYCC cYSOs and the diamonds WISE-identified cYSOs (for both: Class I in red, Class II in green).

## 10 Summary

The study presented in this work was designed to provide a uniform database for sources bright in the mid-infrared (MIR) for the entirety of the Carina Nebula Complex (CNC). While previous studies focused on the historically well-studied immediate surroundings of  $\eta$  Car and the prominently star-forming South Pillars, the explicit aim was to cover the complex out to its poorly studied outlying regions. The Gum 31 region with the stellar cluster NGC 3324, especially, has not historically been recognised as part of the complex. Here it is shown that not only is it connected to the central Carina Nebula (CN) in a way that points towards their being two parts of the same complex, but that it also is an important centre of star formation.

Observational data in the MIR obtained with the *Spitzer* Infrared Array Camera (IRAC) are available to the public from the *Spitzer* Heritage Archive. Large observations of the CNC have been performed, but never before gathered into a point-source catalogue as it is done here. I processed the raw observational data with the MOPEX and APEX programs provided by the *Spitzer* Science Center. Using them, a large catalogue of photometric data, the Spitzer Point-Source Catalogue (SPSC), could be compiled.

It encompasses 338 782 sources all over the CNC, 57 828 of which fall into the Gum 31 area. Of the full catalogue, 244 855 sources are detected in two bands or more, which is a first measure of reliability of point-source detection. A comparatively small number, 43 458 point-like sources, are detected in all four bands. This number is mainly limited by IRAC's longest-wavelength band, which has a lower sensitivity and the least likelihood to pick up point-like sources.

Young stars are identified from the catalogue by their typical infrared excess originating from their circumstellar disks. This infrared excess causes the young stellar objects (YSOs) to be placed in identifiable regions of colour-colour diagrams and thus can be utilised to select candidate young stellar objects (cYSOs) from the catalogue. Incorporating a series of precautions to avoid biasing the selection through catalogue incompleteness for faint objects and contamination through non-YSO exhibiting infrared excesses such as active galactic nuclei or asymptotic giant branch stars, I compiled a catalogue of cYSOs, the Spitzer YSO Catalogue in Carina (SYCC). It contains 759 sources, of which 221 are classified as Class I sources and 538 as Class II sources. The SPSC and consequently the SYCC cover an area of  $2.3^\circ \times 3.0^\circ$  including both the central CN with the well known star-formation region of the South Pillars and outer regions, such as the poorly studied Gum 31 region.

With the aid of these catalogues and combining them with observations in other wavelengths I gathered information on the very young stars in the complex. The catalogues could be matched with the all-sky surveys of 2MASS to cover the near-IR (NIR) and WISE to provide alternative measurements in the MIR. Furthermore they were combined with *Herschel* observations in the far-IR (FIR). For select cases, additional data could be gleaned from *Spitzer* MIPS images and from HAWK-I, VISTA (both NIR) and LABOCA (sub-mm) studies of the CNC.

Combining all these data, it was possible to assemble the spectral energy distributions (SEDs) of selected objects over a wide wavelength range. These SEDs are directly dependent on the properties of the observed object. By fitting the individual SED with a variety of models, the parameters that determine the best-fit model can be taken as a best fit to the object properties. In this way, stellar masses as well as disk and envelope masses can be estimated.

Past studies of the CNC provided lists of objects that are connected to the jets that young stars are observed to emit: Herbig-Haro jets, extended green objects (EGOs) and molecular hydrogen emission-line objects. EGOs are observed in the MIR, but Herbig-Haro jets are bright in optical wavelengths (e. g. with HST) and molecular hydrogen emission-line objects are observed in the NIR (e. g. with HAWK-I). Their sources, however, are YSOs. Therefore this study was able to discover the probable *sources* of the jet phenomena, together with three EGOs and five compact green objects. Out of 55 surveyed jet objects, it was possible to allocate sources for 36. Compared to the number of cYSOs determined in the entire CNC this is low, but the majority of jet phenomena are not observable due to their faintness.

For those 17 objects where enough data points were gathered to allow the assembly of an SED, the SEDs were fitted and stellar parameters obtained. Stellar masses were found to range between  $\sim 1 M_{\odot}$  and  $\sim 10 M_{\odot}$ . Whereas the lower boundary should be due to the detection limit, the upper limit illustrates that no high-mass stars seem currently to be forming in the CNC. By comparing the numbers of optical to infrared (IR) jets, it could also be shown that the majority of stars appear to be forming near the surfaces of clouds.

Furthermore, a region hitherto poorly studied was brought into focus: I characterised the young stellar population of the Gum 31 region, using primarily WISE MIR data. In a way analogous to the selection of cYSOs from IRAC data cYSOs were selected from the WISE all-sky survey. This yields  $\sim 660$  YSOs in the region, compared to  $\sim 300$  from the IRAC catalogue. A closer look is also taken at *Herschel* observations, which demonstrate that Gum 31 is connected to the central CN. *Herschel*-identified protostars and prestellar objects trace a younger population than the MIR cYSOs. They are seen to exhibit clustering behaviour and also to outline the edges of the Gum 31 bubble.

Two different modes of triggered star formation are evidenced in the region. A ‘collect and collapse’ model run with the parameters of the observed H II region leads to a simulated bubble size which is well in agreement with that observed. Radiative triggering, on the other hand, is evidenced by cYSOs found in the heads of dust pillars. In agreement with the results for the central CN, SED fitting for nine objects in and around Gum 31 found no evidence for YSOs with masses above  $\sim 7 M_{\odot}$ . Two further cYSOs are shown to be probable sources of HH jets. The total young stellar population in the Gum 31 area could be estimated to be  $\sim 5000$  YSOs.

The SYCC was employed for a very large-scale search for young stellar clusters. Because it covers the well-studied central CN *as well* as the outlying regions, it can discover new features as well as provide a test for cross-detections with previous studies. The search was a systematic one, employing a nearest-neighbour algorithm to compute the density of cYSOs and an objective cutoff density criterion to define clusters. In the CNC, I detected 29 cYSO clusters. Of those, seven clusters were also detected in prior studies. This corroborates the validity of the cluster search method. In the CNC, 22 new clusters are detected, eight of those within the Gum 31 region. Nine of the clusters are new detections

in regions that were subject to earlier IR studies. It also becomes apparent that Gum 31 is an important centre of star formation, exhibiting eight cYSO clusters.

The comparison of the IRAC cYSOs with those selected from WISE and *Herschel* data demonstrates that those three trace different populations. The *Herschel* pre- and protostars obviously show a different distribution than the Class I and Class II YSOs traced by the two MIR instruments, but it also appears that IRAC traces a slightly older population than WISE does.

In several cases the older IRAC-detected cYSOs are found situated in front of a pillar in which *Herschel*-detected pre- or protostars are embedded. These cYSOs left behind appear in small groups or in clusters according to our definition. This is a ‘smoking gun’ for triggered star formation where a receding pillar leaves behind forming stars in its wake.

For the complete CNC, a young stellar population of  $\sim 200\,000$  is estimated, which would place the main star formation in the central CN, but attests Gum 31 to be a non-negligible home to young stars. I was also able to show that while stars forming in clusters constitute an important part of the young stellar population in the CNC, up to 60% are in a distributed population that does not cluster. This is in agreement with a 50/50 separation attested by earlier studies.

More in-depth follow-up studies and further large studies in other wavelengths would be able to enhance our view of the CNC. This work can only present a sweeping overview over the clusters, whereas many of them show intriguing features that would merit a closer look. Cluster No. 7 near Gum 31, for example is seen as a cluster in the NIR and the FIR and is associated with MIR point-like sources and nebulosity. The Giant Pillar is a complicated structure of overlapping features and would merit closer study of the age structure of its young population.

The catalogue presented here will hopefully prove a useful tool for further studies. It provides photometric information from  $3.6\,\mu\text{m}$  to  $8.0\,\mu\text{m}$  in a compact way and allows a quick lookup of for a given position. Hopefully, it will find use as a resource for large-scale studies or as a look-up table for studies of individual sources.

# A Instrument zeropoints

For the conversions between flux  $F$  in Jansky and magnitudes according to

$$\text{mag} = -2.5 \cdot \log \frac{F}{F_0} \quad (\text{A.1})$$

throughout this work we used the following zero-magnitude fluxes  $F_0$ :

## IRAC

**3.6  $\mu\text{m}$ :** 280.9 Jy

**4.5  $\mu\text{m}$ :** 179.7 Jy

**5.8  $\mu\text{m}$ :** 115.0 Jy

**8.0  $\mu\text{m}$ :** 64.9 Jy

[IRAC Instrument Handbook v2.0.2, 2012]

## WISE

**3.4  $\mu\text{m}$ :** 306.682 Jy

**4.6  $\mu\text{m}$ :** 170.663 Jy

**12  $\mu\text{m}$ :** 29.045 Jy

**22  $\mu\text{m}$ :** 8.284 Jy

[Cutri et al. 2012]

## 2MASS

**J:** 1594 Jy

**H:** 1024 Jy

**K<sub>s</sub>:** 666.7 Jy

[Cohen et al. 2003]

## B Removing contaminants from the WISE YSO catalogue

As described in Sect. 6.3.1, following Koenig et al. [2012] we try to remove the contaminants before selecting YSOs from the WISE All-Sky Data Release. This is done step by step by removing background galaxies (Eq. (6.8), Fig. B.1), active galactic nuclei (AGN) (Eq. (6.9), Fig. B.2a and Eq. (6.10), Fig. B.2b), resolved polycyclic aromatic hydrocarbon (PAH) emission (Eq. (6.11), Fig. B.3a and Eq. (6.11), Fig. B.3a) and shock emission knots (Eq. (6.13), Fig. B.4).

The plots shown below are independent, i. e. the contaminants identified in each step are not removed between the plots and each shows the full sample. This means that the same source could theoretically be flagged as a contaminant by two different methods.

Of the 1 105 290 sources found overall in the region selected from the WISE catalogue ( $2^\circ$  around  $\eta$  Car), we remove a large number during this process: 18996 sources are flagged as background galaxies, 130011 as AGN, 50326 as unresolved PAH regions and 245 as shock

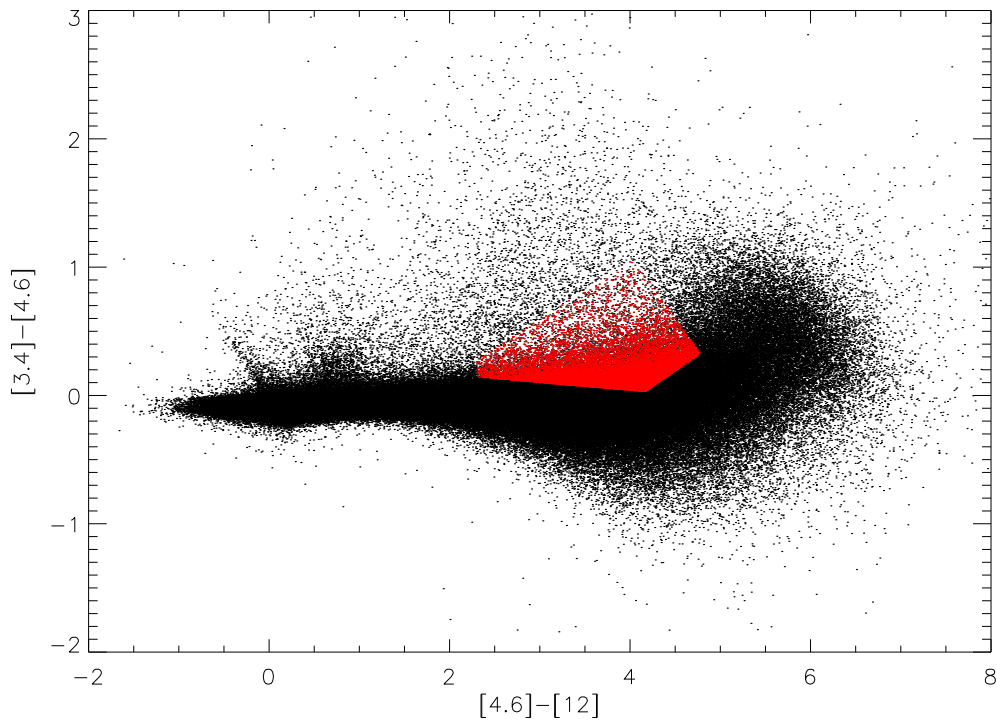
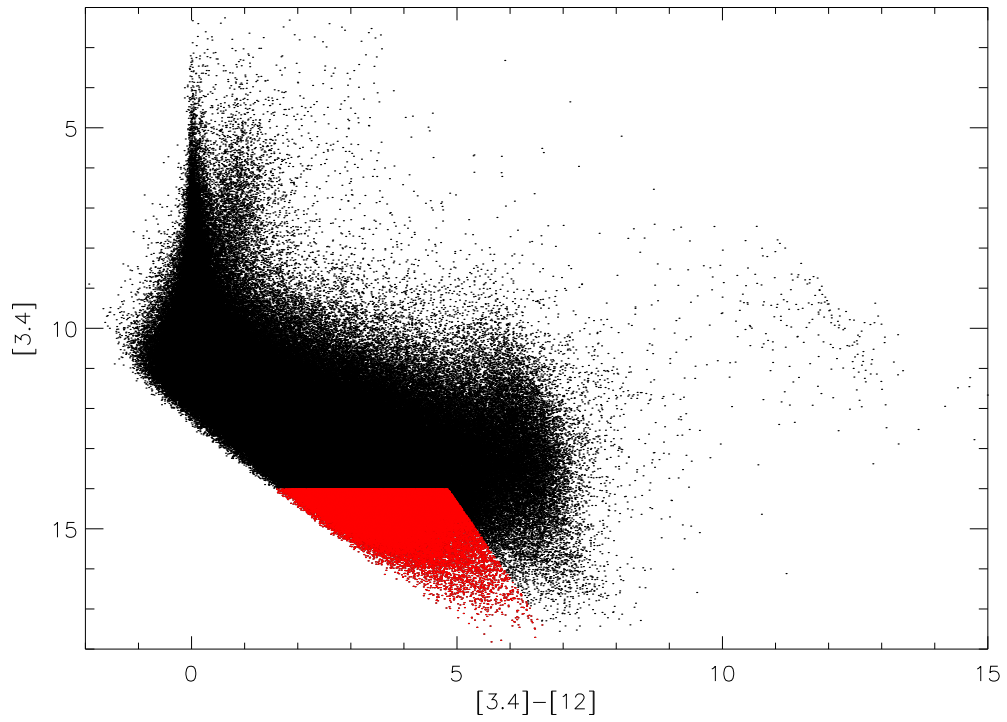
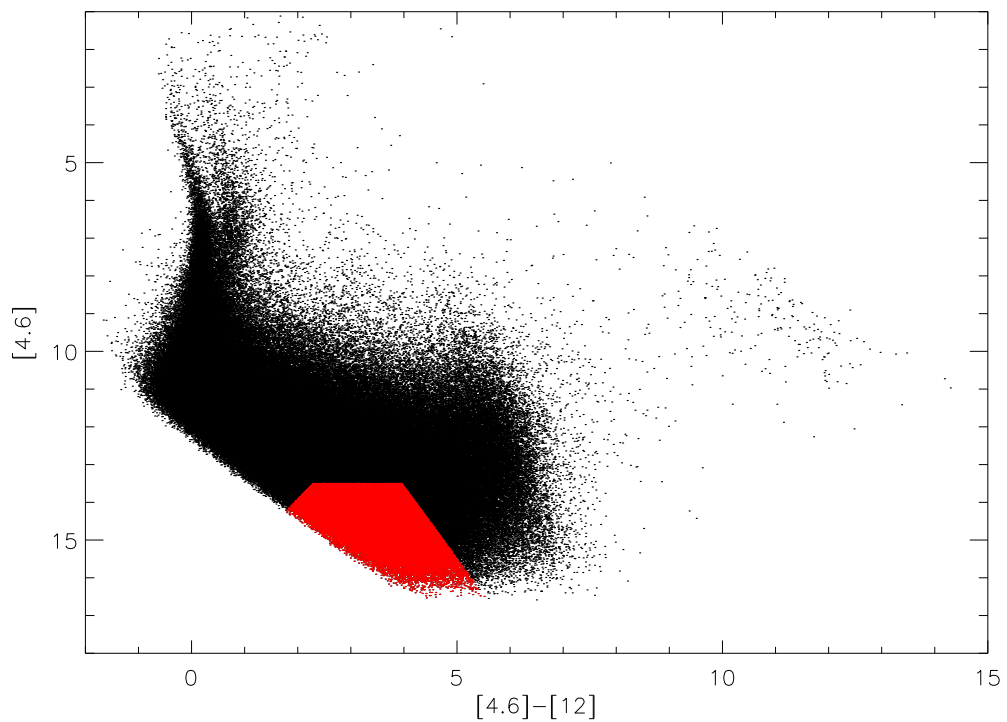


Figure B.1: Colour-colour diagram of WISE catalogue sources: Removing background galaxies (red) following Eq. (6.8). 18996 sources flagged.

*B Removing contaminants from the WISE YSO catalogue*

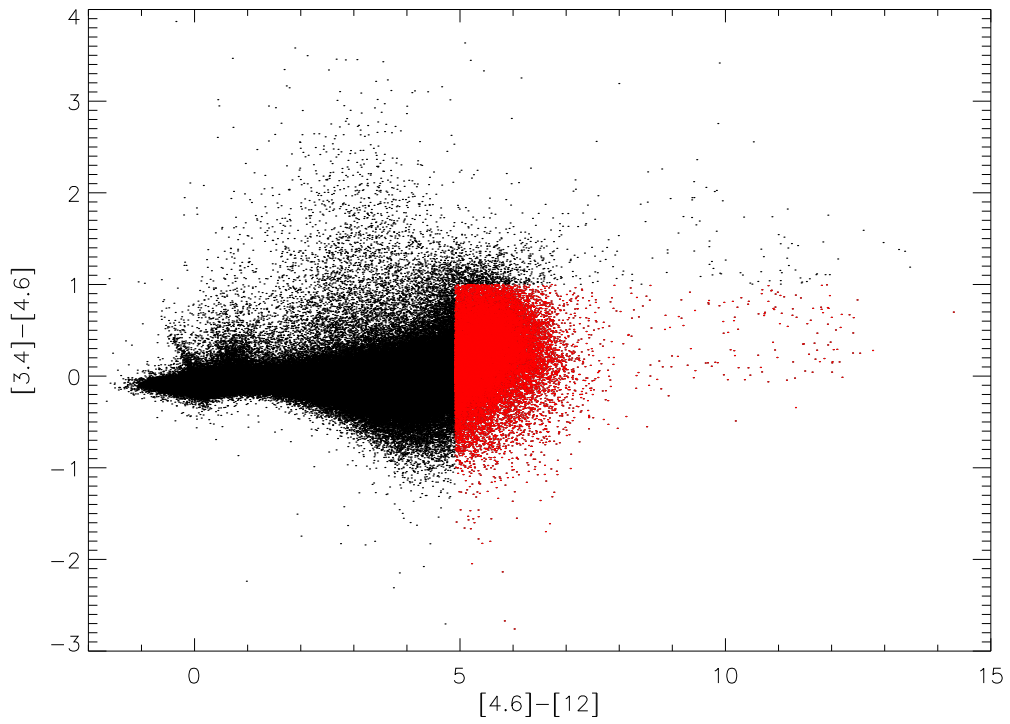


(a) Following Eq. (6.9).

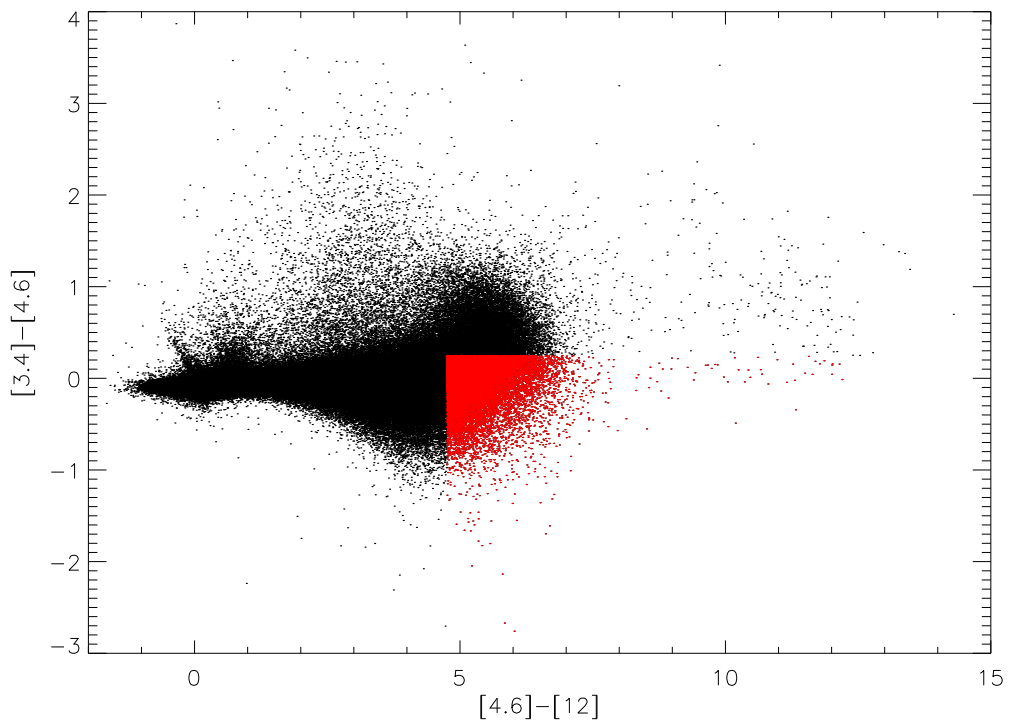


(b) Following Eq. (6.10).

Figure B.2: Colour-colour diagram of WISE catalogue sources: Removing AGN (red). 130011 sources flagged.



(a) Following Eq. (6.11).



(b) Following Eq. (6.12).

Figure B.3: Colour-colour diagram of WISE catalogue sources: Removing PAH regions (red). 50326 sources flagged.

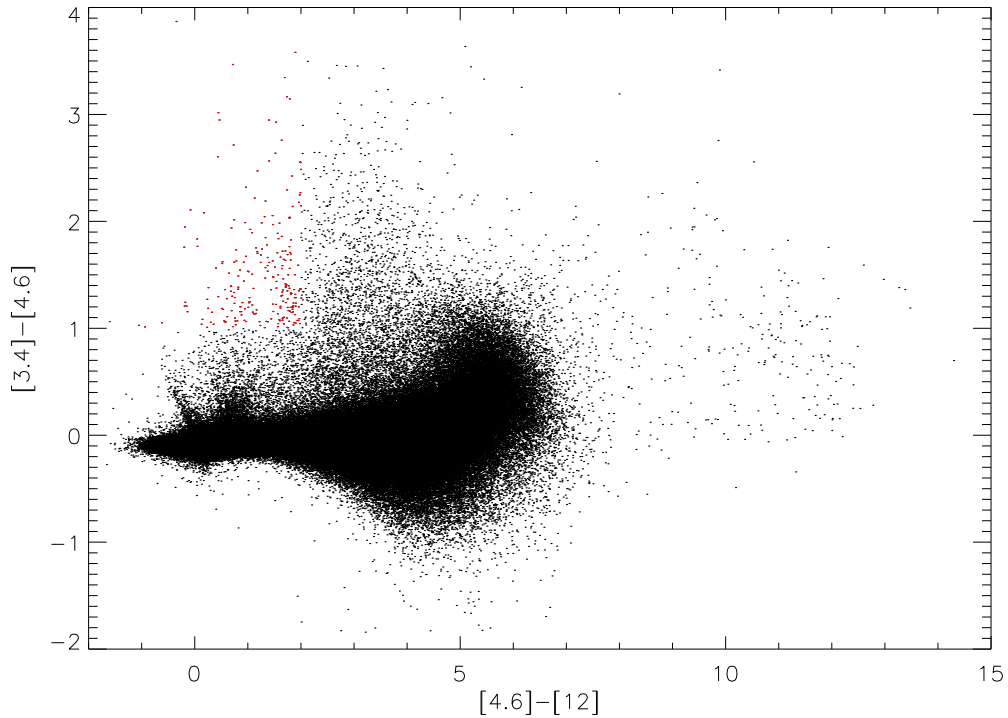


Figure B.4: Colour-colour diagram of WISE catalogue sources: Removing shock emission knots (red) following Eq. (6.13). 245 sources flagged.

emission knots. These numbers, however, are not necessarily additive as described above. After flagging, they are all removed before the cYSOs are selected from the WISE catalogue.

This is of course a simplified approach and as with the YSO selection process itself, the boundaries chosen are an informed choice but not definite. They define a broad region in the colour-colour diagram from which all sources are removed. This might include some sources that were *bona fide* stars, while some contaminants might not be picked up. Because the boundaries were chosen following the experience of previous studies, we are confident that they constitute a good approach and that they make the catalogue of remaining sources more reliable for analysis.

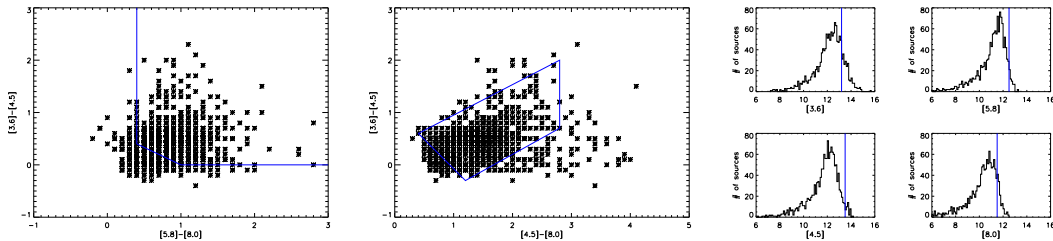
## C Reducing the PCYC in ten easy steps

Though both rely on the same data, within the same region in the central CN, the Pan-Carina YSO Catalogue (PCYC) contains four times as many cysos as the SYCC. To test the influence of the different sensitivities and different methods of obtaining cysos on the final numbers, we treated the PCYC in the same way as we treated the SPSC to obtain the SYCC. This is illustrated step by step in Fig. C.1. In this way, the original PCYC of 1439 cysos reduces to 640 cysos, showing that the method applied for obtaining the SYCC is far more conservative than that applied by Povich et al.

Firstly, to even out the slightly different sensitivities, in Figs. C.1a to C.1d, the same magnitude cuts we chose for the SYCC (Sect. 6.2.2) were applied to the PCYC. This brings the number down from 1439 sources to 1075. The remaining 364 sources were simply too faint to appear in the SYCC.

The major contributor, however, are the different methods of selecting cysos. The  $[3.6] - [4.5]$  vs.  $[5.8] - [8.0]$  colour-colour diagram we utilise in Figs. C.1e and C.1f (Sect. 6.2) excludes a further 389 cysos to bring the total number down to 686. The  $[3.6] - [4.5]$  vs.  $[4.5] - [8.0]$  colour-colour diagram applied in Figs. C.1g and C.1j then removes 46 more.

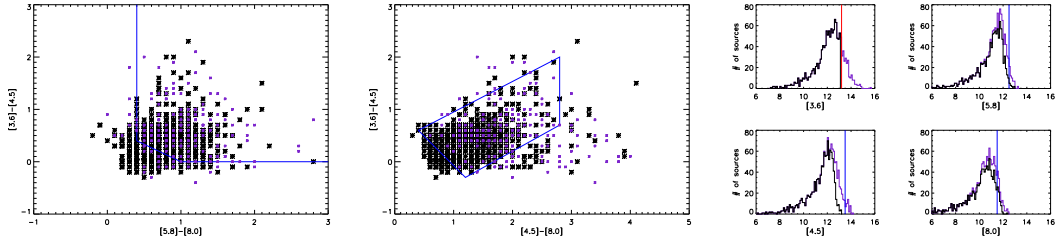
This leaves a total of 640 cysos in the PCYC when exactly the same method is applied to it with which we obtained the SYCC from the SPSC. Figure C.1k clearly shows the large number of purple (i. e. original PCYC) sources that lie far outside the boundaries we chose for YSO identification from colour-colour diagrams. Furthermore, the histograms demonstrate well that our decision to exclude the faintest sources in order to obtain a more reliable catalogue would also exclude many sources included in the PCYC.



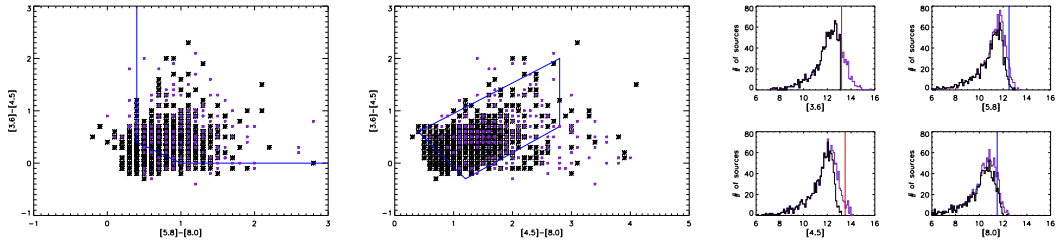
(a) Step 0: The original PCYC (1439 sources).

Figure C.1: The selection criteria with which we obtained the SYCC from the SPSC applied to the PCYC. In each step the process applied is signified by an added red line in the appropriate diagram. The purple symbols and lines always represent the original population of 1439 sources for comparison. In the colour-colour diagrams, on the left, black symbols represent the PCYC sources left after the current step. On the right, their histograms are drawn in black.

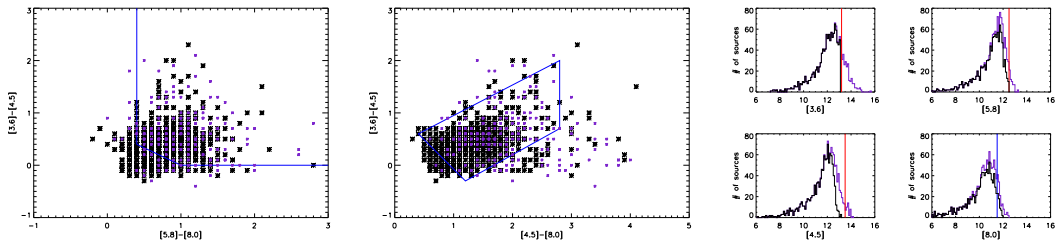
C Reducing the PCYC in ten easy steps



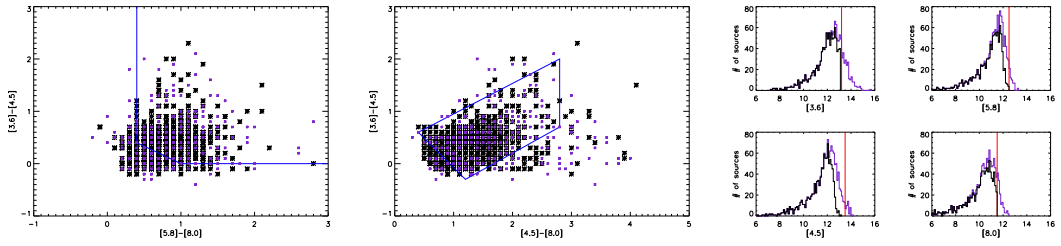
(b) Step 1: Cutting all 3.6  $\mu\text{m}$  magnitudes  $> 13.2$  mag (1146 sources left).



(c) Step 2: Cutting all 4.5  $\mu\text{m}$  magnitudes  $> 13.5$  mag (1146 sources left).

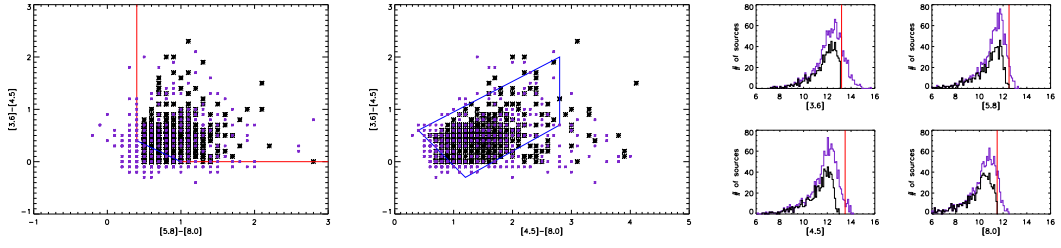


(d) Step 3: Cutting all 5.8  $\mu\text{m}$  magnitudes  $> 12.5$  mag (1134 sources left).

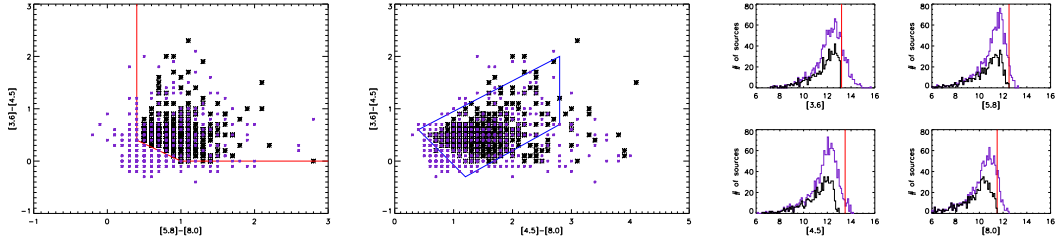


(e) Step 4: Cutting all 8.0  $\mu\text{m}$  magnitudes  $> 11.5$  mag (1075 sources left).

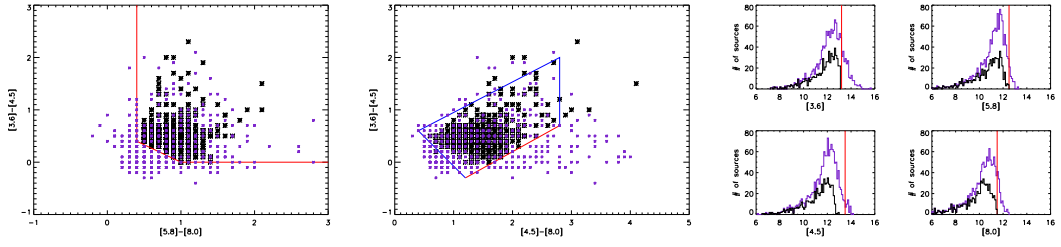
Figure C.1: Continued.



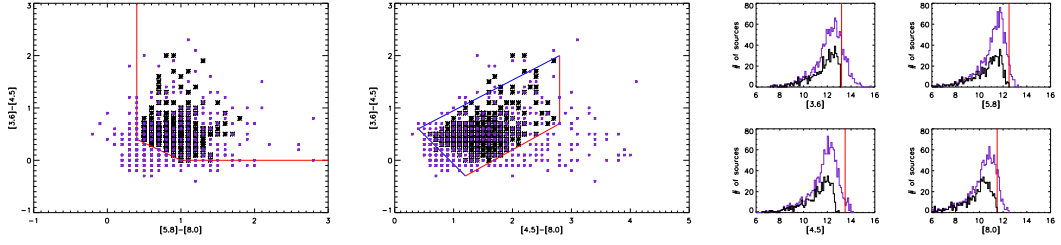
(f) Step 5: Applying Eq. (6.1) (799 sources left).



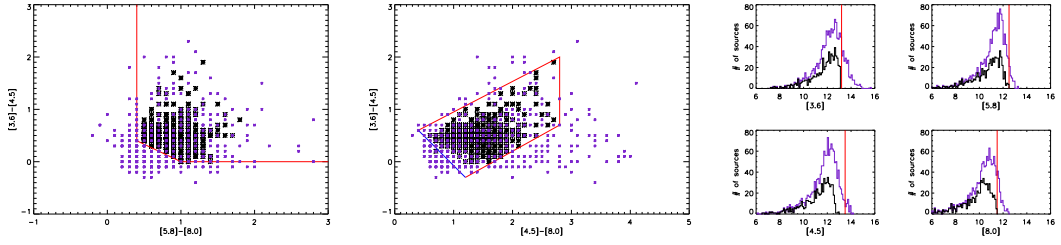
(g) Step 6: Applying Eq. (6.2) (686 sources left).



(h) Step 7: Applying Eq. (6.3) (654 sources left).



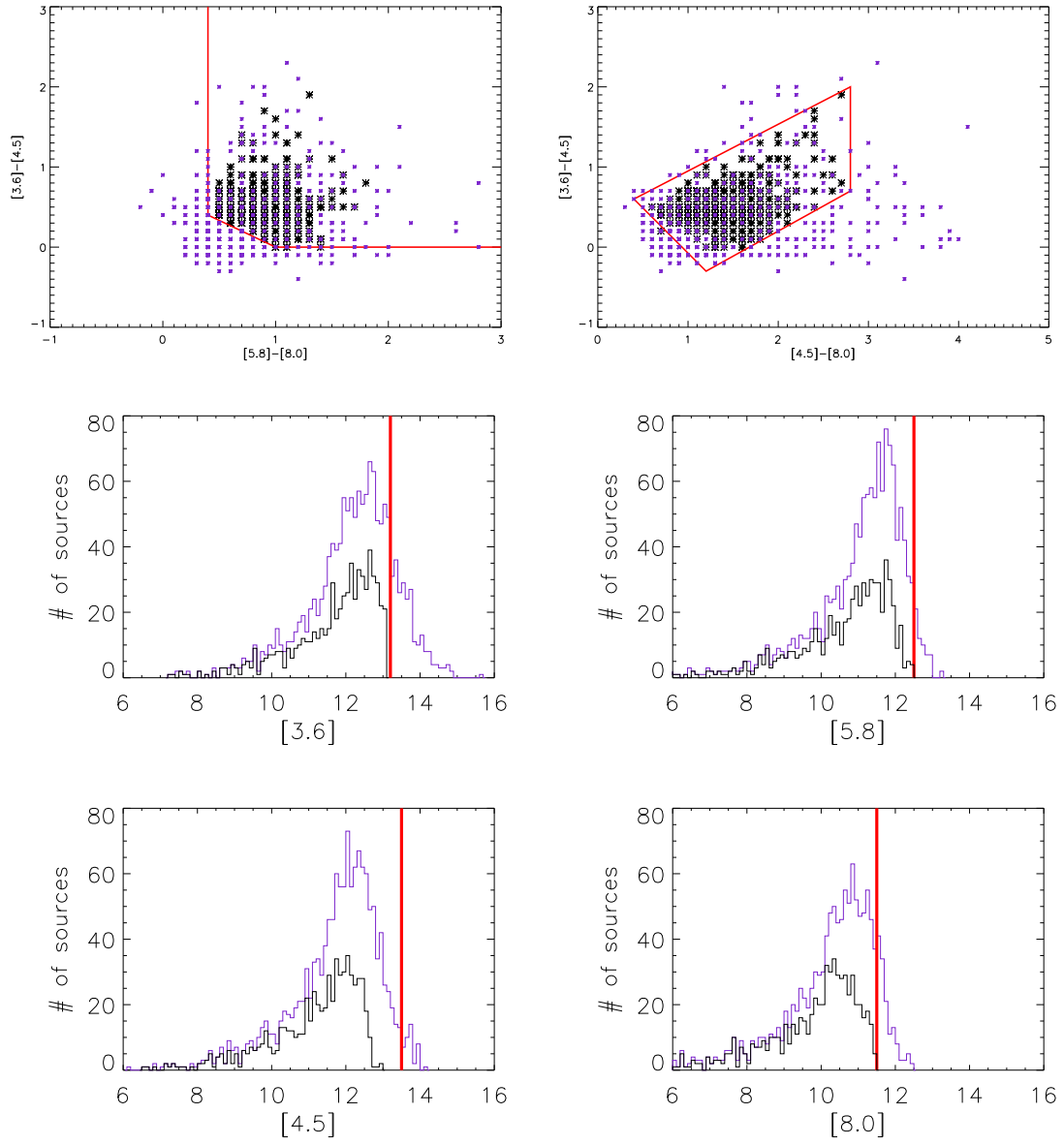
(i) Step 8: Applying Eq. (6.4) (648 sources left).



(j) Step 9: Applying Eq. (6.5) (640 sources left).

Figure C.1: Continued.

C Reducing the PCYC in ten easy steps



(k) Step 10: Applying Eq. (6.6) (640 sources left).

Figure C.1: Continued.

## D Test: Why do we not classify sources as cYSOs from the PCYC when they are in the SYCC?

In Sect. 6.5.2 and Appendix C it is described that after applying all our magnitude cuts and selection criteria for YSOs to the PCYC there are a few (28) sources that appear in the SYCC and the PCYC but not in the reduced PCYC (see Fig. 6.10). I tested individually on all 28 why they were not classified as cYSOs by selecting them from the PCYC although photometry for the PCYC and the SYCC deviates only slightly (cf. Fig. 6.5).

In the majority of cases the reason for this are very small flux differences, which cause a source in the SYCC to fall this side of the YSO border and its counterpart in the PCYC to fall on the far side. Since photometric values for the PCYC are given in magnitudes and only to the first decimal place in the VizieR online catalogue, sometimes the different classification is based on rounding differences. In a number of cases, the PCYC does not have the flux for the 8.0  $\mu\text{m}$  band, whereas the SYCC does. As we require four bands for selection, the PCYC source drops out. There is also small number of cases where a small difference lets the PCYC source fall below the magnitude cutoff we imposed. Several sources violate more than one equation at the same time, which is natural as they use the same colours.

Below, I show some illustrative cases. The IRAC fluxes from the PCYC and the SYCC are compared. To enable better comparison at a glance, for the SYCC I give the magnitude to three decimal places and then round it to one decimal place like the PCYC magnitudes. For clarity, in the last column of each table I only list the one YSO selection criterion that in the PCYC is violated and in the SYCC is not (or, if more than one are violated, one of those).

### J10:44:52.0–59:44:21

	[3.6]	[4.5]	[5.8]	[8.0]	Eq. (6.1)
PCYC	8.5	8.0	7.5	7.2	$0.3 \stackrel{!}{\geq} 0.4 \not\checkmark$
SYCC	$8.413 \approx 8.4$	$7.948 \approx 7.9$	$7.320 \approx 7.5$	$6.822 \approx 6.8$	$0.498 \stackrel{!}{\geq} 0.4 \checkmark$

### J10:46:05.1–59:28:18

	[3.6]	[4.5]	[5.8]	[8.0]	Eq. (6.2)
PCYC	11.5	11.1	10.7	10.3	$0.4 \stackrel{!}{\geq} 0.402 \not\checkmark$
SYCC	$11.459 \approx 11.5$	$11.119 \approx 11.1$	$10.643 \approx 10.6$	$10.114 \approx 10.1$	$0.340 \stackrel{!}{\geq} 0.316 \checkmark$

D Test: Why do we not classify sources as cYSOs from the PCYC when they are in the SYCC?

**J10:44:46.4–59:21:53**

	[3.6]	[4.5]	[5.8]	[8.0]	Eq. (6.3)
PCYC	10.9	10.9	10.6	9.2	$0.0 \stackrel{!}{>} 0.02 \not\checkmark$
SYCC	$10.846 \approx 10.8$	$10.843 \approx 10.8$	$10.554 \approx 10.6$	$9.145 \approx 9.1$	$0.016 \stackrel{!}{>} 0.010 \checkmark$

**J10:42:14.6–60:00:33**

	[3.6]	[4.5]	[5.8]	[8.0]	cutoff [3.6]
PCYC	13.3	12.8	12.1	11.4	$13.3 \stackrel{!}{<} 13.2 \not\checkmark$
SYCC	$13.089 \approx 13.1$	$12.812 \approx 12.8$	$12.342 \approx 12.3$	$11.360 \approx 11.4$	$13.089 \stackrel{!}{<} 13.2 \checkmark$

**J10:44:11.8–59:24:30**

	[3.6]	[4.5]	[5.8]	[8.0]	cutoff [8.0]
PCYC	12.6	12.0	11.7	11.6	$11.6 \stackrel{!}{<} 11.5 \not\checkmark$
SYCC	$112.538 \approx 12.5$	$12.060 \approx 12.1$	$11.526 \approx 12.15$	$10.904 \approx 10.9$	$10.904 \stackrel{!}{<} 11.5 \checkmark$

**J10:45:47.0–60:16:53**

	[3.6]	[4.5]	[5.8]	[8.0]	4 bands
PCYC	11.8	11.0	10.3	–	$\not\checkmark$
SYCC	$11.717 \approx 11.7$	$11.026 \approx 11.0$	$10.176 \approx 10.2$	$8.932 \approx 8.9$	$\checkmark$

## E Minor clusters of young stellar objects

### E.1 The Gum 31 region

About  $8'$  to the south-west of Cluster No. 1 (described in Sect. 9.4.1), there is another, smaller, cYSO overdensity found in conjunction with a Yonekura et al. [2005]  $C^{18}O$  clump (their No. 2). We list it as Cluster No. 2. In this cluster (Fig. E.1) a group of four Class II cYSO is found in a shallow arc in an otherwise unremarkable region in the outer expanses of the Gum 31 ridge. The resolution of the image printed here is not sufficient to see what a closer look reveals: About  $15''$  to the north of the northernmost of these cYSOs there are three extremely green point-like sources to be found within less than  $8''$  of each other. The only Class I candidate in Fig. E.1 also appears very green, i. e. with a  $4.5\ \mu\text{m}$  excess. The same is true for a WISE cYSO candidate that is not classified as such in the SYCC. This

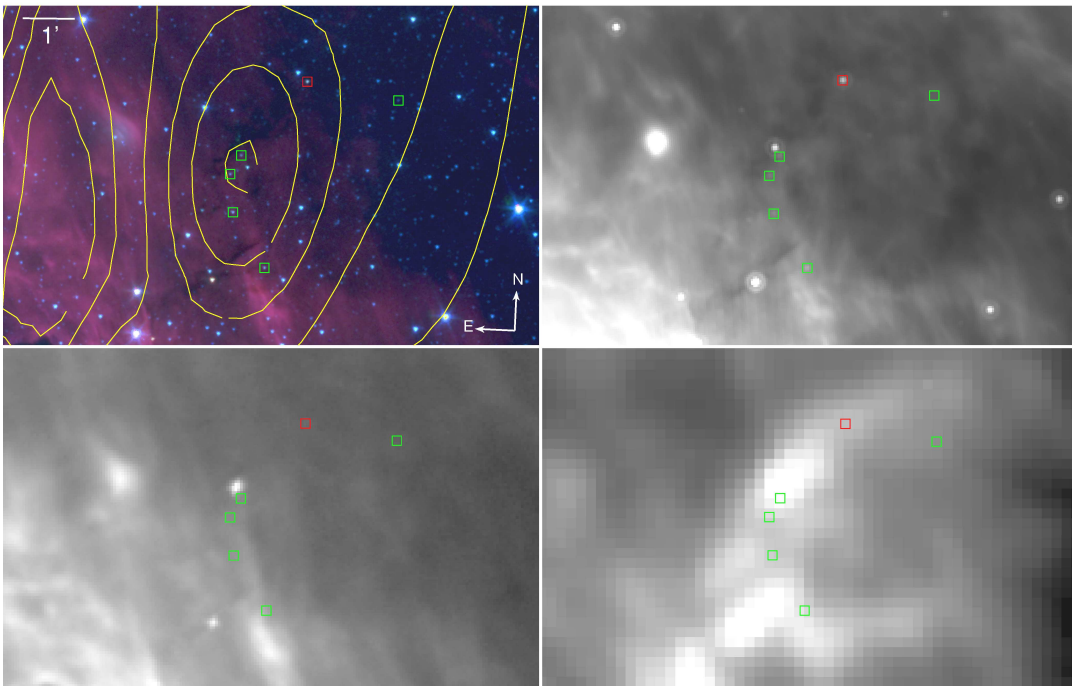


Figure E.1: Cluster No. 2 west of NGC 3324. Upper left: *Spitzer* IRAC RGB image (red:  $8.0\ \mu\text{m}$ , green:  $4.5\ \mu\text{m}$ , blue:  $3.6\ \mu\text{m}$ ), upper right: *Spitzer* MIPS  $24\ \mu\text{m}$  image. Lower left: *Herschel* PACS  $70\ \mu\text{m}$  image, lower right: *Herschel* SPIRE  $500\ \mu\text{m}$  image. The cYSOs are marked by squares, red for Class I, green for Class II. The yellow contours indicating the number density of cYSOs are identical to those in Fig. 9.5.

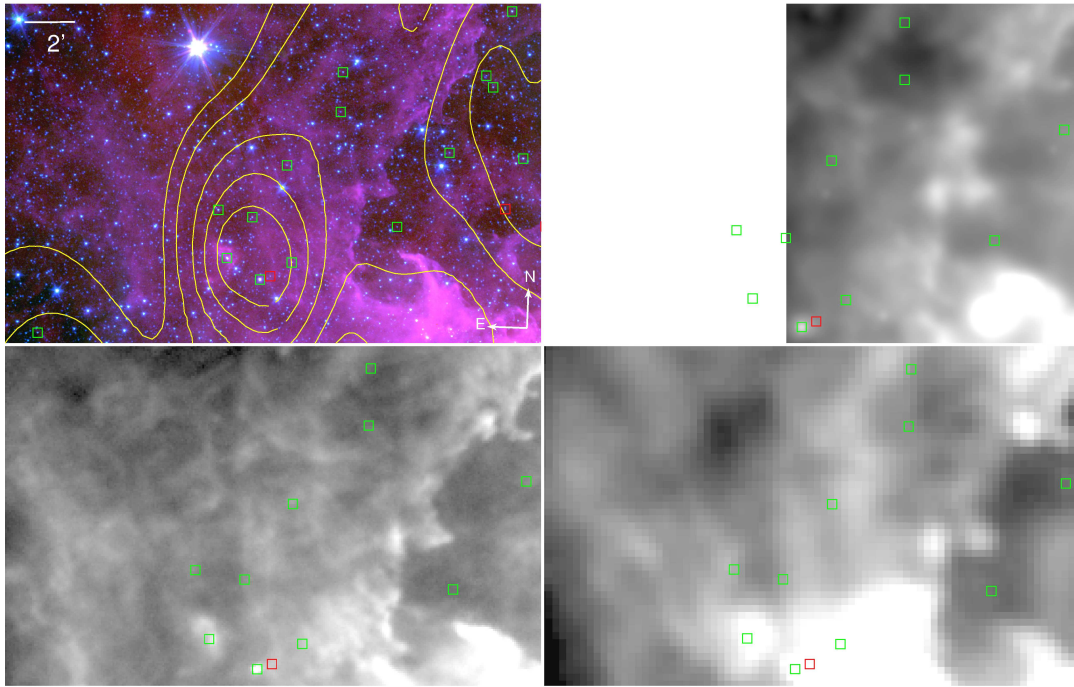


Figure E.2: Cluster No. 5 to the east of the Gum 31 bubble. (Images as in Fig. E.1.)

is the brighter of the two sources found directly to the east of the southernmost Class II candidate in the image.

The Cluster No. 5 shown in Fig. E.2 is not a very prominent one. It is placed to the east of the Gum 31 bubble, in the outermost stretches of the clouds tracing the bubble edge. Seven cYSOs form the cluster, all but one of Class II. Apart from one that is a spatial outlier from the central cluster, they are all classified the same with WISE and there are eight more WISE cYSOs. The cluster does not coincide with an ‘official’  $C^{18}O$  clump published by Yonekura et al. [2005], but their contours show an enhanced density in this place.

Between the central CN and Gum 31, to the west of Tr 14, there is a conspicuous over-density of cYSOs that is readily visible in Fig. 9.5. The close-up in Fig. E.3 shows this Cluster No. 9 to consist of two separate groups of two and three cYSOs each that do not appear to be connected. They are both found in conjunction with wispy tendrils from a nebulosity seen in MIR to FIR, but otherwise unremarkable. Strikingly, though, each of the two groups is associated directly with a bright, point-like source in the  $500\ \mu\text{m}$  image.

## E.2 The outer regions of the survey field

Those clusters at the very edges of our study region at first glance appear to be unconnected, but at closer inspection are associated with IR features that seem to indicate their being real clusters. It is, however, worth to keep in mind that the SYCC sample suffers a strong contamination and that it is therefore possible what we are seeing here is uncon-

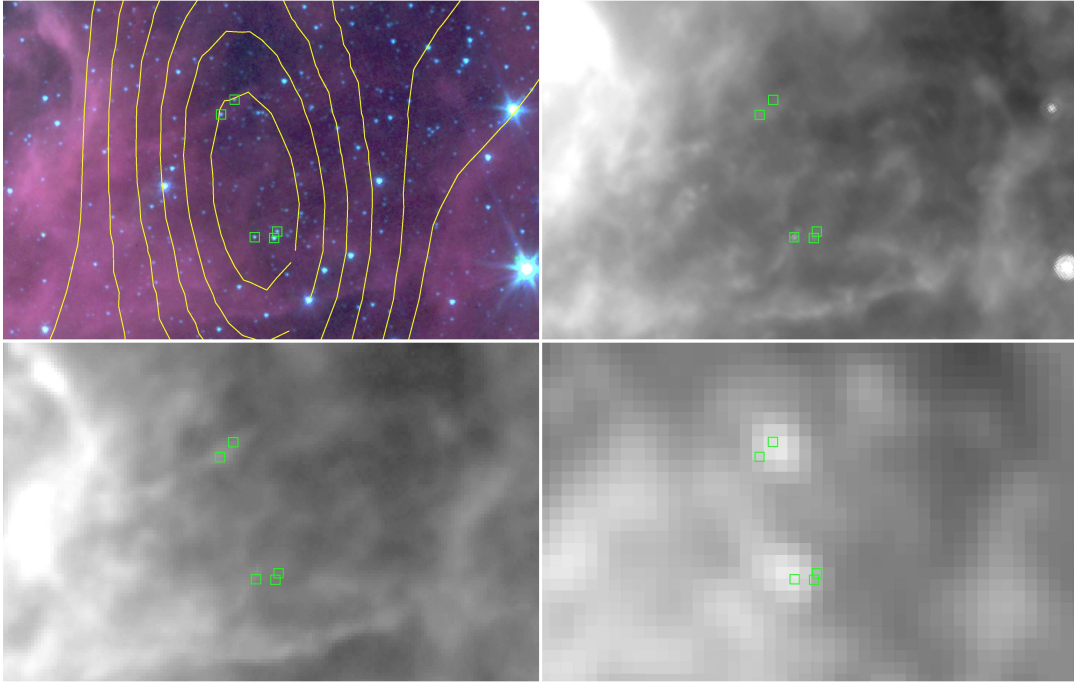


Figure E.3: Cluster No. 9 located between the central CN and Gum 31. (Images as in Fig. E.1.)

nected to the region. If a cluster appears to be associated with the nebula itself and its features are echoed in the dust then it is probably indeed a part of the complex. Outside the complex this test of plausibility is not possible, therefore the clusters described below might not be connected with the CNC itself, but chance projections.

Figure E.4 shows two  $\text{CYSO}$  overdensities, one in the upper left corner ( $\text{C}^{18}\text{O}$  clump No. 1 of Yonekura et al. [2005] and our Cluster No. 6), the other to the upper centre ( $\text{C}^{18}\text{O}$  peak not listed, but apparent). The former, consisting of only three SYCC  $\text{CYSOs}$  and two farther out, is coincident with a bright cloud in the SPIRE  $500\ \mu\text{m}$  image that does not show up as bright at shorter wavelengths but is visible down to  $24\ \mu\text{m}$ . There are also three pre-stellar objects and one protostar found there.

Contrary to that, the elongated cloud front associated with the other overdensity is bright in all images from  $24\ \mu\text{m}$  to  $500\ \mu\text{m}$  and still faintly visible at  $8.0\ \mu\text{m}$ . As the southward pointing ‘nose’ of the density contours shows,  $\text{CYSOs}$  are found all along this cloud, fourteen all in all. For only one of those do we compute a density above our cluster limit, though. The cloud seems to have an undulating surface, with the outsides of the bows pointing in the same direction as the SPIRE-bright cloud described above: Roughly the direction of the southern Gum 31.

The very bright object at the bottom of the MIPS image, also seen in the PACS image, appears to be the nebula GN 10.31.8 described in Sect. 8.4.3, a very dense cluster of WISE  $\text{CYSOs}$ . Two of the above-mentioned SYCC Class II candidates might conceivably belong to this group.

*E* Minor clusters of young stellar objects

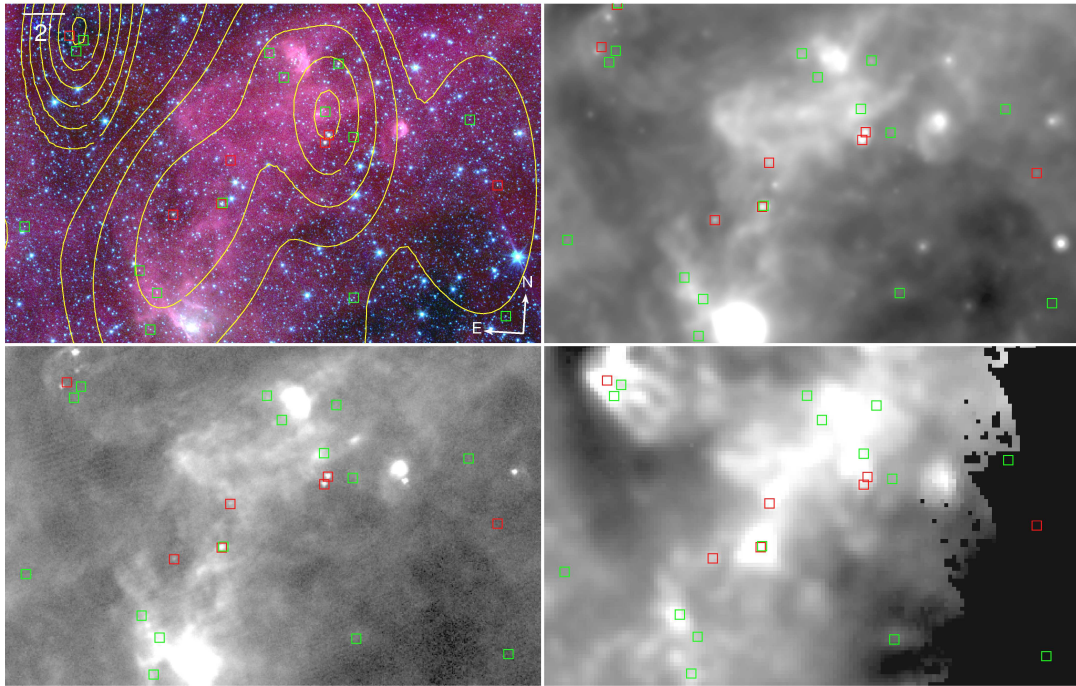


Figure E.4: Cluster No. 6 towards the western edge of the CNC study field and a further overdensity. (Images as in Fig. E.1.)

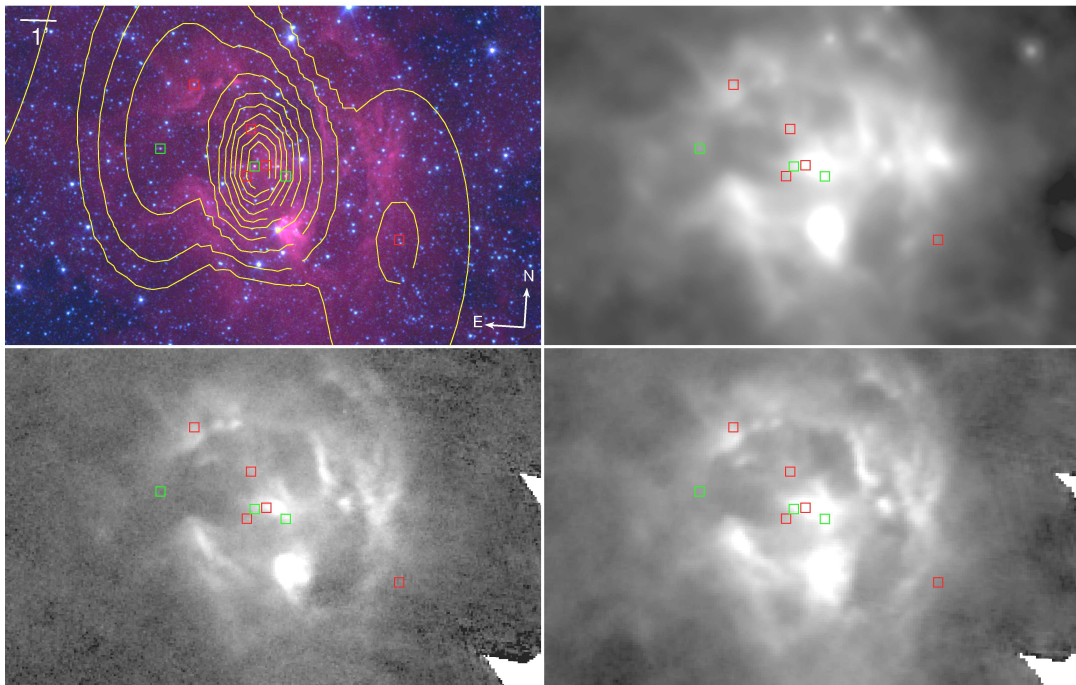


Figure E.5: Cluster No. 8 towards the western edge of the CNC study field. (Images as in Fig. E.1.)

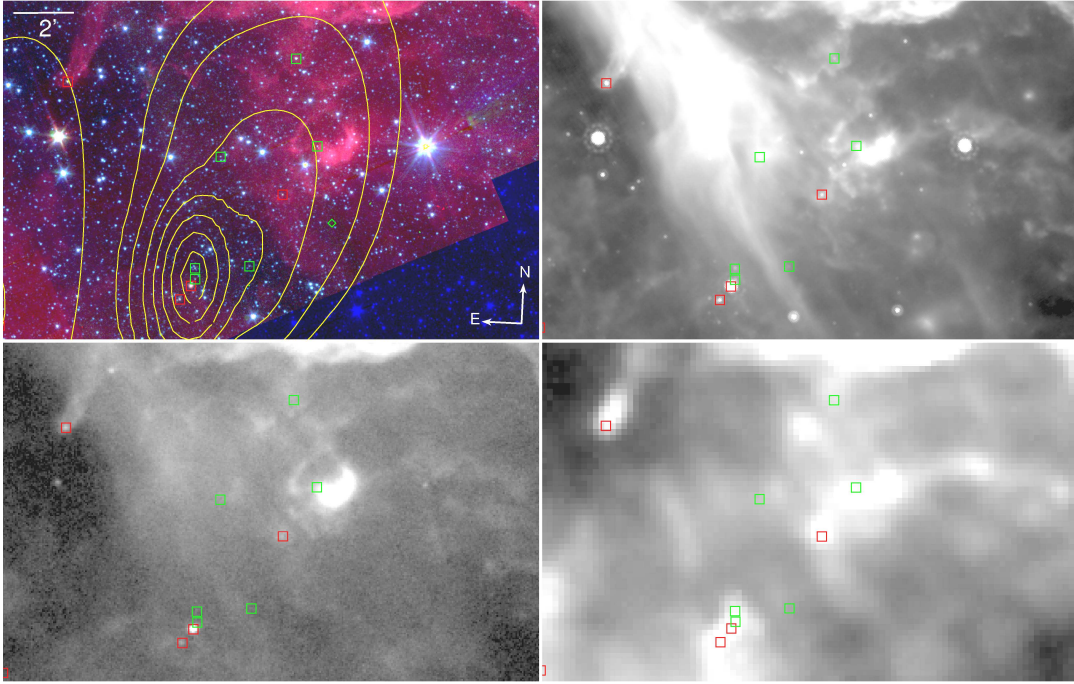


Figure E.6: Cluster No. 29 towards the southern edge of the CNC study field. (Images as in Fig. E.1.)

Cluster No. 8, shown in Fig. E.5, consists of five SYCC cYSOs, three of which are Class I candidates. With WISE, its appearance is similar (7 cYSOs). The cluster is very dense; the central four cYSOs cluster within just  $70''$  (0.8 pc).

In the IRAC RGB image its most eye-catching feature is the bright pink nebula GN 10.29.8 in the centre bottom (pinkness in IRAC RGB images always indicates dominating  $8.0\ \mu\text{m}$  emission). On closer inspection this turns out to be part of a peculiar ring structure in which the cluster is almost perfectly centred. The circle has a diameter of roughly  $3'$  and in its centre an emission maximum is found from NIR to FIR. SIMBAD lists only one massive star in the area, B star TYC 8613-2201-1,  $\sim 2.6'$  offset from this central position.

Cluster No. 29, shown in Fig. E.6, is also tiny, only two Class I candidates and two Class II candidates. In addition, its environment is rather placid. Still, it is one of the densest clusters in our study field.

In the upper left corner of Fig. E.6, a pillar is seen to emanate from the cloud that stretches out along the top edge of the image. Immediately in the pillar head there is a solitary Class I candidate, seen with both IRAC and WISE, well away from other cYSOs. The brightest source found on the extended pillar axis is IRAS 10359-5955. IRAS 10356-5947 is much closer to the pillar head, but is also far less luminous. Right next to IRAS 10356-5947 there is also HD 305357, a K0 star, which as a late-type star should not have sufficient UV flux to be the shaping source.

Together with the pillar we see, especially in the  $24\ \mu\text{m}$  image, a bright strip of nebulosity sweeping from the north-east to the south-west. This appears similar to what was

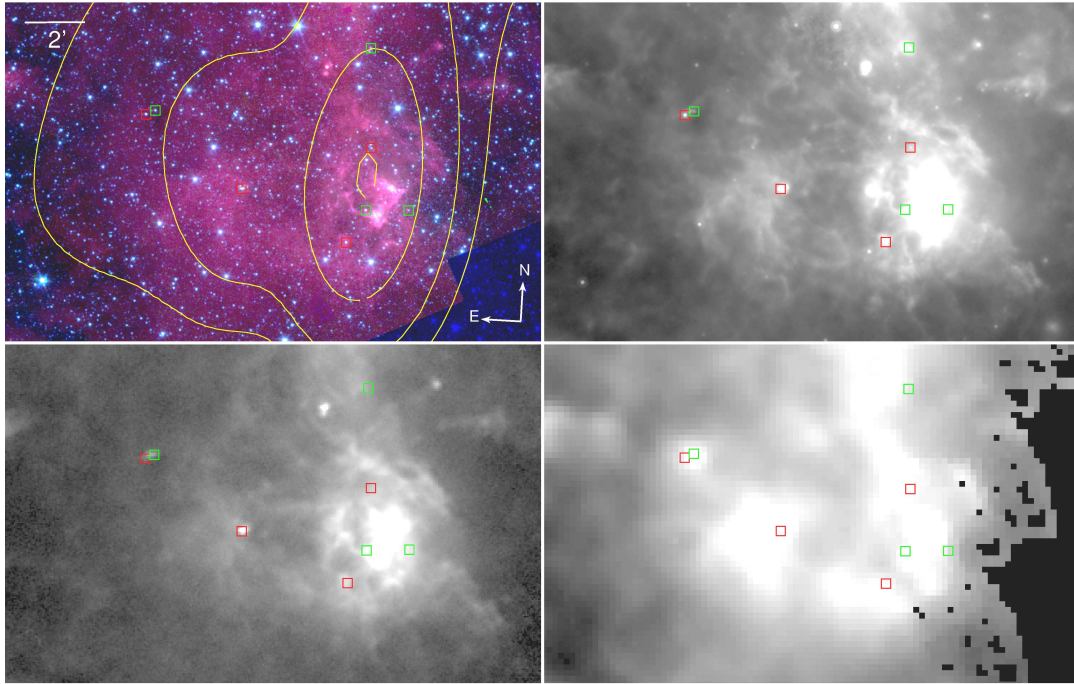


Figure E.7: cYSO overdensity towards the southern edge of the CNC study field. (Images as in Fig. E.1.)

described in connection with Fig. 9.22, however, it is not accompanied by similarly bright  $4.5\ \mu\text{m}$  emission in the IRAC image.

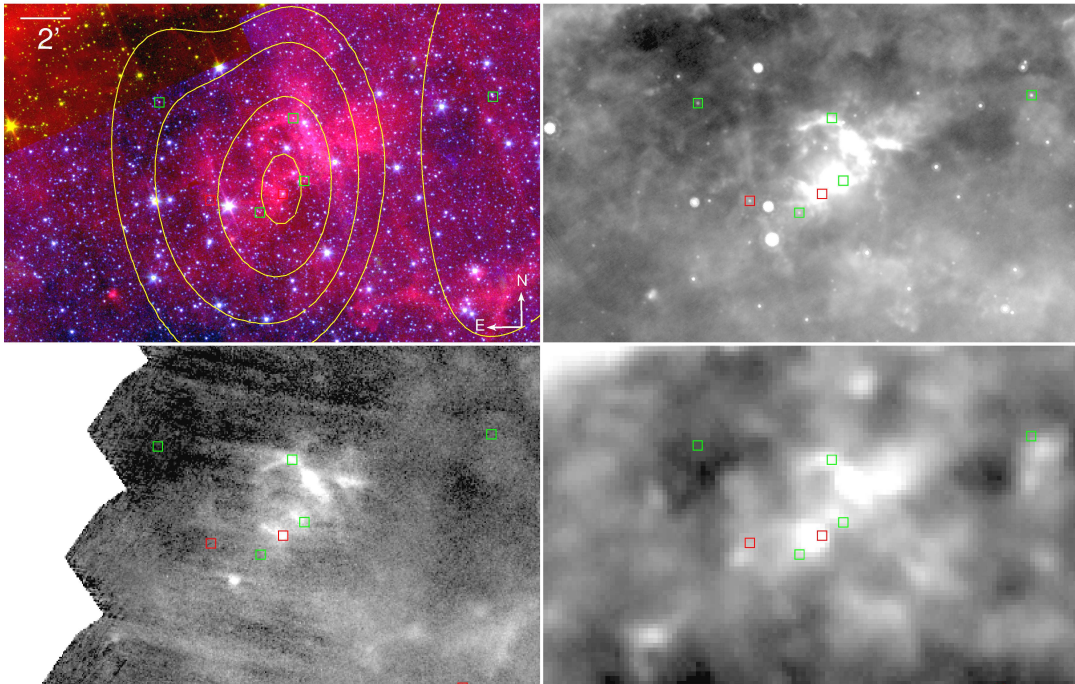
Figure E.7 shows a small cYSO overdensity to the extreme south-west of our study field, with two Class I and Class II candidates each from the SYCC sample. There are considerably more WISE cYSOs, about 15. The H II region GAL 286.42-01.48 (SIMBAD) is brightly seen here in the IRAC RGB image and remains extremely bright all through to the  $500\ \mu\text{m}$  band.

To the north there is a small, previously known H II region (listed in SIMBAD as GAL 286.40-01.35), coincident with (point-like?) sources in the  $24\ \mu\text{m}$  and  $160\ \mu\text{m}$  images. This is accompanied by only a single SYCC source, a Class I candidate. With WISE, however, this is a rich cluster of cYSOs, with 42 cYSOs within just  $2'$ . This cluster is also clearly separate from its apparent environment, because around it no cYSOs are found.

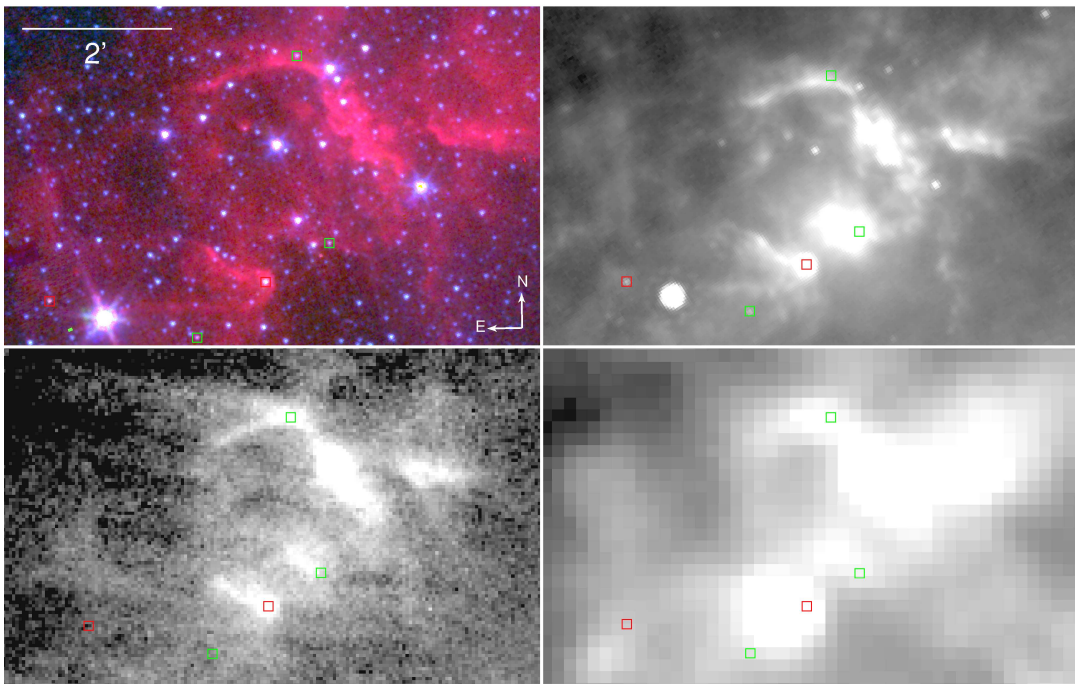
A small arc-like structure of about  $2'$  diameter is found in the south-western corner of our IRAC study field (Fig. E.8). It appears as a two-part structure, consisting of an upper arc and a, smaller, lower one, with apparent gaps to the east and the south-west. As visible in Fig. E.8b, three cYSOs are found in its rim. One of these sources is associated with very bright emission in the MIPS  $24\ \mu\text{m}$  image which does not extend to the FIR. On the contrary, the only Class I candidate of the three is a bright IRAC and MIPS source and though faint in  $70\ \mu\text{m}$ , is bright and point-like again in the  $500\ \mu\text{m}$  image.

The region has not previously been described and does not appear to be associated with any known massive stars. The very bright IR source J105314.3–585927 appears to be placed in the centre of the ring, but has not been studied in detail.

E.2 The outer regions of the survey field



(a)



(b)

Figure E.8: cYSO overdensity in a miniature arc. (Images as in Fig. E.1.)

## F The X-ray clusters of Feigelson et al. [2011]

In Sect. 9.3 we discussed the X-ray clusters of Feigelson et al. [2011] and, where appropriate, described how they corresponded to the clusters we find from the SYCC. For a more comprehensive comparison, Fig. F.1 shows the SYCC clusters again, as in Fig. 9.7. The yellow circles and numbers correspond to Table 9.1. Overlaid, the magenta and cyan circles mark the central positions of the X-ray clusters and groups, respectively.

Their size was arbitrarily chosen and does not correspond to any physical cluster size. The number of cluster members can be obtained from Tables 1 and 2 of Feigelson et al. [2011]. Table 1 lists the clusters, Table 2 the smaller groups. The former are represented by magenta circles in Fig. F.1, the latter by cyan circles.

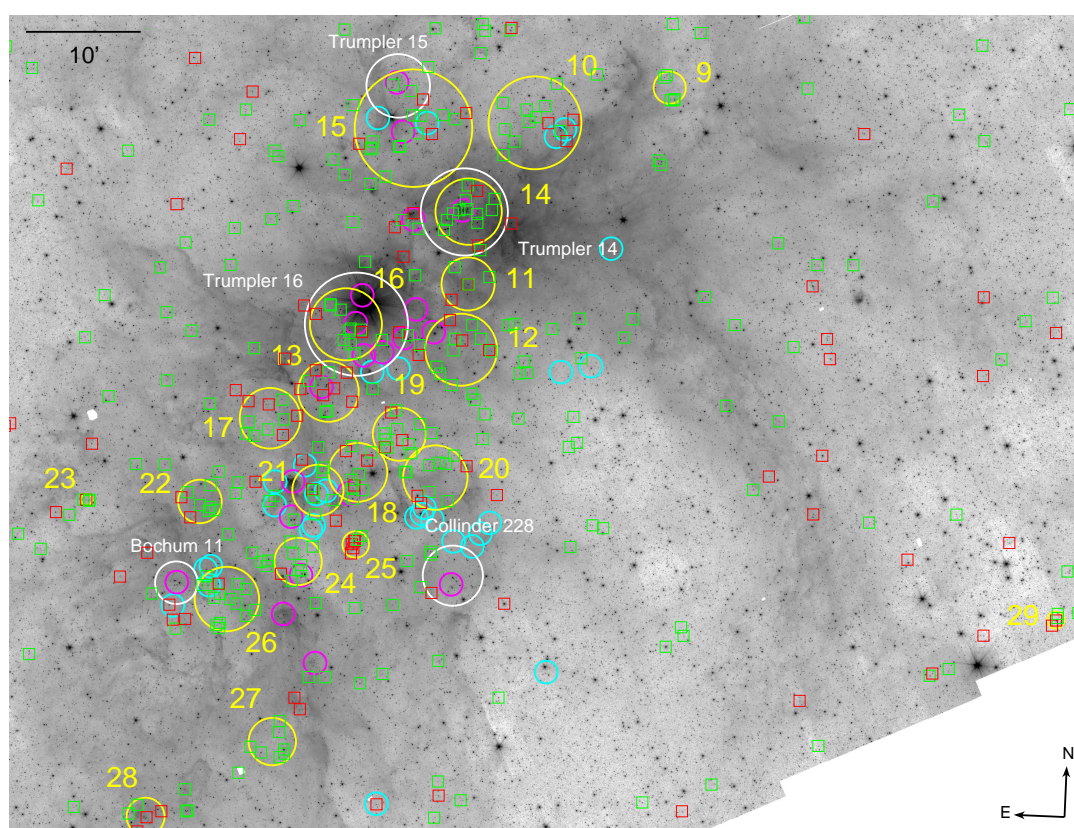


Figure F.1: The figure is identical to Fig. 9.7, but shows the X-ray clusters of Feigelson et al. [2011] overlaid in magenta. The ‘groups’ are drawn in cyan.

# Acknowledgements

**Deutsche Forschungsgemeinschaft** (DFG) supported this work (DFG project number PR569/9-1).

**The Spitzer Science Center Helpdesk** provided much support for working with MOPEX.

**The Spitzer Space Telescope** is operated by the Jet Propulsion Laboratory, California Institute of Technology under a contract with NASA.

**The Herschel Space Observatory** is an ESA spacecraft with science instruments provided by European-led Principal Investigator consortia and with important participation from NASA.

**The Wide-field Infrared Survey Explorer** is a joint project of the University of California, Los Angeles, and the Jet Propulsion Laboratory/California Institute of Technology, funded by the National Aeronautics and Space Administration.

**VISTA science data reduction** up to the creation of the final tile was performed by the Cambridge Astronomy Survey Unit.

**The Two Micron All-Sky Survey** is a joint project of the University of Massachusetts and the Infrared Processing and Analysis Center/California Institute of Technology, funded by the National Aeronautics and Space Administration and the National Science Foundation.

**The STScI Digitised Sky Survey** was produced at the Space Telescope Science Institute under U. S. Government grant NAG W-2166. The images of these surveys are based on photographic data obtained using the Oschin Schmidt Telescope on Palomar Mountain and the UK Schmidt Telescope. The plates were processed into the present compressed digital form with the permission of these institutions.

**The Astrophysics Data System Bibliographic Services** are provided by NASA.

**The SIMBAD database and the VizieR catalogue access tool** are operated at CDS, Strasbourg, France.

# Abbreviations

2MASS	Two Micron All-Sky Survey
ACS	Advanced Camera for Surveys (of the HST)
AGB	asymptotic giant branch (of the HR diagram)
AGN	active galactic nucleus
AOR	astronomical observation request
APEX	Atacama Pathfinder Experiment
APEX	Astronomical Point-source EXtractor
ATLASGAL	APEX Telescope Large Area Survey of the GALaxy
BCD	<i>Spitzer</i> basic calibrated data
BSC	Bandmerge <i>Spitzer</i> catalogue
c2d	<i>Spitzer</i> Legacy Programme “From Molecular Cores to Planet-Forming Disks”
CASU	Cambridge Astronomy Survey Unit ( <a href="http://casu.ast.cam.ac.uk/">http://casu.ast.cam.ac.uk/</a> )
CCCP	<i>Chandra</i> Carina Complex Project
CDS	Centre de Données astronomiques de Strasbourg ( <a href="http://cdsweb.u-strasbg.fr/">http://cdsweb.u-strasbg.fr/</a> )
CGO	compact green object
CGRO	Compton Gamma-Ray Observatory
CN	Carina Nebula
CNC	Carina Nebula Complex
CTIO	Cerro Tololo Inter-American Observatory
cYSO	candidate young stellar object
DAOPHOT	Dominion Astrophysical Observatory photometry software
DCE	data collection event
DFG	<i>Deutsche Forschungsgemeinschaft</i>
DSS	STsci Digitized Sky Survey
EGG	evaporating gaseous globule
EGO	extended green object
ESA	European Space Agency
ESO	European Southern Observatory
FIF	fiducial image frame
FIR	far-IR
FIRST	Far Infrared and Sub-millimetre Telescope (a former name of <i>Herschel</i> )
FITS	flexible image transport system (a file format)
FOV	field of view
F-UV	far-UV
FWHM	full width at half maximum
GAIA	Graphical Astronomy and Image Analysis tool

	( <a href="http://astro.dur.ac.uk/~pdraper/gaia/gaia.html">http://astro.dur.ac.uk/~pdraper/gaia/gaia.html</a> )
GLIMPSE	Galactic Legacy Infrared Mid-Plane Survey Extraordinaire
GMC	giant molecular cloud
GN	Atlas of Galactic Nebulae [Neckel and Vehrenberg 1985, 1987, 1990]
HI	non-ionized hydrogen
HIFI	Heterodyne Instrument for the Far Infrared (onboard <i>Herschel</i> )
HII	ionized hydrogen
HAWK-I	High-Acuity Wide-field <i>K</i> -band Imager (at the ESO Very Large Telescope)
HH jet	Herbig-Haro jet
HR diagram	Hertzsprung-Russell diagram
HST	<i>Hubble</i> Space Telescope
IDL	Interactive Data Language
IMF	initial mass function
IPAC	Infrared Processing and Analysis Center of NASA ( <a href="http://irsa.ipac.caltech.edu/">http://irsa.ipac.caltech.edu/</a> )
IR	infrared
IRAC	Infrared Array Camera (onboard <i>Spitzer</i> )
IRAS	Infrared Astronomical Satellite
IRDC	infrared dark cloud
IRS	Infrared Spectrograph (onboard <i>Spitzer</i> )
ISM	interstellar medium
$L_{\odot}$	solar luminosity, $\sim 3.84 \cdot 10^{26}$ W
LABOCA	Large APEX Bolometer Camera
LBV	luminous blue variable
$M_{\odot}$	solar mass, $\sim 1.99 \cdot 10^{30}$ kg
MHO	molecular hydrogen emission-line object
MIPS	Multiband Imaging Photometer for <i>Spitzer</i>
MIPSCAR	MIPS study of the Carina Nebula
MIR	mid-infrared
MOPEX	Mosaicker and Point source Extractor ( <a href="http://irsa.ipac.caltech.edu/data/SPITZER/docs/dataanalysistools/tools/mopex/">http://irsa.ipac.caltech.edu/data/SPITZER/docs/dataanalysistools/tools/mopex/</a> )
MSX	Midcourse Space Experiment
MYSO	massive young stellar object
NASA	National Aeronautics and Space Administration
NGC	New General Catalogue [Dreyer 1888]
NIR	near-IR
NTT	New Technology Telescope
PACS	Photodetecting Array Camera and Spectrometer (onboard <i>Herschel</i> )
PAH	polyaromatic hydrocarbon
PCYC	Pan-Carina YSO Catalogue of Povich et al. [2011a]
PDR	photo-dissociation region
PI	principal investigator
PID	programme identification number
PMS	pre-main-sequence

PN	planetary nebula
PRF	point response function
PSF	point-spread function
PSP	point-source probability
RADMC	a 2-D Monte-Carlo code for dust continuum radiative transfer circumstellar disks and envelopes [Dullemond and Dominik 2004, <a href="http://www.mpia.de/homes/dullemon/radtrans/radmc/">http://www.mpia.de/homes/dullemon/radtrans/radmc/</a> ]
RGB	red/green/blue
RMS	root mean square
SABOCA	Sub-millimeter APEX Bolometer Camera
SED	spectral energy distribution
SFR	star-formation rate
SHA	<i>Spitzer</i> Heritage Archive ( <a href="http://sha.ipac.caltech.edu/applications/Spitzer/SHA/">http://sha.ipac.caltech.edu/applications/Spitzer/SHA/</a> )
SIMBAD	Set of Identifications, Measurements, and Bibliography for Astronomical Data ( <a href="http://simbad.u-strasbg.fr/simbad/">http://simbad.u-strasbg.fr/simbad/</a> )
SIRTF	Space Infra-Red Telescope Facility (a former name of <i>Spitzer</i> )
SN	supernova
SNR	signal-to-noise ratio
SOFI	Son of ISAAC (at the ESO New Technology Telescope)
SPIRE	Spectral and Photometric Imaging Receiver (onboard <i>Herschel</i> )
SPSC	Spitzer Point-Source Catalogue
SSC	<i>Spitzer</i> Science Center ( <a href="http://ssc.spitzer.caltech.edu/">http://ssc.spitzer.caltech.edu/</a> )
STSCI	Space Telescope Science Institute
sub-mm	sub-millimeter
SYCC	Spitzer YSO Catalogue in Carina
TYC	Tycho Catalogue [Perryman and ESA 1997]
UT	universal time
UV	ultraviolet
VIRCAM	VISTA Infra-Red CAMera
VISTA	Visible and Infrared Survey Telescope for Astronomy
VizieR	astronomical catalogue access tool ( <a href="http://vizier.u-strasbg.fr/viz-bin/VizieR">http://vizier.u-strasbg.fr/viz-bin/VizieR</a> )
VLT	Very Large Telescope
WCS	world coordinate system
WISE	Wide-field Infrared Survey Explorer
WNH star	nitrogen- and helium-rich WR star
WR star	Wolf-Rayet star
YSO	young stellar object
YMF	YSO mass function

# Bibliography

- L. E. Allen, N. Calvet, P. D'Alessio, B. Merin, L. Hartmann, S. T. Megeath, R. A. Gutermuth, J. Muzerolle, J. L. Pipher, P. C. Myers, and G. G. Fazio. Infrared Array Camera (IRAC) Colors of Young Stellar Objects. *ApJS*, 154:363–366, September 2004.
- P. André. Observations of protostars and protostellar stages. In T. Montmerle, C. J. Lada, I. F. Mirabel, and J. Tran Thanh Van, editors, *The Cold Universe*, page 179, 1994.
- P. André, D. Ward-Thompson, and M. Barsony. Submillimeter continuum observations of  $\rho$  Ophiuchi A - The candidate protostar VLA 1623 and prestellar clumps. *ApJ*, 406:122–141, March 1993.
- E. Araya, P. Hofner, M. Sewilo, W. M. Goss, H. Linz, S. Kurtz, L. Olmi, E. Churchwell, L. F. Rodríguez, and G. Garay. An H<sub>2</sub>CO 6 cm Maser Pinpointing a Possible Circumstellar Torus in IRAS 18566+0408. *ApJ*, 669:1050–1057, November 2007.
- J. Bally, B. Reipurth, and C. J. Davis. Observations of Jets and Outflows from Young Stars. *Protostars and Planets V*, pages 215–230, 2007.
- I. Baraffe, G. Chabrier, F. Allard, and P. H. Hauschildt. Evolutionary models for solar metallicity low-mass stars: mass-magnitude relationships and color-magnitude diagrams. *A&A*, 337:403–412, September 1998.
- P. J. Barnes, Y. Yonekura, S. D. Ryder, A. M. Hopkins, Y. Miyamoto, N. Furukawa, and Y. Fukui. Discovery of large-scale gravitational infall in a massive protostellar cluster. *MNRAS*, 402:73–86, February 2010.
- H. Baumgardt, C. Dettbarn, and R. Wielen. Absolute proper motions of open clusters. I. Observational data. *A&AS*, 146:251–258, October 2000.
- R. A. Benjamin, E. Churchwell, B. L. Babler, T. M. Bania, D. P. Clemens, M. Cohen, J. M. Dickey, R. Indebetouw, J. M. Jackson, H. A. Kobulnicky, A. Lazarian, A. P. Marston, J. S. Mathis, M. R. Meade, S. Seager, S. R. Stolovy, C. Watson, B. A. Whitney, M. J. Wolff, and M. G. Wolfire. GLIMPSE. I. An SIRTf Legacy Project to Map the Inner Galaxy. *PASP*, 115:953–964, August 2003.
- E. Bertin and S. Arnouts. SExtractor: Software for source extraction. *A&AS*, 117:393–404, June 1996.
- N. Billot, A. Noriega-Crespo, S. Carey, S. Guieu, S. Shenoy, R. Paladini, and W. Latter. Young Stellar Objects and Triggered Star Formation in The Vulpecula OB Association. *ApJ*, 712:797–812, April 2010.

## Bibliography

- R. van Boekel, P. Ábrahám, S. Correia, A. de Koter, C. Dominik, A. Dutrey, T. Henning, Á. Kóspál, R. Lachaume, C. Leinert, H. Linz, M. Min, L. Mosoni, T. Preibisch, S. Quanz, T. Ratzka, A. Schegerer, R. Waters, S. Wolf, and H. Zinnecker. Disks around young stars with VLTI/MIDI. In *Society of Photo-Optical Instrumentation Engineers (SPIE) Conference Series*, volume 6268 of *Presented at the Society of Photo-Optical Instrumentation Engineers (SPIE) Conference*, July 2006.
- H. Bradt. *Astrophysics Processes. The Physics of Astrophysical Phenomena*. Cambridge University Press, New York, 2008.
- C. Briceño, T. Preibisch, W. H. Sherry, E. A. Mamajek, R. D. Mathieu, F. M. Walter, and H. Zinnecker. The Low-Mass Populations in OB Associations. *Protostars and Planets V*, pages 345–360, 2007.
- P. S. Broos, K. V. Getman, M. S. Povich, L. K. Townsley, E. D. Feigelson, and G. P. Garmire. A Naive Bayes Source Classifier for X-ray Sources. *ApJS*, 194:4, May 2011a.
- P. S. Broos, L. K. Townsley, E. D. Feigelson, K. V. Getman, G. P. Garmire, T. Preibisch, N. Smith, B. L. Babler, S. Hodgkin, R. Indebetouw, M. Irwin, R. R. King, J. Lewis, S. R. Majewski, M. J. McCaughrean, M. R. Meade, and H. Zinnecker. A Catalog of *Chandra* X-ray sources in the Carina Nebula. *ApJS*, 194:2, May 2011b.
- C. Cappa, V. S. Niemela, R. Amorín, and J. Vasquez. The environs of the H II region Gum 31. *A&A*, 477:173–183, January 2008.
- J. M. Carpenter, E. E. Mamajek, L. A. Hillenbrand, and M. R. Meyer. Evidence for Mass-dependent Circumstellar Disk Evolution in the 5 Myr Old Upper Scorpius OB association. *ApJ*, 651:L49–L52, November 2006.
- G. Carraro and F. Patat. Star clusters in the Carina complex: *UBVRI* photometry of NGC 3114, Collinder 228 and vdB-Hagen 99. *A&A*, 379:136–146, November 2001.
- G. Carraro, F. Patat, and H. Baumgardt. Star clusterings in the Carina complex: *UBVRI* photometry of NGC 3324 and Loden 165. *A&A*, 371:107–114, May 2001.
- B. W. Carroll and D. A. Ostlie. *An Introduction to Modern Astrophysics*. Addison-Wesley Publishing Company, Inc., Reading, MA, 1996.
- S. Casertano and P. Hut. Core radius and density measurements in N-body experiments: Connections with theoretical and observational definitions. *ApJ*, 298:80–94, November 1985.
- F. Castelli and R. L. Kurucz. New Grids of ATLAS9 Model Atmospheres. *ArXiv Astrophysics e-prints*, May 2004.
- E. T. Chambers, J. M. Jackson, J. M. Rathborne, and R. Simon. Star Formation Activity of Cores within Infrared Dark Clouds. *ApJS*, 181:360–390, April 2009.
- X. Chen, S. P. Ellingsen, and Z.-Q. Shen. Class I methanol masers: masers with extended green objects. *MNRAS*, 396:1603–1609, July 2009.

- X. Chen, Z.-Q. Shen, J.-J. Li, Y. Xu, and J.-H. He. A Search for Infall Evidence in EGOS. I. The Northern Sample. *ApJ*, 710:150–169, February 2010.
- X. Chen, C.-G. Gan, S. P. Ellingsen, J.-H. He, Z.-Q. Shen, and A. Titmarsh. Newly Identified Extended Green Objects (EGOs) from the *Spitzer* GLIMPSE II Survey. I. Catalog. *ApJS*, 206:9, May 2013.
- J. J. Clariá. NGC 3324. A very young open cluster in the Carina spiral feature. *A&AS*, 27: 145–153, January 1977.
- C. J. Clarke. The photoevaporation of discs around young stars in massive clusters. *MNRAS*, 376:1350–1356, April 2007.
- M. Cohen, W. A. Wheaton, and S. T. Megeath. Spectral Irradiance Calibration in the Infrared. XIV. The Absolute Calibration of 2MASS. *AJ*, 126:1090–1096, August 2003.
- M. Cohen, A. J. Green, M. R. Meade, B. Babler, R. Indebetouw, B. A. Whitney, C. Watson, M. Wolfire, M. J. Wolff, J. S. Mathis, and E. B. Churchwell. Absolute diffuse calibration of IRAC through mid-infrared and radio study of H II regions. *MNRAS*, 374: 979–998, January 2007. doi: 10.1111/j.1365-2966.2006.11209.x.
- P. Collinder. On structured properties of open galactic clusters and their spatial distribution. *Annals of the Observatory of Lund*, 2:1, 1931.
- R. M. Cutri and al. WISE All-Sky Data Release. *VizieR Online Data Catalog*, 2311, April 2012.
- R. M. Cutri, M. F. Skrutskie, S. van Dyk, C. A. Beichman, J. M. Carpenter, T. Chester, L. Cambresy, T. Evans, J. Fowler, J. Gizis, E. Howard, J. Huchra, T. Jarrett, E. L. Kopan, J. D. Kirkpatrick, R. M. Light, K. A. Marsh, H. McCallon, S. Schneider, R. Stiening, M. Sykes, M. Weinberg, W. A. Wheaton, S. Wheelock, and N. Zacarias. 2MASS All-Sky Catalog of Point Sources. *VizieR Online Data Catalog*, 2246, March 2003.
- R. M. Cutri, M. F. Skrutskie, S. Van Dyk, C. A. Beichman, J. M. Carpenter, T. Chester, L. Cambresy, T. Evans, J. Fowler, J. Gizis, E. Howard, J. Huchra, T. Jarrett, E. L. Kopan, J. D. Kirkpatrick, R. M. Light, K. A. Marsh, H. McCallon, S. Schneider, R. Stiening, M. Sykes, M. Weinberg, W. A. Wheaton, S. Wheelock, and N. Zacarias. Explanatory Supplement to the 2MASS All-Sky Data Release and Extended Mission Products. Technical report, 2008.
- R. M. Cutri, E. L. Wright, T. Conrow, J. Bauer, D. Benford, H. Brandenburg, J. Dailey, P. R. M. Eisenhardt, T. Evans, S. Fajardo-Acosta, J. Fowler, C. Gelino, C. Grillmair, M. Harbut, D. Hoffman, T. Jarrett, J. D. Kirkpatrick, D. Leisawitz, W. Liu, A. Mainzer, K. Marsh, F. Masci, H. McCallon, D. Padgett, M. E. Ressler, D. Royer, M. F. Skrutskie, S. A. Stanford, P. L. Wyatt, D. Tholen, C. W. Tsai, S. Wachter, S. L. Wheelock, L. Yan, R. Alles, R. Beck, T. Grav, J. Masiero, B. McCollum, P. McGehee, M. Papin, and M. Wittman. Explanatory Supplement to the WISE All-Sky Data Release Products. Technical report, March 2012.

## Bibliography

- C. J. Cyganowski, B. A. Whitney, E. Holden, E. Braden, C. L. Brogan, E. Churchwell, R. Indebetouw, D. F. Watson, B. L. Babler, R. Benjamin, M. Gomez, M. R. Meade, M. S. Povich, T. P. Robitaille, and C. Watson. A Catalog of Extended Green Objects in the GLIMPSE Survey: A New Sample of Massive Young Stellar Object Outflow Candidates. *AJ*, 136:2391–2412, December 2008.
- C. J. Cyganowski, C. L. Brogan, T. R. Hunter, and E. Churchwell. A Class I and Class II CH<sub>3</sub>OH Maser Survey of EGOS from the Galactic Legacy Infrared Mid-Plane Survey Extraordinaire (GLIMPSE) Survey. *ApJ*, 702:1615–1647, September 2009.
- S. E. Dahm and L. A. Hillenbrand. Spitzer Observations of NGC 2362: Primordial Disks at 5 Myr. *AJ*, 133:2072–2086, May 2007.
- G. B. Dalton, M. Caldwell, A. K. Ward, M. S. Whalley, G. Woodhouse, R. L. Edeson, P. Clark, S. M. Beard, A. M. Gallie, S. P. Todd, J. M. D. Strachan, N. N. Bezawada, W. J. Sutherland, and J. P. Emerson. The VISTA infrared camera. In *Society of Photo-Optical Instrumentation Engineers (SPIE) Conference Series*, volume 6269, July 2006.
- A. Daminieli, A. Kaufer, B. Wolf, O. Stahl, D. F. Lopes, and F. X. de Araújo.  $\eta$  Carinae: Binarity Confirmed. *ApJ*, 528:L101–L104, January 2000.
- C. J. Davis, P. Scholz, P. Lucas, M. D. Smith, and A. Adamson. A shallow though extensive H<sub>2</sub> 2.122- $\mu$ m imaging survey of Taurus-Auriga-Perseus - I. NGC 1333, L1455, L1448 and B1. *MNRAS*, 387:954–968, July 2008.
- J. M. De Buizer and W. D. Vacca. Direct Spectroscopic Identification of the Origin of “Green Fuzzy” Emission in Star-forming Regions. *AJ*, 140:196–202, July 2010.
- K. DeGioia-Eastwood, H. Throop, G. Walker, and K. M. Cudworth. The Star Formation History of Trumpler 14 and Trumpler 16. *ApJ*, 549:578–589, March 2001.
- L. K. Dewangan, D. K. Ojha, B. G. Anandarao, S. K. Ghosh, and S. Chakraborti. Triggered Star Formation around Mid-infrared Bubbles in the G8.14+0.23 H II Region. *ApJ*, 756:151, September 2012.
- E. Diolaiti, O. Bendinelli, D. Bonaccini, L. Close, D. Currie, and G. Parmeggiani. Analysis of isoplanatic high resolution stellar fields by the StarFinder code. *A&AS*, 147:335–346, December 2000.
- M. A. Dopita, I. Evans, and R. D. Schwartz. Herbig-Haro Objects 46 and 47 - Evidence for bipolar ejection from a young star. *ApJ*, 263:L73–L77, December 1982.
- J. L. E. Dreyer. A New General Catalogue of Nebulae and Clusters of Stars, being the Catalogue of the late Sir John F. W. Herschel, Bart, revised, corrected, and enlarged. *MmRAS*, 49:1, 1888.
- C. P. Dullemond and C. Dominik. Flaring vs. self-shadowed disks: The SEDs of Herbig Ae/Be stars. *A&A*, 417:159–168, April 2004.
- C. M. Dutra, E. Bica, J. Soares, and B. Barbuy. New infrared star clusters in the southern Milky Way with 2MASS. *A&A*, 400:533–539, March 2003.

- J. A. Eisner, R. L. Plambeck, J. M. Carpenter, S. A. Corder, C. Qi, and D. Wilner. Proplyds and Massive Disks in the Orion Nebula Cluster Imaged with CARMA and SMA. *ApJ*, 683:304–320, August 2008.
- J. H. Elias. H<sub>2</sub> emission from Herbig-Haro objects. *ApJ*, 241:728–735, October 1980.
- B. G. Elmegreen and C. J. Lada. Sequential formation of subgroups in OB associations. *ApJ*, 214:725–741, June 1977.
- J. Emerson and W. Sutherland. The Visible and Infrared Survey Telescope for Astronomy (VISTA): Looking Back at Commissioning. *The Messenger*, 139:2–5, March 2010.
- ESA. *Herschel* Space Observatory Summary. 2010. <http://sci.esa.int/herschel/34682-summary/>, called: 26 September 2013.
- M. Fang, R. van Boekel, R. R. King, T. Henning, J. Bouwman, Y. Doi, Y. K. Okamoto, V. Roccatagliata, and A. Sicilia-Aguilar. Star formation and disk properties in Pismis 24. *A&A*, 539:A119, March 2012.
- S. Faúndez, L. Bronfman, G. Garay, R. Chini, L.-Å. Nyman, and J. May. SIMBA survey of southern high-mass star forming regions. I. Physical parameters of the 1.2 mm/IRAS sources. *A&A*, 426:97–103, October 2004.
- G. G. Fazio, J. L. Hora, L. E. Allen, M. L. N. Ashby, P. Barmby, L. K. Deutsch, J.-S. Huang, S. Kleiner, M. Marengo, S. T. Megeath, G. J. Melnick, M. A. Pahre, B. M. Patten, J. Polizotti, H. A. Smith, R. S. Taylor, Z. Wang, S. P. Willner, W. F. Hoffmann, J. L. Pipher, W. J. Forrest, C. W. McMurty, C. R. McCreight, M. E. McKelvey, R. E. McMurray, D. G. Koch, S. H. Moseley, R. G. Arendt, J. E. Mentzell, C. T. Marx, P. Losch, P. Mayman, W. Eichhorn, D. Krebs, M. Jhabvala, D. Y. Gezari, D. J. Fixsen, J. Flores, K. Shakoorzadeh, R. Jungo, C. Hakun, L. Workman, G. Karpati, R. Kichak, R. Whitley, S. Mann, E. V. Tollestrup, P. Eisenhardt, D. Stern, V. Gorjian, B. Bhattacharya, S. Carey, B. O. Nelson, W. J. Glaccum, M. Lacy, P. J. Lowrance, S. Laine, W. T. Reach, J. A. Stauffer, J. A. Surace, G. Wilson, E. L. Wright, A. Hoffman, G. Domingo, and M. Cohen. The Infrared Array Camera (IRAC) for the *Spitzer* Space Telescope. *ApJS*, 154:10–17, September 2004.
- D. Fedele, M. E. van den Ancker, T. Henning, R. Jayawardhana, and J. M. Oliveira. Timescale of mass accretion in pre-main-sequence stars. *A&A*, 510:A72, February 2010.
- E. D. Feigelson, K. V. Getman, L. K. Townsley, P. S. Broos, M. S. Povich, G. P. Garmire, R. R. King, T. Montmerle, T. Preibisch, N. Smith, K. G. Stassun, J. Wang, S. Wolk, and H. Zinnecker. X-ray Star Clusters in the Carina Complex. *ApJS*, 194:9, May 2011.
- E. Fernández-Lajús, C. Fariña, A. F. Torres, M. A. Schwartz, N. Salerno, J. P. Calderón, C. von Essen, L. M. Calcaferro, F. Giudici, C. Llinares, and V. Niemela. Long-term optical monitoring of  $\eta$  Carinae. Multiband light curves for a complete orbital period. *A&A*, 493:1093–1097, January 2009.
- M. P. Fitzgerald, R. Hurkens, and A. F. J. Moffat. Bochum 15, a new young stellar aggregate in Puppis. *A&A*, 46:287–291, January 1976.

## Bibliography

- H. C. Ford and the ACS Science Team. The Hubble Space Telescope Advanced Camera for Surveys. In *American Astronomical Society Meeting Abstracts*, volume 32 of *Bulletin of the American Astronomical Society*, page 1421, December 2000.
- J. C. Forte. *UBV* photometry of luminous stars in the field of NGC 3372. *A&AS*, 25: 271–280, July 1976.
- P. N. Foster and A. P. Boss. Triggering Star Formation with Stellar Ejecta. *ApJ*, 468:784, September 1996.
- D. J. Frew. The Historical Record of  $\eta$  Carinae I. The Visual Light Curve, 1595-2000. *Journal of Astronomical Data*, 10:6, December 2004.
- T. Freyer, G. Hensler, and H. W. Yorke. Massive Stars and the Energy Balance of the Interstellar Medium. I. The Impact of an Isolated  $60 M_{\odot}$  Star. *ApJ*, 594:888–910, September 2003.
- B. Gaczkowski, T. Preibisch, T. Ratzka, V. Roccatagliata, H. Ohlendorf, and H. Zinnecker. Embedded YSOs in Carina Nebula complex. *VizieR Online Data Catalog*, 354:99067, November 2012.
- B. Gaczkowski, T. Preibisch, T. Ratzka, V. Roccatagliata, H. Ohlendorf, and H. Zinnecker. Herschel far-infrared observations of the Carina Nebula complex. II. The embedded young stellar and protostellar population. *A&A*, 549:A67, January 2013.
- S. K. Ghosh, K. V. K. Iyengar, T. N. Rengarajan, S. N. Tandon, R. P. Verma, and R. R. Daniel. Far-infrared (120-300 micron) observations of the Carina Nebula. *ApJ*, 330:928, July 1988.
- I. S. Glass. The *JHKL* colours of galaxies. *MNRAS*, 164:155–168, 1973.
- T. de Graauw, S. Lidholm, B. Fitton, J. Beckman, F. P. Israel, H. Nieuwenhuijzen, and J. Vermue. CO  $J = 2 - 1$  observations of southern H II regions. *A&A*, 102:257–264, October 1981.
- T. P. Greene, B. A. Wilking, P. André, E. T. Young, and C. J. Lada. Further mid-infrared study of the  $\rho$  Ophiuchi cloud young stellar population: Luminosities and masses of pre-main-sequence stars. *ApJ*, 434:614–626, October 1994.
- M. J. Griffin, A. Abergel, A. Abreu, P. A. R. Ade, P. André, J.-L. Augueres, T. Babbedge, Y. Bae, T. Baillie, J.-P. Baluteau, M. J. Barlow, G. Bendo, D. Benielli, J. J. Bock, P. Bonhomme, D. Brisbin, C. Brockley-Blatt, M. Caldwell, C. Cara, N. Castro-Rodriguez, R. Cerulli, P. Chaniel, S. Chen, E. Clark, D. L. Clements, L. Clerc, J. Coker, D. Communal, L. Conversi, P. Cox, D. Crumb, C. Cunningham, F. Daly, G. R. Davis, P. de Antoni, J. Delderfield, N. Devin, A. di Giorgio, I. Didschuns, K. Dohlen, M. Donati, A. Dowell, C. D. Dowell, L. Duband, L. Dumaye, R. J. Emery, M. Ferlet, D. Ferrand, J. Fontignie, M. Fox, A. Franceschini, M. Frerking, T. Fulton, J. Garcia, R. Gastaud, W. K. Gear, J. Glenn, A. Goizel, D. K. Griffin, T. Grundy, S. Guest, L. Guillemet, P. C. Hargrave, M. Harwit, P. Hastings, E. Hatziminaoglou, M. Herman, B. Hinde, V. Hristov, M. Huang, P. Imhof, K. J. Isaak, U. Israelsson, R. J. Ivison, D. Jennings,

- B. Kiernan, K. J. King, A. E. Lange, W. Latter, G. Laurent, P. Laurent, S. J. Leeks, E. Lellouch, L. Levenson, B. Li, J. Li, J. Lilienthal, T. Lim, S. J. Liu, N. Lu, S. Madden, G. Mainetti, P. Marliani, D. McKay, K. Mercier, S. Molinari, H. Morris, H. Moseley, J. Mulder, M. Mur, D. A. Naylor, H. Nguyen, B. O'Halloran, S. Oliver, G. Olofsson, H.-G. Olofsson, R. Orfei, M. J. Page, I. Pain, P. Panuzzo, A. Papageorgiou, G. Parks, P. Parr-Burman, A. Pearce, C. Pearson, I. Pérez-Fournon, F. Pinsard, G. Pisano, J. Podosek, M. Pohlen, E. T. Polehampton, D. Pouliquen, D. Rigopoulou, D. Rizzo, I. G. Roseboom, H. Roussel, M. Rowan-Robinson, B. Rownd, P. Saraceno, M. Sauvage, R. Savage, G. Savini, E. Sawyer, C. Scharnberg, D. Schmitt, N. Schneider, B. Schulz, A. Schwartz, R. Shafer, D. L. Shupe, B. Sibthorpe, S. Sidher, A. Smith, A. J. Smith, D. Smith, L. Spencer, B. Stobie, R. Sudiwala, K. Sukhatme, C. Surace, J. A. Stevens, B. M. Swinyard, M. Trichas, T. Tourette, H. Triou, S. Tseng, C. Tucker, A. Turner, M. Vaccari, I. Valtchanov, L. Vigroux, E. Virique, G. Voellmer, H. Walker, R. Ward, T. Waskett, M. Weilert, R. Wesson, G. J. White, N. Whitehouse, C. D. Wilson, B. Winter, A. L. Woodcraft, G. S. Wright, C. K. Xu, A. Zavagno, M. Zemcov, L. Zhang, and E. Zonca. The *Herschel*-SPIRE instrument and its in-flight performance. *A&A*, 518:L3, July 2010.
- M. Gritschneider, A. Burkert, T. Naab, and S. Walch. Detailed Numerical Simulations on the Formation of Pillars Around HII Regions. *ApJ*, 723:971–984, November 2010.
- R. A. Gutermuth, P. C. Myers, S. T. Megeath, L. E. Allen, J. L. Pipher, J. Muzerolle, A. Porras, E. Winston, and G. Fazio. *Spitzer* Observations of NGC 1333: A Study of Structure and Evolution in a Nearby Embedded Cluster. *ApJ*, 674:336–356, February 2008.
- K. E. Haisch, Jr., E. A. Lada, and C. J. Lada. Disk Frequencies and Lifetimes in Young Clusters. *ApJ*, 553:L153–L156, June 2001a.
- K. E. Haisch, Jr., E. A. Lada, and C. J. Lada. Circumstellar Disks in the IC 348 Cluster. *AJ*, 121:2065–2074, April 2001b.
- K. Hamaguchi, R. Petre, H. Matsumoto, M. Tsujimoto, S. S. Holt, Y. Ezoe, H. Ozawa, Y. Tsuboi, Y. Soong, S. Kitamoto, A. Sekiguchi, and M. Kokubun. *Suzaku* Observation of Diffuse X-Ray Emission from the Carina Nebula. *PASJ*, 59:151–161, January 2007.
- K. Hamaguchi, M. F. Corcoran, Y. Ezoe, L. Townsley, P. Broos, R. Gruendl, K. Vaidya, S. M. White, T. Strohmayer, R. Petre, and Y.-H. Chu. A Smoking Gun in the Carina Nebula. *ApJ*, 695:L4–L9, April 2009.
- A. Hanslmeier. *Einführung in die Astronomie und Astrophysik*. Spektrum Akademischer Verlag, Berlin, Heidelberg, 2007.
- G. Haro. Herbig's Nebulous Objects Near NGC 1999. *ApJ*, 115:572, May 1952.
- G. Haro. H $\alpha$  Emission Stars and Peculiar Objects in the Orion Nebula. *ApJ*, 117:73, January 1953.
- P. Harvey, B. Merín, T. L. Huard, L. M. Rebull, N. Chapman, N. J. Evans, II, and P. C. Myers. The *Spitzer* c2d Survey of Large, Nearby, Interstellar Clouds. IX. The Serpens YSO Population as Observed with IRAC and MIPS. *ApJ*, 663:1149–1173, July 2007.

## Bibliography

- P. M. Harvey, W. F. Hoffmann, and M. F. Campbell. Far-infrared observations of the Carina I and II H II regions. *ApJ*, 227:114–120, January 1979.
- P. M. Harvey, N. Chapman, S.-P. Lai, N. J. Evans, II, L. E. Allen, J. K. Jørgensen, L. G. Mundy, T. L. Huard, A. Porras, L. Cieza, P. C. Myers, B. Merín, E. F. van Dishoeck, K. E. Young, W. Spiesman, G. A. Blake, D. W. Koerner, D. L. Padgett, A. I. Sargent, and K. R. Stapelfeldt. The *Spitzer* c2d Survey of Large, Nearby, Interstellar Clouds. II. Serpens Observed with IRAC. *ApJ*, 644:307–325, June 2006.
- C. Hayashi. Evolution of Protostars. *ARA&A*, 4:171 et seqq., 1966.
- G. H. Herbig. The Spectrum of the Nebulosity Surrounding T Tauri. *ApJ*, 111:11, January 1950.
- G. H. Herbig. The Spectra of Two Nebulous Objects Near NGC 1999. *ApJ*, 113:697–699, May 1951.
- J. Hernández, L. Hartmann, T. Megeath, R. Gutermuth, J. Muzerolle, N. Calvet, A. K. Vivas, C. Briceño, L. Allen, J. Stauffer, E. Young, and G. Fazio. A *Spitzer* Space Telescope Study of Disks in the Young  $\sigma$  Orionis Cluster. *ApJ*, 662:1067–1081, June 2007.
- J. J. Hester, P. A. Scowen, R. Sankrit, T. R. Lauer, E. A. Ajhar, W. A. Baum, A. Code, D. G. Currie, G. E. Danielson, S. P. Ewald, S. M. Faber, C. J. Grillmair, E. J. Groth, J. A. Holtzman, D. A. Hunter, J. Kristian, R. M. Light, C. R. Lynds, D. G. Monet, E. J. O’Neil, Jr., E. J. Shaya, P. K. Seidelmann, and J. A. Westphal. *Hubble* Space Telescope WFPC 2 Imaging of M16: Photoevaporation and Emerging Young Stellar Objects. *AJ*, 111:2349, June 1996.
- D. Hoffleit. A preliminary survey of nebulosities and associated B-stars in Carina. *Annals of Harvard College Observatory*, 119:37–68, 1953.
- D. Hollenbach, D. Johnstone, S. Lizano, and F. Shu. Photoevaporation of disks around massive stars and application to ultracompact H II regions. *ApJ*, 428:654–669, June 1994.
- J. L. Hora, S. Carey, J. Surace, M. Marengo, P. Lowrance, W. J. Glaccum, M. Lacy, W. T. Reach, W. F. Hoffmann, P. Barmby, S. P. Willner, G. G. Fazio, S. T. Megeath, L. E. Allen, B. Bhattacharya, and M. Quijada. Photometry using the Infrared Array Camera on the *Spitzer* Space Telescope. *PASP*, 120:1233–1243, November 2008.
- J. R. Houck, T. L. Roellig, J. van Cleve, W. J. Forrest, T. Herter, C. R. Lawrence, K. Matthews, H. J. Reitsema, B. T. Soifer, D. M. Watson, D. Weedman, M. Huisjen, J. Troeltzsch, D. J. Barry, J. Bernard-Salas, C. E. Blacken, B. R. Brandl, V. Charmandaris, D. Devost, G. E. Gull, P. Hall, C. P. Henderson, S. J. U. Higdon, B. E. Pirger, J. Schoenwald, G. C. Sloan, K. I. Uchida, P. N. Appleton, L. Armus, M. J. Burgdorf, S. B. Fajardo-Acosta, C. J. Grillmair, J. G. Ingalls, P. W. Morris, and H. I. Teplitz. The Infrared Spectrograph (IRS) on the *Spitzer* Space Telescope. *ApJS*, 154:18–24, September 2004.

- R. Q. Huang and K. N. Yu. *Stellar Astrophysics*. Springer-Verlag Singapore, Singapore, 1998.
- R. Indebetouw, J. S. Mathis, B. L. Babler, M. R. Meade, C. Watson, B. A. Whitney, M. J. Wolff, M. G. Wolfire, M. Cohen, T. M. Bania, R. A. Benjamin, D. P. Clemens, J. M. Dickey, J. M. Jackson, H. A. Kobulnicky, A. P. Marston, E. P. Mercer, J. R. Stauffer, S. R. Stolovy, and E. Churchwell. The Wavelength Dependence of Interstellar Extinction from 1.25 to 8.0  $\mu\text{m}$  Using GLIMPSE Data. *ApJ*, 619:931–938, February 2005.
- IPAC. About 2MASS. 2006. <http://www.ipac.caltech.edu/2mass/overview/about2mass.html>, called: 29 September 2013.
- IRAC Instrument and Instrument Support Teams. *IRAC Instrument Handbook v2.0.2*. 2012. <http://irsa.ipac.caltech.edu/data/SPITZER/docs/irac/iracinstrumenthandbook/>.
- IRAC Instrument and Instrument Support Teams. *IRAC Instrument Handbook v2.0.3*. 2013. <http://irsa.ipac.caltech.edu/data/SPITZER/docs/irac/iracinstrumenthandbook/>.
- M. J. Irwin, J. Lewis, S. Hodgkin, P. Bunclark, D. Evans, R. McMahon, J. P. Emerson, M. Stewart, and S. Beard. VISTA data flow system: pipeline processing for WFCAM and VISTA. In P. J. Quinn & A. Bridger, editor, *Society of Photo-Optical Instrumentation Engineers (SPIE) Conference Series*, volume 5493, pages 411–422, September 2004.
- J. H. Jeans. The Stability of a Spherical Nebula. *Royal Society of London Philosophical Transactions Series A*, 199:1–53, 1902.
- H. L. Johnson. Interstellar Extinction in the Galaxy. *ApJ*, 141:923, April 1965.
- N. V. Kharchenko, A. E. Piskunov, S. Röser, E. Schilbach, and R.-D. Scholz. Astrophysical parameters of Galactic open clusters. *A&A*, 438:1163–1173, August 2005.
- M. K. Kim, T. Hirota, M. Honma, H. Kobayashi, T. Bushimata, Y. K. Choi, H. Imai, K. Iwadate, T. Jike, S. Kamenno, O. Kameya, R. Kamohara, Y. Kan-Ya, N. Kawaguchi, S. Kuji, T. Kurayama, S. Manabe, M. Matsui, N. Matsumoto, T. Miyaji, T. Nagayama, A. Nakagawa, C. S. Oh, T. Omodaka, T. Oyama, S. Sakai, T. Sasao, K. Sato, M. Sato, K. M. Shibata, Y. Tamura, and K. Yamashita. SiO Maser Observations toward Orion-KL with VERA. *PASJ*, 60:991–, October 2008.
- M. Klassen, R. E. Pudritz, and T. Peters. Simulating protostellar evolution and radiative feedback in the cluster environment. *MNRAS*, 421:2861–2871, April 2012.
- H. A. Kobulnicky, B. L. Babler, M. J. Alexander, M. R. Meade, B. A. Whitney, and E. B. Churchwell. Effects of Diffuse Background Emission and Source Crowding on Photometric Completeness in *Spitzer* Space Telescope IRAC Surveys: the GLIMPSE Catalogs and Archives. *ApJS*, 207:9, July 2013.
- X. P. Koenig, D. T. Leisawitz, D. J. Benford, L. M. Rebull, D. L. Padgett, and R. J. Assef. Wide-field Infrared Survey Explorer Observations of the Evolution of Massive Star-forming Regions. *ApJ*, 744:130, January 2012.

## Bibliography

- C. Kramer, M. Cubick, M. Röllig, K. Sun, Y. Yonekura, M. Aravena, F. Bensch, F. Bertoldi, L. Bronfman, M. Fujishita, Y. Fukui, U. U. Graf, M. Hitschfeld, N. Honingh, S. Ito, H. Jakob, K. Jacobs, U. Klein, B.-C. Koo, J. May, M. Miller, Y. Miyamoto, N. Mizuno, T. Onishi, Y.-S. Park, J. L. Pineda, D. Rabanus, H. Sasago, R. Schieder, R. Simon, J. Stutzki, N. Volgenau, and H. Yamamoto. Clumpy photon-dominated regions in Carina. I. [C I] and mid-J CO lines in two  $4' \times 4'$  fields. *A&A*, 477:547–555, January 2008.
- P. Kroupa. The Initial Mass Function of Stars: Evidence for Uniformity in Variable Systems. *Science*, 295:82–91, January 2002.
- R. P. Kudritzki, J. Puls, D. J. Lennon, K. A. Venn, J. Reetz, F. Najarro, J. K. McCarthy, and A. Herrero. The wind momentum-luminosity relationship of galactic A- and B-supergiants. *A&A*, 350:970–984, October 1999.
- C. J. Lada. Star formation - From OB associations to protostars. In M. Peimbert & J. Jugaku, editor, *Star Forming Regions*, volume 115 of *IAU Symposium*, pages 1–17, 1987.
- C. J. Lada, A. A. Muench, K. L. Luhman, L. Allen, L. Hartmann, T. Megeath, P. Myers, G. Fazio, K. Wood, J. Muzerolle, G. Rieke, N. Siegler, and E. Young. *Spitzer* Observations of IC 348: The Disk Population at 2-3 Million Years. *AJ*, 131:1574–1607, March 2006.
- E. A. Lada and C. J. Lada. Near-infrared images of IC 348 and the luminosity functions of young embedded star clusters. *AJ*, 109:1682–1696, April 1995.
- G. Lyngå and N. Hansson. Nebulae of the Southern Milky Way. An Atlas. *A&AS*, 6:327, August 1972.
- J. Maíz-Apellániz, N. R. Walborn, H. Á. Galué, and L. H. Wei. A Galactic O Star Catalog. *ApJS*, 151:103–148, March 2004.
- D. Makovoz and F. R. Marleau. Point-Source Extraction with MOPEX. *PASP*, 117:1113–1128, October 2005.
- R. K. Mann and J. P. Williams. A Submillimeter Array Survey of Protoplanetary Disks in the Orion Nebula Cluster. *ApJ*, 725:430–442, December 2010.
- A. P. Marston, W. T. Reach, A. Noriega-Crespo, J. Rho, H. A. Smith, G. Melnick, G. Fazio, G. Rieke, S. Carey, L. Rebull, J. Muzerolle, E. Egami, D. M. Watson, J. L. Pipher, W. B. Latter, and K. Stapelfeldt. DR 21: A Major Star Formation Site Revealed by *Spitzer*. *ApJS*, 154:333–338, September 2004.
- M. J. McCaughrean, J. T. Rayner, and H. Zinnecker. Discovery of a molecular hydrogen jet near IC 348. *ApJ*, 436:L189–L192, December 1994.
- S. T. Megeath, P. Cox, L. Bronfman, and P. R. Roelfsema. Evidence for ongoing star formation in the Carina nebula. *A&A*, 305:296, January 1996.
- A. B. Men'shchikov and T. Henning. Radiation transfer in circumstellar disks. *A&A*, 318: 879–907, February 1997.

- K. M. Menten, M. J. Reid, J. Forbrich, and A. Brunthaler. The distance to the Orion Nebula. *A&A*, 474:515–520, November 2007.
- E. Mentuch, R. G. Abraham, K. Glazebrook, P. J. McCarthy, H. Yan, D. V. O’Donnell, D. Le Borgne, S. Savaglio, D. Crampton, R. Murowinski, S. Juneau, R. G. Carlberg, I. Jørgensen, K. Roth, H.-W. Chen, and R. O. Marzke. A Near-Infrared Excess in the Continuum of High-redshift Galaxies: A Tracer of Star Formation and Circumstellar Disks? *ApJ*, 706:1020–1035, December 2009.
- V. Minier, S. P. Ellingsen, R. P. Norris, and R. S. Booth. The protostellar mass limit for 6.7 GHz methanol masers. I. A low-mass YSO survey. *A&A*, 403:1095–1100, June 2003.
- MIPS Instrument and MIPS Instrument Support Teams. *MIPS Instrument Handbook v3.0*. 2011. <http://irsa.ipac.caltech.edu/data/SPITZER/docs/mips/mipsinstrumenthandbook/>.
- A. F. J. Moffat and N. Vogt. Southern open star clusters IV. *UBV-H $\beta$*  photometry of 26 clusters from Monoceros to Vela. *A&AS*, 20:85–124, April 1975a.
- A. F. J. Moffat and N. Vogt. Southern open star clusters V. *UBV-H $\beta$*  photometry of 20 clusters in Carina. *A&AS*, 20:125–153, April 1975b.
- A. F. J. Moffat and N. Vogt. Southern open star clusters VI. *UBV-H $\beta$*  photometry of 18 clusters from Centaurus to Sagittarius. *A&AS*, 20:155–182, April 1975c.
- Post-BCD Tools Team and Science User Support Team. *MOPEX User’s Guide v18.4.0*. 2010. <http://irsa.ipac.caltech.edu/data/SPITZER/docs/dataanalysistools/tools/mopex/mopexusersguide/>.
- D. Moro and U. Munari. The Asiago Database on Photometric Systems (ADPS). I. Census parameters for 167 photometric systems. *A&AS*, 147:361–628, December 2000.
- J. C. Mottram, M. G. Hoare, S. L. Lumsden, R. D. Oudmaijer, J. S. Urquhart, T. L. Sheret, A. J. Clarke, and J. Allsopp. The RMS survey: mid-infrared observations of candidate massive YSOs in the southern hemisphere. *A&A*, 476:1019–1111, December 2007.
- A. Muench, K. Getman, L. Hillenbrand, and T. Preibisch. Star Formation in the Orion Nebula I: Stellar Content. In B. Reipurth, editor, *Handbook of Star Forming Regions, Volume I*, page 483, December 2008.
- NASA. The Last of the Great Observatories. 2007. [http://www.nasa.gov/missions/deepspace/MI\\_CM\\_Feature\\_01.html](http://www.nasa.gov/missions/deepspace/MI_CM_Feature_01.html), called: 25 September 2013.
- T. Neckel and H. Vehrenberg. *Atlas Galaktischer Nebel. (Atlas of Galactic Nebulae). Part I: R.A. 0<sup>h</sup> 00<sup>m</sup> - 12<sup>h</sup> 00<sup>m</sup>; Decl. +90° - -33°*. Treugesell-Verlag, Düsseldorf, 1985.
- T. Neckel and H. Vehrenberg. *Atlas Galaktischer Nebel. (Atlas of Galactic Nebulae). Part II: R.A. 12<sup>h</sup> 00<sup>m</sup> - 24<sup>h</sup> 00<sup>m</sup>; Decl. +90° - -33°*. Treugesell-Verlag, Düsseldorf, 1987.
- T. Neckel and H. Vehrenberg. *Atlas Galaktischer Nebel. (Atlas of Galactic Nebulae). Part III: R.A. 00<sup>h</sup> 00<sup>m</sup> - 24<sup>h</sup> 00<sup>m</sup>; Decl. -33° - -90°*. Treugesell-Verlag, Düsseldorf, 1990.

## Bibliography

- V. V. Nesterov, A. V. Kuzmin, N. T. Ashimbaeva, A. A. Volchkov, S. Röser, and U. Bastian. The Henry Draper Extension Charts: A catalogue of accurate positions, proper motions, magnitudes and spectral types of 86933 stars. *A&AS*, 110:367, April 1995.
- A. Noriega-Crespo, P. Morris, F. R. Marleau, S. Carey, A. Boogert, E. van Dishoeck, N. J. Evans, II, J. Keene, J. Muzerolle, K. Stapelfeldt, K. Pontoppidan, P. Lowrance, L. Allen, and T. L. Bourke. A New Look at Stellar Outflows: *Spitzer* Observations of the HH 46/47 System. *ApJS*, 154:352–358, September 2004.
- H. Ohlendorf, T. Preibisch, B. Gaczkowski, T. Ratzka, R. Grellmann, and A. F. McLeod. Jet-driving protostars identified from infrared observations of the Carina Nebula complex. *A&A*, 540:A81, April 2012.
- H. Ohlendorf, T. Preibisch, B. Gaczkowski, T. Ratzka, J. Ngoumou, V. Roccatagliata, and R. Grellmann. Discovering young stars in the Gum 31 region with infrared observations. *A&A*, 552:A14, April 2013a.
- H. Ohlendorf, T. Preibisch, V. Roccatagliata, and T. Ratzka. Clustering properties of the young stellar population in the Carina Nebula Complex derived from a wide-field *Spitzer* survey. *AJ*, 2013b. submitted.
- I. Oliveira, B. Merín, K. M. Pontoppidan, E. F. van Dishoeck, R. A. Overzier, J. Hernández, A. Sicilia-Aguilar, C. Eiroa, and B. Montesinos. Optical Characterization of A New Young Stellar Population in the Serpens Molecular Cloud. *ApJ*, 691: 672–686, January 2009.
- F. Patat and G. Carraro. Star clusterings in the Carina complex: *UBVRI* photometry of Bochum 9, 10 and 11. *MNRAS*, 325:1591–1602, August 2001.
- S. Pekruhl, T. Preibisch, F. Schuller, and K. Menten. The clump mass function of the dense clouds in the Carina nebula complex. *A&A*, 550:A29, February 2013.
- M. A. C. Perryman and ESA, editors. *The HIPPARCOS and TYCHO catalogues. Astrometric and photometric star catalogues derived from the ESA HIPPARCOS Space Astrometry Mission*, volume 1200 of *ESA Special Publication*, 1997.
- A. Pickles and É. Depagne. All-Sky Spectrally Matched *UBVRI-ZY* and *u'g'r'i'z'* Magnitudes for Stars in the Tycho-2 Catalog. *PASP*, 122:1437–1464, December 2010.
- A. M. Pires, C. Motch, R. Turolla, A. Treves, and S. B. Popov. The isolated neutron star candidate 2XMM J104608.7-594306. *A&A*, 498:233–240, April 2009.
- Planck* Collaboration, P. A. R. Ade, N. Aghanim, M. Arnaud, M. Ashdown, J. Aumont, C. Baccigalupi, M. Baker, A. Balbi, A. J. Banday, and et al. *Planck* early results. I. The *Planck* mission. *A&A*, 536:A1, December 2011.
- A. Poglitsch, C. Waelkens, N. Geis, H. Feuchtgruber, B. Vandenbussche, L. Rodriguez, O. Krause, E. Renotte, C. van Hoof, P. Saraceno, J. Cepa, F. Kerschbaum, P. Agnèse, B. Ali, B. Altieri, P. Andreani, J.-L. Augeres, Z. Balog, L. Barl, O. H. Bauer, N. Belbachir, M. Benedettini, N. Billot, O. Boulade, H. Bischof, J. Blommaert, E. Callut, C. Cara, R. Cerulli, D. Cesarsky, A. Contursi, Y. Creten, W. De Meester, V. Doublier,

- E. Doumayrou, L. Duband, K. Exter, R. Genzel, J.-M. Gillis, U. Grözinger, T. Henning, J. Herreros, R. Huygen, M. Inguccio, G. Jakob, C. Jamar, C. Jean, J. de Jong, R. Katterloher, C. Kiss, U. Klaas, D. Lemke, D. Lutz, S. Madden, B. Marquet, J. Martignac, A. Mazy, P. Merken, F. Montfort, L. Morbidelli, T. Müller, M. Nielbock, K. Okumura, R. Orfei, R. Ottensamer, S. Pezzuto, P. Popesso, J. Putzeys, S. Regibo, V. Reveret, P. Royer, M. Sauvage, J. Schreiber, J. Stegmaier, D. Schmitt, J. Schubert, E. Sturm, M. Thiel, G. Tofani, R. Vavrek, M. Wetzstein, E. Wieprecht, and E. Wiezorrek. The Photodetecting Array Camera and Spectrometer (PACS) on the *Herschel* Space Observatory. *A&A*, 518:L2, July 2010.
- M. S. Povich and B. A. Whitney. Evidence for Delayed Massive Star Formation in the M17 Proto-OB association. *ApJ*, 714:L285–L289, May 2010.
- M. S. Povich, E. Churchwell, J. H. Bieging, M. Kang, B. A. Whitney, C. L. Brogan, C. A. Kulesa, M. Cohen, B. L. Babler, R. Indebetouw, M. R. Meade, and T. P. Robitaille. The Extended Environment of M17: A Star Formation History. *ApJ*, 696:1278–1306, May 2009.
- M. S. Povich, N. Smith, S. R. Majewski, K. V. Getman, L. K. Townsley, B. L. Babler, P. S. Broos, R. Indebetouw, M. R. Meade, T. P. Robitaille, K. G. Stassun, B. A. Whitney, Y. Yonekura, and Y. Fukui. A Pan-Carina Young Stellar Object Catalog: Intermediate-mass Young Stellar Objects in the Carina Nebula Identified Via Mid-infrared Excess Emission. *ApJS*, 194:14, May 2011a.
- M. S. Povich, L. K. Townsley, P. S. Broos, M. Gagné, B. L. Babler, R. Indebetouw, S. R. Majewski, M. R. Meade, K. V. Getman, T. P. Robitaille, and R. H. D. Townsend. Candidate X-ray-emitting OB Stars in the Carina Nebula Identified Via Infrared Spectral Energy Distributions. *ApJS*, 194:6, May 2011b.
- T. Preibisch, A. G. A. Brown, T. Bridges, E. Guenther, and H. Zinnecker. Exploring the Full Stellar Population of the Upper Scorpius OB association. *AJ*, 124:404–416, July 2002.
- T. Preibisch, S. Hodgkin, M. Irwin, J. R. Lewis, R. R. King, M. J. McCaughrean, H. Zinnecker, L. Townsley, and P. Broos. Near-infrared Properties of the X-ray-emitting Young Stellar Objects in the Carina Nebula. *ApJS*, 194:10, May 2011a.
- T. Preibisch, T. Ratzka, T. Gehring, H. Ohlendorf, H. Zinnecker, R. R. King, M. J. McCaughrean, and J. R. Lewis. Detection of a large massive circumstellar disk around a high-mass young stellar object in the Carina Nebula. *A&A*, 530:A40, June 2011b.
- T. Preibisch, T. Ratzka, B. Kuderna, H. Ohlendorf, R. R. King, S. Hodgkin, M. Irwin, J. R. Lewis, M. J. McCaughrean, and H. Zinnecker. Deep wide-field near-infrared survey of the Carina Nebula. *A&A*, 530:A34, June 2011c.
- T. Preibisch, F. Schuller, H. Ohlendorf, S. Pékruhl, K. M. Menten, and H. Zinnecker. A deep wide-field sub-mm survey of the Carina Nebula complex. *A&A*, 525:A92, January 2011d.

## Bibliography

- T. Preibisch, V. Roccatagliata, B. Gaczkowski, and T. Ratzka. *Herschel* far-infrared observations of the Carina Nebula complex. I. Introduction and global cloud structure. *A&A*, 541:A132, May 2012.
- N. Przybilla, K. Butler, S. R. Becker, and R. P. Kudritzki. Quantitative spectroscopy of BA-type supergiants. *A&A*, 445:1099–1126, January 2006.
- A. C. Raga and B. Reipurth. Herbig-Haro Jets Emerging from a Neutral Cloud into a H II region. In C. Allen, editor, *Revista Mexicana de Astronomia y Astrofisica Conference Series*, volume 40 of *Revista Mexicana de Astronomia y Astrofisica*, vol. 27, pages 15–23, April 2004.
- S. Ragan, T. Henning, O. Krause, J. Pitann, H. Beuther, H. Linz, J. Tackenberg, Z. Balog, M. Hennemann, R. Launhardt, N. Lippok, M. Nielbock, A. Schmiedeke, F. Schuller, J. Steinacker, A. Stutz, and T. Vasyunina. The Earliest Phases of Star Formation (EPoS): a *Herschel* key program. The precursors to high-mass stars and clusters. *A&A*, 547:A49, November 2012.
- J. M. Rathborne, K. J. Brooks, M. G. Burton, M. Cohen, and S. Bontemps. The giant pillars of the Carina Nebula. *A&A*, 418:563–576, May 2004.
- W. T. Reach, J. Rho, A. Tappe, T. G. Pannuti, C. L. Brogan, E. B. Churchwell, M. R. Meade, B. Babler, R. Indebetouw, and B. A. Whitney. A *Spitzer* Space Telescope Infrared Survey of Supernova Remnants in the Inner Galaxy. *AJ*, 131:1479–1500, March 2006.
- L. M. Rebull, D. L. Padgett, C.-E. McCabe, L. A. Hillenbrand, K. R. Stapelfeldt, A. Noriega-Crespo, S. J. Carey, T. Brooke, T. Huard, S. Terebey, M. Audard, J.-L. Monin, M. Fukagawa, M. Güdel, G. R. Knapp, F. Menard, L. E. Allen, J. R. Angione, C. Baldovin-Saavedra, J. Bouvier, K. Briggs, C. Dougados, N. J. Evans, N. Flagey, S. Guieu, N. Grosso, A. M. Glauser, P. Harvey, D. Hines, W. B. Latter, S. L. Skinner, S. Strom, J. Tromp, and S. Wolf. The Taurus *Spitzer* Survey: New Candidate Taurus Members Selected Using Sensitive Mid-Infrared Photometry. *ApJS*, 186:259–307, February 2010.
- B. C. Reed. Catalog of Galactic OB Stars. *AJ*, 125:2531–2533, May 2003.
- B. Reipurth. General Catalogue of Herbig-Haro Objects. *VizieR Online Data Catalog*, 5104:0, June 2000.
- B. Reipurth and J. Bally. Herbig-Haro Flows: Probes of Early Stellar Evolution. *ARA&A*, 39:403–455, 2001.
- G. H. Rieke, E. T. Young, C. W. Engelbracht, D. M. Kelly, F. J. Low, E. E. Haller, J. W. Beeman, K. D. Gordon, J. A. Stansberry, K. A. Misselt, J. Cadien, J. E. Morrison, G. Rivlis, W. B. Latter, A. Noriega-Crespo, D. L. Padgett, K. R. Stapelfeldt, D. C. Hines, E. Egami, J. Muzerolle, A. Alonso-Herrero, M. Blaylock, H. Dole, J. L. Hinz, E. Le Floch, C. Papovich, P. G. Pérez-González, P. S. Smith, K. Y. L. Su, L. Bennett, D. T. Frayer, D. Henderson, N. Lu, F. Masci, M. Pesenson, L. Rebull, J. Rho, J. Keene, S. Stolovy, S. Wachter, W. Wheaton, M. W. Werner, and P. L. Richards. The Multiband Imaging Photometer for *Spitzer* (MIPS). *ApJS*, 154:25–29, September 2004.

- T. P. Robitaille, B. A. Whitney, R. Indebetouw, K. Wood, and P. Denzmore. Interpreting Spectral Energy Distributions from Young Stellar Objects. I. A Grid of 200,000 yso Model SEDs. *ApJS*, 167:256–285, December 2006.
- T. P. Robitaille, B. A. Whitney, R. Indebetouw, and K. Wood. Interpreting Spectral Energy Distributions from Young Stellar Objects. II. Fitting Observed SEDs Using a Large Grid of Precomputed Models. *ApJS*, 169:328–352, April 2007.
- V. Roccatagliata, J. Bouwman, T. Henning, M. Gennaro, E. Feigelson, J. S. Kim, A. Sicilia-Aguilar, and W. A. Lawson. Disk Evolution in OB Associations: Deep *Spitzer*/IRAC Observations of IC 1795. *ApJ*, 733:113, June 2011.
- V. Roccatagliata, T. Preibisch, T. Ratzka, and B. Gaczkowski. Herschel far-infrared observations of the Carina Nebula complex. III. Detailed cloud structure and feedback effects. *A&A*, 554:A6, June 2013.
- M. Salatino, P. de Bernardis, S. Masi, and G. Polenta. The Spectral Energy Distribution of the Carina Nebula from Far-infrared to Radio Wavelengths. *ApJ*, 748:1, March 2012.
- S. Schmeja. Identifying star clusters in a field: A comparison of different algorithms. *Astronomische Nachrichten*, 332:172, February 2011.
- F. Schuller, K. M. Menten, Y. Contreras, F. Wyrowski, P. Schilke, L. Bronfman, T. Henning, C. M. Walmsley, H. Beuther, S. Bontemps, R. Cesaroni, L. Deharveng, G. Garay, F. Herpin, B. Lefloch, H. Linz, D. Mardones, V. Minier, S. Molinari, F. Motte, L.-Å. Nyman, V. Reveret, C. Risacher, D. Russeil, N. Schneider, L. Testi, T. Troost, T. Vasyunina, M. Wienen, A. Zavagno, A. Kovacs, E. Kreysa, G. Siringo, and A. Weiß. ATLASGAL - The APEX telescope large area survey of the Galaxy at 870  $\mu\text{m}$ . *A&A*, 504:415–427, September 2009.
- F. Selman, J. Melnick, G. Bosch, and R. Terlevich. The ionizing cluster of 30 Doradus. III. Star-formation history and initial mass function. *A&A*, 347:532–549, July 1999.
- J. D. Simon, A. D. Bolatto, B. A. Whitney, T. P. Robitaille, R. Y. Shah, D. Makovoz, S. Stanimirović, R. H. Barbá, and M. Rubio. The *Spitzer* Survey of the Small Magellanic Cloud: Discovery of Embedded Protostars in the H II Region NGC 346. *ApJ*, 669:327–336, November 2007.
- G. Siringo, E. Kreysa, C. De Breuck, A. Kovacs, A. Lundgren, F. Schuller, T. Stanke, A. Weiss, R. Guesten, N. Jethava, T. May, K. M. Menten, H.-G. Meyer, M. Starkloff, and V. Zakosarenko. A New Facility Receiver on APEX: The Submillimetre APEX Bolometer Camera, SABOCA. *The Messenger*, 139:20–23, March 2010.
- M. F. Skrutskie, R. M. Cutri, R. Stiening, M. D. Weinberg, S. Schneider, J. M. Carpenter, C. Beichman, R. Capps, T. Chester, J. Elias, J. Huchra, J. Liebert, C. Lonsdale, D. G. Monet, S. Price, P. Seitzer, T. Jarrett, J. D. Kirkpatrick, J. E. Gizis, E. Howard, T. Evans, J. Fowler, L. Fullmer, R. Hurt, R. Light, E. L. Kopan, K. A. Marsh, H. L. McCallon, R. Tam, S. Van Dyk, and S. Wheelock. The Two Micron All Sky Survey (2MASS). *AJ*, 131:1163–1183, February 2006.

## Bibliography

- M. D. Smith and A. Rosen. Synthetic *Spitzer* Infrared Array Camera band maps from simulations of protostellar jets. *MNRAS*, 357:1370–1376, March 2005.
- M. D. Smith, B. O’Connell, and C. J. Davis. The excitation within the molecular hydrogen jets of the protostellar outflow HH 212. *A&A*, 466:565–577, May 2007.
- N. Smith. A census of the Carina Nebula - I. Cumulative energy input from massive stars. *MNRAS*, 367:763–772, April 2006a.
- N. Smith. Erratum: A census of the Carina Nebula - I. Cumulative energy input from massive stars. *MNRAS*, 368:1983–1984, June 2006b.
- N. Smith. The Structure of the Homunculus. I. Shape and Latitude Dependence from H<sub>2</sub> and [Fe II] Velocity Maps of  $\eta$  Carinae. *ApJ*, 644:1151–1163, June 2006c.
- N. Smith and K. J. Brooks. A census of the Carina Nebula - II. Energy budget and global properties of the nebulosity. *MNRAS*, 379:1279–1292, August 2007.
- N. Smith and K. J. Brooks. The Carina Nebula: A Laboratory for Feedback and Triggered Star Formation. In Reipurth, B., editor, *Handbook of Star Forming Regions, Volume II*, page 138, December 2008.
- N. Smith, M. P. Egan, S. Carey, S. D. Price, J. A. Morse, and P. A. Price. Large-Scale Structure of the Carina Nebula. *ApJ*, 532:L145–L148, April 2000.
- N. Smith, J. Bally, and K. J. Brooks. HH 666: The Axis of Evil in the Carina Nebula. *AJ*, 127:2793–2808, May 2004.
- N. Smith, K. G. Stassun, and J. Bally. Opening the Treasure Chest: A Newborn Star Cluster Emerges from Its Dust Pillar in Carina. *AJ*, 129:888–899, February 2005.
- N. Smith, J. Bally, and N. R. Walborn. HST/ACS H $\alpha$  imaging of the Carina Nebula: outflow activity traced by irradiated Herbig-Haro Jets. *MNRAS*, 405:1153–1186, June 2010a.
- N. Smith, M. S. Povich, B. A. Whitney, E. Churchwell, B. L. Babler, M. R. Meade, J. Bally, R. D. Gehrz, T. P. Robitaille, and K. G. Stassun. *Spitzer* Space Telescope observations of the Carina nebula: the steady march of feedback-driven star formation. *MNRAS*, 406:952–974, August 2010b.
- S. W. Stahler and F. Palla. *The Formation of Stars*. Wiley-VCH Verlag GmbH & Co. KGaA, 2004.
- M. Tapia, M. Roth, R. A. Vázquez, and A. Feinstein. Imaging study of NGC 3372, the Carina nebula - I. *UBVR IJHK* photometry of Tr 14, Tr 15, Tr 16 and Car I. *MNRAS*, 339:44–62, February 2003.
- R. I. Thompson, B. A. Smith, and J. J. Hester. Embedded Star Formation in the Eagle Nebula. *ApJ*, 570:749–757, May 2002.

- L. K. Townsley, P. S. Broos, Y.-H. Chu, M. Gagné, G. P. Garmire, R. A. Gruendl, K. Hamaguchi, M.-M. Mac Low, T. Montmerle, Y. Nazé, M. S. Oey, S. Park, R. Petre, and J. M. Pittard. The *Chandra* Carina Complex Project: Deciphering the Enigma of Carina's Diffuse X-ray Emission. *ApJS*, 194:15, May 2011a.
- L. K. Townsley, P. S. Broos, M. F. Corcoran, E. D. Feigelson, M. Gagné, T. Montmerle, M. S. Oey, N. Smith, G. P. Garmire, K. V. Getman, M. S. Povich, N. Ramage Evans, Y. Nazé, E. R. Parkin, T. Preibisch, J. Wang, S. J. Wolk, Y.-H. Chu, D. H. Cohen, R. A. Gruendl, K. Hamaguchi, R. R. King, M.-M. Mac Low, M. J. McCaughrean, A. F. J. Moffat, L. M. Oskinova, J. M. Pittard, K. G. Stassun, A. ud-Doula, N. R. Walborn, W. L. Waldron, E. Churchwell, J. S. Nichols, S. P. Owocki, and N. S. Schulz. An Introduction to the *Chandra* Carina Complex Project. *ApJS*, 194:1, May 2011b.
- R. J. Trumpler. Preliminary results on the distances, dimensions and space distribution of open star clusters. *Lick Observatory Bulletin*, 14:154–188, 1930.
- S. Van Dyk, M. Werner, and N. Silbermann. *Spitzer Space Telescope Handbook v2.1*. 2013. <http://irsa.ipac.caltech.edu/data/SPITZER/docs/spitzermission/missionoverview/spitzertelescopehandbook/>.
- R. Voss, P. Martin, R. Diehl, J. S. Vink, D. H. Hartmann, and T. Preibisch. Energetic feedback and  $^{26}\text{Al}$  from massive stars and their supernovae in the Carina region. *A&A*, 539:A66, March 2012.
- N. R. Walborn. Some characteristics of the  $\eta$  Carinae complex. *ApJ*, 179:517 et seq., January 1973.
- N. R. Walborn. The Stellar Content of the Carina Nebula. In V. Niemela, N. Morrell, and A. Feinstein, editors, *Revista Mexicana de Astronomia y Astrofisica Conference Series*, volume 2 of *Revista Mexicana de Astronomia y Astrofisica*, vol. 27, page 51, June 1995.
- N. R. Walborn, I. D. Howarth, D. J. Lennon, P. Massey, M. S. Oey, A. F. J. Moffat, G. Skalkowski, N. I. Morrell, L. Drissen, and J. W. Parker. A New Spectral Classification System for the Earliest O Stars: Definition of Type O2. *AJ*, 123:2754–2771, May 2002.
- J. Wang, E. D. Feigelson, L. K. Townsley, P. S. Broos, K. V. Getman, S. J. Wolk, T. Preibisch, K. G. Stassun, A. F. J. Moffat, G. Garmire, R. R. King, M. J. McCaughrean, and H. Zinnecker. A *Chandra* ACIS Study of the Young Star Cluster Trumpler 15 in Carina and Correlation with Near-infrared Sources. *ApJS*, 194:11, May 2011.
- B. A. Whitney, K. Wood, J. E. Bjorkman, and M. J. Wolff. Two-dimensional Radiative Transfer in Protostellar Envelopes. I. Effects of Geometry on Class I Sources. *ApJ*, 591:1049–1063, July 2003.
- B. A. Whitney, M. Sewilo, R. Indebetouw, T. P. Robitaille, M. Meixner, K. Gordon, M. R. Meade, B. L. Babler, J. Harris, J. L. Hora, S. Bracker, M. S. Povich, E. B. Churchwell, C. W. Engelbracht, B.-Q. For, M. Block, K. Misselt, U. Vijh, C. Leitherer, A. Kawamura, R. D. Blum, M. Cohen, Y. Fukui, A. Mizuno, N. Mizuno, S. Srinivasan, A. G. G. M. Tielens, K. Volk, J.-P. Bernard, F. Boulanger, J. A. Frogel, J. Gallagher, V. Gorjian, D. Kelly, W. B. Latter, S. Madden, F. Kemper, J. R. Mould, A. Nota, M. S.

## Bibliography

- Oey, K. A. Olsen, T. Onishi, R. Paladini, N. Panagia, P. Perez-Gonzalez, W. Reach, H. Shibai, S. Sato, L. J. Smith, L. Staveley-Smith, T. Ueta, S. Van Dyk, M. Werner, M. Wolff, and D. Zaritsky. *Spitzer* Sage Survey of the Large Magellanic Cloud. III. Star Formation and  $\sim 1000$  New Candidate Young Stellar Objects. *AJ*, 136:18–43, July 2008.
- A. P. Whitworth and H. Zinnecker. The formation of free-floating brown dwarves and planetary-mass objects by photo-erosion of prestellar cores. *A&A*, 427:299–306, November 2004.
- A. P. Whitworth, A. S. Bhattal, S. J. Chapman, M. J. Disney, and J. A. Turner. Fragmentation of shocked interstellar gas layers. *A&A*, 290:421–427, October 1994.
- J. P. Williams and L. A. Cieza. Protoplanetary Disks and Their Evolution. *ARA&A*, 49:67–117, September 2011.
- E. Winston, S. T. Megeath, S. J. Wolk, J. Muzerolle, R. Gutermuth, J. L. Hora, L. E. Allen, B. Spitzbart, P. Myers, and G. G. Fazio. A Combined *Spitzer* and *Chandra* Survey of Young Stellar Objects in the Serpens Cloud Core. *ApJ*, 669:493–518, November 2007.
- S. J. Wolk, P. S. Broos, K. V. Getman, E. D. Feigelson, T. Preibisch, L. K. Townsley, J. Wang, K. G. Stassun, R. R. King, M. J. McCaughrean, A. F. J. Moffat, and H. Zinnecker. The Chandra Carina Complex Project View of Trumpler 16. *ApJS*, 194:12, May 2011.
- E. L. Wright, P. R. M. Eisenhardt, A. K. Mainzer, M. E. Ressler, R. M. Cutri, T. Jarrett, J. D. Kirkpatrick, D. Padgett, R. S. McMillan, M. Skrutskie, S. A. Stanford, M. Cohen, R. G. Walker, J. C. Mather, D. Leisawitz, T. N. Gautier, III, I. McLean, D. Benford, C. J. Lonsdale, A. Blain, B. Mendez, W. R. Irace, V. Duval, F. Liu, D. Royer, I. Heinrichsen, J. Howard, M. Shannon, M. Kendall, A. L. Walsh, M. Larsen, J. G. Cardon, S. Schick, M. Schwalm, M. Abid, B. Fabinsky, L. Naes, and C.-W. Tsai. The Wide-field Infrared Survey Explorer (WISE): Mission Description and Initial On-orbit Performance. *AJ*, 140:1868, December 2010.
- Y. Yonekura, S. Asayama, K. Kimura, H. Ogawa, Y. Kanai, N. Yamaguchi, P. J. Barnes, and Y. Fukui. High-Mass Cloud Cores in the  $\eta$  Carinae Giant Molecular Cloud. *ApJ*, 634:476–494, November 2005.
- P. Zeidler. A deep near-infrared survey of the Carina Nebula with the VISTA telescope. Master’s thesis, Ludwig-Maximilians-Universität München, September 2013.
- H. Zinnecker and H. W. Yorke. Toward Understanding Massive Star Formation. *ARA&A*, 45:481–563, September 2007.

# List of Figures

2.1	Hertzsprung-Russell diagram. . . . .	15
2.2	Artists impression of a YSO with disk. . . . .	18
2.3	YSOs classes. . . . .	19
3.1	Clusters in the CNC . . . . .	26
3.2	HST image of the ionisation front bordering NGC 3324 . . . . .	27
3.3	WFI image of the central CN. . . . .	29
3.4	HAWK-I NIR image of the CN. . . . .	30
4.1	<i>Spitzer</i> instrument wavelength ranges. . . . .	37
4.2	IRAC bandpasses. . . . .	39
4.3	IRAC sensitivity. . . . .	40
4.4	IRAC instrument layout. . . . .	41
4.5	Overview: CNC multi-wavelength study fields. . . . .	43
4.6	Magnitude histograms for the WISE All-Sky Data Release in the environs of the CNC. . . . .	46
4.7	Evolutionary tracks on WISE colour-magnitude diagrams. . . . .	47
4.8	Comparison: Resolution of 2MASS and HAWK-I. . . . .	49
5.1	Overlapping apertures in a crowded field. . . . .	53
5.2	Overview: IRAC astronomical observation requests (AORS) . . . . .	55
5.3	Outline of the AORS. . . . .	56
5.4	Mosaicker and Point source Extractor (MOPEX): Image segmentation . . . . .	57
5.5	MOPEX: Image interpolation . . . . .	59
5.6	PAHs in the IRAC bands. . . . .	65
5.7	Magnitude histograms for the SPSC in the full CNC. . . . .	66
5.8	Evolutionary tracks on IRAC colour-magnitude diagrams. . . . .	67
5.9	BSC and SPSC in the Treasure Chest. . . . .	69
5.10	Photometry differences between BSC and Smith et al. [2010b] . . . . .	70
5.11	Position offsets between BSC and Smith et al. [2010b] . . . . .	71
5.12	Photometry differences between SPSC and Smith et al. [2010b] . . . . .	71
6.1	Colour-colour diagram using all <i>Spitzer</i> IRAC bands. . . . .	74
6.2	Colour-colour diagram using three <i>Spitzer</i> IRAC bands. . . . .	75
6.3	Testing different magnitude cuts for the SYCC . . . . .	76
6.4	Colour-colour diagram using three WISE bands. . . . .	79
6.5	Magnitude differences between PCYC and SYCC. . . . .	82
6.6	Comparing magnitude histograms for PCYC and SYCC. . . . .	83
6.7	Comparing magnitude histograms for PCYC and SYCC after reduction. . . . .	84
6.8	Comparing colour-colour diagrams for PCYC and SYCC. . . . .	84

List of Figures

6.9	Comparing colour-colour diagrams for PCYC and SYCC after reduction. . . . .	85
6.10	Comparing the SYCC and the PCYC. . . . .	86
7.1	Overview: Jet sources in the CNC . . . . .	91
7.2	HH903 in <i>Hubble</i> Space Telescope (HST) H $\alpha$ and <i>Spitzer</i> 4.5 $\mu$ m . . . . .	93
7.3	HH jets with IR sources . . . . .	99
7.4	MHOs with IR sources . . . . .	100
7.5	EGOs with IR sources. . . . .	101
7.6	Model parameters derived from SED fits. . . . .	102
7.7	CGOs with IR sources. . . . .	103
7.8	SEDs of jet sources . . . . .	104
8.1	The Gum 31 region and its connection to the central CN . . . . .	109
8.2	Overview of the Gum 31 region . . . . .	110
8.3	Magnitude histograms for the SPSC in Gum 31. . . . .	112
8.4	Colour-temperature map and hydrogen column-density map. . . . .	114
8.5	Colour-colour diagram using all <i>Spitzer</i> IRAC bands. . . . .	116
8.6	Colour-colour diagram for WISE . . . . .	117
8.7	<i>Herschel</i> point-like sources . . . . .	119
8.8	WISE-identified cYSOs . . . . .	120
8.9	cYSOs found in the tips of pillars . . . . .	122
8.10	Close-up of the VISTA <i>H</i> -band image within the cluster G286.21+0.17 . . . . .	124
8.11	Cluster G286.21+0.17 and its immediate surroundings from NIR to FIR . . . . .	124
8.12	Cluster G286.38–0.26 from NIR to FIR . . . . .	126
8.13	SEDs for cYSOs in Gum 31 . . . . .	131
8.14	The HH jets and their probable sources . . . . .	134
9.1	Overview: Comparison regions to correct for YSO catalogue contamination. . . . .	138
9.2	SYCC cYSOs and <i>Herschel</i> -identified pre- and protostellar objects . . . . .	140
9.3	Density of SYCC cYSOs in the CNC (large-scale). . . . .	142
9.4	Density of SYCC cYSOs in the CNC (small-scale). . . . .	143
9.5	Density of SYCC cYSOs in the CNC (nearest neighbour). . . . .	144
9.6	Finding clusters: Histogram and map . . . . .	146
9.7	The cYSO clusters in the CNC. . . . .	148
9.8	The cYSO clusters in the Gum 31 region. . . . .	149
9.9	cYSOs in the Gum 31 region. . . . .	151
9.10	Cluster No. 7. . . . .	152
9.11	Cluster No. 4 in the vicinity of NGC 3324. . . . .	154
9.12	Cluster No. 3 inside the Gum 31 bubble. . . . .	155
9.13	cYSOs associated with G286.21+0.17. . . . .	156
9.14	Cluster No. 1. . . . .	157
9.15	Cluster No. 14, associated with Tr 14. . . . .	158
9.16	Cluster No. 10 between Tr 14 and Tr 15. . . . .	159
9.17	Cluster No. 15, associated with Tr 15. . . . .	159
9.18	Cluster No. 16, associated with Tr 16. . . . .	160
9.19	Clusters No. 13 and 17 near Tr 16. . . . .	161
9.20	cYSO clusters inside the South Pillars. . . . .	162

9.21	Close-up on Cluster No. 25. . . . .	163
9.22	Cluster No. 22, north of the South Pillars. . . . .	163
9.23	Cluster No. 23, to the east of the South Pillars. . . . .	164
9.24	Cluster No. 26 within a cavity in the South Pillars. . . . .	164
9.25	Cluster No. 27 in the foot of the Giant Pillar. . . . .	165
9.26	Cluster No. 28 to the south-east of the Giant Pillar. . . . .	166
9.27	cYSOs in the Giant Pillar. . . . .	172
B.1	Colour-colour diagram WISE: Removing galaxies. . . . .	177
B.2	Colour-colour diagram WISE: Removing AGN. . . . .	178
B.3	Colour-colour diagram WISE: Removing PAH regions. . . . .	179
B.4	Colour-colour diagram WISE: Removing shock emission knots. . . . .	180
C.1	Reducing the PCYC. . . . .	181
E.1	Cluster No. 2 west of NGC 3324. . . . .	187
E.2	Cluster No. 5 to the east of the Gum 31 bubble. . . . .	188
E.3	Cluster No. 9 located between the central CN and Gum 31. . . . .	189
E.4	Cluster No. 6 towards the western edge of the CNC study field. . . . .	190
E.5	Cluster No. 8 towards the western edge of the CNC study field. . . . .	190
E.6	Cluster No. 29 towards the southern edge of the CNC study field. . . . .	191
E.7	cYSOs overdensity towards the southern edge of the CNC study field. . . . .	192
E.8	cYSO overdensity in a small arc. . . . .	193
F.1	X-ray clusters of Feigelson et al. [2011] . . . . .	194

# List of Tables

4.1	IRAC detector and image characteristics. . . . .	40
4.2	Completeness and sensitivity limits for WISE data. . . . .	45
5.1	Overview: IRAC observations . . . . .	54
5.2	Numbers of detected sources in the SPSC. . . . .	64
5.3	Completeness and sensitivity limits for IRAC observations. . . . .	68
7.1	Overview: Infrared detections for sources of jet objects . . . . .	92
7.2	Fluxes for sources of jet objects. . . . .	97
7.3	Model parameters for the jet sources . . . . .	105
8.1	Overview of observations with <i>Spitzer</i> , <i>Herschel</i> and VISTA in Gum 31. . . . .	111
8.2	Source fluxes. . . . .	128
8.3	Model parameters for the sources in Gum 31. . . . .	133
9.1	Clusters of IRAC cYSOs. . . . .	150